Fakultät für Maschinenwesen
Lehrstuhl für Angewandte Mechanik

Nonlinear Model Order Reduction and Substructuring for Structural Dynamics Analysis

Non-intrusive Methods

Morteza Karamooz Mahdiabadi

Vollständiger Abdruck der von der Fakultät für Maschinenwesen der Technischen Universität München zur Erlangung des akademischen Grades eines

Doktor-Ingenieurs (Dr.-Ing.)

genehmigten Dissertation.

Vorsitzender: Prof. Phaedon-Stelios Koutsourelakis, Ph.D.

Prüfer der Dissertation:

1. Prof. Dr. ir. Daniel J. Rixen

2. Prof. Matthew S. Allen, Ph.D.

Die Dissertation wurde am 27.06.2019 bei der Technischen Universität München eingereicht und durch die Fakultät für Maschinenwesen am 02.10.2019 angenommen.

Acknowledgement

This dissertation is the result of my research work from 2014 to 2019 at the Chair of Applied Mechanics, Technical University of Munich. Many people have helped and supported me to successfully finish this research work and I would like to sincerely thank all of them.

First off, I would like to thank Prof. Daniel Rixen for giving me the opportunity to do my PhD at the Chair of Applied Mechanics, and also for all the discussions that we had during my work. I learned from him a lot of lessons in the field of structural dynamics and applied mechanics. He also inspired me with his open mindedness, patience and hardworking attitude during the time I worked under his supervision.

Many thanks to the examination committee for taking time and reviewing this dissertation. Special thanks to Prof. Matt Allen for his comments to improve this work.

I had a great time at the Chair of Applied Mechanics during my PhD work in a helpful and friendly atmosphere, because of my great colleagues. I would like to thank them for all of their helps, our discussions, and also for making me enjoy my time at the Chair. My special gratitude to Andreas Bartl, Christian Meyer, Eva-Maria Dewes, Andreas Krinner, Michael Leistner, Christian Wagner, Andreas Seibold, Michael Häußler, Ahmed El Mahmoudi, Tobias Berninger and Georg Mayr for their helps and the nice time we had together.

I also had a chance to supervise many great and talented students during my work at the Chair, whom their discussions and collaborations made me significantly improve my research work. My sincere appreciations go to my students Duo Xu, Erhard Buchmann, Yongle Qi, Philipp Schaefer, Antoine Brandt and Francesco De crecenso.

Finally and foremost, I would like to thank my parents for their love, prayers and endless support during my whole life. I express my endless gratitude to my wife, Zahra, who did more than here share during the toughest times in our life and always supported me with love. Words are unable to reflect what I feel about her in my heart and I just owe her a lot. I dedicate this dissertation to my wife, Zahra, and my two daughters, Kosar and Zeinab.

Zurich, October 28, 2019 *Morteza Karamooz Mahdiabadi*

Abstract

Model order reduction approaches speed up the design and analysis of high-dimensional finite element problems by reducing their size while approximately maintaining the same behavior as the full-order finite element model. As industrial structures such as wind turbines or air vehicles become more complex, it is crucial to include non-linear effects in their finite element models for a realistic representation. However, dynamic analysis of large nonlinear structures is a computationally expensive and sometimes inadmissible exercise, demanding model reduction for their investigation. A few challenges exist in model reduction of nonlinear finite element models: 1. How can one reduce a nonlinear model when it is developed in a commercial finite element package, which often is the case for industrial applications? 2. Which reduction basis is very accurate, easy to compute, and robust for different loading conditions? To cope with the first challenge, non-intrusive model order reduction methods are presented in the first part of this dissertation. We investigate several basis selection methods for non-intrusive model reduction and develop three different bases for different non-intrusive approaches. We apply our proposed methods to various flat and curved structures and show that our developed reduction bases present accurate and efficient results.

Furthermore, when a nonlinear multi-component structure is under investigation, whose different components contain numerous degrees-of-freedom and they are developed by different parties in parallel, it is usually not possible to reduce the model of the structure monolithically. Therefore, nonlinear substructuring methods are introduced, which decompose the multi-component structure into smaller components (or substructures), reduce the model of each component independently, and finally assemble the nonlinear reduced order models of all substructures to build the reduced model of the whole assembly. The second part of this work investigates non-intrusive modal substructuring of nonlinear structures. We first develop a nonlinear substructuring based on an augmented free-interface method with interface reduction as an alternative of nonlinear Hurty/Craig-Bampton method. Afterwards, we develop a non-intrusive-based nonlinear substructuring approach based on modal derivatives that remedy some limitations of other methods. We apply our proposed methods to different nonlinear multi-component examples and confirm their improvements by dynamic validations under random sound pressures.

Zusammenfassung

Ansätze zur Modellordnungsreduktion beschleunigen die Analyse hochdimensionaler Finite-Elemente-Probleme, indem sie deren Größe reduzieren und dabei etwa das gleiche Verhalten wie das Finite-Elemente-Modell des detaillierten Models beibehalten. Da industrielle Strukturen wie Windkraftanlagen oder Luftfahrzeuge immer größer und komplexer werden, werden nichtlineare Effekte immer wichtiger, um realitätsnahe Finite Elemente Modelle zu erhalten. Die dynamische Analyse großer nichtlinearer Strukturen ist jedoch eine (teils zu) rechenintensive Aufgabe, die eine Modellreduktion für ihre Untersuchung erfordert. Einige Herausforderungen bestehen in der Modellreduktion von nichtlinearen Finite-Elemente-Modellen: 1. Wie kann man ein nichtlineare Modell reduzieren, wenn es in einem kommerziellen Finite-Elemente-Paket entwickelt wird, was bei industriellen Anwendungen oft der Fall ist? 2. Welche Reduktionsbasis ist einfach zu berechnen und liefert trotzdem gute Ergebnisse für unterschiedliche Belastungsbedingungen? Um die erste Herausforderung zu bewältigen, werden im ersten Teil dieser Arbeit nicht-intrusive Methoden zur Modellordnungsreduktion vorgestellt. Wir untersuchen mehrere Basisauswahlmethoden zur nicht-intrusiven Modellreduktion und entwickeln drei verschiedene Reduktionsbasen. Wir wenden unsere vorgeschlagenen Methoden auf verschiedene flache und gekrümmte Strukturen an und zeigen, dass unsere entwickelten Reduktionsbasen genaue und effiziente Ergebnisse liefern.

Darüber hinaus ist es bei der Untersuchung einer nichtlinearen Mehrkomponentenstruktur, deren verschiedene Komponenten zahlreiche Freiheitsgrade enthalten und die von verschiedenen Parteien parallel entwickelt werden, in der Regel nicht möglich, das Modell der Struktur monolithisch zu reduzieren. Daher werden nichtlineare Substrukturierungsmethoden eingeführt, die die Mehrkomponentenstruktur in kleinere Komponenten (oder Substrukturen) zerlegen, das Modell jeder Komponente unabhängig voneinander reduzieren und schließlich die nichtlinearen Modelle reduzierter Ordnung aller Substrukturen zusammensetzen, um das reduzierte Modell der gesamten Baugruppe aufzubauen. Der zweite Teil dieser Arbeit untersucht die nicht-intrusive modale Substrukturierung nichtlinearer Strukturen. Zuerst entwickeln wir eine nichtlineare Substrukturierung auf Basis der augmentierten Free-Interface-Methode mit Schnittstellenreduktion als Alternative zur nichtlinearen Hurty/Craig-Bampton-Methode. Anschließend entwickeln wir einen nicht-intrusiven nichtlinearen Substrukturierungsansatz auf Basis modaler Ableitungen, welcher bestimmte Grenzen anderer Methoden aufhebt. Wir wenden unsere Methoden auf verschiedene nichtlineare Mehrkomponenten-Beispiele an und bestätigen deren Verbesserungen durch dynamische Validierungen unter zufälligem Schalldruck.

Contents

1 Introduction **1**
- 1.1 Motivation . . . 1
- 1.2 Nonlinear model order reduction: Intrusive vs. Non-intrusive . . . 4
- 1.3 Basis selection for non-intrusive ROM . . . 8
- 1.4 Nonlinear dynamic substructuring . . . 9
- 1.5 Scope of the work . . . 12
- 1.6 Own contributions . . . 13

I Nonlinear model order reduction **15**

2 Fundamentals of nonlinear full- and reduced-order FE models **17**
- 2.1 Introduction . . . 17
- 2.2 Strong and weak forms for for structural dynamic problems . . . 17
- 2.3 Discretization using finite element formulation . . . 18
- 2.4 Nonlinear model order reduction . . . 20
- 2.5 Solution techniques . . . 21
  - 2.5.1 Static analysis . . . 22
  - 2.5.2 Dynamic analysis . . . 23
- 2.6 Validation of nonlinear ROMs . . . 26
  - 2.6.1 Random response prediction . . . 28
  - 2.6.2 Power spectral density . . . 28

3 Force-based non-intrusive MOR **31**
- 3.1 Introduction . . . 31
  - 3.1.1 Implicit Condensation . . . 32
  - 3.1.2 Expansion of the membrane DOFs . . . 34
- 3.2 Basis Selection Methods . . . 36
  - 3.2.1 Mode Displacement . . . 36
  - 3.2.2 Mode Acceleration Correction . . . 38
  - 3.2.3 Modal Truncation Augmentation . . . 39
- 3.3 Numerical Example . . . 40
- 3.4 Summary . . . 44

4 Displacement-based non-intrusive MOR **47**
- 4.1 Introduction . . . 47
- 4.2 Non-intrusive model order reduction . . . 48
  - 4.2.1 Enforced Displacement . . . 49

4.2.2 Enhanced Enforced Displacement 51
4.3 Basis selection: simulation-free methods 54
4.3.1 Linear vibration modes 54
4.3.2 Dual modes 55
4.3.3 Modal derivatives: a new basis for non-intrusive ROM 57
4.4 Numerical examples 60
4.4.1 Beam models 61
4.4.2 Panel model 73
4.5 Remarks on displacement-based non-intrusive MOR 79
4.6 summary 81

5 Evaluation and comparison of non-intrusive NLROMs 83
5.1 Examples 84
5.1.1 Shallow-curved model 85
5.1.2 Deep-curved model 87
5.2 Concluding remarks on non-intrusive ROM methods 87
5.3 Summary 89

II Nonlinear dynamic substructuring 91

6 Common linear substructuring methods: primal assembly 93
6.1 Introduction 93
6.2 Fixed-interface method 93
6.2.1 Hurty/Craig-Bampton basis 95
6.3 Free-interface mode methods 96
6.3.1 Goldman-Hou basis 99
6.3.2 Augmented free-interface: MacNeal/Rubin-Martinez basis . . . 100
6.4 Interface Reduction for free- and fixed-interface methods 101
6.4.1 System level interface reduction 102
6.4.2 Local level interface reduction 103
6.5 Primal assembly of linear substructures 106
6.6 Numerical example 108
6.6.1 Simply supported beams 108
6.6.2 Coupling of two panel models 110
6.7 Summary 113

7 Non-intrusive nonlinear substructuring based on ICE 115
7.1 Introduction 115
7.2 Generalized Applied Force for MOR at substructure level 115
7.3 Nonlinear modal substructuring: primal assembly 118
7.4 Numerical examples 119
7.4.1 Simply supported beams 119
7.4.2 Simply-supported panels 123
7.5 summary 129

8 Improving non-intrusive substructuring with modal derivatives 131
8.1 Introduction 131

8.2 Governing equations for substructures' ROMs 132
8.3 Enhanced Craig-Bampton reduction basis: non-intrusive approach . . . 133
8.4 Non-intrusive development of substructures' NLROMs 136
8.4.1 Enhanced Applied Force for substructuring 136
8.4.2 Enforced Displacement for substructuring 137
8.5 Coupling of substructures' NLROM 140
8.6 Application to beam models 141
8.7 Application on nonlinear panels 150
8.8 Summary 161

9 Evaluation of the nonlinear substructuring methods to arch models 163
9.1 Deep-curved arch 164

III Closure 167

10 Conclusion and future work 169
10.1 Summary and conclusion of part I 169
10.2 Summary and conclusion of part II 171
10.3 Future work 172
10.3.1 Non-intrusive MOR and substructuring with nonlinear manifold 173
10.3.2 Non-intrusive MOR for flexible multi-body systems 173
10.3.3 Modal derivative-based non-intrusive ROM and substructuring under thermal field 173
10.3.4 Modal derivative-based nonlinear substructuring with free-interface modes 174

A Construction of static equations for ICE method 183

B Supplementary plot of Chapter 8 185

Bibliography 187

Nomenclature

Operators

$\dot{(\cdot)}$	...	time derivative	$(\cdot)^T$	...	transpose
$\ddot{(\cdot)}$	...	second time derivative	$(\cdot)^{-1}$	...	inverse
$+$	...	least squares	$null$	...	null space
$BlockDiag$	...	block diagonalize			

Greek Letters

β	...	Newmark parameter	ϵ	...	error
γ	...	Newmark parameter	θ	...	(static) modal derivative
ϕ	...	eigenmode	Ω	...	diagonal eigenvalue matrix
∇	...	gradient operator	∇	...	gradient operator
ω	...	eigenfrequency	Φ	...	matrix of eigenmodes
σ	...	Cauchy stress tensor	Φ_{mt}	...	matrix of MTA vectors
ρ	...	density	Ψ	...	matrix of constraint modes

Latin Letters

h_k	...	element shape function	S_x	...	power spectral density
h	...	increment	s	...	second
m	...	number	s_i	...	scaling factor
n	...	number	V	...	volume
R_x	...	auto correlation	W_i	...	maximum desired displacement
S	...	surface			

Boldface Latin Letters

$\ddot{\boldsymbol{a}}$	...	body acceleration
$\boldsymbol{B}$	...	Boolean matrix
$\boldsymbol{d}_k$	...	node displacement vector
$\boldsymbol{D}$	...	damping matrix
$\hat{\boldsymbol{D}}$	...	reduced damping matrix
$\boldsymbol{D}^t$	...	tangent damping matrix
$\boldsymbol{f}$	...	applied force vector
$\hat{\boldsymbol{f}}$	...	reduced applied force vector
$\boldsymbol{f}_{int}$	...	restoring force
$\boldsymbol{g}$	...	interface force/body force
$\boldsymbol{J}$	...	Jacobian matrix
$\hat{\boldsymbol{K}}$	...	reduced stiffness matrix
$\boldsymbol{K}^{(2)}$	...	quadratic stiffness coefficient tensor
$\hat{\boldsymbol{K}}^{(2)}$	...	reduced quadratic stiffness coefficient tensor
$\boldsymbol{K}^{(3)}$	...	cubic stiffness coefficient tensor
$\hat{\boldsymbol{K}}^{(3)}$	...	reduced cubic stiffness coefficient tensor
$\boldsymbol{K}$	...	stiffness matrix
$\boldsymbol{K}^t$	...	tangent stiffness matrix
$\boldsymbol{L}_e$	...	element localization matrix
$\boldsymbol{L}$	...	localization matrix
$\boldsymbol{M}$	...	mass matrix
$\hat{\boldsymbol{M}}$	...	reduced mass matrix
$\boldsymbol{n}$	...	normal vector to surface
$\boldsymbol{P}_{IR}$	...	inertial relief projection matrix
$\boldsymbol{q}$	...	modal displacement vector
$\dot{\boldsymbol{q}}$	...	modal velocity vector
$\ddot{\boldsymbol{q}}$	...	modal acceleration vector
$\boldsymbol{Q}_1(\boldsymbol{q})$	...	quadratic stiffness tensor
$\boldsymbol{Q}_2(\boldsymbol{q})$	...	cubic stiffness tensor
$\hat{\boldsymbol{r}}$	...	vector of residuals
$\boldsymbol{t}$	...	surface traction
$\boldsymbol{T}$	...	substructure reduction basis
$\boldsymbol{u}$	...	displacement vector
$\dot{\boldsymbol{u}}$	...	velocity vector
$\ddot{\boldsymbol{u}}$	...	acceleration vector
$\boldsymbol{V}$	...	monolithic reduction basis
$\boldsymbol{V}_m$	...	membrane transformation basis
$\boldsymbol{W}$	...	maximum modal interaction matrix

Abbreviations

AF	...	Applied Force
BVP	...	Boundary Value Problem
CM	...	Constraint Modes
CMS	...	Component Mode Synthesis
DOF	...	Degree of Freedom
EC	...	Exact Compatibility
ED	...	Enforced Displacement
EED	...	Enhanced Enforced Displacement
EHCB	...	Enhanced Hurty/Craig-Bampton
EOM	...	Equation of Motion
Eq	...	Equation
FE	...	Finite Element
Fig.	...	Figure
FT	...	Fourier Transform
GH	...	Goldman-Hou
HCB	...	Hurty/Craig-Bampton
ICE	...	Implicit Condensation and Expansion
IR	...	Interface Reduction
LL	...	Local Level
MA	...	Mode Acceleration
MMI	...	Maximum Modal Interaction
MOR	...	Model Order Reduction
MRM	...	MacNeal/Rubin-Martinez
MTA	...	Modal Truncation Augmentation
NLHCB	...	Nonlinear Hurty/Craig-Bampton
NLROM	...	Nonlinear Reduced Order Model
NNM	...	Nonlinear Normal Mode
NSC	...	Nonlinear Stiffness Coefficient
ODE	...	Ordinary Differential Equation
RBM	...	Rigid Body Modes
RFA	...	Residual Flexibility Attachment
ROM	...	Reduced Order Model
SL	...	System Level
SPL	...	Sound Pressure Level
SVD	...	Singular Value Decomposition
Tol	...	Tolerance
VM	...	Vibration Mode
WC	...	Weak Compatibility

Chapter 1

Introduction

This Chapter is partly extracted from the author's work in [65]. In this article, Karamooz had the idea of the work and performed the literature review. Karamooz implemented a considerable part of the work and wrote the manuscript. Xu conducted the primary part of numerical studies and discussed the work. Bartl, Tiso and Rixen gave useful inputs in the discussions of the work and proof-read the article. Rixen supervised the work. Furthermore, this dissertation is mainly based on the author's works in [65–68, 70, 71]

1.1 Motivation

The rapid development of technologies has led to the production of large and complex structural systems, which require an ever increasing computational power for their design and analysis. Despite the exponential growth in the computer's performances, predicted by Moore [101], the required computational power outgrowth the development of computer's developments. Therefore, it is calling for the development of numerical methods, which reduce the computational costs while maintaining the high accuracy of the analysis.
One of the very efficient ways to reduce the computational costs and simultaneously keep high accuracies in the design and analysis of large engineering problems is *Model Order Reduction* (MOR). The idea of MOR is to approximate the motion of a large engineering problem with a high dimension by a Reduced Order Model (ROM) that contain a significantly reduced dimension. The ROM is expected to have almost the same behavior as the full-dimensional problem in a static or dynamic analysis with much less computational burden than the full-order system. While MOR approaches have been investigated in a variety of fields of studies e.g. electrical engineering [8, 24, 41, 53, 139], control theory [79, 89, 100, 140], fluid dynamics [3, 16, 86, 123], etc., the focus of the present work is the investigation and development of MOR methods in structural dynamics engineering problems.
To analyze the dynamics of a complex structure, it is commonly discretized to numerous Degrees-Of-Freedom (DOFs) using the Finite Element (FE) method [6, 12, 13, 42, 161] with a fine mesh to capture all design properties of the model. The FE model of the structure is then either simulated directly to obtain the time response of the system (which is computationally expensive or inadmissible) or reduced to a compact ROM, which can be rapidly analyzed and simulated. As a result, engineers can take advantage of such detailed models with numerous number of DOFs and simultaneously avoid prohibitively expensive computational costs of their simulation by reducing the DOFs of the model.

Figure 1.1: Schematic of the Helios prototype in idle (down configuration) and operating (above configuration) conditions [110, 156]

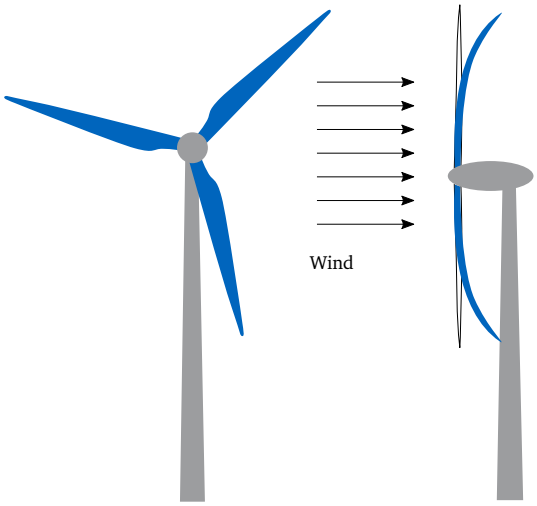

Figure 1.2: Schematic of deformation of wind turbine blades under wind flow.

Since more than half a century, linear MOR techniques in structural dynamics have been widely investigated, developed and applied to many linear structural dynamics problems, see e.g. [1, 4, 9, 34, 49]. However, linear modeling for some systems under certain conditions and loading levels do not apply anymore. Instead, nonlinear models have to be developed and investigated in these cases, which is generally more computationally expensive. Nonlinearity in structural dynamics can have a variety of sources and forms, of which nonlinear constitutive law for material [10, 43, 108], geometric nonlinearity [5, 59, 106, 160], nonlinear damping [32, 74], contact [87, 143], multi-physical interactions [97, 117, 142] are some examples. In this work, we mainly consider the nonlinear structural problems with linear material properties and geometric nonlinearity, which is caused by large deformations in the system.
Geometric nonlinearity occurs in many applications such as automotive [77, 109], wind energy [90, 127, 168] or air vehicle [11, 46] industries, which comprise for instance thin-walled and/or light weight components operating under relatively high level of excitation. As an example, Fig. 1.1 shows the Helios Prototype air vehicle [110, 156], which can operate in high altitudes using solar energy produced by high efficiency solar cell that are deviced across the upper surface of its wings. Investigating such structures is important due to its potential to pave the path for further technologies in *green* airplanes, which operate with solar energies. As it can be seen in Fig. 1.1, the aircraft is almost straight in idle condition, while it exhibits large deformations during operating conditions, making it necessary to consider geometric nonlinear effect in its dynamic analysis.
As the second example of structures with geometrically nonlinear effect, consider the schematic of a multi-megawatt wind turbine of Fig. 1.2. Since many countries have aimed to supply larger parts of their energy from *renewable* sources [1], it has become more demanding to develop and optimize wind turbine structures. The blades of wind turbines are made of thin-walled composite materials that make them exhibit large deformation under high speed of wind loading, as shown in Fig. 1.2.

[1] As an example, the European Commission has targeted to supply 20% of its total energy from renewable sources [38] by 2020.

Accordingly, to develop and analyze these nonlinear structures, a number of nonlinear MOR techniques have been developed in recent decades. One efficient nonlinear MOR approach is to develop a NonLinear Reduced Order Model (NLROM), independent from nonlinear element formulations of the FE code. This approach is especially beneficial when the full-order model is built in a FE analysis package, provided by a third party, which do not release the internals of its code, (for instance, commercial FE software). This MOR approach is known as *non-intrusive* or *indirect* approach, which has been successfully applied to many applications [47, 114, 116, 119, 120]. However, the research challenges in this approach are still reducing the computational costs for the development of NLROMs, and selecting "cheap" and accurate reduction bases. The first aim of this dissertation is to further develop non-intrusive methods to increase their accuracy as well as efficiency. Therefore, this work proposes four reduction bases for non-intrusive methods. These bases consist of two alternatives of non-intrusive *Modal Derivatives* (MDs), *Modal Truncation Augmentations* (MTA) and *Mode Acceleration* (MA) correction. It has been shown, that the proposed methods can increase the accuracy of the NLROMS while the computational efficiency is reduced or remained the same as before.
Furthermore, many large industrial products (e.g. consider wind turbine of Fig. 1.3) are composed of several components (or substructures), which can not be designed or analyzed monolithocally. This is because firstly several components of these structures are developed by different parties in parallel, who can not share all the information of their models due to commercial reasons. Secondly, the model of the whole structure is so large that it can not be reduced at once. As a result, *Dynamic substructuring* approaches have been investigated in recent decades to solve these problems. Dynamic substructuring (or Component Mode Synthesis (CMS)) enables engineers to decompose a large/complex dynamic model into smaller components (or substructures), reduce the model of each substructure separately, and couple the ROM of all substructures to build the ROM of the full-order structure, which is computationally practical. By reducing the model of a structure using dynamic substructuring the following advantages can be gained:

- It allows speeding up the model reduction process (offline time) as well as simulation time (online time) of the full-order model by performing parallel reduction of substructures as well as parallel time integration of the substructures' ROMs.
- It expedites optimization processes when only one substructure is under investigation, because the other substructures can be used unchanged.
- It facilitates collaboration of different companies and parties by letting them to shared a ROM of their developed substructure (instead of the whole model data) while keeping their confidentialities.
- It allows coupling of experimentally measured components with numerically derived FE model of substructures [37, 69].

While linear dynamic substructuring techniques have been widely developed in the 1960s and 1970s [25, 26, 28, 56–58, 88, 135], method development in substructuring of nonlinear systems have become an attractive field of study in recent years (e.g. see [85, 157, 163]). Therefore, the second purpose of this dissertation is to

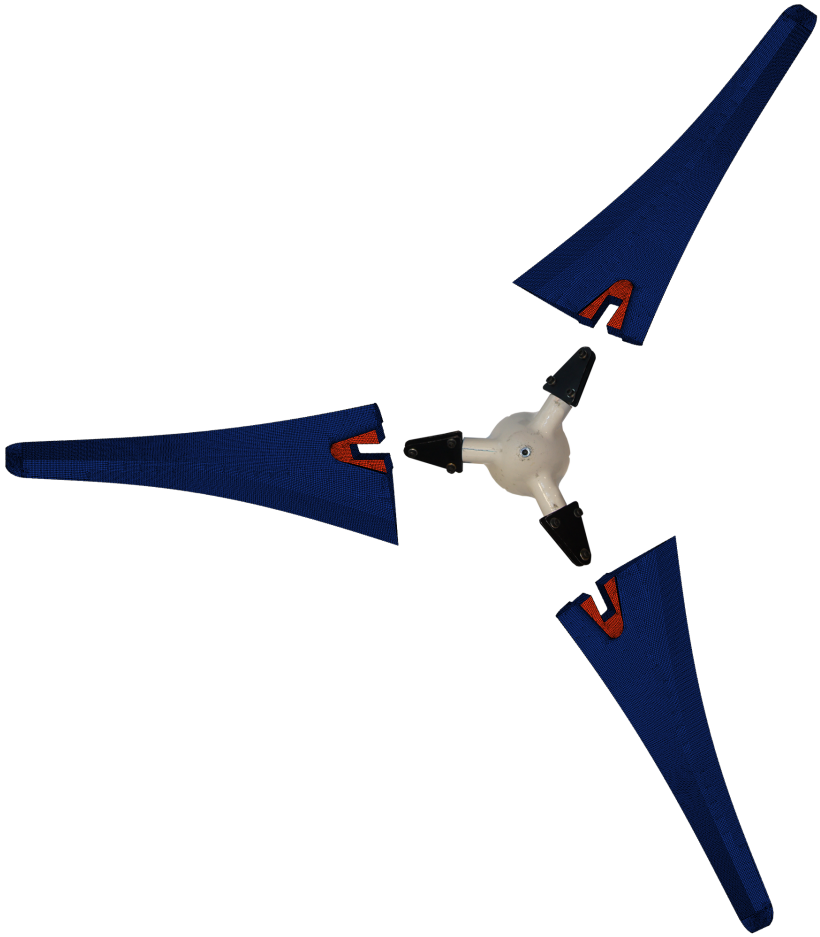

Figure 1.3: Schematic of the rotor assembly of the Ampair 600 wind turbine [37].

expand on the nonlinear dynamic substructuring methods in accuracy, persistency, and computational efficiency. The nonlinear substructuring methods investigated and developed in this work are based on non-intrusive MOR methods. Firstly, we have presented a free-interface-based reduction basis as an alternative for the already existing nonlinear substructuring approach. Secondly, we propose a novel dynamic substructuring method, which can be used under various loading conditions. We demonstrate in this dissertation that the proposed methods present accurate and robust results compared to the other non-intrusive-based substructuring methods.

1.2 Nonlinear model order reduction: Intrusive vs. Non-intrusive

Nonlinear modeling of many industrial structures are crucial to accurately predict their dynamic responses, which are computationally expensive to analyze, demanding MOR. However, nonlinear MOR of such structures often face two challenges. The first one is to find a convenient reduction basis that is easy to compute and represents the essential properties of the nonlinear full-order model accurately, which is more discussed in section 1.3. The second challenge is the determination of the reduced nonlinear internal forces (also known as restoring forces). To address the later challenge, nonlinear MOR methods can be classified into two categories depending

on how the nonlinear internal forces are reduced: *intrusive* and *non-intrusive* methods. The intrusive (or direct) methods [61, 144, 158] are based on obtaining the reduced internal forces by direct projection of the full-order nonlinear internal forces onto a reduced set of generalized (or modal) coordinates. These methods are usually efficient but require specialized codes that release access to the nonlinear element formulations or closed form Equations Of Motion (EOM).
In case a nonlinear reduced order model is to be developed in a direct approach the mass, damping and linear as well as nonlinear stiffness tensors are pre- and post-multiplied with a pre-selected reduction basis, $\boldsymbol{V}$, to build the NLROM. However, the computational cost to simulate the time histories from the NLROM is not extensively reduced, because computation of the reduced nonlinear internal forces as well as its Tangent Stiffness (TS) is still expensive for each time step. Let us consider the EOM for a geometric nonlinear FE model as

$$\boldsymbol{M}\ddot{\boldsymbol{u}}(t)+\boldsymbol{D}\dot{\boldsymbol{u}}(t)+\boldsymbol{f}_{int}(\boldsymbol{u}(t))=\boldsymbol{f}(t) \tag{1.1}$$

The schematic of the dimension of matrix operations for this equation and also after order reduction is shown in Fig. 1.4. As can be seen from this figure, the matrix operation of the reduced nonlinear internal vector is even more than the full-order one. Therefore, unlike the linear systems, only projection of the full order model to the set of reduced coordinates does not noticeably reduce the simulation time.

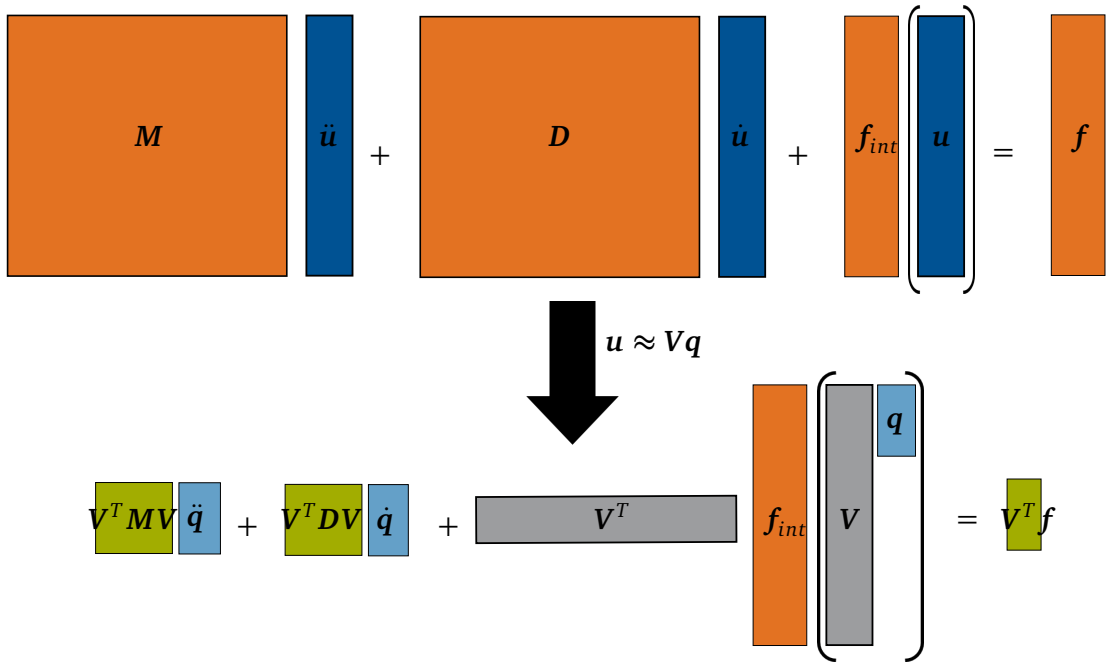

Figure 1.4: Schematic of the matrix operation for the full model and the NLROM.

Accordingly, a further step is investigated in literature to approximate the nonlinear internal forces. This approximation can be performed either using linearization methods [125, 126] or applying the so-called *hyper-reduction* methods, which can drastically speed up the computation of reduced restoring force vector at the cost of approximating it. There are a number of hyper-reduction methods developed in recent years such as Energy Conserving Sampling and Weighting (ECSW) [39], Discrete Empirical Interpolation Method (DEIM) [20] , or approximation through (Taylor) polynomial expansions, to name a few. The ECSW method is based on taking a

few weighted elements in the system, which have the highest contribution to approximate the virtual work of the nonlinear restoring forces due to specific excitations. Whereas, DEIM is based on the interpolation of the nonlinear restoring force under certain excitations, by computing it at a few well selected nodes. Furthermore, the coefficients of an approximation by polynomial expansion can be obtained by differentiation of the nonlinear restoring forces. While the hyper-reduction methods are efficient for many applications, they usually face three challenges:

1. Most of the hyper-reduction methods (e.g. ECSW, DEIM) are load-dependent approaches, meaning the hyper-reduced model is only appropriate for a special load case and as soon as the loading condition is changed, a new hyper-reduced model has to be developed for the system.

2. To apply most of the hyper-reduction methods, a closed form for EOM is required, which is only the case for specialized FE code (i.e. they are intrusive methods).

3. A dynamic simulation of the full-order model is generally required to perform common hyper-reduction methods, although some quasi simulation-free approaches have been recently proposed for certain cases, see [62, 137].

Alternatively, the non-intrusive methods [98] can be applied to any (commercial) FE analysis package, as long as the FE package is capable of performing nonlinear static analysis. Typically, the reduced nonlinear force is expressed as a vector-valued polynomial form of the modal amplitudes directly multiplied by unknown coefficients. For a geometric nonlinear structure, it is usually sufficient to expand the polynomials up to cubic terms. The unknown coefficients are called Nonlinear Stiffness Coefficients (NSCs), and are identified by the specific non-intrusive MOR technique at hand. All non-intrusive methods are based on prescribing selected inputs (either as forces or displacements) to the FE package and the corresponding output obtained from it. Then the NSCs are identified based on the given inputs and outputs, as shown in Fig. 1.5. As a result, the indirect methods seem to be efficient in case the structures are developed in commercial FE analysis packages (which is the case for many industrial applications), since there is no need to construct the nonlinear FE tensors of the full structure.
In the literature, two non-intrusive procedures are present to determine the NSCs. The first one is the force-based method called Applied Force (AF) or *Implicit Condensation* (IC) method, which was first introduced by McEwan et al. in [95, 96]. This method defines a set of representative static forces associated to combination of linear low frequency modes (which are typically transverse-dominated ones for shell-like structures) to be applied statically to the full model and solve for the corresponding nonlinear displacements. The displacements obtained in this way implicitly contain the nonlinear coupling between the modes (e.g. transverse-membrane coupling or stretching effect). Therefore, the NLROM developed in this way can accurately approximate the nonlinear dynamic response of transverse DOFs without using other ingredients in the identification procedure. To also correctly predict the response for the in-plane motion, Hollkamp and Gordon [54] proposed an extension to the IC method, known under the name of *Implicit Condensation and Expansion* (ICE).

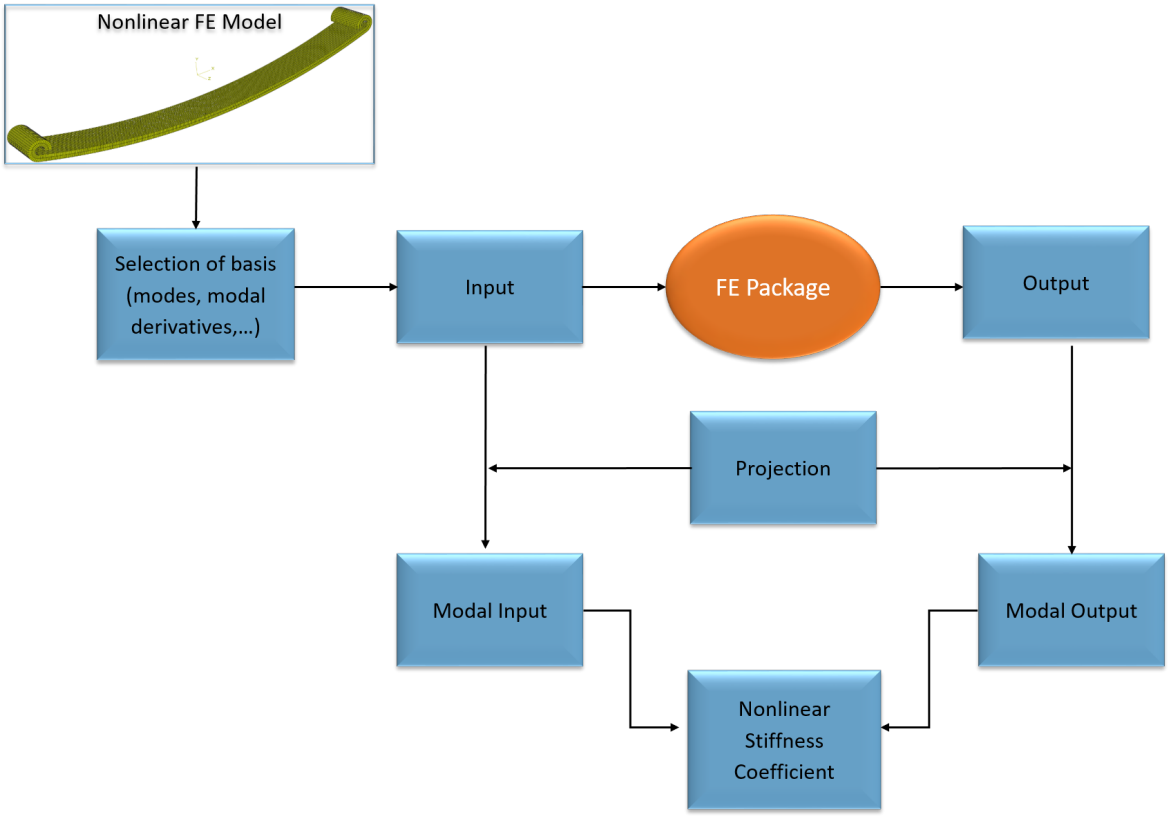

Figure 1.5: Work flow of non-intrusive model order reduction.

In fact, ICE retrieves the motion of membrane DOFs using the proposed post-processing by Hollkamp et al. [54], without adding more vectors to the reduction basis. However, this post-processing method is only valid when the relation between the transverse and membrane coordinates are quadratic (e.g. flat and shallow-curved structures). For instance, Spottswood et al. [150] discussed that the expansion part of the ICE method does not work for shallow-curved structures under thermal loads. This is due to the fact that the assumption of ICE for approximating the membrane motion is not fulfilled.

Another widely used non-intrusive MOR approach is the *Enforced Displacement* (ED) (also known as STEP (STiffness Evaluation Procedure)) method, which was first introduced by Muravyov and Rizzi [103] and later developed in [76, 116]. In this method, selected static displacements that trigger nonlinearity are prescribed to the model through the FE package. The FE package then computes the required reaction forces to create the statically assigned displacements and the NSCs are obtained by solving a set of linear equations given the input displacements and output forces. To reduce the number of required nonlinear static solutions, Perez et al. [116] used the Tangent Stiffness (TS) matrices due to assigned static displacements, instead of reaction forces for identifying the NSCs. They showed that in this way the number of needed nonlinear static solutions reduces significantly, leading to less offline computational costs for the development of NLROMs. The TS-based method of Perez et al. is called the *Enhanced Enforced Displacement* (EED) method here.

The basis vectors in (E)ED method have to feature displacement fields that properly account for in-plane and out-of-plane (stretching effect) coupling. We show in this

work that the (E)ED method (equipped with our proposed basis) does not have the restriction of ICE for estimating the membrane-dominated DOFs.

1.3 Basis selection for non-intrusive ROM

As discussed before, a challenge of developing an accurate and compact NLROM is the selection of a reduction basis. It is desired to consider the following properties while selecting a reduction basis for nonlinear ROMs:

- It must contain all the linear modes of the system in the frequency band of excitation.
- It must convey all necessary nonlinear properties of the system, including modal interactions between the modes.
- It should be compact enough to be able to reduce the computational costs after reduction.
- It should be computationally "cheap" to be obtained.
- It should be possibly obtained in a "load-independent" procedure, such that the resulting NLROM is valid for a variety of loading conditions.

One class of the reduction bases is the *data driven* approach. Proper Orthogonal Decomposition (POD) [22, 72] and Smooth Orthogonal Decomposition (SOD) [21] are two examples of this approach. Despite a very good accuracy that can be acquired using these methods, they convey two issues in their computation. The first problem is that these methods are based on a dynamic simulation of the full-order system, which is computationally expensive. The second issue is that these methods are load-dependent, meaning they are valid for one special load case and for different loading conditions they have to be recomputed. Alternatively, our purpose in this dissertation is to expand the so-called *simulation-free* approaches for non-intrusive ROM, which do not require a dynamic simulation of the full-order system.
The force-based non-intrusive ROM (IC) usually requires a truncated set of low-frequency linear Vibration Modes (VMs), which are transverse-dominated modes for shell-like structures, to develop NLROM. Although this basis does not contain membrane VMs, it can accurately develop the NLROM. This is because application of static forces based on transverse-dominated VMs already induces the nonlinear coupling between the modes (see [54, 95, 96]).
In some cases, where the system operates under certain load distributions, ICE can be improved by considering the effect of load distribution on the truncated VMs. In this work, we compute the (nonlinear) static contribution of the truncated modes due to an excitation, which is known as Modal Truncation Augmentation (MTA) for linear structures. The MTA modes are augmented to the linear modes in the reduction basis, to increase the accuracy of the NLROMs due to an special excitation. The MTA can in fact be seen as equivalent to dual modes but for ICE.
Furthermore, for the displacement-based methods, the first investigated reduction basis to reduce the linear matrices as well as identify the NSCs of the NLROM is taking

the linear Vibration Modes (VM), which is successfully applied to many applications, see e.g. [103, 119, 121]. However, the main disadvantage of this method is that keeping only the first few VMs, which are transverse-dominated modes, does not suffice to build an accurate NLROM. Rather, membrane-dominated modes, which are typically high-frequency modes, also have to be identified and augmented in the reduction basis. While manual identification of the important membrane-dominated VMs is a difficult but feasible work for simple structures, it becomes nearly impossible for complex structures.
To circumvent the manual selection of membrane modes required for displacement-based methods, the dual modes were proposed [76] and validated in some applications [93, 94, 116]. In fact, the concept of dual modes attempts to compute the coupling effect of the modes in a systematic way, using a set of representative static loads to obtain them. The dual modes are obtained by applying a set of representative static forces to the full-order FE model and obtaining the corresponding displacements. These displacements are then orthogonalized to the VMs and a POD analysis is performed to select the those vectors that have the maximum contribution in the system's response. However, by only looking at the POD vectors corresponding to maximum singular values, one might need a lot of dual modes in the reduction basis, which lead to relatively large NLROMs. Therefore, Perez et al. [115, 116] took only those dual modes that have the maximum contribution in a specific load case. This approach reduces the number of dual modes but the resulting NLROM is load-dependent.
In this work we propose *non-intrusive Modal Derivatives* (MDs) as a novel basis for displacement-based non-intrusive MOR techniques. We discuss that while the computation of MDs is easier than manual selection of membrane modes and dual modes, they deliver more accurate NLROMs in dynamic simulation of geometric nonlinear structures under random excitation. We present an approach to compute the MDs non-intrusively using finite different, which is a relatively cheap process and then select them in a load-independent manner. The NLROMs obtained with the proposed basis not only can be used under several loading conditions, but also increase the accuracy of the simulated time and frequency responses. The improvement obtained by our proposed method does not increase the offline and online computational costs.

1.4 Nonlinear dynamic substructuring

This section is extracted from the author's publication in [65]. In this article, Karamooz had the idea of the work and performed the literature review. Karamooz implemented a considerable part of the work and wrote the manuscript. Xu conducted the primary part of numerical studies and discussed the work. Bartl, Tiso and Rixen gave very useful inputs in the discussions of the work and proof-read the article. Rixen supervised the work.

Large and complex structures usually comprise many components that are designed by different parties and cannot be reduced or analyzed monolithically. Therefore, the *Component Modes Synthesis* (CMS) approach (also known as Dynamic Substructuring (DS)) has been widely studied in the last decades to improve analysis efficiency and enable parallel computing. The idea behind the CMS method is that a large struc-

ture is decomposed into smaller components (or substructures). Each substructure is reduced or analyzed separately using its component modes, and finally, the reduced models of all substructures are coupled through their interfaces to build up the ROM of the assembly.
The component modes (or reduction bases) used in the CMS techniques may be classified to fixed, free, and hybrid interface mode methods [25]. The first CMS method was introduced in the 1960s by Hurty [57, 58], which is a fixed-interface mode method. His method comprises a set of truncated fixed-interface modes in addition to Rigid Body Modes (RBMs) and Constraint Modes (CMs). This method was later modified by Craig and Bampton [26] who showed that if the CMs of all interface DOFs are included in the reduction basis, RBMs can be omitted from the reduction basis without losing accuracy. In this work, we refer to the method proposed in [26] as the *Hurty/Craig-Bampton* (HCB) method, since it is also based on the work of Hurty. While the classical HCB method has been extensively used and studied because of its simplicity, two main remarks should be made for this method:

1. To compute or measure the fixed-interface modes, the interface needs to be constrained, making testing challenging.
2. The set of interface DOFs for the reduced model remains the same as the original one.

As an alternative to the fixed-interface CMS method, the free-interface mode method was proposed by Goldman [45] and Hou [56], which is called the Goldman-Hou (GH) method here. In this method, a truncated number of free interface modes in addition to the RBMs are chosen in the reduction basis of each substructure. Therefore, they do not change the natural BCs of the system (like for computing fixed-interface modes in HCB method) but fail to approximate statically the modes that are deleted from the reduction basis. As a first attempt to solve this problem, MacNeal [88] used the so-called *attachment modes* to approximate the contribution of the interface loads on truncated modes. Afterwards, Rubin [135] developed the *residual flexibility* concept for both mass and stiffness matrices, but he failed to show that his method is based on the Rayleigh-Ritz method.
Later, Craig and Chang [27, 29, 30] demonstrated that the MacNeal and Rubin methods are based on the Rayleigh-Ritz approach and also developed a generalized way to couple the substructures reduced with CMS methods. Martinez et al. [91, 92] reformulated the method of Rubin and simplified his method by casting it in a reduction basis set in the same format as the HCB basis, which is straightforward to use. The augmented free-interface mode reduction basis based on the work of MacNeal, Rubin, and Martinez et al. will be called the *MacNeal/Rubin-Martinez* (MRM) method here.
In contrast to the linear CMS methods that are widely investigated, classified and compared in literature, few works have investigated dynamic substructuring for nonlinear structures. Wenneker and Tiso [157] recently developed a substructuring method for geometrically nonlinear structures. They attempted to extend HCB and MRM reduction bases using the concept of *Modal Derivatives* explained in [61] for fixed and free interface modes, respectively. Wu et al. [163–165] also extended this method for flexible multibody dynamics. However, their method can only reduce a model in an intrusive manner, requiring specialized nonlinear FE codes to be applied.

The first nonlinear modal substructuring method based on the non-intrusive approach was presented by Kuether et al. [84]. They developed the NLROM for each substructure by taking the HCB reduction basis once, and another time, the free-interface modes (GH basis) of each substructure to reduce the linear mass and stiffness matrices. In order to identify the NSCs, they employed the ICE method, which does not require separate imposition of membrane modes. To generate the nonlinear static forces required in ICE, they used the columns of HCB and GH transformation matrices. They compared these results and showed that their nonlinear HCB method performs by far better than the nonlinear GH substructuring method. However, they did not investigate the effect of the augmented free-interface (MRM) method in nonlinear substructuring. Therefore, as the next contribution of this dissertation, we have developed a nonlinear substructuring approach based on augmented free-interface method. We compare our method with the previous methods and show that our method is beneficial compared to the other two methods.
Most of the classical CMS methods developed in the 1960s and 1970s studied the reduction of internal DOFs, where no connection to the neighboring substructures exist. However, in case there are numerous DOFs at the interface of the reduced substructures, the final ROM obtained from the classical CMS methods can still be large, because they keep all the interface DOFs in physical domain. Since the last decades, several Interface Reduction (IR) methods have been proposed to overcome this problem. Craig and Chang [31] first introduced three interface reduction techniques where they reduced the boundary DOFs by applying either a Ritz representation, Guyan reduction or modal reduction of the interface coordinates. They concluded that modal reduction is advantageous over the other two methods. Since their methods reduce the boundary coordinates of the coupled system, it is called *System Level* (SL) interface reduction. This method was further investigated by Castanier et al. [18] where they called the reduced constraint modes the *Characteristic Constraint* (CC) modes. Tran [155] developed the SL-IR method on free- and hybrid-interface mode methods and showed that the attachment modes can be reduced in the same manner as constraint modes.
The SL-IR method can largely reduce the interface DOFs while maintaining the same accuracy as the HCB method. However, the challenge is that the interface reduction can only be done after assembly of substructures, and not at the substructure level. This is a disadvantage for cases where the reduction of interface DOFs at a local (or substructure) level is desired. To tackle this issue, *Local Level* (LL) interface reduction methods have been proposed. Hong et al. [55] suggested a LL-IR for the HCB method that is based on the *Exact Compatibility* (EC) of boundary DOFs of neighboring substructures. In this method, the constraint modes of each substructure are reduced separately. The reduced constraint modes of the substructures are then cast into a matrix and orthogonalized with respect to each other. Keuther et al. [82] recommended a *Weak Compatibility* (WC) of the boundary coupling while the interface DOFs are reduced locally. They also developed the SL and LL-WC interface reduction method for the nonlinear HCB method.
A review of interface reduction techniques on the HCB method is presented by Krattiger et al. [80]. However, to the authors' knowledge, no study exists in the literature that shows the performance of different IR methods on the free-interface reduction approach for nonlinear substructuring. In this work, we further develop the three

mentioned IR methods for augmented free-interface nonlinear substructuring and compare these result with their counterpart for nonlinear HCB. We show that our proposed method performs better than the nonlinear HCB for high level of load levels.
The nonlinear substructuring based on ICE can only accurately predict the response of the system with the mentioned assumption of quadratic relation between membrane and transverse motion. For instance, ICE may not lead to accurate NLROMs for a deep-curved structure, as investigated in Chapter 5. We develop a novel substructuring approach, which can be used in a more general case of loading condition and structures than the ICE-based substructuring method. This method extends either ED and EED for substructuring, instead of the work of Kuether et al. [82, 84, 85] that expand ICE. As a reduction basis, we introduce a linear component modes basis (here HCB), which is augmented by non-intrusive MDs of the selected component modes to accurately estimate nonlinear modal interactions. The coupled model in this way does not have the limitation of ICE anymore to accurately approximate the membrane motion. The proposed method is also combined with interface reduction technique and compared to the ICE based substructuring approaches. We show in this dissertation that our proposed nonlinear substructuring approach is superior to the previous non-intrusive-based substructuring method, for the examples treated sofar.

1.5 Scope of the work

The flowchart of the scope of this dissertation is depicted in Fig. 1.6. As it can be seen from this figure, the first part of this dissertation investigates monolithic MOR techniques. Chapter 2 studies the governing equations for full-order FE model as well as the reduced-order one. Furthermore, a few solution techniques that are used in this work are briefly outlined. Chapter 3 investigates the force-based non-intrusive ROMs, i.e. IC and ICE, and presents their proposed improvements. Chapter 4 studies the displacement-based non-intrusive ROMs, i.e. ED and EED, and the new bases are demonstrated and assessed. As the closure of this part, we apply the investigated methods of Chapters 3 and 4 to different FE models in Chapter 5. We compare these methods and draw some concluding remarks for the first part of this work.
The second part of this dissertation examines the nonlinear modal substructuring, which is necessary to reduce the dimension of multi-component structures. Chapter 6 introduces the most common linear CMS methods as well as interface reduction techniques that are further used for nonlinear substructuring. Chapter 7 presents the nonlinear modal substructuring based on ICE method and a discussion of its improvement using free-interface mode approach. Moreover, Chapter 8 proposes a new nonlinear substructuring approach, which is more general than the previous methods and can be used also for curved structures with and without combined loading conditions. In the last chapter of part II (Chapter 9), we compare the investigated methods in Chapters 7 and 8 and discuss the situations where each method can be used. Finally Chapter 10 presents a summary of the work and discusses the concluding remarks.

1.6 Own contributions

In this dissertation, method development in non-intrusive model order reduction and dynamic substructuring for nonlinear finite element models is aimed. In terms of non-intrusive ROM the following contribution has been performed

- All of the currently available non-intrusive ROM methods, namely ED, EED, IC and ICE are implemented in a MATLAB code. These methods are furthermore applied to several structures and their accuracy, stability and computational efficiency are assessed statically as well as dynamically.
- The accuracy of ICE is improved by extending the mode acceleration and modal truncation augmentation methods for nonlinear model reduction. This improvement is achieved by computing the effect of applied loads' distribution on the truncated linear VMs of the system and published in [70].
- The accuracy and computational efficiency of the displacement-based ROM methods are increased by introducing a non-intrusive modal derivative-based approach to compute NSCs of an NLROM. The results of the developed approach are compared with the other available methods. This work is submitted for publication in [66].

In the second part, where nonlinear substructuring based on non-intrusive methods are investigated, the following contributions are carried out

- Common free- and fixed-interface linear dynamic substructuring methods are implemented and compared with each other. Three interface reduction methods, namely, system level, local level with exact compatibility and local level with weak compatibility, are extended for the free-interface CMS method and compared to the fixed-interface approach. To the author's knowledge, the local level interface reduction methods have been used only for the fixed-interface methods so far. We show that this extension is more accurate than the fixed-interface method.
- An augmented free-interface nonlinear substructuring with interface reduction based on ICE is presented, which can be seen as an alternative of the nonlinear substructuring approach based on HCB. We furthermore discuss the advantages and improvements of the proposed method. This work is published in [65].
- A novel non-intrusive based modal substructuring of nonlinear FEs is developed that is more accurate and generic than the ICE based substructuring methods. The proposed method contains a set of component modes (e.g., HCB) augmented by their corresponding non-intrusive (static) MDs as the reduction basis. To reduce the offline computational costs and avoid the limitation of the ICE method under combined loading, the displacement methods of ED and EED are used to identify NSCs of the system. This work is in preparation for submission in [71].

Finally, all the methods are applied to different numerical examples and their results are discussed and summarized.

Figure 1.6: Flowchart for the scope of the main chapters of this dissertation.

Part I

Nonlinear model order reduction

Chapter 2

Fundamentals of nonlinear full- and reduced-order FE models

2.1 Introduction

This chapter reviews the derivation of nonlinear reduced-order models' governing equations by starting from a brief explanation of the nonlinear FE method in structural dynamics. Here the pure displacement-based governing equations are sought, which are usually more convenient in structural dynamics problems. The first step in obtaining the FE formulations is an explanation of the *Strong* and *Weak* forms for writing the balance equations and then discretisation of the continues balance equations using the FE method. This leads to a set of Ordinary Differential Equations (ODEs), which can not usually be solved analytically. Therefore, in the last part of this chapter numerical static and dynamic solution methods are outlined.

2.2 Strong and weak forms for for structural dynamic problems

One way to derive the elastodynamic equilibrium Equations (Eqs) of a body V with surface boundary S is to express the balance of body momentum in its current (deformed) configuration, which gives (see [13] for more details)

$$\int_S \boldsymbol{t}\, dS + \int_V \rho \boldsymbol{g}\, dV = \int_V \rho \ddot{\boldsymbol{a}} dV, \tag{2.1}$$

where $\boldsymbol{t}$ and $\boldsymbol{g}$ are the surface traction and the overall body force (e.g. gravity acceleration), respectively, subjected to the elastic body. The body mass density and acceleration are denoted by ρ and $\ddot{\boldsymbol{a}}$, correspondingly. In the next step, the surface traction can be written in terms of the Cauchy stress tensor $\boldsymbol{\sigma}$ and the normal vector to the body surface, $\boldsymbol{n}$. Afterwards, the Gauss' divergence theorem is used to give

$$\int_S \boldsymbol{t}\, dS = \int_S \boldsymbol{n} \cdot \boldsymbol{\sigma}\, dS = \int_V \boldsymbol{\nabla} \cdot \boldsymbol{\sigma}\, dV. \tag{2.2}$$

By introducing Eq. (2.2) into (2.1) the balance equation reads

$$\int_V (\boldsymbol{\nabla} \cdot \boldsymbol{\sigma} + \rho \boldsymbol{g} - \rho \ddot{\boldsymbol{a}}) dV = 0. \tag{2.3}$$

Since Eq. (2.3) must apply for any volume of the body, it results

$$\boldsymbol{\nabla} \cdot \boldsymbol{\sigma} + \rho \boldsymbol{g} - \rho \ddot{\boldsymbol{a}} = 0 \qquad \text{for } \boldsymbol{a} \in V. \tag{2.4}$$

Furthermore, the displacement and force boundary conditions on the surface are defined as

$$\boldsymbol{n} \cdot \boldsymbol{\sigma} = \boldsymbol{t}_b \qquad \text{for } \boldsymbol{a} \in S_\sigma \tag{2.5}$$

$$\boldsymbol{a} = \boldsymbol{a}_b \qquad \text{for } \boldsymbol{a} \in S_a \tag{2.6}$$

where $\boldsymbol{a}$ is the displacement field of the body, and $\boldsymbol{t}_b$ and $\boldsymbol{a}_b$ are the applied traction and displacements on the surface of the body. The part of the body surface under displacement or Dirichlet boundary condition is denoted by S_a and the part under force or Neumann boundary is denoted by S_σ. The set of Eqs. (2.4 - 2.6) is known as strong form of the Boundary Value Problem (BVP). To apply the FE method, the balance equations together with the Neumann boundary (Eq. (2.6)) must be fulfilled in a weak form. To do so, the principle of *virtual work* is usually used in the context of structural dynamics with the divergence theorem to write the total virtual work of the body as (for more details see [12, 13])

$$\delta W = \int_V \rho \delta \boldsymbol{a}^T \ddot{\boldsymbol{a}} \, dV + \int_V (\boldsymbol{D}\, \delta \boldsymbol{a})^T \boldsymbol{\sigma} \, dV - \int_V \rho \delta \boldsymbol{a}^T \boldsymbol{g} \, dV - \int_S \delta \boldsymbol{a}^T \boldsymbol{t} \, dS = 0 \tag{2.7}$$

where

$$\boldsymbol{D}^T = \begin{bmatrix} \frac{d}{dx} & 0 & 0 & \frac{d}{dy} & 0 & \frac{d}{dz} \\ 0 & \frac{d}{dy} & 0 & \frac{d}{dx} & \frac{d}{dz} & 0 \\ 0 & 0 & \frac{d}{dz} & 0 & \frac{d}{dy} & \frac{d}{dx} \end{bmatrix}, \tag{2.8}$$

and δW is the virtual work due to a prescribed virtual displacement $\delta \boldsymbol{a}$. It should be noted that the Eq. (2.8) is obtained without any assumption about the amount of the deformation, nor for the material behavior of the body. Therefore, it is valid for linear and nonlinear solid mechanics with an arbitrary material constitutive law.

2.3 Discretization using finite element formulation

Solving the Eq. (2.7) for a continuous body is only possible for a few simple problems. To solve the balance equations for complex structures, the continuous space of the structure's body is discretized to smaller elements, which have a limited number of nodes (DOFs) and the only fundamental unknowns of the elements are the displacements of the nodes. The displacement field of each element with p nodes can then be approximated as

$$\boldsymbol{a}_e(\boldsymbol{X}, t) \approx \sum_{k=1}^{p} h_k(\boldsymbol{X})\, \boldsymbol{d}_k(t), \tag{2.9}$$

where $h_k(X)$ is the k^{th} shape function of an element that satisfies the compatibility boundary conditions. The shape functions are usually a polynomial function of the isoparametric local coordinates $\boldsymbol{X} = [\xi, \eta, \zeta]$. The displacement vector of the k^{th} node is denoted by $\boldsymbol{d}_k = \left[d_x, d_y, d_z\right]^T$. Furthermore, the continuous displacement field of the element with the interpolation of the node displacements (Eq. (2.9)) can be written in a compact form as

$$\boldsymbol{a}_e = \boldsymbol{H}\boldsymbol{d}_e, \tag{2.10}$$

where

$$\boldsymbol{d}_e = [\boldsymbol{d}_1, \boldsymbol{d}_2, \ldots, \boldsymbol{d}_n]^T, \tag{2.11}$$

is the vector containing the displacement of all nodes of the element concatenated in a column and

$$\boldsymbol{H} = \begin{bmatrix} h_1 & 0 & 0 & h_2 & 0 & 0 & \cdots & h_k & 0 & 0 & \cdots & h_n & 0 & 0 \\ 0 & h_1 & 0 & 0 & h_2 & 0 & \cdots & 0 & h_k & 0 & \cdots & 0 & h_n & 0 \\ 0 & 0 & h_1 & 0 & 0 & h_2 & \cdots & 0 & 0 & h_k & \cdots & 0 & 0 & h_n \end{bmatrix} \in \mathbb{R}^{(3\times 3n)}, \tag{2.12}$$

is the concatenated form of the shape functions. The displacement field of each element can be transformed to a global displacement vector using

$$\boldsymbol{d}_e = \boldsymbol{L}_e\boldsymbol{u} \tag{2.13}$$

where $\boldsymbol{L}_e$ is the localization matrix that expresses the global position of each matrix. In case the global and local coordinates have parallel axes, the localization matrix contains only zeros and ones in its components. Otherwise, it comprises sines and cosines to transform the global axes to the local one. Introducing the Eqs. (2.10) and (2.13) into (2.7) reads

$$\begin{aligned} \sum_{e=1}^{n_e} \int_{V_e} \rho(\boldsymbol{H}\boldsymbol{L}_e\delta\boldsymbol{u})^T\boldsymbol{H}\boldsymbol{L}_e\ddot{\boldsymbol{u}}\, dV + \sum_{e=1}^{n_e} \int_{V_e} (\boldsymbol{D}\boldsymbol{H}\boldsymbol{L}_e\,\delta\boldsymbol{u})^T\boldsymbol{\sigma}\, dV = \\ \sum_{e=1}^{n_e} \int_{V_e} \rho(\boldsymbol{H}\boldsymbol{L}_e\delta\boldsymbol{u})^T\boldsymbol{g}\, dV + \sum_{e=1}^{n_e} \int_{S_e} (\boldsymbol{H}\boldsymbol{L}_e\delta\boldsymbol{u})^T\boldsymbol{t}\, dS \end{aligned} \tag{2.14}$$

This equation can be expressed in the form

$$\boldsymbol{M}\ddot{\boldsymbol{u}} + \boldsymbol{f}_{\text{int}} = \boldsymbol{f} \tag{2.15}$$

where

$$\boldsymbol{M} = \sum_{e=1}^{n_e} \boldsymbol{L}_e^T \int_{V_e} \rho\boldsymbol{H}^T\boldsymbol{H}\, dV\, \boldsymbol{L}_e \tag{2.16}$$

is called the global mass matrix,

$$\boldsymbol{f}_{\text{int}} = \sum_{e=1}^{n_e} \boldsymbol{L}_e^T \int_{V_e} (\boldsymbol{D}\boldsymbol{H})^T\boldsymbol{\sigma}\, dV \tag{2.17}$$

is known as internal (or restoring) force vector, and

$$\boldsymbol{f} = \sum_{e=1}^{n_e} \boldsymbol{L}_e^T \int_{V_e} \rho \boldsymbol{H}^T \boldsymbol{g} \, dV + \sum_{e=1}^{n_e} \boldsymbol{L}_e^T \int_{S_e} \boldsymbol{H}^T \boldsymbol{t} \, dS \tag{2.18}$$

is the vector of applied external loads. It is common in the context of model-order reduction for structural dynamics that the internal force vector is split into a linearized part $\boldsymbol{K}^{(1)}$ (known as linear stiffness) and a nonlinear part $\boldsymbol{f}_{nl}$ as

$$\boldsymbol{f}_{int} = \boldsymbol{K}^{(1)}\boldsymbol{u} + \boldsymbol{f}_{nl}(\boldsymbol{u}). \tag{2.19}$$

Furthermore, a viscous damping term in the form $\boldsymbol{D}\dot{\boldsymbol{u}}$ is added to the governing EOM to take the dissipation into account. Finally, the EOM for the discretized FE model is given by

$$\boldsymbol{M}\ddot{\boldsymbol{u}} + \boldsymbol{D}\dot{\boldsymbol{u}} + \boldsymbol{K}^{(1)}\boldsymbol{u} + \boldsymbol{f}_{nl}(\boldsymbol{u}) = \boldsymbol{f} \tag{2.20}$$

The discretized EOM (2.20) for large nonlinear problems comprises numerous Degrees-Of-Freedom (DOFs), which is very expensive to be solved. Therefore, Model Order Reduction (MOR) methods are applied to this equation.

2.4 Nonlinear model order reduction

The first aim of MOR techniques is to find a reduction basis $\boldsymbol{V} \in \mathbb{R}^{(n\times m)}$, which transforms the displacement DOFs of the full-order FE model, $\boldsymbol{u} \in \mathbb{R}^{(n\times 1)}$, to a reduced set of generalized DOFs, $\boldsymbol{q} \in \mathbb{R}^{(m\times 1)}$ as

$$\boldsymbol{u}(t) \approx \boldsymbol{V}\boldsymbol{q}(t), \tag{2.21}$$

such that $m << n$ and simultaneously the reduced model can accurately represent the full-order FE model. Substitution of Eq. (2.21) into (2.20) results in an error induced because of the approximation of (2.21) :

$$\boldsymbol{M}\boldsymbol{V}\ddot{\boldsymbol{q}} + \boldsymbol{D}\boldsymbol{V}\dot{\boldsymbol{q}} + \boldsymbol{K}^{(1)}\boldsymbol{V}\boldsymbol{q} + \boldsymbol{f}_{nl}(\boldsymbol{V}\boldsymbol{q}) = \boldsymbol{f} + \boldsymbol{r} \tag{2.22}$$

where $\boldsymbol{r}$ is the residual error due to projection approximation. In order to nullify this error, the EOM must be projected to a space, which is orthogonal to it. This orthogonalization process, known as the Galerkin approach, can be performed using the same basis as the reduction basis or a different one. In this work, the EOM is projected by the same basis as the reduction basis to remove the residual error, because it becomes equivalent to the principle of virtual work [44]. This is

$$\boldsymbol{V}^T\boldsymbol{M}\boldsymbol{V}\ddot{q} + \boldsymbol{V}^T\boldsymbol{D}\boldsymbol{V}\dot{\boldsymbol{q}} + \boldsymbol{V}^T\boldsymbol{K}^{(1)}\boldsymbol{V}\boldsymbol{q} + \boldsymbol{V}^T\boldsymbol{f}_{nl}(\boldsymbol{V}\boldsymbol{q}) = \boldsymbol{V}^T\boldsymbol{f}, \tag{2.23}$$

This equation can be written in the compact form as

$$\hat{\boldsymbol{M}}\ddot{\boldsymbol{q}} + \hat{\boldsymbol{D}}\dot{\boldsymbol{q}} + \hat{\boldsymbol{K}}^{(1)}\boldsymbol{q} + \hat{\boldsymbol{f}}_{nl}(\boldsymbol{q}) = \hat{\boldsymbol{f}} \tag{2.24}$$

where

$$\begin{aligned}
&\hat{\boldsymbol{M}} = \boldsymbol{V}^T \boldsymbol{M} \boldsymbol{V} \\
&\hat{\boldsymbol{K}}^{(1)} = \boldsymbol{V}^T \boldsymbol{K} \boldsymbol{V} \\
&\hat{\boldsymbol{D}} = \boldsymbol{V}^T \boldsymbol{D} \boldsymbol{V} \\
&\hat{\boldsymbol{f}}_{nl}(\boldsymbol{q}) = \boldsymbol{V}^T \boldsymbol{f}_{nl}(\boldsymbol{V}\boldsymbol{q}) \\
&\hat{\boldsymbol{f}} = \boldsymbol{V}^T \boldsymbol{f}
\end{aligned} \tag{2.25}$$

While the dimension of the linear terms in Eq. (2.25) is significantly reduced, the computational costs to compute the reduced nonlinear restoring force is high, because to compute it in each time step, the full-order nonlinear restoring force has to be computed in each solution step and then projected to the reduced space, as shown in Fig 1.4. The second problem of computing the Eq. (2.25) is that in case the FE model of the structure is developed in a commercial software, the nonlinear internal force vector is not released by the FE code to directly project it to the reduced space. In order to address the mentioned problems of projection-based nonlinear ROM, we have studied the non-intrusive MOR methods in the entire dissertation. In the non-intrusive techniques, the reduced internal force vector is approximated as a Taylor series expansion up to cubic terms of generalized coordinates as [1]

$$\hat{\boldsymbol{f}}_{int}(\boldsymbol{q}) = \hat{\boldsymbol{K}}^{(1)}\boldsymbol{q} + (\hat{\boldsymbol{K}}^{(2)} \cdot \boldsymbol{q}) \cdot \boldsymbol{q} + \left[(\hat{\boldsymbol{K}}^{(3)} \cdot \boldsymbol{q}) \cdot \boldsymbol{q}\right] \cdot \boldsymbol{q} \tag{2.26}$$

In the next step, the unknown coefficients corresponding to quadratic and cubic terms are identified based on static inputs, which are given to the commercial software and the resulting outputs from it. By introducing Eq. (2.26) to (2.24), the i^{th} EOM for the NLROM reads

$$\hat{M}_{ij}\ddot{q}_j + \hat{D}_{ij}\dot{q}_j + \hat{K}^{(1)}_{ij}q_j + \hat{K}^{(2)}_{ijl}q_j q_l + \hat{K}^{(3)}_{ijlp}q_j q_l q_p = \hat{f}_i \tag{2.27}$$

The unknown quadratic and cubic coefficients, $\hat{K}_{ijl}$ and $\hat{K}_{ijlp}$, are called the Nonlinear Stiffness Coefficients (NSCs). The NSCs can be obtained either by direct differentiation of the nonlinear internal force vector (in case the closed form EOM is available, requiring specialized codes) or estimated using non-intrusive methodologies, which is the main focus of this work. The two available non-intrusive MOR approaches in structural dynamics are discussed and developed in Chapters 3 and 4.

2.5 Solution techniques

Depending on the type of the application, engineers require to solve the governing nonlinear FE equation either statically or dynamically. The main aim of this dissertation is dynamic solution of such equations, however, since the static solution is usually much faster than the dynamic one and can give a rapid insight into the correctness of the dynamic solution, it is briefly explained as a useful tool here. Next, the common static and dynamic approaches will be outlined.

[1] For the case of geometric nonlinear von-Karman shell and beam as well as geometric nonlinear solid elements, this expression is exact. Otherwise, it is an approximation of the nonlinear restoring force.

2.5.1 Static analysis

It is sometimes sufficient to solve the EOM (2.20) statically. Therefore this equation reduces to

$$\underbrace{\boldsymbol{K}^{(1)}\boldsymbol{q} + \boldsymbol{f}_{nl}(\boldsymbol{q})}_{\boldsymbol{f}_{\text{int}}} = \boldsymbol{f} \tag{2.28}$$

One method to solve this equation is the Newton-Raphson method, which is explained next.

Newton-Raphson Method

The Newton-Raphson method is an iterative approach, which looks for a solution by linearizing the equation around an equilibrium point. To solve a nonlinear static problem under a certain load case, it is divided into incrementing series of load cases as [12, 102]

$$\boldsymbol{f}_l = \sum_{r=1}^{l} \Delta \boldsymbol{f}_r. \tag{2.29}$$

Then a solution is sought for each load increment based on the previous step starting with an initial value $\boldsymbol{q}_0$. The residual vector $\boldsymbol{r}(\boldsymbol{q})$ to be minimized in each step can be written as

$$\boldsymbol{r}(\boldsymbol{q}) = \boldsymbol{f}_{int}(\boldsymbol{q}) - \boldsymbol{f} = \boldsymbol{0}. \tag{2.30}$$

Now, consider for the step $n+1$, a displacement vector $\boldsymbol{q}_{n+1}$ is desired, which can fulfill the Eq. (2.30) under the load case $\boldsymbol{f}_{n+1}$:

$$\boldsymbol{r}(\boldsymbol{q}_{n+1}) = \boldsymbol{f}_{int}(\boldsymbol{q}_{n+1}) - \boldsymbol{f}_{n+1} = \boldsymbol{0} \tag{2.31}$$

This displacement vector is then defined as

$$\boldsymbol{q}_{n+1} = \boldsymbol{q}_n + \Delta \boldsymbol{q}_n. \tag{2.32}$$

The unknown in this Eq. is the increment displacement vector, $\Delta \boldsymbol{q}_n$, assuming that the displacement vector for the previous step is already obtained. To obtain this unknown vector, Eq. (2.32) is introduced into (2.31) and (2.31) is then linearized around the previous step displacement vector, giving

$$\boldsymbol{r}(\boldsymbol{q}_{n+1}) = \boldsymbol{r}(\boldsymbol{q}_n + \Delta \boldsymbol{q}_n) = \boldsymbol{r}(\boldsymbol{q}_n) + \boldsymbol{J}_r(q)\Big|_{q=q_n} \Delta \boldsymbol{q}_n = 0, \tag{2.33}$$

where

$$\boldsymbol{J}_r(\boldsymbol{q})\Big|_{q=q_n} = \begin{bmatrix} \frac{\partial f_{\text{int}_1}}{\partial q_1} & \cdots & \frac{\partial f_{\text{int}_1}}{\partial q_m} \\ \vdots & \ddots & \vdots \\ \frac{\partial f_{\text{int}_m}}{\partial q_1} & \cdots & \frac{\partial f_{\text{int}_m}}{\partial q_m} \end{bmatrix} = \boldsymbol{K}^t(\boldsymbol{q}_n), \tag{2.34}$$

is the Jacobian of the residual expression and it can be shown that it is equal to the Tangent Stiffness (TS) matrix, $\boldsymbol{K}^t(\boldsymbol{q}_n)$, of the system. By computing the TS matrix, the required displacement increment is obtained from Eq. (2.33) as

$$\Delta \boldsymbol{q}_n^k = -\boldsymbol{K}^t(\boldsymbol{q}_n^k)^{(-1)}\, \boldsymbol{r}(\boldsymbol{q}_n^k). \tag{2.35}$$

Therefore, $\boldsymbol{q}_{n+1}$ can be obtained from Eq. (2.32) and substituted into Eq. (2.31) to check the convergence of this Eq. In case this displacement does not fulfill the Eq. (2.31), a new $\boldsymbol{q}_{n+1}^{k+1}$ is computed in an iteration process as

$$\boldsymbol{q}_{n+1}^{k+1} = \boldsymbol{q}_{n+1}^{k} + \Delta \boldsymbol{q}_{n+1}^{k} \tag{2.36}$$

where k is the iteration counter. Once the residual becomes smaller than a certain tolerance, the load is incremented to the next step and the same procedure is performed to obtain the desired displacement under the final load case. A flowchart of the Newton-Raphson process to obtain the final displacement solution is shown in Fig. 2.1. While the Newton-Raphson can be applied to a variety of static problems, it can sometimes converge to wrong solution for unstable problems for instance like the thermal buckling. In these cases, the *Arc-length* method can be employed [129].

2.5.2 Dynamic analysis

To solve dynamic problems, time integration schemes are employed. The Newmark method [107] is a very popular time integration scheme in the field of structural dynamics, because it provides a direct formula for the time integration of second-order differential equations. The time integration scheme can be obtained either in *explicit* or *implicit* forms. In case the displacement vector of the time integration in each time step depends only on the parameters of the previous step, it is called explicit. On the other hand, if the displacement vector and its time-derivatives depend also on the parameters of the current step, it is called implicit. While the explicit time integration method is faster than the implicit one, it is only conditionally stable. In contrast, the parameters of the implicit one can be adjusted such that the integration becomes unconditionally stable.
Since the implicit case has been widely used throughout this dissertation, it is explained here without the derivation (a detailed discussion is in [44]). Consider the EOM of a nonlinear dynamic problem as

$$\begin{cases} \boldsymbol{M}\ddot{\boldsymbol{q}}(t) + \boldsymbol{f}(\boldsymbol{q}, \dot{\boldsymbol{q}}) = \boldsymbol{p}(\boldsymbol{q}, t) \\ \boldsymbol{q}(t=0) = \boldsymbol{q}_0 \\ \dot{\boldsymbol{q}}(t=0) = \dot{\boldsymbol{q}}_0 \end{cases} \tag{2.37}$$

where $\boldsymbol{f}$ is a general nonlinear force vector (also contains damping) and $\boldsymbol{p}$ denotes the external applied loads vector. The initial displacement and velocity vectors are denoted by $\boldsymbol{q}_0$ and $\dot{\boldsymbol{q}}_0$. Let us then define the residual vector $\boldsymbol{r}$ by rewriting the EOM as

$$\boldsymbol{r}(\boldsymbol{q}, \dot{\boldsymbol{q}}, \ddot{\boldsymbol{q}}) = \boldsymbol{M}\ddot{\boldsymbol{q}}(t) + \boldsymbol{f}(\boldsymbol{q}, \dot{\boldsymbol{q}}) - \boldsymbol{p}(\boldsymbol{q}, t) = \boldsymbol{0}. \tag{2.38}$$

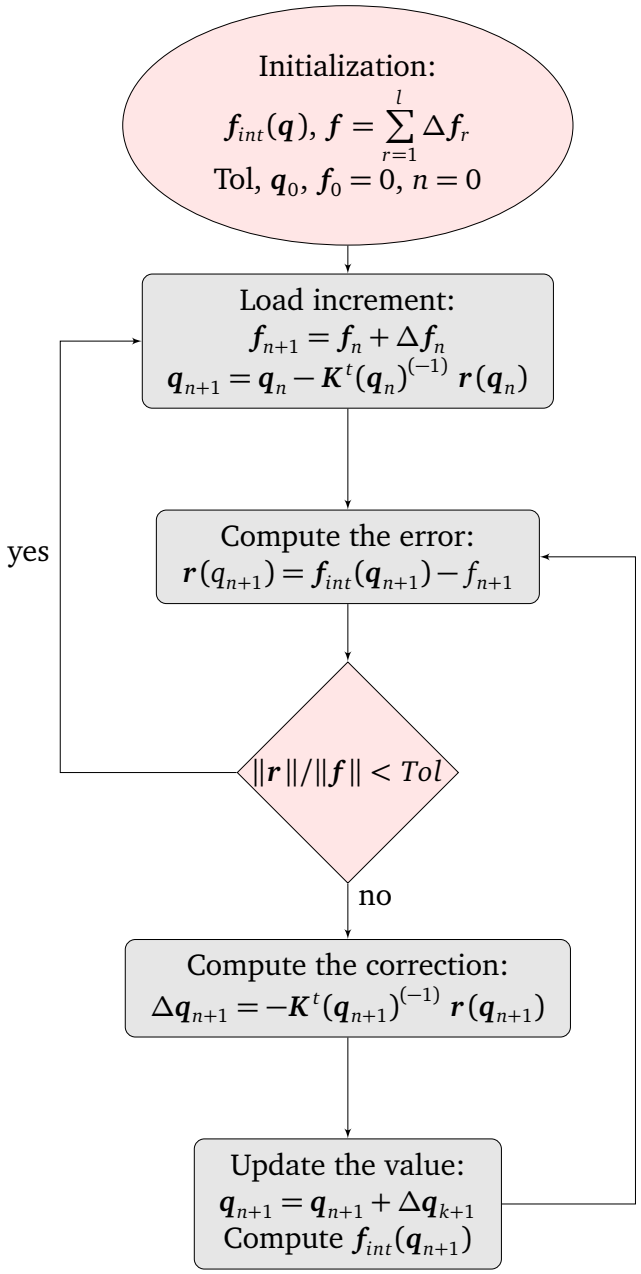

Figure 2.1: Flowchart of the nonlinear static solution using Newton-Raphson [33].

The aim is then to obtain the displacement, velocity and acceleration vectors such that the residual is smaller than a given tolerance. The Newmark time integration expressions for the $(n+1)^{th}$ time step can be derived as

$$\begin{aligned} \ddot{\boldsymbol{q}}_{n+1} &= \tfrac{1}{\beta h^2}(\boldsymbol{q}_{n+1} - \boldsymbol{q}^*_{n+1}), \\ \dot{\boldsymbol{q}}_{n+1} &= \dot{\boldsymbol{q}}^*_{n+1} + \tfrac{\gamma}{\beta h}(\boldsymbol{q}_{n+1} - \boldsymbol{q}^*_{n+1}), \end{aligned} \tag{2.39}$$

where

$$\begin{aligned} \boldsymbol{q}^*_{n+1} &= \boldsymbol{q}_n + h\dot{\boldsymbol{q}}_n + (\tfrac{1}{2} - \beta)h^2\ddot{\boldsymbol{q}}_n, \\ \dot{\boldsymbol{q}}^*_{n+1} &= \dot{\boldsymbol{q}}_n + (1-\gamma)h\ddot{\boldsymbol{q}}_n \end{aligned} \tag{2.40}$$

are the displacement and velocity predictors, respectively. The scalars γ and β are the integration parameters, which can be adjusted before starting the integration. The time increment is denoted by h. By introducing (2.39) and (2.40) into (2.38), the residual expression can be obtained only in terms of one unknown $\boldsymbol{q}_{n+1}$ as

$$\boldsymbol{r}(q_{n+1}) = \boldsymbol{0} \tag{2.41}$$

The unknown displacement vector can then be obtained in an iterative process by linearizing the residual vector. Let us consider the k^{th} iteration of the displacement vector $\boldsymbol{q}_{n+1}$ and denote its estimation by $\boldsymbol{q}^k_{n+1}$. Using the linearization approximation, the estimation for the next iteration can be then written as

$$\boldsymbol{r}(\boldsymbol{q}^{k+1}_{n+1}) = \boldsymbol{r}(\boldsymbol{q}^k_{n+1}) + \boldsymbol{J}_r(q)\Big|_{q=\boldsymbol{q}^k_{n+1}} \Delta\boldsymbol{q}^k_{n+1} = \boldsymbol{0} \tag{2.42}$$

where

$$\boldsymbol{J}_r(\boldsymbol{q}) = \frac{\partial \boldsymbol{f}}{\partial \boldsymbol{q}} + \frac{\partial \boldsymbol{f}}{\partial \dot{\boldsymbol{q}}}\frac{\partial \dot{\boldsymbol{q}}}{\partial \boldsymbol{q}} + \boldsymbol{M}\frac{\partial \ddot{\boldsymbol{q}}}{\partial \boldsymbol{q}} - \frac{\partial \boldsymbol{p}}{\partial \boldsymbol{q}} \tag{2.43}$$

is the Jacobian matrix of the residual expression. The term $\frac{\partial \boldsymbol{f}}{\partial \boldsymbol{q}}$ is the Jacobian that represents the tangent stiffness matrix of the system $\boldsymbol{K}^t$; $\frac{\partial \boldsymbol{f}}{\partial \dot{\boldsymbol{q}}}$ is the tangent damping denoted by $\boldsymbol{D}^t$; $\frac{\partial \boldsymbol{p}}{\partial \boldsymbol{q}}$ is the variation of the external applied forces with respect to the displacement vector. Furthermore, the variation of the velocity and acceleration vectors with respect to the displacement can be obtained as

$$\begin{aligned} \frac{\partial \ddot{\boldsymbol{q}}}{\partial \boldsymbol{q}} &= \tfrac{1}{\beta h^2}\boldsymbol{I} \\ \frac{\partial \dot{\boldsymbol{q}}}{\partial \boldsymbol{q}} &= \tfrac{\gamma}{\beta h} \end{aligned} \tag{2.44}$$

Therefore, the Jacobian matrix can be written in the following form:

$$\boldsymbol{J}_r(\boldsymbol{q}) = \boldsymbol{K}^t + \frac{\gamma}{\beta h}\boldsymbol{D}^t + \frac{1}{\beta h^2}\boldsymbol{M}. \tag{2.45}$$

The nonlinear Eq. (2.41) is solved for each step in an iterative process to obtain the displacement increment $\Delta\boldsymbol{q}^k$. Then, their corresponding velocity and acceleration increment vectors are obtained by

$$\begin{aligned} \Delta\dot{\boldsymbol{q}}^k &= \tfrac{\gamma}{\beta h}\Delta\boldsymbol{q}^k, \\ \Delta\ddot{\boldsymbol{q}}^k &= \tfrac{1}{\beta h^2}\Delta\boldsymbol{q}^k. \end{aligned} \tag{2.46}$$

This iteration continues for each step until the norm of residual vector converges to a defined criterion (tolerance) and then the next time step is iterated. A flowchart of the nonlinear Newmark scheme is depicted in Fig. 2.2. Furthermore, in case of high-frequency artificial eigenvalues, HHT [51] and Generalized-α [23] methods have been proposed. These methods introduce a numerical damping for high frequencies while keeping an accurate response for low frequency band of interest.

2.6 Validation of nonlinear ROMs

To make sure that the developed NLROMs are accurate enough, they usually have to be validated dynamically, depending on the underlying application. One way to dynamically validate the NLROMs in industries, is to compare the NLROM's nonlinear response with experimental measurements, under the same loading conditions, see e.g. [113, 148, 149]. However, in academia it is usual to validate the dynamic response of an NLROM with its full-order model.
To dynamically validate an NLROM, one can compute the time response of the NLROM under a certain load case and compare its full-model counterpart as done e.g. in [62, 136, 137]. However, validating the NLROM under this condition does not assure an engineer if it also operates accurately under different levels of excitation within a desired frequency band.
Alternatively, Kuether et al. [83] used Nonlinear Normal Modes (NNMs) to validate an NLROM. NNMs provide an insight into how the system responds to different load scenarios and can capture a wide range of response amplitudes experienced by the structure. NNMs were first defined by Rosenberg in [134] as a periodic motion of the system, in which all DOFs reach the equilibrium position at the same time (synchronous motion). The definition was further extended by Kerschen et al. in [73] as *not necessarily synchronous periodic responses*. Although orthogonality and modal superposition are no longer applicable for NNMs, they show other unique properties compared to the linear normal modes, such as modal interactions, bifurcation, and frequency-energy dependency.
Peeters et al. proposed to compute NNMs with numerical continuation methods in [112]. In order to find the periodic motion of the system, a shooting function is defined to indicate the difference between the system's motion at $t = 0$ and $t = T$. The free response of the nonlinear system to a prescribed initial condition is only then periodic, when the shooting function is smaller than a given tolerance. In this way, the boundary value problem is transferred into initial value problem that can be solved with a shooting method. The branch of an NNM is followed with the pseudo-arclength algorithm presented in [112]. Prediction and correction steps are used to find the periodic solution, where Jacobian matrices are employed in prediction and correction steps and play a huge roll in computational efficiency.
The further development of this method by Kuether et al. in [83] made it feasible to compute the NNMs of models built in a commercial FE package. The Applied Modal Force (AMF) method defines the initial displacement as the nonlinear static response of the system to a prescribed external force, which is a weighted truncated subset of linear mode shapes. The weighting factors, termed as modal force amplitude, are to be determined with pseudo-arclength continuation. The individual variables are

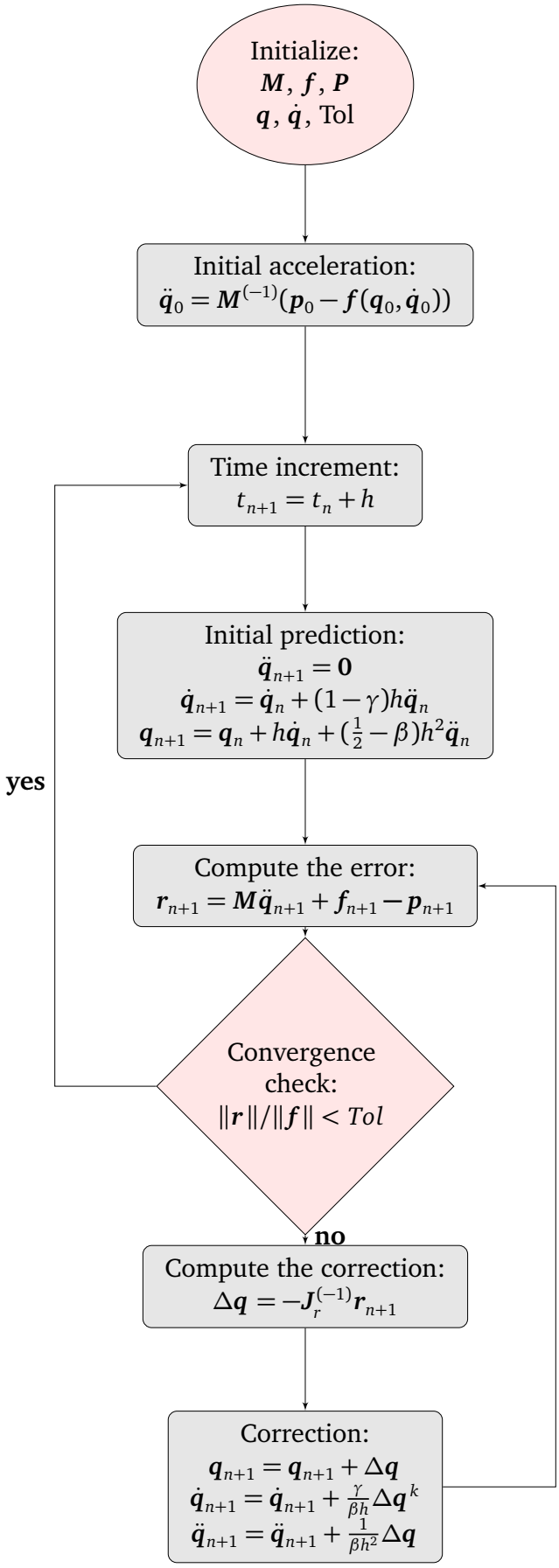

Figure 2.2: Flowchart of the implicit Newmark method [44].

thus reduced from n to the number of truncated weighting factors m. In this way, the computational burden caused by Jacobian matrices, is reduced. Only one mode is used to define the initial displacement at first. The contribution of the remaining modes is monitored. While the energy in the system rises, corresponding modes will be activated if necessary.
The most important disadvantage of using NNMs as validation metric is that they are much more expensive than time integration to be obtained. Therefore, they are avoided in this work. The main goal of this dissertation is dynamic validation of the NLROMs under random excitation (which are mostly sound pressures) with a desired frequency band and different excitation levels. This can guarantee the performance of the developed NLROMs with less cost than the NNMs. To check the convergence of developed NLROMs in the desired frequency band, power spectral densities of the full and reduced models are compared, which will be explained later in this chapter.

2.6.1 Random response prediction

Since many large structures such as air vehicles or wind turbines are operating under random pressures, this work attempts to validate NLROMs under different random sound pressure levels, which are generated using a *white noise* in time and uniformly distributed in space. The reason to choose this kind of excitation is to check the convergence of the developed NLROMs in a broad band excitation frequencies with different intensity levels.
A white noise signal is an uncorrelated random signal, which has the same strength (or power) at each frequency [17]. A discrete white noise time signal is a series of uncorrelated variables, which have a zero mean value and a finite variance. In case a white noise time signal follows a multivariate normal distribution, it is called a Gaussian white noise [151].
Furthermore, the *Sound Pressure Level* (SPL) is given in decibel (dB) and is defined as [128]

$$SPL = 20\log_{10}\left(\frac{P_{rms}}{P_{ref}}\right) \tag{2.47}$$

where P_{rms} is the root-mean-square of the sound pressure signal and $P_{ref} = 2\times10^{-5}$ Pa is the reference pressure in the air. To evaluate the nonlinear responses under different SPLs, power spectral density is used, which is explained next.

2.6.2 Power spectral density

The Power Spectral Density (PSD) expresses the intensity of a signal in a frequency spectrum. It is mathematically defined as the Fourier Transform (FT) of the auto-correlation of a variable function X:

$$S_X(\omega) = FT\left[R_X(\tau)\right] = \int_{-\infty}^{\infty} R_X(\tau)\, e^{-j\omega\tau} d\tau \tag{2.48}$$

where

$$R_X(\tau) = \int_{-\infty}^{\infty}\int_{-\infty}^{\infty} x_1 x_2 f(x_1, x_2; \tau)\, dx_1 dx_2 \tag{2.49}$$

is the *autocorrelation* function of X, $x_1 = X(t)$, $x_2 = X(t+\tau)$ and $f(x_1, x_2; \tau)$ is the second-order density function [81]. It can be shown that for a zero-mean random signal, which is measured in the time interval $[0, T]$, the autocorrelation can be estimated as

$$\bar{R}_X(\tau) = \frac{1}{T - |\tau|} \int_0^{T-|\tau|} X(t) X(t+\tau)\, dt, \quad 0 \leq \tau \leq T \tag{2.50}$$

and its corresponding PSD may be written as

$$\bar{S}_X(\tau) = \int_{-T}^{T} \bar{R}_X(\tau) e^{-j\omega\tau} d\tau \tag{2.51}$$

In case of a discrete time signal, the Eq. (2.50) can be discretized as

$$\bar{R}_X(h) = \frac{1}{N} \sum_{i=1}^{N-h-1} X_i X_{i+h} \tag{2.52}$$

where h is a time increment. The estimated PSD (also known as *periodogram*) can finally be given by

$$\bar{S}_N(\omega) = \frac{1}{N} \left| \sum_{k=0}^{N-1} X_k e^{-j\omega k} \right|^2 = \frac{|X_N(\omega)|^2}{N} \tag{2.53}$$

It can be shown that as the number of samples increases, the periodogram converges to the true PSD, namely,

$$S_X(w) = \lim_{N\to\infty} E\left[\bar{S}_N(\omega)\right] \tag{2.54}$$

where operator $E[.]$ is the mean or expected value of a variable. Furthermore, to filter the noise in a signal and obtain a consistent PSD, the *time-windowing* approach has to be applied to the time signal (see [111, 152] for more detail)

Chapter 3

Force-based non-intrusive MOR

This chapter is mainly extracted from the author's work in [70]. In this paper, Karamooz had the idea of the work, derived the numerical results and wrote the manuscript. Rixen gave useful inputs in the discussions of the work and proof-read the paper. Rixen supervised the work.

3.1 Introduction

This chapter investigates the Implicit Condensation and Expansion method, which is a force-based non-intrusive ROM approach. As mentioned before, to identify NSCs of an NLROM, appropriate inputs have to be assigned to the FE package, which also capture nonlinear interactions between the modes. E.g., for shell-like structures (i.e. beams, shells and plates) the input has to trigger the coupling between bending and membrane (in-plane) displacement (also called stretching effects). Two approaches have been considered in the literature to determine the unknown parameters. In the first approach, which is introduced in [95], the procedure of fitting the NLROM to the full-order FE model is conducted by prescribing series of selected static loads to the FE package to be solved for the corresponding displacements. This method is referred to as *Applied Force (AF) or Implicit Condensation* (IC). In the second class of approaches, which are discussed in Chapter 4, a set of pre-processed displacements are statically prescribed to the FE package to obtain the corresponding reaction forces and identify the NSCs (referred to as the *Enforced Displacement* (ED) Method).
The main advantage of the IC method over displacement-based methods is that it is usually sufficient to use a truncated number of linear Vibration Modes (VMs) (which are transverse-dominated for shell-like structures) to accurately predict the response of transverse-dominated displacements of the system. In other words, the membrane-stretching effect is implicitly taken into account when imposing static forces on the model. However, to be able to accurately predict membrane-dominated vibrations, the expansion procedure introduced by Hollkamp and Gordon [54] must be performed, which is called *Implicit Condensation and Expansion* (ICE).
For identification of the NSCs with ICE, linear VMs are often used to generate the inputs for prescription to the FE package. However, we know from linear structural dynamics that taking a few modes in the modal response of a linear system for linear model reduction without considering the static deflection of the truncated modes due to spatial distribution of external loads will cause inaccuracies in the system. The Mode Acceleration (MA) [1, 34, 130] and Modal Truncation Augmentation (MTA)

[34, 35, 130] methods have been widely studied to best approximate the effect of modal truncation on the spatial distribution of applied loads in the linear systems.
In this chapter, we propose extending the MA and MTA methods for nonlinear response prediction. In the first approach, the contribution of the truncated modes are assumed linear and quasi-statically affect the response of the system. Consequently, these quasi-static deflections due to applied loads are computed from the linear flexibility matrix of the FE model and added to the dynamic response of the NLROM, which is developed from the ICE method. In the second approach, Modal Truncation (MT) vectors are first computed from the residual spatial distribution of the applied loads. Afterwards, these vectors are appended to the reduced mode basis and the stiffness coefficient identification of ICE is performed with the new reduction basis.

3.1.1 Implicit Condensation

Let us recall from Chapter 2 that the EOM for a geometric nonlinear structure is written as

$$\hat{\boldsymbol{M}}\ddot{\boldsymbol{q}} + \hat{\boldsymbol{D}}\dot{\boldsymbol{q}} + \hat{\boldsymbol{K}}^{(1)}\boldsymbol{q} + \hat{\boldsymbol{f}}_{\boldsymbol{nl}}(\boldsymbol{q}) = \hat{\boldsymbol{f}}, \tag{3.1}$$

where the i^{th} component of the nonlinear restoring force is given by

$$\hat{f}_{nl_i} = \hat{K}^{(2)}_{ijl} q_j q_l + \hat{K}^{(3)}_{ijlp} q_j q_l q_p, \tag{3.2}$$

and $\hat{K}^{(2)}_{ijl}$ and $\hat{K}^{(3)}_{ijlp}$ are the components of the third-and-fourth-order stiffness tensors or NSCs, to be identified by ICE.
The IC method was first developed by McEwan et al. [95] and later extended by Hollcamp and Gordon [54] to improve the approximation of in-plane motions. This method attempts to identify the unknown NSCs based on prescription of selected static forces to the nonlinear FE-EOM to solve for the corresponding displacements. The procedure can be employed in any FE package, which is capable of performing nonlinear static FE analysis. Since the loads in IC are enforced statically, the velocity and acceleration in Eq. (3.1) are equal to zero, giving

$$\hat{\boldsymbol{K}}\boldsymbol{q} + \hat{\boldsymbol{f}}_{\boldsymbol{nl}}(\boldsymbol{q}) = \hat{\boldsymbol{f}}, \tag{3.3}$$

or

$$\hat{K}_{ij} q_j + \hat{K}^{(2)}_{ijl} q_j q_l + \hat{K}^{(3)}_{ijlp} q_j q_l q_p = \hat{f}_i, \tag{3.4}$$

for the i^{th} component of Eq. (3.3). By applying a set of static loads to solve Eq. (3.3) for their corresponding displacements, the NSCs can be obtained using any regression analysis method. Let us assume that the static loads are formed from a combination of weighted basis vectors, $\boldsymbol{V}_i$, which activate all the nonlinear coupling between the modes, namely

$$\boldsymbol{f} = s_1\boldsymbol{V}_1 + s_2\boldsymbol{V}_2 + ... + s_m\boldsymbol{V}_m = \sum_{i=1}^{m} s_i\boldsymbol{V}_i, \tag{3.5}$$

where s_i is the scalar weighting factor corresponding to its vector, $\boldsymbol{V}_i$. The most common choice for the basis vectors $\boldsymbol{V}_i$, is a truncated number of eigenmodes of the linearized EOM, as used by McEwan et al. [95] in the original IC method. This choice is based on the idea of the Mode Displacement method (see section (3.2.1)). Additionally, for the case that the basis vectors are the truncated linear (transverse) eigenmodes, Gordon and Hollcamp [46] proposed a physically meaningful value for the scaling factor. In other words, they defined a scaling factor for each mode as the force, which is required to linearly obtain the maximum desired displacement as

$$s_i = \frac{W_{i_{\max}}}{V_{i_{\max}}} \omega_i^2, \tag{3.6}$$

where, $W_{i_{\max}}$, $V_{i_{\max}}$, and ω_i denote the maximum desired displacement for the linearized EOM, the maximum (translational) eigenmode component and the eigenfrequency, respectively, all for the i^{th} mode. The eigenmodes, $V_{i_{\max}}$, are usually normalized with respect to the mass matrix. The maximum desired displacement, $W_{i_{\max}}$, is usually chosen in the order of the thickness of the structure. The computed scaling factors from Eq. (3.6) are used in both positive and negative signs to generate the prescribing forces.
A certain number of such static loads are generated and assigned to the FE code to obtain the corresponding displacements. These forces are afterwards projected onto the modal domain to be substituted in Eq. (3.4).

$$\hat{\boldsymbol{f}} = \boldsymbol{V}^T \boldsymbol{f}. \tag{3.7}$$

Likewise, the displacement is projected onto the reduced set of generalized coordinates by solving

$$\boldsymbol{u} = \boldsymbol{V}\boldsymbol{q} \tag{3.8}$$

for $\boldsymbol{q}$. The linear stiffness of the FE model is usually available from the FE package. Therefore, the reduced linear stiffness matrix in (3.4) can be calculated directly from Eq. (2.25) before performing IC. All the p load cases and their corresponding displacements are then transformed to modal domain and put in a matrix form as

$$\boldsymbol{K}_{nl}\boldsymbol{G}_{nl} = \boldsymbol{F}_{nl}, \tag{3.9}$$

where $\boldsymbol{K}_{nl}$ is the matrix containing unknown NSCs and $\boldsymbol{G}_{nl}$ and $\boldsymbol{F}_{nl}$ are the matrices of known parameters. We explain more in Appendix A the ingredients of these matrices. The number of NSCs, which dominantly contribute in the nonlinear behavior of a structure can be drastically reduced depending on the type of the FE model (e.g. flat or curves), nonlinearity, loading condition, etc. For instance, if a structure is symmetric with respect to transverse modes, initially flat and geometric nonlinear, one can neglect all quadratic terms as well as those cubic terms which contain the multiplication of more than two generalized coordinates, as shown by McEwan et al. [96]. In other words, the NSCs consisting of more than three unequal indices are zero:

$$\hat{K}^{(3)}_{ijlp} = 0 \quad for \quad i \neq j \neq l \neq p. \tag{3.10}$$

Consequently, in this case, the nonlinear restoring force in Eq. (3.2) for the r^{th} EOM is reduced to

$$f_{r_i} = \hat{K}^{(3)}_{ijjp} {q_j}^2 q_p + \hat{K}^{(3)}_{ijjj} {q_j}^3. \tag{3.11}$$

However, it has been shown in the literature (e.g. see [46, 75]) that for many structures such as cantilevered or curved FE models, the truncated form of the nonlinear restoring force (Eq. (3.11)) no longer applies. In this work, the full form of the quadratic and cubic terms with the presence of all NSCs is investigated, for the sake of generality.
For the case of a geometrical nonlinear FE problem, it is sufficient to generate the required loads for IC using permutations of one, two and three basis vectors. One usual possibility to choose the basis vectors for the static loads is to set them equal to the columns of the reduction basis matrix $\boldsymbol{V}$, multiplied with the stiffness matrix as

$$\boldsymbol{f} = \boldsymbol{K}(\boldsymbol{V}_i s_i + \boldsymbol{V}_j s_j + \boldsymbol{V}_k s_k) \qquad i, j, k = 0, 1, 2, ..., m, \tag{3.12}$$

In this case, the scaling factor to obtain the required force for the linear maximum desired displacement defined by [46] is

$$s_i = \frac{W_{i_{\max}}}{V_{i_{\max}}}, \tag{3.13}$$

Finally, recalling that each scaling factor is used with both signs, the total number of required prescribing forces [46] is given by

$$2m + 4_m C_2 + 8_m C_2, \tag{3.14}$$

where

$${}_m C_r = \frac{m!}{(m-r)!\, r!}. \tag{3.15}$$

Once all the prescribed loads and their corresponding displacements are calculated from the nonlinear static analysis, the NCSs are computed from a regression analysis procedure, e.g. as explained in [95].

3.1.2 Expansion of the membrane DOFs

This section is extracted from the author's publication in [65]. In this article, Karamooz had the idea of the work and performed the literature review. Karamooz implemented a considerable part of the work and wrote the manuscript. Xu conducted the primary part of numerical studies and discussed the work. Bartl, Tiso and Rixen gave very useful inputs in the discussions of the work and proof-read the article. Rixen supervised the work.

The IC method can only accurately estimate the motion of those DOFs that are spanned by the reduction basis in Eq. (3.8). The reduction basis usually includes the first few modes of the system, which are generally transverse-dominated modes

in shell-like structures. This means that the IC method cannot precisely approximate the membrane-dominated motions of the system, which are generally high-frequency modes. This issue becomes more important for analyses, such as stress/strain computation of geometrically nonlinear problems, where the membrane effect plays a non-negligible role. To solve this problem, Hollkamp and Gordon [54] proposed an expansion method for the approximation of membrane displacements from the nonlinear static analysis of transverse-dominated modes, without increasing the number of load cases to be prescribed to the FE package. In other words, their method performs as a post processing procedure. They called this method *Implicit Condensation and Expansion* (ICE). Next, this method is briefly explained.
To start with the ICE method, an improved displacement vector, $\boldsymbol{u}_{total}$, is defined that comprises the transverse-dominated displacement of Eq. (3.8) supplemented by a new vector, $\boldsymbol{u}_m$, representing the membrane-dominated motion:

$$\boldsymbol{u}_{total} = \boldsymbol{u} + \boldsymbol{u}_m. \tag{3.16}$$

The membrane motion vector is then decomposed in a transformation matrix and the membrane generalized coordinates:

$$\boldsymbol{u}_m = \boldsymbol{V}_m \boldsymbol{\theta} \tag{3.17}$$

where $\boldsymbol{V}_m$ denotes the membrane transformation matrix and $\boldsymbol{\theta}$ is the vector of generalized coordinates representing the in-plane motion. Accordingly, substituting Eq. (3.17) into (3.16) gives

$$\boldsymbol{u}_{total} = \boldsymbol{V}\boldsymbol{q} + \boldsymbol{V}_m \boldsymbol{\theta}. \tag{3.18}$$

Consider now that the displacement solutions to all the p static load cases in the IC method and their corresponding generalized membrane and transverse coordinates are embedded in the columns of matrices. This reads

$$\boldsymbol{U}_{total} = \boldsymbol{V}\boldsymbol{Q} + \boldsymbol{V}_m \boldsymbol{\Theta}, \tag{3.19}$$

with $\boldsymbol{U}_{total}$, $\boldsymbol{Q}$ and $\boldsymbol{\Theta}$ denoting the matrices of full-static solutions, generalized transverse and generalized membrane coordinates, respectively, and each of their columns serve as the values for individual static load cases. Since the transformation basis, $\boldsymbol{V}$ is transverse-dominated, and $\boldsymbol{V}_m$ is the membrane-dominated one, it is assumed that these two matrices are orthogonal to each other. Therefore, the transverse modal coordinates can be obtained as

$$\boldsymbol{Q} = \boldsymbol{V}^{+}\boldsymbol{U}_{total}. \tag{3.20}$$

Now, the vector of membrane coordinates is defined to have a quadratic relationship with the ones of transverse coordinates, as introduced by Nash [104]:

$$\boldsymbol{\theta} = \begin{bmatrix} q_1^2 & q_1q_2 & q_1q_3 & \cdots & q_1q_m & q_2^2 & q_2q_3 & \cdots & q_{m-1}^2 & q_{m-1}q_n & q_m^2 \end{bmatrix}^T \tag{3.21}$$

Finally, the only unknown in Eq. (3.19) becomes the basis set for the membrane motion. Solving Eq. (3.19) for the membrane basis matrix gives

$$\boldsymbol{V}_m \approx (\boldsymbol{U}_{total} - \boldsymbol{V}\boldsymbol{Q})\boldsymbol{\Theta}^{+}. \tag{3.22}$$

To compute the time histories for the membrane DOFs, first the basis set for the membrane motion is computed from Eq. (3.22) using the static displacement solution and the corresponding generalized transverse coordinates. Afterwards, the NLROM for the generalized transverse DOFs are integrated as for the IC method to obtain $q_1, q_2, \ldots, q_m$. Finally, the improved displacement time histories that also contain the membrane motion are obtained using Eq. (3.18) (with $\boldsymbol{\theta}$ computed as in (3.21)) for the whole time steps.

3.2 Basis Selection Methods

The accuracy of the developed NLROM by ICE method, strongly depends on the "correct" selection of the basis vectors in Eq. (3.12).
The original IC method selects the load bases using the idea of Mode Displacement (MD) method for linear FE models. The projection in MD method contains a truncated number of linear modes based on mode superposition [1, 25, 159]. When using the MD method, the applied loads on the system will also be projected by the reduction basis, which can then change the spatial shape of these loads. This is because it is usual to choose the truncated modes that only contain the excitation frequencies of the applied loads. However, these modes do not necessarily represent the spatial shape of the applied loads accurately. To solve this problem for the linear elastic FE model, Mode Acceleration (MA) [1, 34, 130] and Modal Truncation Augmentation (MTA) methods [34, 35, 130] have been developed in the literature.
In this work, we aim to extend these methods to the nonlinear FE structures. First, we give an overview of the classical MD method, in order to further explain why this method can cause inaccuracies in the dynamic response of systems.

3.2.1 Mode Displacement

Let us define the governing EOM for the linearized Eq. (2.20) as

$$\boldsymbol{M}\ddot{\boldsymbol{u}}(t) + \boldsymbol{C}\dot{\boldsymbol{u}}(t) + \boldsymbol{K}\boldsymbol{u}(t) = \boldsymbol{f}(t) = \boldsymbol{F}_0\,\boldsymbol{g}(t), \tag{3.23}$$

where, the applied load vector, $\boldsymbol{f}(t)$ is decomposed into a constant matrix, $\boldsymbol{F}_0$ ($n \times k$, where k is the number of spatial distribution vectors), which represents its spatial distribution, and a time varying vector, $\boldsymbol{g}(t)$ ($k \times 1$).
According to the MD method, to reduce the dimension of the system, the displacement of the system is approximated by a superposition of a truncated number of modes multiplied by their corresponding coordinates:

$$\boldsymbol{u} = \boldsymbol{\Phi}\boldsymbol{q} = \sum_{i=1}^{m} q_i \boldsymbol{\varphi}_i, \tag{3.24}$$

Here, $\boldsymbol{\Phi}$ ($n \times m$, where m is the number of kept modes in the superposition) is the reduction basis matrix containing the kept eigenmodes of the system in its columns and $\boldsymbol{q}$ is the vector of the reduced number of modal coordinates. The i^{th} modal

coordinate and eigenmode of the system are denoted by q_i and φ_i, respectively. The eigenvalue problem for obtaining the i^{th} eigenmode of Eq. (3.23) is given as

$$(\boldsymbol{K} - \omega_i^2 \boldsymbol{M})\varphi_i = 0, \tag{3.25}$$

where, the i^{th} eigenfrequency of the system is denoted by ω_i. The eigenmodes of the system are usually mass normalized such that:

$$\begin{aligned} &\boldsymbol{\Phi}^T \boldsymbol{M} \boldsymbol{\Phi} = \boldsymbol{I}, \\ &\boldsymbol{\Phi}^T \boldsymbol{K} \boldsymbol{\Phi} = \boldsymbol{\Omega} = \text{diag}(\omega_1^2, \omega_2^2, ..., \omega_k^2), \end{aligned} \tag{3.26}$$

the matrix $\boldsymbol{\Omega}$ here is a diagonal matrix that contains the square of the eigenfrequencies of the system in its diagonals, and $\boldsymbol{I}$ is the identity matrix. The set of k uncoupled equations of motion is obtained by substituting eq. (3.24) in (3.23) and premultiplying (3.23) with $\boldsymbol{\Phi}^T$:

$$\ddot{\boldsymbol{q}} + \boldsymbol{\Omega} \boldsymbol{q} = \hat{\boldsymbol{F}}_0 \boldsymbol{g}, \tag{3.27}$$

where

$$\hat{\boldsymbol{F}}_0 = \boldsymbol{\Phi}^T \boldsymbol{F}_0. \tag{3.28}$$

McEwan et al. [95] took the MD projection basis also for reduction of the nonlinear FE-EOM, namely

$$\boldsymbol{V} = \begin{bmatrix} \varphi_1 & \varphi_2 & \dots & \varphi_m. \end{bmatrix} \tag{3.29}$$

Therefore, the NLROM can then be written in the following form

$$\ddot{\boldsymbol{q}} + \boldsymbol{\Omega} \boldsymbol{q} + \hat{\boldsymbol{f}}_{nl}(\boldsymbol{q}) = \hat{\boldsymbol{F}}_0 \boldsymbol{g} \tag{3.30}$$

The prescribing static forces are computed from Eq. (3.12) to be further employed in the IC method (section (7.2)) and identify the NSCs. After development of the (nonlinear) ROM, the velocity and acceleration vector of the physical DOFs can be obtained from the corresponding ones in the ROM as

$$\dot{\boldsymbol{u}} = \boldsymbol{\Phi} \dot{\boldsymbol{q}} = \sum_{i=1}^{k} \dot{q}_i \varphi_i, \tag{3.31}$$

and

$$\ddot{\boldsymbol{u}} = \boldsymbol{\Phi} \ddot{\boldsymbol{q}} = \sum_{i=1}^{k} \ddot{q}_i \varphi_i. \tag{3.32}$$

In the procedure for choosing the number of kept modes in the reduction basis, it is usually the case that the eigenvectors are kept such that their corresponding eigenfrequencies cover the excitation frequencies imposed by the time varying part of the

applied load, $\boldsymbol{g}(t)$, with a predefined margin. However, choosing the modes in this way can cause inaccuracies due to the poor approximation of the spatial distribution of the applied loads by the chosen reduction basis. To quantify the error of the spatial distribution approximation caused by truncation of the eigenmodes in the reduction basis, let us define the residual spatial distribution matrix, $\boldsymbol{F}_r$, which is the portion of the full spatial distribution matrix not represented by the superposition of the kept modes. The residual spatial distribution matrix is obtained by subtracting the spatial distribution represented by the truncated eigenmodes from the full spatial distribution matrix, $\boldsymbol{F}_0$:

$$\boldsymbol{F}_r = \boldsymbol{F}_0 - \boldsymbol{F}_t, \tag{3.33}$$

where the spatial distribution represented by the truncated eigenmodes is given by

$$\boldsymbol{F}_t = \boldsymbol{M}\boldsymbol{\Phi}\boldsymbol{\Phi}^T\boldsymbol{F}_0 \tag{3.34}$$

The residual spatial distribution, $\boldsymbol{F}_r$, is in fact the part of the full spatial distribution, which is lost due to the use of its truncated mode representation. Accordingly, the more the number of modes in the reduction basis are taken, the smaller $\boldsymbol{F}_r$ becomes. However, choosing too many modes in the reduction basis which can reasonably reduce $\boldsymbol{F}_r$, may lose the advantage of computational efficiency achieved by the MD method. To reduce the loss of spatial distribution of the applied load and simultaneously take the advantage of dealing with just a few sets of equation of motions, Mode Acceleration [1, 34, 130] and Modal Truncation Augmentation [34, 35, 130] methods have been developed. These will be explained next.

3.2.2 Mode Acceleration Correction

The mode acceleration method [1, 34, 124, 130] is proposed to minimize the error of spatial distribution of the applied loads induced by modal representation of them in linear FE analysis. The idea of the MA method is based on the definition that the kept modes in the MD method comprise all the frequency content that exist in the applied loads to the system. Therefore, the response of the system due to the truncated modes is quasi-static and contains no dynamics. In other words, the truncated modes do not make any appreciable contribution to the velocity and acceleration of the system and the acceleration, for example, can be computed using Eq. (3.32). The truncated modes affect only the displacement of the system, and therefore, the only parameter which has to be modified is the displacement.
To compute the modified displacement from the MA method, let us consider the governing equations of motion (3.23) and rewrite it in the following form:

$$\boldsymbol{K}\boldsymbol{u} = \boldsymbol{f} - \boldsymbol{M}\ddot{\boldsymbol{u}}. \tag{3.35}$$

Since by definition the truncated modes quasi-statically affect the response of the system, the acceleration of Eq. (3.35) can be directly substituted by Eq. (3.32), and

Eq. (3.35) is solved for the displacement:

$$\boldsymbol{u} = \boldsymbol{K}^{(-1)}\boldsymbol{f} - \boldsymbol{K}^{(-1)}\boldsymbol{M}\sum_{i=1}^{k}\ddot{q}_i\boldsymbol{\varphi}_i. \tag{3.36}$$

From Eq. (3.27), the acceleration for the i^{th} generalized coordinate is written as

$$\ddot{q}_i = {\boldsymbol{\varphi}_i}^T\boldsymbol{f} - {\omega_i}^2 q_i, \tag{3.37}$$

Substituting eq. (3.37) in (3.36) and rearranging (3.36) gives

$$\boldsymbol{u} = \boldsymbol{K}^{(-1)}\boldsymbol{f} - \boldsymbol{K}^{(-1)}\boldsymbol{M}\sum_{i=1}^{k}({\boldsymbol{\varphi}_i}^T\boldsymbol{f} - {\omega_i}^2 q_i)\boldsymbol{\varphi}_i. \tag{3.38}$$

Finally, from eq. (3.38), the displacement achieved by the MA method is derived:

$$\boldsymbol{u} = \sum_{i=1}^{k} q_i\boldsymbol{\varphi}_i + (\boldsymbol{K}^{(-1)} - \sum_{i=1}^{k}\frac{\boldsymbol{\varphi}_i{\boldsymbol{\varphi}_i}^T}{\omega_i^2})\boldsymbol{f}. \tag{3.39}$$

If a structure contains rigid body modes, the linear stiffness matrix is singular and the generalized inverse methods have to be used. In this chapter, the generalized coordinates, $\boldsymbol{q}$, are first computed from the NLROM in Eq. (3.30) and substituted in Eq. (3.39) instead of (3.24) to correct, in a post-processing step, the linear quasi-static effect of the truncated modes on the external loads.

3.2.3 Modal Truncation Augmentation

The method of Modal Truncation augmentation [34, 35, 130] compensates for the inaccuracies in the modal representation of the spatial distribution of the applied loads by appending some correction vectors to the reduction basis. MTA employs the Rayleigh-Ritz method to compute the modal truncation (MT) vectors, which has the advantage of being mathematically consistent.
To compute the MT vectors, we start from the computation of the Ritz vectors by a static problem under the residual force distribution:

$$\boldsymbol{K}\boldsymbol{X} = \boldsymbol{F}_r, \tag{3.40}$$

where, $\boldsymbol{X}$ is the static displacement matrix, which comprises the static displacement (Ritz) vectors in its columns. Afterwards, the reduced mass matrix, $\bar{\boldsymbol{M}}$, and stiffness matrix, $\bar{\boldsymbol{K}}$ are obtained using these Ritz vectors:

$$\bar{\boldsymbol{K}} = \boldsymbol{X}^T\boldsymbol{K}\boldsymbol{X}, \tag{3.41}$$

$$\bar{\boldsymbol{M}} = \boldsymbol{X}^T \boldsymbol{M} \boldsymbol{X}, \tag{3.42}$$

The reduced eigenvalue problem is then given by

$$(\bar{\boldsymbol{K}} - \omega_i^2 \bar{\boldsymbol{M}}) \boldsymbol{v}_i. \tag{3.43}$$

Here, the i^{th} eigenvector and eigenfrequency of the reduced eigenvalue problem are denoted by ω_i and $\boldsymbol{v}_i$, respectively. This procedure is performed to obtain a set of numerically stable MT vectors. The MT vectors are consequently defined by

$$\boldsymbol{\Phi}_{mt} = \boldsymbol{X} \boldsymbol{V}, \tag{3.44}$$

where, the matrix $\boldsymbol{V}$ contains the reduced eigenvectors, $\boldsymbol{v}_i$, in its columns. Finally, the new reduction basis according to the MTA method is constructed by appending the MT vector to the set of kept modes $\boldsymbol{\Phi}$, namely

$$\boldsymbol{\Psi} = [\ \boldsymbol{\Phi} \quad \boldsymbol{\Phi}_{mt}\ ], \tag{3.45}$$

Now, the procedure of model reduction is exactly the same as the MD method, except that the new reduction basis, $\boldsymbol{\Psi}$, is used as the reduction basis to obtain the displacement and acceleration as

$$\boldsymbol{u} = \boldsymbol{\Psi}\, \boldsymbol{q}, \tag{3.46}$$

and

$$\ddot{\boldsymbol{u}} = \boldsymbol{\Psi}\, \ddot{\boldsymbol{q}}. \tag{3.47}$$

The novelty of this work is that we propose to use the MT vectors in addition to the linear modes as the basis vectors in the identification procedure of ICE . In other words, we define the following reduction basis to identify the NSCs as

$$\boldsymbol{V} = [\ \boldsymbol{\Phi} \quad \boldsymbol{\Phi}_{mt}\ ], \tag{3.48}$$

to compensate for the spatial representation of the external loads in the nonlinear restoring forces. In th next section we study the performance of the proposed methods.

3.3 Numerical Example

To assess the accuracy of the proposed approach, a two-side clamped geometric nonlinear beam model is investigated, as shown in Fig. 3.1. The material, geometry, and mesh properties of the model are illustrated in Table 3.1. The structure is modeled in Abaqus® and the nonlinear static analysis required in ICE are performed therein. The model is imposed under two load distributions: a point load and a uniformly

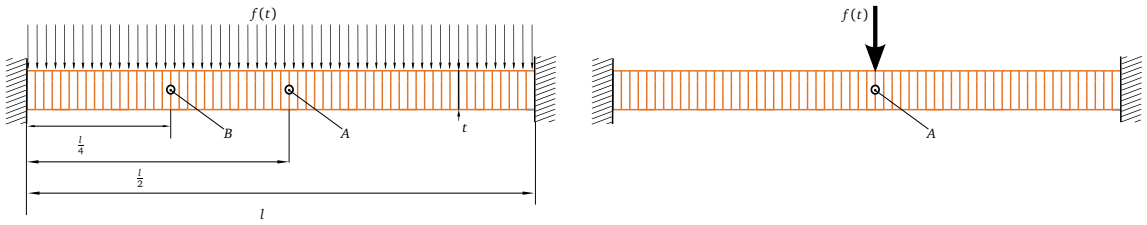

(a) Beam under distributed load **(b)** Beam under point load

Figure 3.1: Schematic of the two side clamped beam model.

	Property (dimension)	**Value**
Material	Mass density (kg/m^3)	7870
	Young's modulus (GPa)	2.05×10^{11}
	Poisson's ratio	0.28
Geometry	l (mm)	300
	t (mm)	1
FE model	Element-type	Timoshenko (Abaqus B21)
	Number of Elements	60
	Number of DOFs	177

Table 3.1: Geometry, material and FE model properties of the investigated flat beam model.

distributed sound pressure as shown in Figs. 3.1b and 3.1a, respectively. Both load distributions are random signals in time and are applied to the structure in two intensity levels. The frequency band of excitation for both load cases is 0-800 Hz.
The NLROMs are developed using the proposed bases and are compared with the full-model as well as the NLROMs based only on linear modes. The time integration for the NLROMs are performed by implicit Newmark scheme with a time step of 5×10^{-5} and for five seconds duration. To compare the performance of the NLROMs, Power Spectral Densities (PSD) of the time signals are computed and compared. Furthermore, the relative error of selected DOFs in time are computed and compared. The relative error is given by

$$\epsilon_n = \frac{\left\| \boldsymbol{u}_{full,n} - \boldsymbol{u}_{ROM,n} \right\|}{u_{average,n}} \times 100 \tag{3.49}$$

where $\boldsymbol{u}_{full,n}$, $\boldsymbol{u}_{ROM,n}$ and $u_{average,n}$ are the time response of the full model, the ROM model and the root-mean-square of the full model's time signal, respectively, all for the n^{th} DOF. To identify the NSCs of the developed NLROMs, the value of the maximum desired displacement to have the most accurate results is chosen as

$$W_{i_{\max}} = \tfrac{1}{4}t, \tag{3.50}$$

where, t is the thickness of the beam. All the NLROMs are developed in MATLAB® and using the ICE method. For this example, we developed three NLROMs with the same size but with different reduction bases as

- The first six linear VMs (NLROM-6VM).

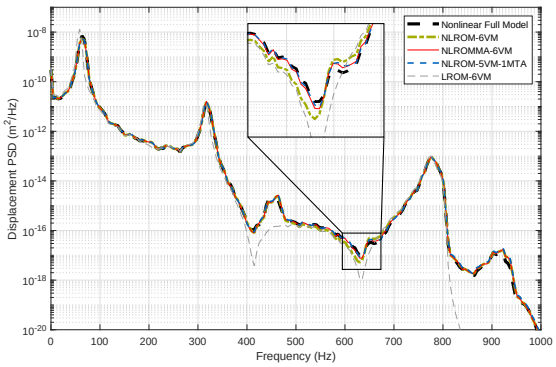

(a) Transverse PSD of point A under 135 dB

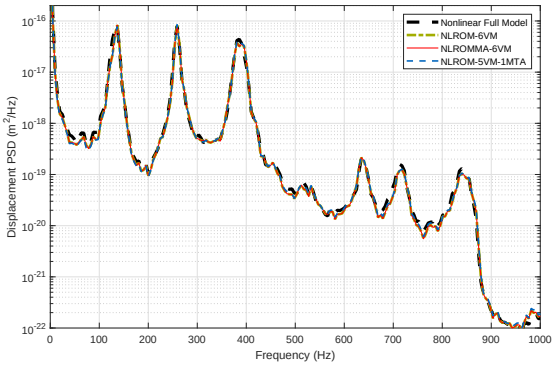

(b) Membrane PSD of point B under 135 dB

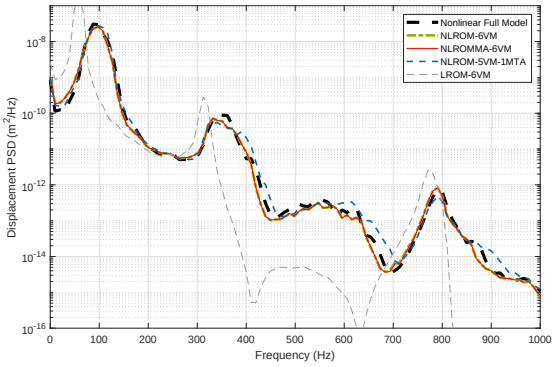

(c) Transverse PSD of point A under 150 dB

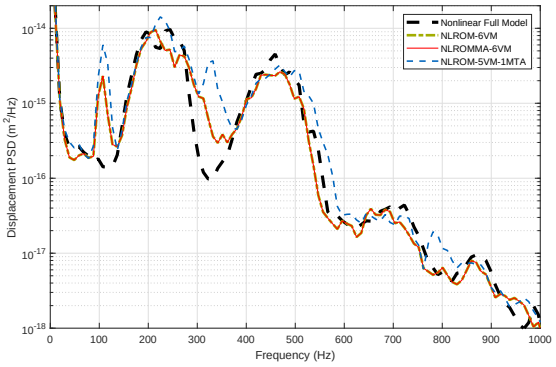

(d) Membrane PSD of point B under 150 dB

Figure 3.2: PSDs Comparison of three NLROMs: NLROM-6VM, NLROMMA-6VM, NLROM-5VM-1MTA with the full-order model and linear reduced model (LROM-6VM) under two excitation levels of 135dB and 150dB.

- The first six linear VMs augmented with the MA method explained in section (3.2.2) (NLROMMA-6VM).
- The first five linear VMs in companion with one MT vector proposed in section (3.2.3) (NLROM-5VM-1MTA).

These NLROMs are compared with the full-order model as well as the linear reduced model with 6 linear VMs in its basis (LROM-6VM). In fact, the LROM is employed here to show the difference between the linear and nonlinear responses. Fig. 3.2 shows the PSD comparison of the mentioned NLROMs under two uniform distributed sound pressures with 135dB and 150dB Sound Pressure Levels (SPL). The PSDs for the transverse direction of point A and membrane direction of point B are shown (see Fig. (3.1a)), because the maximum transverse and membrane motion occur near these two points, respectively. For both relatively low and and high levels of excitations, the transverse PSD has been improved (Figs. 3.2a and 3.2c) by adding one MTA vector instead of one linear VM in the reduction basis, while the improvement by the MA method is much smaller than MTA. However, the PSD in the membrane direction has not been importantly improved for both low and high level of excitation. To observe the improvement of the NLROM with MTA in the basis, the relative

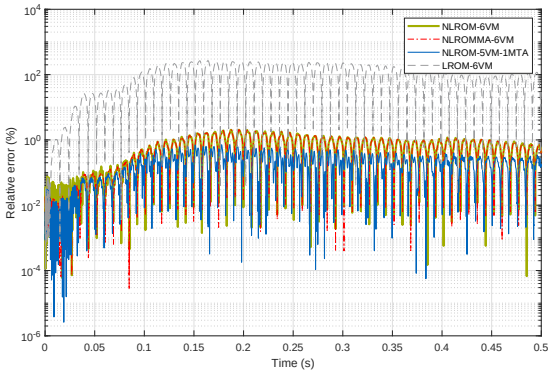

(a) Transverse DOF of point A under 135 dB

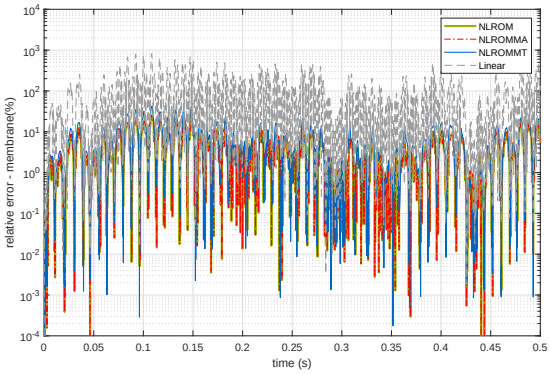

(b) Membrane DOF of point B under 135 dB

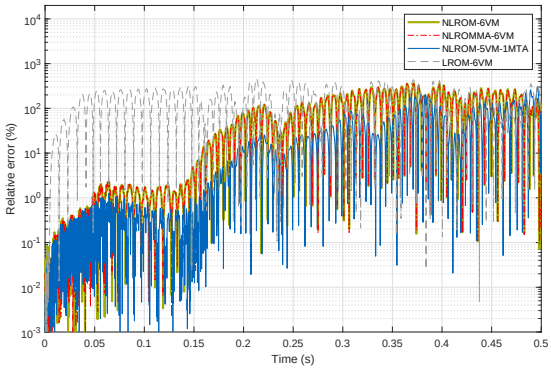

(c) Transverse DOF of point A under 150 dB

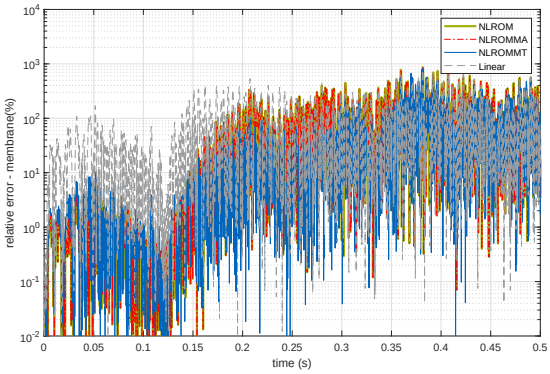

(d) Membrane DOF of point B under 150 dB

Figure 3.3: Relative error comparison for the first half seconds (out of five seconds) of the time signals that are used to compute the PSDs of Fig. 3.2.

error for the first half second of the time integration used in Fig. 3.2 is depicted in Fig. 3.3. This figure confirms that the relative error for the transverse direction of the NLROM with MTA (Figs. 3.3a and Fig. 3.3c) is smaller compared to all other developed ROMs. The improvement of the transverse direction is not observed when they are expanded to obtain the membrane motion (Figs. 3.3b and Fig. 3.3d).
The same analysis is performed when a point load is applied to the structure (see Fig. 3.1b), which is a random signal in time. Fig. 3.4 shows the PSD comparison of the transverse direction of point A as well as the in-plane direction of point B for two excitation levels with RMS of 0.5N and 2N. Fig. 3.5 demonstrates the relative error of the same DOFs under the same loads for the first half seconds of time integration. The accuracy of the transverse direction for the low level of excitation is improved (Figs 3.4a), while this improvement is very small for the high level of excitation. This is because the induced error for high level of excitation is not only because of approximation of load distribution, rather due to activation of interaction of lower modes with high frequency modes.
Furthermore, the effect of higher order terms of the MTA vectors considered in [130] is not investigated in this work, because first it is shown that this improvement is slight even for linear models. Secondly, taking the higher order terms in the reduction

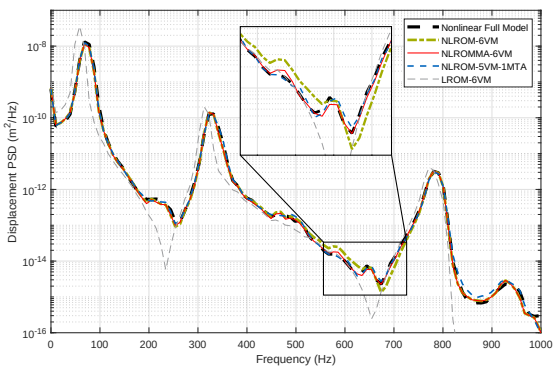

(a) Transverse PSD of point A under 0.5 N

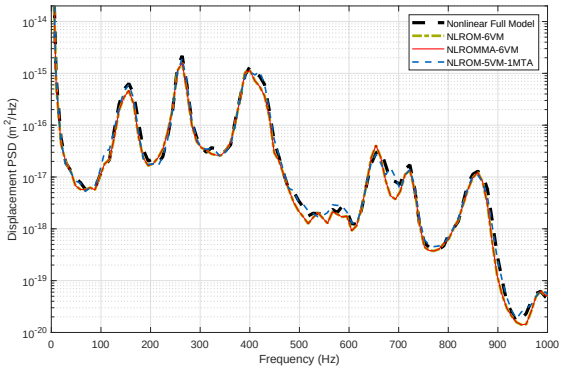

(b) Membrane PSD of point B under 0.5 N

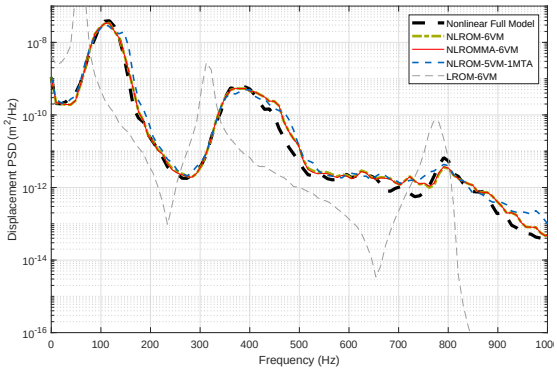

(c) Transverse PSD of point A under 2 N

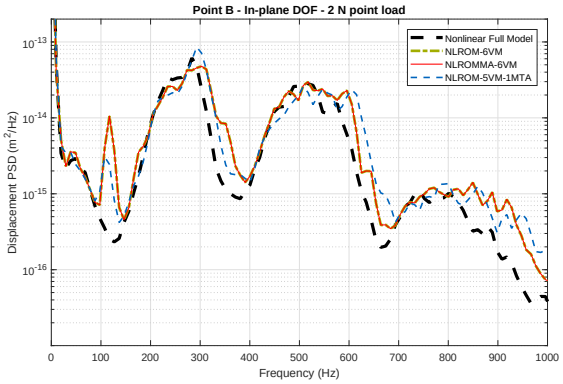

(d) Membrane PSD of point B under 2 N

Figure 3.4: PSDs Comparison of three NLROMs: NLROM-6VM, NLROMMA-6VM, NLROM-5VM-1MTA with the full-order model and linear reduced model (LROM-6VM) under two point loads of 0.5 and 2 N.

basis leads to increasing the dimension of the NLROM, which is usually not desired.

3.4 Summary

This chapter extends the Mode Acceleration Correction and Modal Truncation Augmentation methods in nonlinear model order reduction. To develop the nonlinear reduced order model, a force-based non-intrusive approach has been employed. This has the advantage that the model order reduction procedure can be performed in any FE package without requiring direct access to the nonlinear finite element equations of motion of the full-order model. In this way, a set of static loads has to be generated and applied to the nonlinear FE formulation, which is called the Applied Force or ICE method. In the original ICE, the static loads are constructed using a truncated number of linear (transverse) eigenmodes, which are in the frequency range of interest with a margin and a scaling factor that can trigger the nonlinear restoring force. However, these modes are not able to accurately approximate the spatial distribution of the external excitation. Therefore, in this work we extended the classical force bases with two new methods in nonlinear model order reduction field.

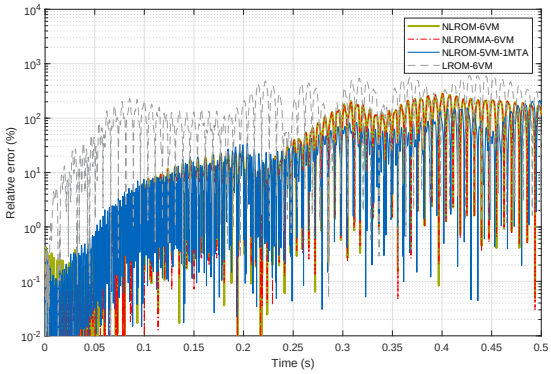

(a) Transverse DOF of point A under 0.5 N

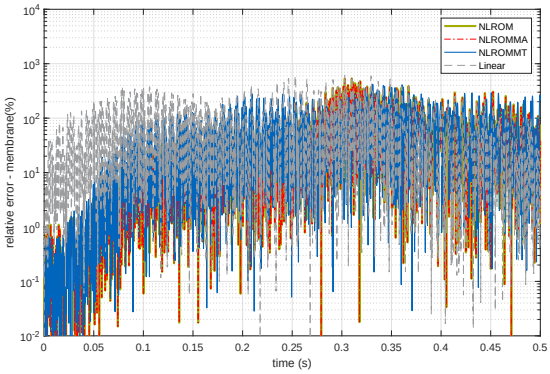

(b) Membrane DOF of point B under 0.5 N

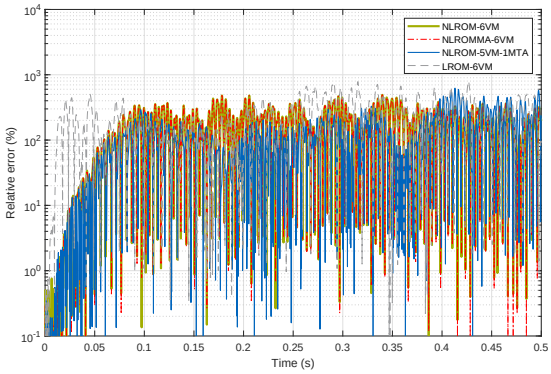

(c) Transverse DOF of point A under 2 N

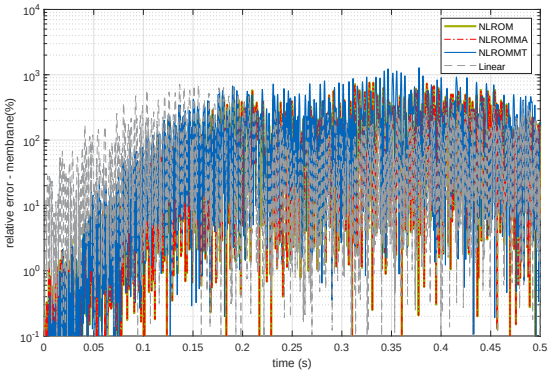

(d) Membrane DOF of point B under 2 N

Figure 3.5: Relative error comparison for the first half seconds (out of five seconds) of the time signals that are used to compute the PSDs of Fig. 3.4.

In the MA method, the displacements computed from the original ICE are augmented by linear static contribution of truncated modes due to external loads. Furthermore, in the MTA method, the quasi-static contribution of truncated modes is obtained using the Rayleigh-Ritz method, as Modal Truncation (MT) vectors. These vectors are afterwards employed as new basis vectors to generate the static loads required for the identification of the Nonlinear Stiffness Coefficients (NSC) in ICE.
The two proposed methods are implemented for a clamped-clamped beam example with geometric nonlinear effects. A random excitation is imposed on the structure to check the accuracy of the proposed methods. It has been shown that the MA method does not improve the time response of the NLROM when the response is in the nonlinear regime. However, the proposed nonlinear MTA method discernibly enhances the accuracy of the NLROM for distributed load cases and more slightly for point load cases. This improvement is mostly achieved for transverse vibration of the system.

Chapter 4

Displacement-based non-intrusive MOR

This chapter is extracted from the author's work in [66], which is submitted for publication. In this article, Karamooz had the idea of the work, derived the numerical results for the shown examples, and wrote the manuscript. Brandt conducted parts of the numerical implementations, discussed the work and proof-read the article. Tiso and Rixen gave very useful inputs in the discussions of the work, proof-read the article and modified it. Rixen supervised the work.

4.1 Introduction

The Implicit Condensation and Expansion method that we investigated in Chapter 3 has two main challenges. First, it can only be used to build NLROMs with a small number of DOFs, because the number of required nonlinear static solutions is a cubic function of the number of modal coordinates of the the NLROM. Second, the assumption of ICE to retrieve the in-plane motion of a shell-like structure is only valid when the relationship between transverse and membrane coordinates is quadratic, which is only valid for certain cases. This will be discussed more in Chapter 5, where the methods are compared.
An alternative approach for non-intrusive MOR is the *Enforced Displacement* (ED) (also known as STEP (STiffness Evaluation Procedure)) method, which was first introduced by Muravyov and Rizzi [103]. In this method, selected static displacements that trigger nonlinearity are prescribed to the model through the FE package. The FE package then computes the required reaction forces and the NSCs are obtained by solving a set of linear equations given the input displacements and output forces. To reduce the number of nonlinear static solutions in NSCs identification, Perez et al. [116] used the Tangent Stiffness (TS) matrices due to assigned static displacements, instead of reaction forces for identifying the NSCs. They showed that in this way the number of required nonlinear static solutions reduces significantly, leading to less offline computational costs for the development of NLROMs. The TS-based method of Perez et al. is called the *Enhanced Enforced Displacement* (EED) method here.
The accuracy of the developed NLROM in the non-intrusive methods highly depends on the "correct" selection of assigning displacement bases. For instance, in the MOR of shell-like structures, choosing a set of truncated vibration modes as displacement bases in (E)ED, which are bending-dominated modes, does not deliver accurate NLROMs. Instead, the membrane-dominated modes also have to be manually selected

and augmented to the input displacements to achieve accurate results[1], which is a cumbersome work and the challenge of this method [98, 133].
In order to cope with this problem, *Dual* or *Companion* modes are proposed in [76] to capture the nonlinear interaction between the vibration modes. The idea is to enforce a set of selected static load cases from the kept linear modes to the system and compute the corresponding nonlinear displacements. These displacements are then orthogonalized to the linear modes kept in the basis and appended to them in the reduction basis. By this, the basis is enriched in a quasi-systematic way to approximate the nonlinear response of the NLROM accurately. However, the main issue with the dual modes is that, to be able to acquire good results using this approach, a relatively large number of representative load cases are required to be generated from near linear to strong nonlinear responses. Moreover, the procedure for the selection of the important dual mode is in many cases load-dependent and based on trial and error, which can be expensive for large structures.
In this chapter, we propose appending non-intrusively computed *Modal Derivatives* (MDs) to a basis of dominant vibration modes to form a reduction basis for a non-intrusive ROM. To compute the MDs non-intrusively, two different strategies are outlined, namely for the cases where either the tangent stiffness or nonlinear reaction forces are available from a nonlinear static solution.
The first advantage of the proposed method is that by using MDs, one does not require manual selection of membrane-dominated modes demanded to accurately develop the NLROM. Instead, the most important nonlinear features of the full-order response are conveyed by non-intrusive MDs, which are systematically derived from the originating vibration modes (i.e do not require trial and error selection) and are easy to compute. The second advantage is that the MDs are selected in a load-independent manner and the resulting NLROM can be valid for a range of loading conditions. The accuracy as well as the computational efficiency of the proposed method is evaluated by applying it to different FE models subject to various random sound pressure levels. These results are also compared with the results of the NLROMs, which are obtained by using either only linear modes or linear modes augmented with dual modes in the reduction basis. The validation is carried out by comparing the Power Spectral Density (PSD) of the displacements of the NLROMs and the full model. Our results indicate that the method we propose improves accuracy when compared to other available non-intrusive techniques, without increasing offline and online costs.

4.2 Non-intrusive model order reduction

Let us rewrite the governing equations for an FE model with linear material properties and large deformations (i.e. geometric nonlinearity) and n Degrees-Of-Freedom (DOFs) as (for more details see e.g. [12, 13])

$$\boldsymbol{M}\ddot{\boldsymbol{u}}(t)+\boldsymbol{D}\dot{\boldsymbol{u}}(t)+\boldsymbol{f}_{int}(\boldsymbol{u}(t))=\boldsymbol{f}(t), \tag{4.1}$$

[1] In case of curved structures, this augmentation is not necessarily membrane-dominated, see [146].

where the mass matrix is denoted by $\boldsymbol{M}$ and $\boldsymbol{f}_{int}$ is the nonlinear internal force vector modeling geometric nonlinearity. In this work, a linear viscous damping (denoted by $\boldsymbol{D}$) is adopted. The displacement and external force vectors are $\boldsymbol{u}$ and $\boldsymbol{f}$, respectively. Following standard notation, time derivative is indicated by $\dot{(\,)}$. Note that in Eq. (4.1) and the remainder of this work the time-dependency is omitted for the sake of simplicity, unless otherwise indicated.
In order to obtain a ROM for Eq. (4.1), a reduction basis must be defined, which maps the full-order model with n DOFs, to a reduced set of m generalized coordinates, with $m << n$, namely

$$\boldsymbol{u} \approx \boldsymbol{V}\boldsymbol{q}, \tag{4.2}$$

where $\boldsymbol{V}$ $(n \times m)$ is the reduction basis and $\boldsymbol{q}$ $(m \times 1)$ denotes the vector of the reduced set of generalized coordinates. The ROM is then achieved by introducing Eq. (4.2) to (4.1) and pre-multiplying it by $\boldsymbol{V}^T$ (the superscript T denotes the transpose of the matrix) to enforce the generated errors due to model reduction orthogonal to the reduction basis, as explained in Chapter 2. The nonlinear reduced internal force vector is approximated by a Taylor series expansion up to cubic terms

$$\hat{\boldsymbol{f}}_{int}(\boldsymbol{q}) = \hat{\boldsymbol{K}}^{(1)}\boldsymbol{q} + (\hat{\boldsymbol{K}}^{(2)}.\boldsymbol{q}).\boldsymbol{q} + \left[(\hat{\boldsymbol{K}}^{(3)}.\boldsymbol{q}).\boldsymbol{q}\right].\boldsymbol{q}. \tag{4.3}$$

The NSCs, $\hat{\boldsymbol{K}}^{(2)}$ and $\hat{\boldsymbol{K}}^{(3)}$ in Eq. (4.3) can be obtained either by direct projection of the full-order tensors (in case $\boldsymbol{f}_{int}$ is of polynomial form up to cubic terms, as is the case for linear solid elements and von-Karman shells) or by identification through non-intrusive methods. If the FE model of the structure is developed in a commercial FE analysis package, there is usually no access to the nonlinear stiffness tensors of the underlying structure. Therefore, to obtain the NSCs of the reduced model, we explain two displacement-based non-intrusive MOR techniques next.

4.2.1 Enforced Displacement

The Enforced Displacement (ED) method was first developed by Muravyov and Rizzi [103], and later modified by Kim et al [76] for the case where the linear stiffness matrix is also unknown. The ED method is based on enforcing a series of nonlinear static displacements to the FE model, and computing the corresponding forces required to create these displacements. Having the applied displacement and the corresponding forces, the unknown coefficients can be computed by solving a series of linear algebraic equations.
Since the identification procedure here is based on static cases, Eq. (4.1) for the NLROM reduces to

$$\hat{K}^{(1)}_{ij}q_j + \hat{K}^{(2)}_{ijl}q_jq_l + \hat{K}^{(3)}_{ijlp}q_jq_lq_p = \hat{f}_i. \tag{4.4}$$

The first step in the ED parameter identification methodology is the construction of two different displacements (in case the linear stiffness is available) from each single generalized coordinate while all other coordinates are zero, i.e.

$$\boldsymbol{u}^{(a)} = q^{(a)}_r\boldsymbol{V}_r, \quad a = 1,2, \qquad r = 1,2,...,m, \tag{4.5}$$

where $\boldsymbol{u}^{(1)}$ and $\boldsymbol{u}^{(2)}$ are the static displacement fields to be given to the FE package; $q_r^{(1)}$ and $q_r^{(2)}$ are different scaling factors for the r^{th} generalized coordinate ($r = 1, 2, ..., m$), and $\boldsymbol{V}_r$ is the r^{th} column of the reduction basis matrix. To form the two required displacement vectors for each generalized coordinate, usually one scaling factor is chosen with different signs. By static imposition of the displacement fields of Eq. (4.5) to the structure, all the stiffness coefficients corresponding to two or three different generalized coordinates are zero (e.g. $K_{ijl}^{(2)} = K_{ijlp}^{(3)} = 0, j \neq l \neq p$). The modal forces corresponding to these displacements for the i^{th} equation of (4.4) are then given by

$$\hat{f}_i^{(a)} = \boldsymbol{V}_i^T \boldsymbol{f}^{(a)} \quad a = 1, 2, \tag{4.6}$$

where $\boldsymbol{f}^{(1)}$ and $\boldsymbol{f}^{(2)}$ are the reaction forces due to the applied displacement in physical domain and $\hat{f}_i^{(1)}$ and $\hat{f}_i^{(2)}$ are the i^{th} component of their counterparts in modal domain ($i = 1, 2, ..., m$). By substituting Eqs. (4.5) and (4.6) into Eq. (4.4) one obtains

$$\hat{K}_{ir}^{(1)} q_r^{(a)} + \hat{K}_{irr}^{(2)} (q_r^{(a)})^2 + \hat{K}_{irrr}^{(3)} (q_r^{(a)})^3 = \hat{f}_i^{(1)}, \quad a = 1, 2, \tag{4.7}$$

which lead to the solution of all unknown coefficients in the form of $\hat{K}_{irr}^{(2)}$ and $\hat{K}_{irrr}^{(3)}$, in Eq. (4.7). Note that if the reduced linear stiffness is not obtained in advance from direct projection of the full-order linear stiffness, then three static displacement per each generalized coordinate must be imposed in Eq. (4.5) to also compute $\hat{K}_{ir}$ [76]. In the next step, a combination of two columns of the reduction basis with different generalized coordinates are imposed on the system while all other modes are zero, namely

$$\boldsymbol{u} = \begin{bmatrix} \boldsymbol{V}_{(r)} & \boldsymbol{V}_{(s)} \end{bmatrix} \begin{bmatrix} q_r & -q_r & q_r \\ q_s & -q_s & -q_s \end{bmatrix}, \; s \geq r. \tag{4.8}$$

The corresponding forces required to induce the three displacements are then computed and projected in the modal domain to obtain the components of the modal force needed to be substituted in Eq. (4.4). This leads to three Eqs., which are utilized to obtain the unknown parameters $\hat{K}_{irs}^{(2)}$, $\hat{K}_{irss}^{(3)}$, and $\hat{K}_{issr}^{(3)}$ corresponding to the multiplication of two different modal coordinates ($q_r \neq q_s$). It should be mentioned here that due to the symmetry of the stiffness tensors, the elements of the nonlinear stiffness tensors $\hat{K}_{ijl}^{(2)}$ and $\hat{K}_{ijlp}^{(3)}$ are only computed and stored for the case where $p > l > j$.

The last step in the parameter estimation procedure of ED method is the identification of the unknown NSCs corresponding to the combination of three different modes, i.e. $\hat{K}_{irst}^{(3)}$. To do so, a combination of three different generalized coordinates are employed, as

$$\boldsymbol{u} = \begin{bmatrix} \boldsymbol{V}^{(r)} & \boldsymbol{V}^{(s)} & \boldsymbol{V}^{(t)} \end{bmatrix} \begin{Bmatrix} q_r & q_s & q_t \end{Bmatrix}^T, \; t \geq s \geq r. \tag{4.9}$$

Imposing these nonlinear static displacements result in the corresponding forces, which are transformed to the modal domain and introduced to Eq. (4.4), leading to the identification of NSCs of the form $\hat{K}_{irst}^{(3)}$. The number of the nonlinear static solutions required to develop an NLROM with m DOFs is

$$N = 2m + 3\,{}_mC_2 + {}_mC_3 \tag{4.10}$$

where

$$ {}_mC_r = \frac{m!}{(m-r)!\,r!} \tag{4.11} $$

As can be seen in Eq. (4.10), the number of required nonlinear static solutions of the ED method is in the same order as ICE ($O(m^3)$), which limits the number of possible DOFs in the NLROM. In order to reduce the order of required static solutions, the Enhanced ED (EED) method was proposed by [116] and is explained in the next section.

Generalized coordinates factor

Theoretically, a variety of magnitudes of the generalized coordinates (scaling factors) $\boldsymbol{q}$ can be applied to the ED method. However, in practice these values must be large enough to trigger geometric nonlinearity in the system and not too large, to avoid convergence problem of the solution in the FE package. For instance, Mignolet et al. [99] have studied different scaling factors for transverse and membrane motion of shell-like structures. It is usually suggested to prescribe scaling factors, which result in one thickness deformation of the structure for transverse-dominated modes and $\frac{1}{10}$ to $\frac{1}{100}$ of that for membrane-dominated modes (or other augmentations to the transverse-dominated modes, like dual modes or modal derivatives).

4.2.2 Enhanced Enforced Displacement

The Enhanced Enforce Displacement method was first introduced by Perez et al. [116], and further validated for nonlinear structures under thermal, aerodynamic and acoustic loading conditions in [93, 94]. The key idea of the EED method is employing the TS matrix, instead of the restoring forces of the FE model, due to an imposed displacement. The TS matrix contains more information about the NSCs than the restoring forces, resulting in the identification of more coefficient from one nonlinear static analysis.
To identify the NSCs of an NLROM with EED, let us assume that the FE package, in which the nonlinear model is developed, releases the TS matrix out of a nonlinear static analysis (this is the case for many commercial software, e.g. Abaqus, Nastran, etc.). The TS matrix of the full-order model from a nonlinear static analysis is then mapped into the reduced space of generalized coordinates using the previously defined reduction basis (section 4.3). This gives

$$ \hat{\boldsymbol{K}}^t(\boldsymbol{q}) = \boldsymbol{V}^T \boldsymbol{K}^t(\boldsymbol{u}) \boldsymbol{V}, \tag{4.12} $$

where $\hat{\boldsymbol{K}}^t$ and $\boldsymbol{K}^t$ are the TS matrices for the reduced- and full-order models, respectively. The TS matrix is the Jacobian of the nonlinear restoring force vector with respect to generalized coordinates, namely,

$$ \hat{\boldsymbol{K}}^t = \boldsymbol{J}_{\hat{f}_{\text{int}}}(\boldsymbol{q}) = \begin{bmatrix} \frac{\partial \hat{f}_{\text{int}_1}}{\partial q_1} & \cdots & \frac{\partial \hat{f}_{\text{int}_1}}{\partial q_m} \\ \vdots & \ddots & \vdots \\ \frac{\partial \hat{f}_{\text{int}_m}}{\partial q_1} & \cdots & \frac{\partial \hat{f}_{\text{int}_m}}{\partial q_m} \end{bmatrix}, \tag{4.13} $$

where its ir^{th} component is

$$\begin{aligned}\hat{K}^t_{ir} &= \frac{\partial \hat{f}_{\text{int}_i}}{\partial q_r} = \frac{\partial}{\partial q_r}[K^{(1)}_{ij}q_j + K^{(2)}_{ijl}q_j q_l + K^{(3)}_{ijlp}q_j q_l q_p] \\ &= K^{(1)}_{ir} + [K^{(2)}_{ijr} + K^{(2)}_{irj}]q_j + [K^{(3)}_{ijlr} + K^{(3)}_{ijrl} + K^{(3)}_{irjl}]q_j q_l.\end{aligned} \tag{4.14}$$

Similar to the ED method, to obtain the first set of unknown NSCs, two static displacements are formed per each single generalized coordinate, as per Eq. (4.5). Then, the ir^{th} element of the resulting TS in modal domain yields

$$\hat{K}^{t^{(a)}}_{ir} = K^{(1)}_{ir} + [K^{(2)}_{ijr} + K^{(2)}_{irj}]q^{(a)}_j + [K^{(3)}_{ijjr} + K^{(3)}_{ijrj} + K^{(3)}_{irjj}](q^{(a)}_j)^2,\ a = 1, 2. \tag{4.15}$$

Let us recall the assumption of section 4.2.1 that the coefficients of the form $K^{(2)}_{ijl}$ and $K^{(3)}_{ijlp}$ are put to zero except the case where $p > l > j$, due to symmetry of the tensors. This assumption splits Eq. (4.15) into three conditions, namely

$$\begin{aligned}\hat{K}^{t^{(a)}}_{ir} &= K^{(1)}_{ir} + K^{(2)}_{ijr}q^{(a)}_j + K^{(3)}_{ijjr}(q^{(a)}_j)^2 \quad if\ \ j < r, \\ \hat{K}^{t^{(a)}}_{ir} &= K^{(1)}_{ir} + 2K^{(2)}_{irr}q^{(a)}_j + 3K^{(3)}_{irrr}(q^{(a)}_j)^2 \quad if\ \ j = r, \\ \hat{K}^{t^{(a)}}_{ir} &= K^{(1)}_{ir} + K^{(2)}_{irj}q^{(a)}_j + K^{(3)}_{irjj}(q^{(a)}_j)^2 \quad if\ \ j > r.\end{aligned} \tag{4.16}$$

For each condition, there are two unknowns corresponding to the quadratic and cubic NSCs, which are obtained using the corresponding modal coordinates and TS components from the two previously performed static analyzes. In this way, all the coefficients in the form of $\hat{K}^{(2)}_{irj}$, $\hat{K}^{(3)}_{irjj}$, $\hat{K}^{(3)}_{ijjr}$, and $\hat{K}^{(3)}_{irrr}$ are identified, given that the linear stiffness is previously computed from Eq. (2.25).
The second and final step, is the identification of those cubic NSCs, $\hat{K}^{(3)}_{ijlr}$, where $j \neq l \neq r$. Static displacements of the form

$$\boldsymbol{u} = \boldsymbol{V}_j q_j + \boldsymbol{V}_l q_l, \tag{4.17}$$

have to be enforced on the FE model to attain the TS matrices demanded for the last step. After transforming the TS to the modal domain, its ir^{th} component is written as

$$\hat{K}^t_{ir} = K^{(1)}_{ir} + [K^{(2)}_{ijr}q_j + K^{(2)}_{ilr}q_l] + [K^{(3)}_{ijlr}q_j q_l + K^{(3)}_{ijjr}q^2_j + K^{(3)}_{illr}q^2_l]. \tag{4.18}$$

The only unknown in this equation is $K^{(3)}_{ijlr}$, which can then be computed.
As can be seen in the identification procedure of the EED method, the displacements from a combination of three generalized coordinates are no longer required to identify all the coefficients. The exact number of static cases required is given by

$$N = 2m + {}_mC_2. \tag{4.19}$$

Therefore, the order of nonlinear static analysis reduces from $O(m^3)$ to $O(m^2)$. The work flows of ED as well as EED are shown in the flowchart of Fig. 4.1. Furthermore, Fig. 4.2 shows the rate of growth of the required nonlinear static solution versus the number of generalized coordinates in the NLROM for ED and EED methods. This figure shows a significant reduction of the static solutions for the EED method compared to the ED method while the number of DOFs in the NLROMs are increased, which results in less computational costs for reducing the model.

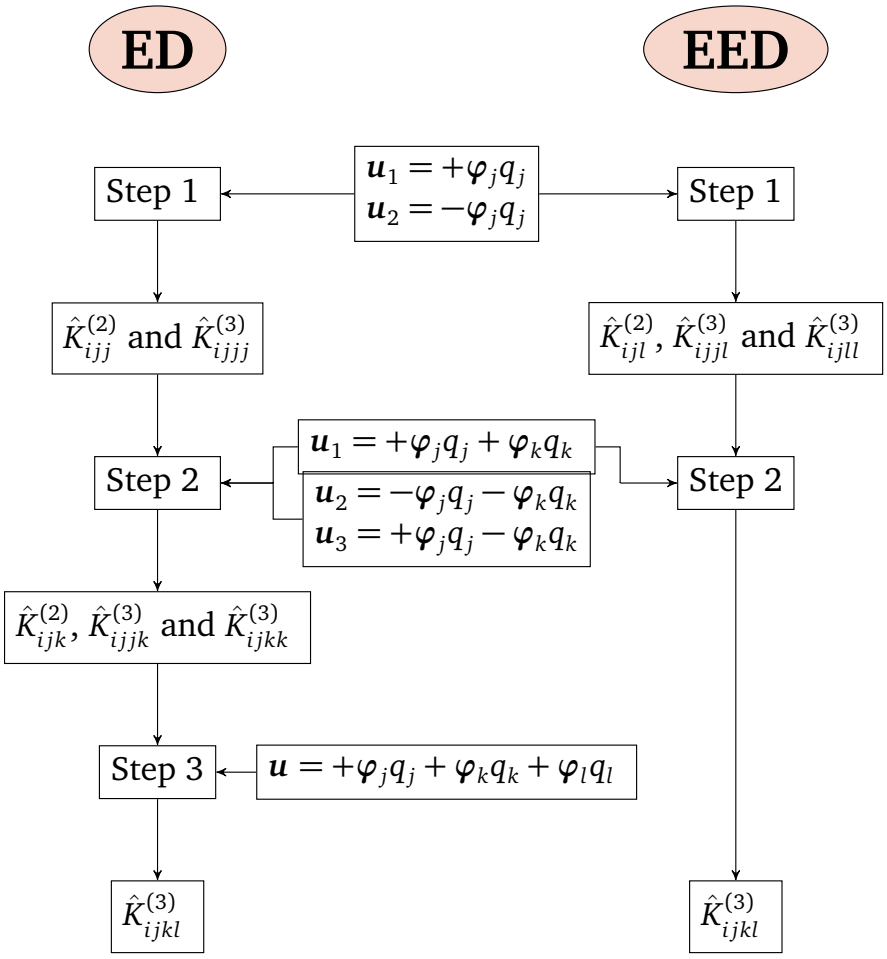

Figure 4.1: Flowchart of the steps to identify nonlinear stiffness coefficients of an NLROM using ED and EED.

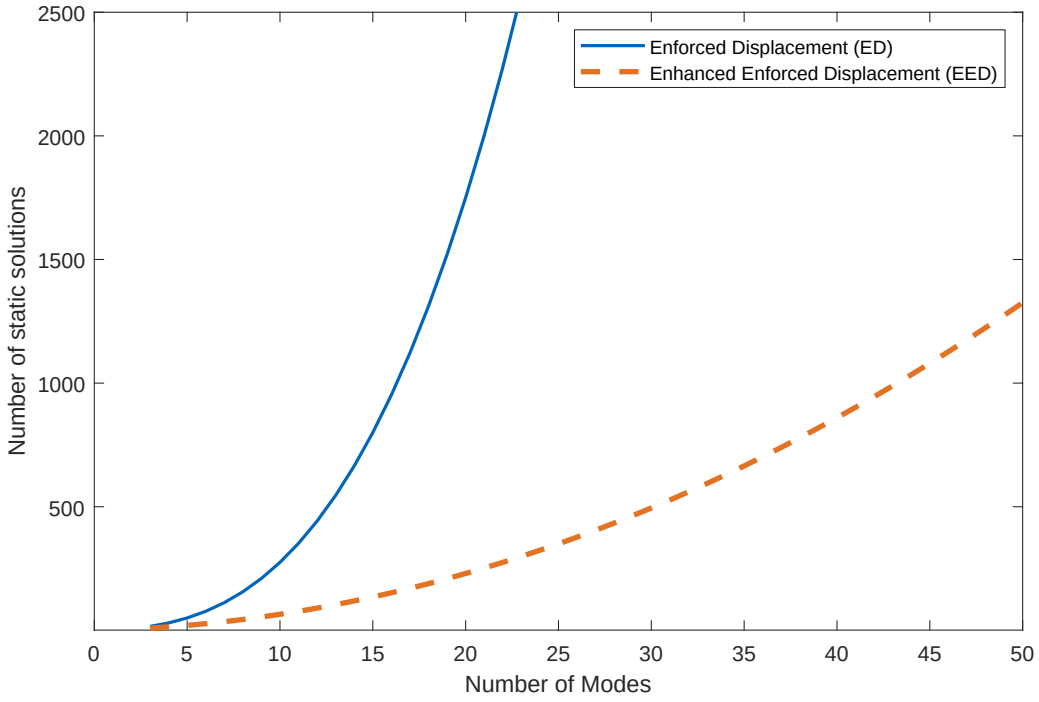

Figure 4.2: The number of required nonlinear static solutions versus the number of kept modes in the reduction basis for the ED and EED methods.

4.3 Basis selection: simulation-free methods

As mentioned before, selection of an appropriate basis for nonlinear model reduction techniques is one of the key challenges. The reduction basis should generally contain all the linear modes of the system in the frequency band of excitation and convey the main nonlinear features of the response. It should furthermore be computationally cheap and possibly load-independent.
There are generally two types of reduction bases in the context of nonlinear ROM. The first class of bases is derived by *data driven* methods, which are based on performing a dynamic simulation of the full-order model. Examples of these approaches are Proper Orthogonal Decomposition (POD) or Smooth Orthogonal Decomposition (SOD) (see [22, 50, 118, 120, 132, 158]). These methods are not considered in this work, as we aim at both avoiding the need of time integration of the full system and devise a basis construction that is not load dependent. To this end, we look at the so-called *simulation-free* methods, which do not require full dynamic simulation and yield a basis that is not dependent of the specific excitation. As such, the resulting ROM can be valid for different loading conditions. While methods along this line already exist, here we propose a new basis suitable for non-intrusive ROM methods.

4.3.1 Linear vibration modes

The original ED method in [103] proposed the use of linear Vibration Modes (VMs) as the basis for projection of the full-order linear matrices as well as identification of

the NSCs. This basis has been further investigated in different works (see e.g. [119, 121, 133]). The VMs are the solution of the eigenvalue problem associated to the linearized system, namely,

$$(\boldsymbol{K}^{(1)} - \omega_j^2 \boldsymbol{M})\boldsymbol{\varphi}_j = 0, \tag{4.20}$$

where ω_j and $\boldsymbol{\varphi}_j$ are the j^{th} eigenfrequency and linear VM of the system, respectively. A set of these modes are then selected according to the frequency band of interest to form the reduction basis matrix as

$$\boldsymbol{V} = [\boldsymbol{\varphi}_1, \boldsymbol{\varphi}_2, \cdots, \boldsymbol{\varphi}_m]. \tag{4.21}$$

The linear VMs are usually mass-normalized before being used in NSCs identification procedure. The number of VMs can be highly reduced if they are selected according to a specified spatial load distribution [119, 121, 133].
However, the main disadvantage of this basis is that selection of a set of truncated VMs does not suffice for the basis, because they are usually not well representing the nonlinear behavior. For instance, when the structure is made of plates and shells, the low-frequency modes are typically of a bending nature, and as such, they do not feature axial displacements that are needed to represent the nonlinear bending-stretching coupling. Therefore, to complete the basis in this way, a few high frequency membrane-dominated modes must be identified and augmented to the basis to develop an accurate NLROM. Manual identification of the membrane-dominated modes for simple structures is a difficult but feasible work. However, for complex structures, the computation and selection of the required high frequency modes becomes an unfeasible approach. Therefore, it is desiderable to find an accurate basis in a systematic way.

4.3.2 Dual modes

In order to avoid the manual selection of membrane modes in the primary basis of ED (section 4.3.1), dual modes are proposed (cf. [76]) and further investigated in many applications (e.g. see [48, 75, 93, 94, 116]). The key concept of dual modes is based on the selection of a set of representative static forces to be applied to the full-order model and solving for the corresponding displacements with nonlinear static solutions. These displacements are then orthogonalized to the linear modes basis to leave only the nonlinear effects therein. There are generally three generations of the dual modes investigated in [76]. However, it is shown in [98, 116] that it is usually sufficient to choose the set of representative forces in the form of

$$\boldsymbol{f}_i^{(r)} = \alpha_i^{(r)} \boldsymbol{K}^{(1)} \boldsymbol{\varphi}_i, \qquad i \triangleq dominant\ mode \tag{4.22}$$

and

$$\boldsymbol{f}_{ij}^{(r)} = \frac{\alpha_i^{(r)}}{2} \boldsymbol{K}^{(1)} [\boldsymbol{\varphi}_i + \boldsymbol{\varphi}_j], \qquad i \triangleq dominant\ mode,\ and\ i \neq j \tag{4.23}$$

to obtain the corresponding displacement sets. Here, the r^{th} load case and scaling factor are denoted by $\boldsymbol{f}^{(r)}$ and $\alpha_i^{(r)}$, respectively. Note that a *dominant* mode in this

context is loosely defined as a mode, which contributes the most in the nonlinear response of the system. Furthermore, several scaling factors $\alpha_i^{(r)}$ with positive and negative signs have to be chosen and imposed on the system such that the corresponding displacements range from near linear to strongly nonlinear responses. Afterwards, the dual modes are mass-orthogonalized to the kept linear modes and one another using the Gram–Schmidt process.
The next step consists in performing a sequential POD of the representative dual modes for each combination of modes with different scaling factors, and selecting them according to their maximum singular values as well as strain energies, as explained in [76, 98]. Consider the displacement vectors, $\boldsymbol{x}_{s,1}, \boldsymbol{x}_{s,2}, \ldots, \boldsymbol{x}_{s,p}$, are obtained with p scaling factors from the s^{th} combination of modes in (4.22) or (4.23). These vector are cast into a matrix as

$$\boldsymbol{D}_s = \left[\boldsymbol{x}_{s,1}, \boldsymbol{x}_{s,2}, \ldots, \boldsymbol{x}_{s,p}\right], \tag{4.24}$$

which are then orthogonalized to the linear modes and the previously selected duals. Afterwards, a POD is applied to Eq. (4.24) to select the left singular values with the corresponding k highest left singular values, $\boldsymbol{\psi}_{s,1}, \boldsymbol{\psi}_{s,2}, \ldots, \boldsymbol{\psi}_{s,k}$, as potential dual modes. To obtain the final dual modes from these singular vectors, their corresponding strain energy measures are computed as

$$E_{s,r} = \left(\sum_{j=1}^{p} \beta_{r,j}^2\right) \boldsymbol{\psi}_{s,r}^T \boldsymbol{K}^{(1)} \boldsymbol{\psi}_{s,r}, \tag{4.25}$$

where

$$\beta_{r,j} = \frac{\boldsymbol{\psi}_{s,r}^T \boldsymbol{x}_{s,j}}{\boldsymbol{\psi}_{s,r}^T \boldsymbol{\psi}_{s,r}}. \tag{4.26}$$

The Eq. (4.25) introduces those left singular vectors, which are mostly present in the nonlinear displacements obtained from different scaling factors, and also have the highest strain energy. Accordingly, those singular vectors $\boldsymbol{\psi}_{s,r}$ are selected, which have the maximum value of $E_{s,r}$.
Alternatively, the dual modes can be selected regarding their contribution in a specific loading condition, as performed by Perez et al. [116], which results in very accurate NLROMs. However, the issue with the procedure explained in [116] is that the modes are load-dependent, meaning that they are selected for a specific load case, in a trial and error procedure. Therefore, to compare the efficiency of this basis with our proposed alternative (non-intrusive model derivatives), we apply the POD to the representative dual modes and take the singular vectors corresponding to both maximum singular values from the POD analysis and maximum induced strain energy, as done in [76]. Furthermore, in this work we found that performing the orthogonalization procedure of the duals modes after the POD process (instead of before it) can also lead to accurate results. One issue with the construction of the dual modes is that dominant modes in Eqs. (4.22) and (4.23) are loosely defined in the literature without presenting clear criteria to select them. Instead, we propose the use of non-intrusive modal derivatives, which not only can be computed in a systematic way (without manual selection of modes and load-independent), but also can deliver accurate NLROMs.

4.3.3 Modal derivatives: a new basis for non-intrusive ROM

In this section, we propose MDs for non-intrusive MOR methodology. While the linear vibration modes can greatly approximate the motion of linear systems, it is not the case for approximating nonlinear structures. This is because the tangent stiffness $\boldsymbol{K}^t(\boldsymbol{u})$ matrix of the system is displacement-dependent and therefore, the eigenmodes out of each tangent stiffness eigenvalue problem is different from linear vibration modes. As a result, the motion of the system can be written in the form of eigenmodes (also called shape functions) that are a function of a reduced set of coordinates multiplied with the corresponding generalized coordinates as

$$\boldsymbol{u} \approx \boldsymbol{u}_{eq} + \sum_{i=1}^{m} \boldsymbol{\varphi}_i(\boldsymbol{q})\, \boldsymbol{q}_i. \tag{4.27}$$

To account for the effect of change of TS at least up to the second order, Idelsohn and Cardona [60] developed the displacement vector as a Taylor series expansion, at $\boldsymbol{q} = \boldsymbol{0}$, which gives

$$\boldsymbol{u} = \boldsymbol{u}_{eq} + \frac{\partial \boldsymbol{u}}{\partial \boldsymbol{q}}\bigg|_{q=0} \boldsymbol{q} + \tfrac{1}{2} \frac{\partial^2 \boldsymbol{u}}{\partial \boldsymbol{q}\, \partial \boldsymbol{q}}\bigg|_{q=0} : (\boldsymbol{q} \otimes \boldsymbol{q}) + H.O.T. \tag{4.28}$$

By introducing Eq. (4.27) into Eq. (4.28), we obtain

$$\Delta \boldsymbol{u} = \boldsymbol{u}(q) - \boldsymbol{u}_{eq} \approx \sum_{i=1}^{m} \boldsymbol{\varphi}_i(\boldsymbol{q} = \boldsymbol{0}) q_i + \sum_{i=1}^{m} \sum_{j=1}^{m} \tfrac{1}{2} \left[\frac{\partial \boldsymbol{\varphi}_i}{\partial q_j}(\boldsymbol{q} = \boldsymbol{0}) + \frac{\partial \boldsymbol{\varphi}_j}{\partial q_i}(\boldsymbol{q} = \boldsymbol{0}) \right] q_i q_j. \tag{4.29}$$

This equation expresses that the nonlinear displacement of a system can be approximated as a superposition of linear eigenmodes of the system and corresponding derivatives. By introducing a new generalized coordinate, η_r, for each quadratic term, $q_i q_j$, Eq. (4.29) is obtained as a superposition of linear modes and their derivatives. Lastly, the reduction basis can be written in the form

$$\boldsymbol{V} = \left[\boldsymbol{\varphi}_1, \boldsymbol{\varphi}_2, \cdots, \boldsymbol{\varphi}_m, \boldsymbol{\theta}_{11}, \frac{1}{2}(\boldsymbol{\theta}_{12} + \boldsymbol{\theta}_{21}), \cdots, \frac{1}{2}(\boldsymbol{\theta}_{ij} + \boldsymbol{\theta}_{ji}), \cdots, \boldsymbol{\theta}_{mm} \right], \tag{4.30}$$

where

$$\boldsymbol{\theta}_{ij} = \frac{\partial \boldsymbol{\varphi}_i}{\partial q_j}, \tag{4.31}$$

is called the ij^{th} MD of the system.
The main advantage of using MDs instead of membrane-dominated or Dual modes is that they enrich the linear transverse-dominated basis in a systematic and load-independent manner. Furthermore, it will be shown in this work that augmenting the linear modes with MDs in the reduction basis represents very accurate results compared to the other two bases (sections 4.3.1 and 4.3.2) under the same condition.

Calculation of modal derivatives

There are different ways to compute the MDs (e.g. see [60, 61, 105, 144]). In this work we consider two of them, which can be computed non-intrusively. To obtain the ij^{th} MD, Eq. (4.20) is differentiated with respect to the generalized coordinate q_j, giving

$$\left(\boldsymbol{K}^{(1)} - \omega_i^2 \boldsymbol{M}\right) \frac{\partial \boldsymbol{\varphi}_i}{\partial q_j} = \left(\frac{\partial \omega_i^2}{\partial q_j}\boldsymbol{M} - \frac{\partial \boldsymbol{K}}{\partial q_j}\right)\boldsymbol{\varphi}_i. \tag{4.32}$$

The derivative of the eigenvalue, $\frac{\partial \omega_i^2}{\partial q_j}$ is obtained by multiplying Eq. (4.32) with $\boldsymbol{\varphi}_i^T$. This value is then introduced to Eq. (4.32) leading to only one unknown, which is the MD. However, the coefficient of the MD in the left hand side of Eq. (4.32) is singular according to Eq. (4.20). Therefore, to solve this equation for the MDs, Nelson [105] proposed a generalized solution of Eq. (4.32) as

$$\frac{\partial \boldsymbol{\varphi}_i}{\partial q_j} = \boldsymbol{v}_i + c_i \boldsymbol{\varphi}_i, \tag{4.33}$$

where $\boldsymbol{v}_i$ is the particular solution and $c_i\boldsymbol{\varphi}_i$ is the homogeneous solution of the MD. According to the Nelson's method, the solution of the MD is then split into the following form

$$\frac{\partial \boldsymbol{\varphi}_i}{\partial q_j} = \begin{Bmatrix} \boldsymbol{v}_i^{(1)} \\ 0 \\ \boldsymbol{v}_i^{(3)} \end{Bmatrix} + c_i \begin{Bmatrix} \boldsymbol{\varphi}_i^{(1)} \\ \varphi_{i_r} \\ \boldsymbol{\varphi}_i^{(3)} \end{Bmatrix}, \tag{4.34}$$

where the superscripts (1) and (3) for the vectors denote the 1^{th} to $(r-1)^{th}$ and $(r+1)^{th}$ to n^{th} components of the vectors $\boldsymbol{v}_i$ and $\boldsymbol{\varphi}_i$, respectively. Furthermore, the r^{th} component of the vectors are chosen such that it is zero for $\boldsymbol{v}_i$ and a nonzero value (φ_{i_r}) for $\boldsymbol{\varphi}_i$. Now the components of the vector $\boldsymbol{v}_i$ can be obtained by substituting Eq. (4.34) into (4.32). The last unknown in Eq. (4.33) is the coefficient c_i, which can be achieved by employing the mass normalization relation (i.e. $\boldsymbol{\varphi}_i^T \boldsymbol{M} \boldsymbol{\varphi}_i = 1$) and differentiating the i^{th} mode with respect to q_j. This gives

$$2\boldsymbol{\varphi}_i^T \boldsymbol{M} \frac{\partial \boldsymbol{\varphi}_i}{\partial q_j} = 2\boldsymbol{\varphi}_i^T \boldsymbol{M}(\boldsymbol{v}_i + c_i\boldsymbol{\varphi}_i) = 0 \rightarrow c_i = -\boldsymbol{\varphi}_i^T \boldsymbol{M} \boldsymbol{v}_i. \tag{4.35}$$

It should be noted that Nelson's method can be used when all the eigenvalues are assumed to be distinct. In case multiple eigenvalues exist in a system, the generalized inverse method can be used to obtain the MDs [7, 40, 44]. Lastly, the computed MDs have to be orthogonalized to the kept linear modes and one another to avoid singularity problems in the basis.

Static modal derivatives

Regardless of which method is used to compute the MDs, a factorization of the dynamic stiffness matrix (Eq. 4.32) is required for each $\boldsymbol{\varphi}_i$. To avoid performing the

factorization procedure, Idelsohn and Cardona [61] approximated the MDs by neglecting the inertia terms. Accordingly, Eq. (4.32) is simplified to

$$\boldsymbol{K}^{(1)}\frac{\partial \boldsymbol{\varphi}_i}{\partial q_j} = \frac{\partial \boldsymbol{K}^t}{\partial q_j}\boldsymbol{\varphi}_i. \tag{4.36}$$

The MDs obtained from Eq. (4.36) are called *Static* MDs (SMDs). The computation of SMDs is easier than the MDs since the linear stiffness matrix, $\boldsymbol{K}^{(1)}$, needs to be factorized only once. A mechanical interpretation of the SMDs is discussed in [136].

Non-intrusive computation of (S)MDs

Since the aim of this work is the improvement of the non-intrusive ROM method using MDs, it is necessary to compute them in a non-intrusive manner. As a result, a finite difference scheme can be used to obtain (S)MDs. There are two cases where the (S)MDs can be computed. The first case is when the FE package releases the TS for each nonlinear static solution (this is the case for many commercial software, e.g. Abaqus, Nastran, etc.). Then the derivative of the TS can be achieved using for instance a central finite difference as

$$\left.\frac{\partial \boldsymbol{K}^t(\boldsymbol{\varphi}_j q_j)}{\partial q_j}\right|_{q_j=0} = \frac{\boldsymbol{K}^t(\boldsymbol{u}=\boldsymbol{\varphi}_j h) - \boldsymbol{K}^t(\boldsymbol{u}=-\boldsymbol{\varphi}_j h)}{2h}, \tag{4.37}$$

where h is a small perturbation in the direction of the j^{th} mode. A numerical study for the selection of h is performed in [138]. The second case is when the FE package only releases the reaction forces due to nonlinear static displacements. In this case, the right hand side of Eqs. (4.32) and (4.36) can be written in terms of the second derivative of the nonlinear internal forces as

$$\frac{\partial \boldsymbol{K}^t}{\partial q_j}\boldsymbol{\varphi}_i = \frac{\partial^2 \boldsymbol{f}_{\text{int}}}{\partial q_j \partial \boldsymbol{u}}\frac{\partial \boldsymbol{u}}{\partial q_i} = \frac{\partial^2 \boldsymbol{f}_{\text{int}}}{\partial q_i \partial q_j}. \tag{4.38}$$

The numerical mixed derivatives of the nonlinear internal force obtained with central finite difference is given by

$$\left.\frac{\partial^2 \boldsymbol{f}_{\text{int}}}{\partial q_i \partial q_j}\right|_{\substack{q_i=0\\q_j=0}} = \frac{\boldsymbol{f}_{\text{int}}(\boldsymbol{u}=\boldsymbol{\varphi}_i h_i+\boldsymbol{\varphi}_j h_j) - \boldsymbol{f}_{\text{int}}(\boldsymbol{u}=\boldsymbol{\varphi}_i h_i-\boldsymbol{\varphi}_j h_j) - \boldsymbol{f}_{\text{int}}(\boldsymbol{u}=-\boldsymbol{\varphi}_i h_i+\boldsymbol{\varphi}_j h_j) + \boldsymbol{f}_{\text{int}}(\boldsymbol{u}=-\boldsymbol{\varphi}_i h_i-\boldsymbol{\varphi}_j h_j)}{4h_i h_j}. \tag{4.39}$$

Once the required tangent stiffnesses or nonlinear internal forces for each increment in Eqs. (4.37) and (4.39) are obtained from the corresponding nonlinear static analyzes, the right hand side of Eqs. (4.32) (for MDs) and (4.36) (for SMDs) are calculated and accordingly the (S)MD are obtained in a non-intrusive manner.

Load-independent selection of modal derivatives

The total number of added basis vectors in Eq. (4.30) due to (S)MDs is given by

$$N = {}_mC_2 + m, \tag{4.40}$$

which means that the number of (S)MDs increases in order $O(m^2)$ with respect to the number of linear modes. Therefore, to still keep the NLROMs compact, only a few of the most significant (S)MDs should be kept. To select the most important (S)MDs, a few methods are available in the literature, which are mostly heuristic criteria. In this work, the method of *Maximum Modal Interaction* (MMI) [64, 154] with a slight modification is used. The MMI criterion simply considers the modal time response of a linear modal model, and takes the product of two arbitrary modal amplitudes as an indication of the potential interaction of these modes in the nonlinear regime. Note that the reduced modal model is obtained from the projection of mass and linear stiffness matrices by mass-normalized VMs. The pairs yielding the largest interactions are then giving the indexes of the MDs to be included in the basis. More specifically, a weighting matrix $\boldsymbol{W}$ is defined such that its ij^{th} component is obtained as

$$W_{ij} = \int_0^T \left| q_i(t)\, q_j(t) \right| dt, \tag{4.41}$$

where W_{ij} denotes the weighting value corresponding to the (S)MD $\boldsymbol{\theta}_{ij}$. Moreover, $q_i(t)$ is the response of the i^{th} generalized mode in a linear time integration due to an external load. It should be noted that the original MMI method takes the same external loading as the load, which is aimed to be applied to the full and reduced systems for validation. However, this way makes the selection of the (S)MDs load-dependent. In order to select the (S)MDs in a load-independent approach, a random excitation with the desired frequency range of interest is applied to the linear reduced model to compute the weighting matrix. In this way, we propose to choose the (S)MDs in a load-independent manner.
Consider the reduced EOM (2.24), which is linearized and contains no damping as

$$\hat{\boldsymbol{M}}\ddot{\boldsymbol{q}}(t) + \hat{\boldsymbol{K}}^{(1)}\boldsymbol{q}(t) = \hat{\boldsymbol{f}}(t), \tag{4.42}$$

Now, we choose the components of the external load vector $\boldsymbol{f}(t)$ as a Gaussian random signal in time with an arbitrary load distribution in space. Since this force randomly excites the model in a desired frequency band and its load distribution is not the same as the one we use later for the simulation of our examples, we call it the load-independent selections of (S)MDs. For instance, we take the same random amplitude for the forces/moments that are applied to all dofs, in the examples of this chapter. The linearized modal coordinates q_i, $i = 1, 2, \ldots, m$, are then integrated under this excitation and used in Eq. (4.41) for all time steps to obtain the components of the MMI matrix. It can be seen that the weighting matrix is symmetric while in general only SMDs are symmetric and MDs are not symmetric (see [64]). This does not cause any problem for the selection of MDs, because if a MD θ_{ij} is selected to be in the basis, it will be added by its counterpart θ_{ji} to be symmetrized (as in Eq. (4.30)) and then added to the reduction basis.

4.4 Numerical examples

To examine the performance of the proposed non-intrusive MOR approach, three numerical examples featuring geometric nonlinearities are discussed here. The three

examples are made of beam (flat and curved) and shell elements using Abaqus®. All models are excited by sound pressure in the transverse direction, which is randomly distributed in time and uniform in space. The frequency range of excitation of the loads is between $0-800$ Hz and each example is excited with two different average Sound Pressure Levels (SPLs).
The NLROMs are developed using the proposed basis and compared with the full model as well as the NLROMs based on two previously developed bases for non-intrusive ROM, namely linear modes and dual modes. The NLROMs are developed using both the ED and EED methods, only to compare their offline computational costs. However, only the results of ED is shown here, due to its time integration stability compared to EED (EED is more compared to other methods in Chapter 5). Additionally, the required derivatives to compute the non-intrusive (S)MDs are obtained using the TS matrices (Eq. (4.37)). The performance of the NLROMs are assessed by monitoring the displacement PSD of their nonlinear time response. The time integration of the NLROMs is performed using the implicit Newmark scheme, which we implemented in MATLAB® and the full model is implicitly integrated in Abaqus. All the models are time-integrated for 5 seconds with the constant time increment of 5×10^{-5} to compute their PSDs. For all the time integrations, a Rayleigh damping in the form $D = \alpha \boldsymbol{M} + \beta \boldsymbol{K}$ is used. All the simulations in this study are performed on a desktop PC with 32 GB RAM and Intel® Xeon® CPU (3.6 GHz). Lastly, to compare the time response of the NLROMs, the relative error of the selected DOFs are computed as explained in Chapter 3 (Eq. (3.49)).

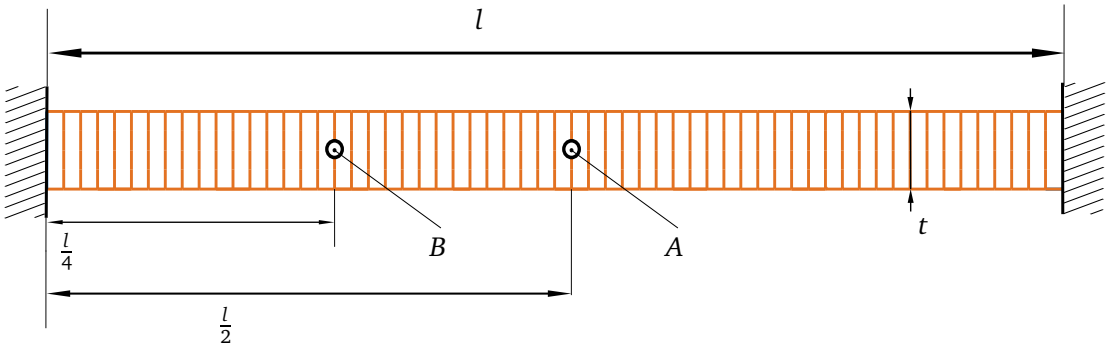

Figure 4.3: Schematic of the clamped-clamped flat beam model.

4.4.1 Beam models

Flat beam

The first investigated model is a two-side clamped geometric nonlinear flat beam FE model, shown in Fig. 4.3. The material, geometry and FE model properties of this structure are illustrated in Table 3.1. The NLROMs of this model are developed using the proposed non-intrusive SMDs as well as MDs. For this example, two average SPL levels of 135 dB and 150 dB are applied to the model. All the models are time-integrated for 5 seconds with the constant time increment of 5×10^{-5}. The coefficients

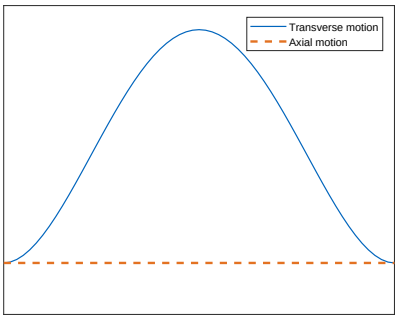

(a) φ_1 : $\omega_1 = 58.3$ Hz

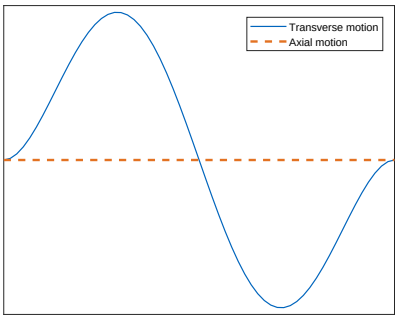

(b) φ_2 : $\omega_2 = 160.7$ Hz

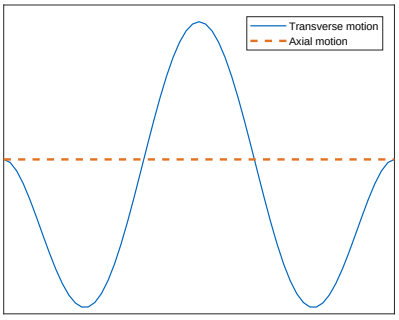

(c) φ_3 : $\omega_3 = 315.1$ Hz

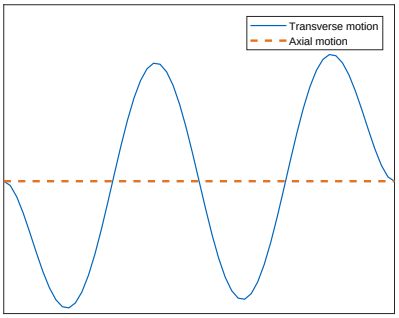

(d) φ_4 : $\omega_4 = 520.9$ Hz

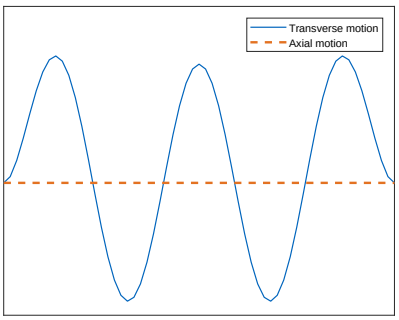

(e) φ_5 : $\omega_5 = 778.2$ Hz

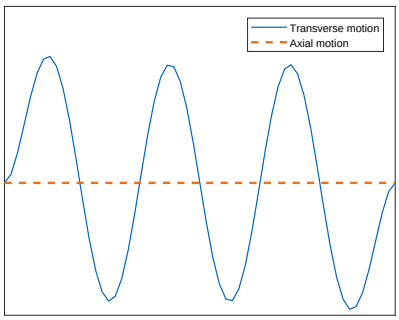

(f) φ_6 : $\omega_6 = 1087.1$ Hz

Figure 4.4: The first six vibration modes of the flat beam model.

of the Rayleigh damping are chosen such that the damping ratios for all modes in the excitation frequency are less than 1% ($\alpha = 6.8$, $\beta = 3.75 \times 10^{-6}$).
To have an insight into the shape of the linear modes and (S)MDs, the first six linear modes of the beam structure are depicted in Fig. 4.4, and the six SMDs stemming from the first three VMs are shown in Fig. 4.5. For a flat beam, the first VMs are transverse dominated, while the corresponding SMDs are in-plane dominated, as shown in Figs. 4.4 and 4.5, respectively. As the shapes of the MDs and SMDs are very similar to each other, the MD shapes are not shown here.
Additionally, the MMI heuristic criterion for the first seven generalized DOFs are

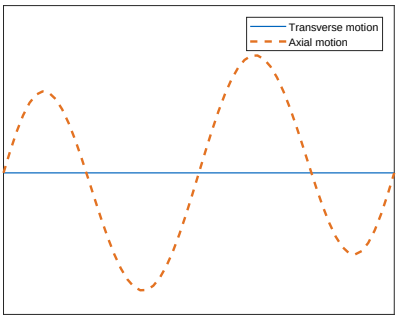

(a) $\theta_{11} = \frac{\partial \phi_1}{\partial q_1}$

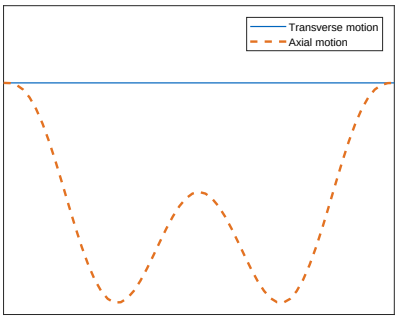

(b) $\theta_{12} = \theta_{21} = \frac{\partial \phi_1}{\partial q_2}$

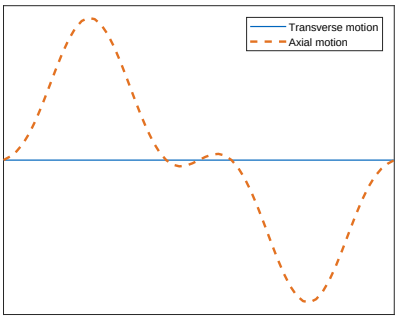

(c) $\theta_{13} = \theta_{31} = \frac{\partial \phi_1}{\partial q_3}$

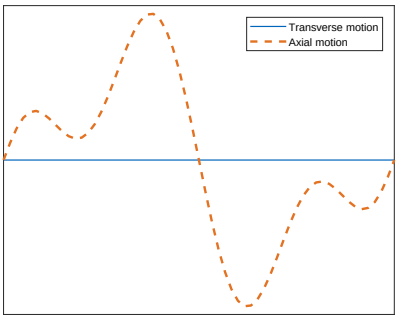

(d) $\theta_{22} = \frac{\partial \phi_2}{\partial q_2}$

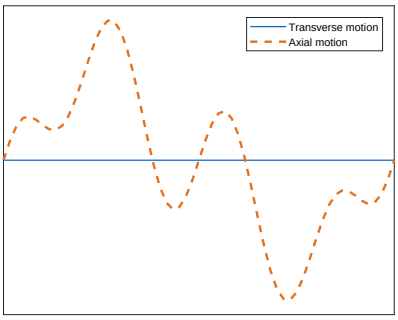

(e) $\theta_{33} = \frac{\partial \phi_3}{\partial q_3}$

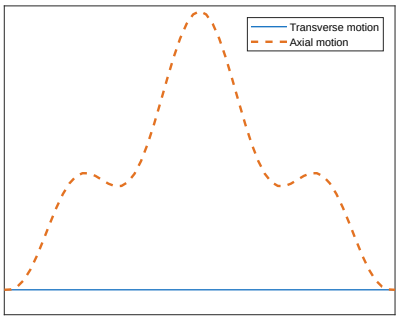

(f) $\theta_{23} = \theta_{32} = \frac{\partial \phi_2}{\partial q_3}$

Figure 4.5: Displacement of the first six SMDs of the flat beam model in axial and transverse directions.

computed using the time integration of the linear reduced system and depicted in Fig. 4.6. The darkest squares indicate the mode pairs likely to interact the most when nonlinearities are present. Following this idea, the (S)MDs corresponding to such indexes are computed and inserted in the reduction basis. Since the excitation for computation of MMI is random, the selected (S)MDs might be slightly different for each time that the NLROM is developed. However, this slight difference in the selection of (S)MDs has a minimal effect on the nonlinear time responses.

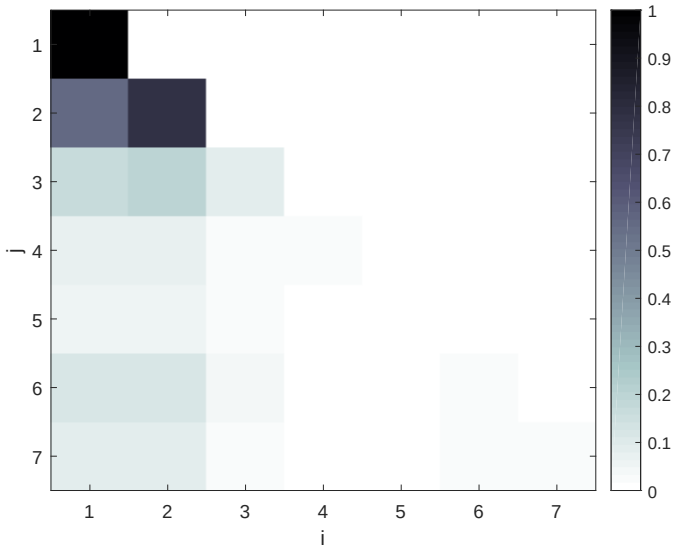

Figure 4.6: Maximum modal interaction matrix values for the flat beam model with seven linear modes in the basis. Since this matrix is symmetric, only the lower triangle is shown.

NLROM	ED offline	EED offline
NLROM-5VM-5Dual	275	65
NLROM-5VM-5SMD	275	65
NLROM-5VM-5MD	275	65

Table 4.1: Number of nonlinear static solutions (offline computational cost), only for NSCs identification part of the flat beam's NLROMs.

Model	online time (sec.)
Full model	5356
NLROM-5VM-5Dual	30
NLROM-5VM-5SMD	30
NLROM-5VM-5MD	31
NLROM-10VM	31

Table 4.2: Online time for integration of flat beams's NLROMs and full model for 5 seconds under 150 dB load.

Convergence check

To perform a convergence check study and also evaluate the numbers of required linear VMs as well as (S)MDs, the NLROMs with different number of generalized coordinates are developed and compared to the full-order model. Fig. 4.7 shows the PSD comparison of NLROMs under the 150 dB SPL load and using different numbers of linear modes and (S)MDs with the PSD of the full-order model for transverse motion of point A and in-plane displacement of point B (see Fig. 4.3). This is done since the maximum transverse and in-plane displacements of the beam model due to this load occurs near points A and B, respectively. The transverse PSD of the NLROMs developed by SMD (Fig. 4.7a), as well as by MDs (Fig. 4.7b), converge to the full solution of the nonlinear full-order model by increasing the number of linear

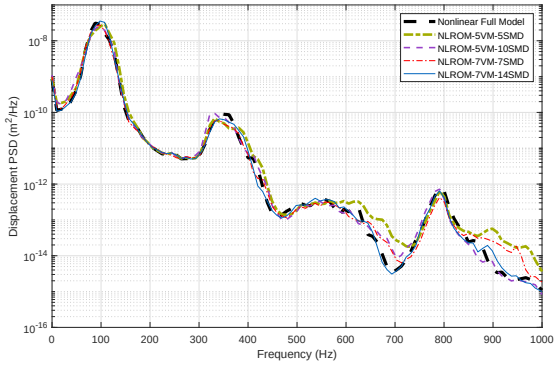

(a) Transverse DOF, point A, NLROMs with SMDs.

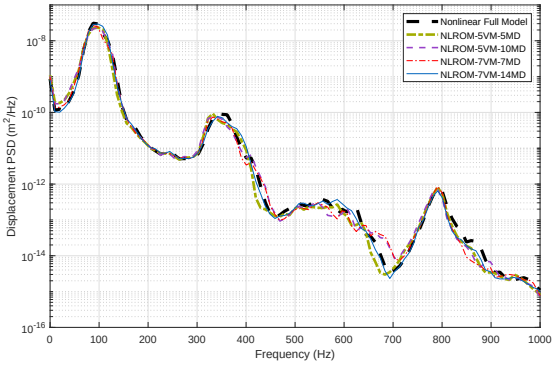

(b) Transverse DOF, point A, NLROMs with MDs.

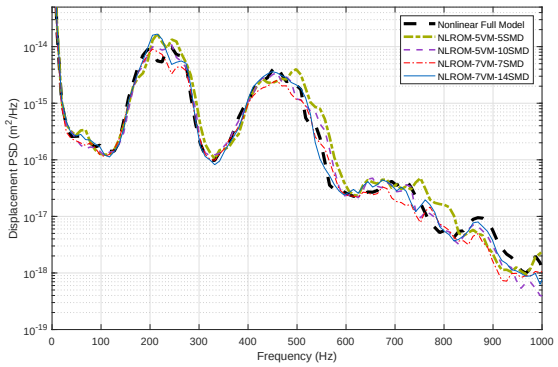

(c) Membrane DOF, point B, NLROMs with SMDs.

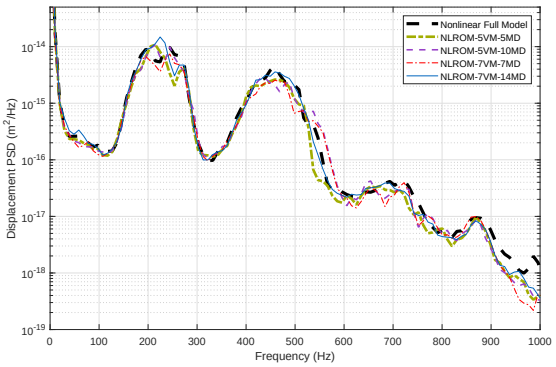

(d) Membrane DOF, point B, NLROMs with MDs.

Figure 4.7: The flat beam's displacement power spectral densities for convergence check of transverse and in-plane DOFs of the points A and B, respectively, under 150 dB SPL. The NLROM are developed using VMs augmented once with SMDs and another time with MDs.

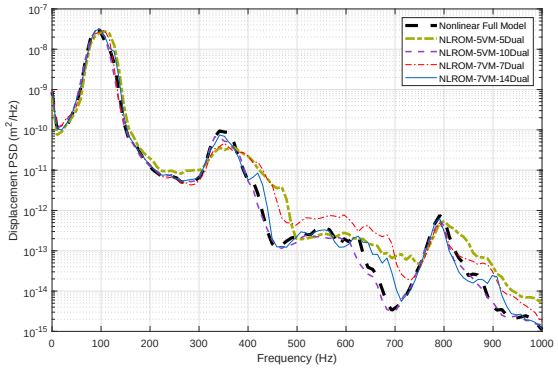

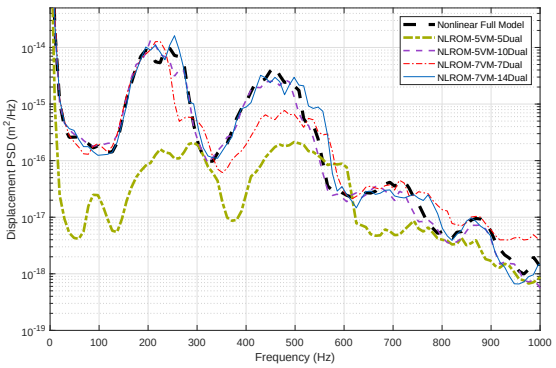

(a) Transverse DOF, point A, NLROMs with dual modes. **(b)** Membrane DOF, point B, NLROMs with dual modes.

Figure 4.8: Flat beam's PSDs for convergence check of transverse and in-plane DOFs of the points A and B, respectively, under 150 dB SPL. The NLROM are developed using VMs augmented with dual modes.

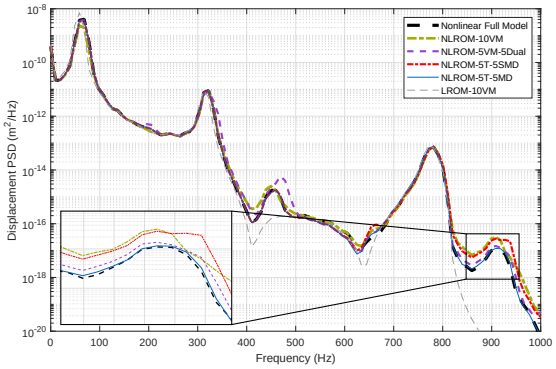

(a) Transverse DOF of point A under 135 dB.

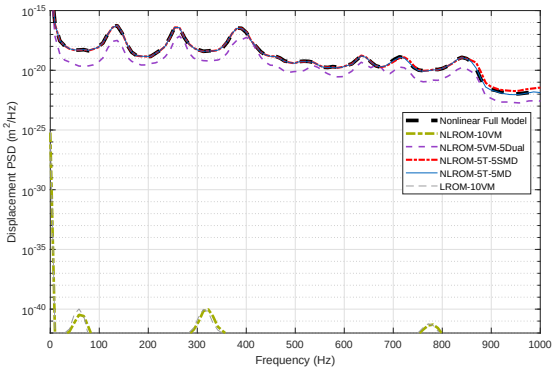

(b) Membrane DOF of point B under 135 dB.

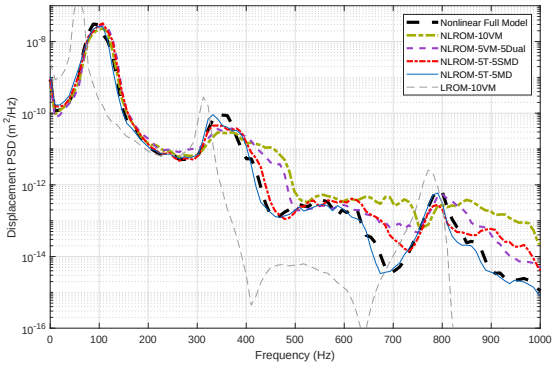

(c) Transverse DOF of point A under 150 dB.

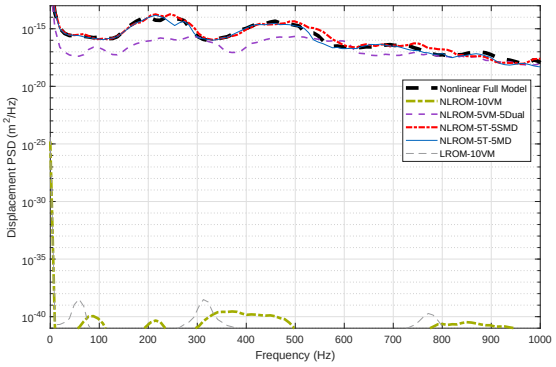

(d) Membrane DOF of point B under 150 dB.

Figure 4.9: The flat beam's PSD comparison for the NLROMs developed by 5VM-5SMD, 5VM-5MD, 5VM-5Dual and 10VM with the full-order model and the linear reduced model (10VM). The PSDs are obtained under two load cases of 135 dB and 150 dB SPLs.

modes and corresponding (S)MDs in the basis (the number of used VM as well as (S)MDs are shown in the legend of each figure). Likewise, the accuracy of the in-plane PSDs of the NLROMs have been improved by increasing the numbers of linear modes and (S)MDs (Figs 4.7c and 4.7d) present in the basis. These results confirm the convergence of the proposed approach.
Furthermore, the convergence check study is performed for the NLROMs relying on linear modes and dual modes (Fig. 4.8) under the same loading condition as the NLROMs based on (S)MDs. To obtain the dual modes of each NLROM, 10 scaling factors α (see. Eqs. (4.22) and (4.23)) ranging from -2.5 to 2.5 are selected and the corresponding displacements are obtained for sequential POD analysis, which is explained in section 4.3.2. As can be seen in Fig. 4.8, the NLROMs developed by linear and dual modes have converged to the full-order solution in a similar manner as the NLROM developed by VM and (S)MDs (Fig. 4.7).

Comparison of reduction bases

To further compare the performance of different bases, four NLROMs are developed, with the same number of basis vectors in the reduction basis, as:

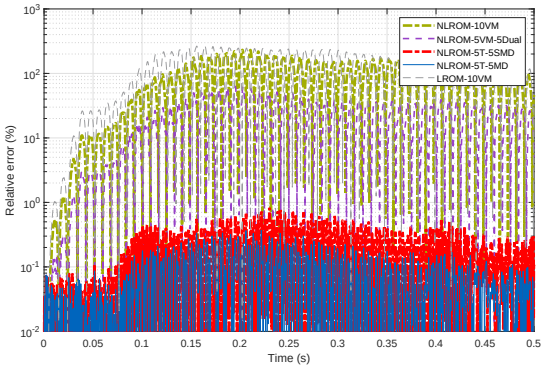

(a) Transverse DOF of point A under 135 dB.

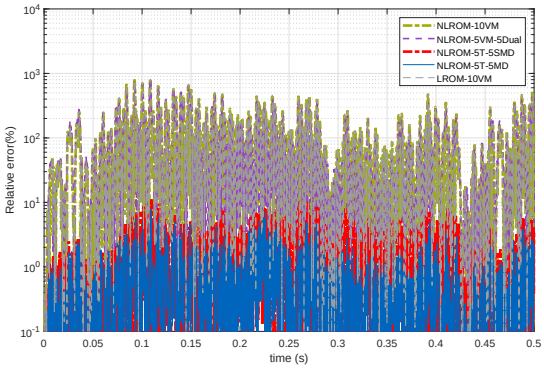

(b) Membrane DOF of point B under 135 dB.

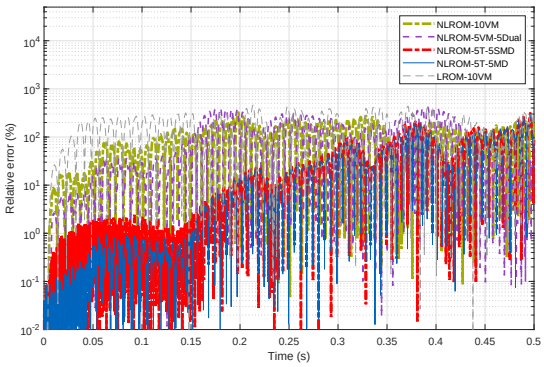

(c) Transverse DOF of point A under 150 dB.

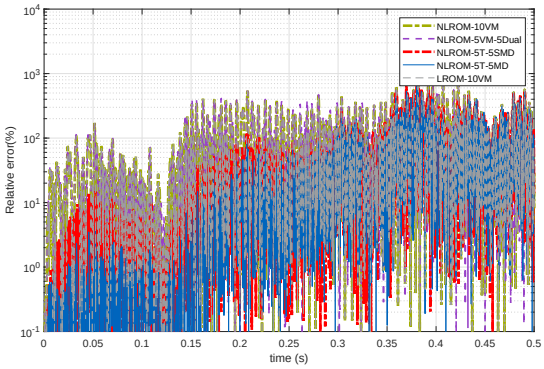

(d) Membrane DOF of point B under 150 dB.

Figure 4.10: Relative error comparison for the flat beam's NLROMs developed by 5VM-5SMD, 5VM-5MD, 5VM-5Dual and 10VM with the full-order model and the linear reduced model (10VM). The relative errors are obtained under two load cases of 135 dB and 150 dB SPLs.

- The first 10 linear vibration modes (NLROM-10VM).
- The first 5 linear vibration modes augmented with 5 dual modes (NLROM-5VM-5Dual).
- The first 5 linear vibration modes augmented with 5 static modal derivatives (NLROM-5VM-5SMD).
- The first 5 linear vibration modes augmented with 5 modal derivatives (NLROM-5VM-5MD).

These NLROMs are compared with the full-order response and the linear ROM with 10 vibration modes (LROM-10VM). The PSD comparison of the transverse DOF of point A and in-plane DOF of point B under two loading conditions with an average SPL of 135 dB and 150 dB are shown in Fig 4.9. The maximum displacement for this example (under 150 dB) is 2.7 times the thickness. This figure confirms the accuracy of the NLROMs based on MDs compared to other NLROMs for both transverse and membrane DOFs, especially as the excitation level increases (see Figs. 4.9c and 4.9d). Additionally, the NLROM based on SMD has almost the same order of accuracy as the NLROM based on dual modes for transverse motion, while its accuracy for

the membrane motion is higher than the NLROM based on dual modes. It should be noted that if the NLROM based on dual modes is developed by only selecting those modes and duals, which have the maximum contribution for this specific load distribution (load-dependent), one can obtain excellent results for this NLROM as shown in [114].
To better observe the improvement of the proposed method, the relative error for the first half second (from the whole five seconds) of the time integrations used in PSD computation of Fig. 4.9 are shown in Fig. 4.10 under both excitation levels for transverse direction of point A (Fig. 4.10a and 4.10c), as well as in-plane direction of point B (Fig. 4.10b and 4.10d). As can be seen from this figure, both SMDs and MDs have reduced the relative error of the time signal for both directions, and the NLROM based on MDs has the minimum relative error among other NLROMs. The total number of generalized DOFs in the developed NLROMs to accurately represent the full-order model in the whole range of $0-1000$ Hz under different loading conditions is only 10, which is approximately 6% of the total DOFs of the full-order model.

Computational costs

To compare the computational efficiency of the developed approach, the required time to develop the NLROMs (offline cost) as well as the the required time to integrate the NLROMs and full-order model (online costs) are compared for the simulations used in Fig. 4.9. The offline computational cost comparison for building the four NLROMs used in Fig. 4.9 are shown in Table 4.1. As can be seen from this table, the accuracy achieved by (S)MDs does not increase the offline computational costs for development of the NLROMs. Since the developed NLROMs are valid for a variety of load cases with excitation frequency of $0-800$ Hz, the "one-time" offline cost to compute the NLROMs is amortized when they are used for time simulations under several loading conditions. Furthermore, the online computational costs for 5 seconds time integration of the NLROMs are compared with the full-order model in Table 4.2. As can be seen, the required online time for all four NLROMs are in the same order, because they all have the same number of the generalized DOFs. The required time for integration of these models are approximately 172 times faster than the full-order model, leading to highly efficient reduced models.

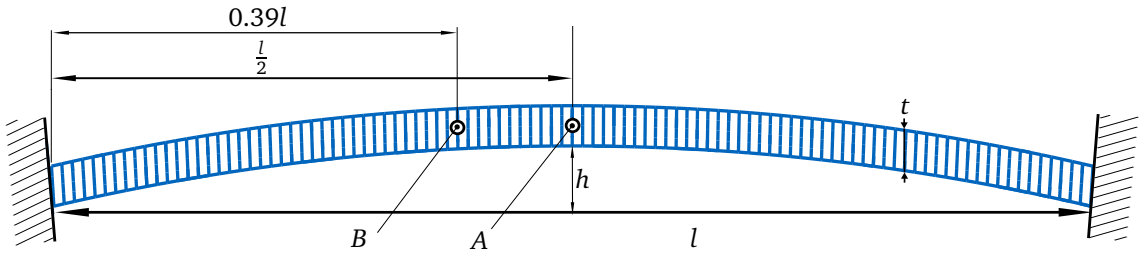

Figure 4.11: Schematic of the curved beam model.

Curved beam

The second example of this work is a curve beam structure, because it has been shown in many works (see e.g. [19, 47, 150]) that it has a more complex nonlinear dynamic

behavior than the flat beam due to the linear coupling between its transverse and in-plane motion. The schematic of this model is depicted in Fig. 4.11 and its material, geometry and mesh properties are illustrated in Table 4.3. The shape of the first six VMs of the model is depicted in Fig. 4.12 for both transverse and membrane directions. As shown in this figure, although these modes are transverse dominated, their membrane motion is also nonzero, which is unlike the flat beam model (Fig. 4.4). Moreover, the first six SMDs of the curved beam is shown in Fig. 4.13. In contrast to the SMDs of the flat beam (Fig. 4.5), these SMDs are not membrane-dominated anymore due to the coupling between the linear modes.
To select the (S)MDs in the reduction basis of the NLROMs, the MMI criterion is used for the first five modes. The (S)MD are then chosen according to the components of the MMI matrix with maximum values. Since the convergence check analysis is already performed for the flat beam, for the sake of brevity it is not repeated for the curved beam.

Comparison of reduction bases

To compare the performance of the proposed approach, two random excitations with SPLs of 158 dB and 168 dB are applied to the model for five seconds, and time integrations are performed with similar conditions as the flat beam. The NLROM of the curved beam model is developed using the following bases.

- The first 15 linear vibration modes (NLROM-15VM).
- The first 5 linear vibration modes augmented with 10 dual modes (NLROM-5VM-10Dual).
- The first 5 linear vibration modes augmented with 10 static modal derivatives (NLROM-5VM-10SMD).
- The first 5 linear vibration modes augmented with 10 modal derivatives (NLROM-5VM-10MD).

These NLROMs are compared with the full-order model and the linear ROM using 15 VMs modes and under two mentioned excitations. Like the flat beam model, to obtain the dual modes of each NLROM, 10 scaling factors α ranging from -2.5 to 2.5 are

	Property (dimension)	**Value**
Material	Mass density (kg/m^3)	7870
	Young's modulus (GPa)	2.05×10^{11}
	Poisson's ratio	0.28
Geometry	l (mm)	400
	h (mm)	12
	t (mm)	2
FE model	Element-type	Timoshenko (Abaqus B21)
	Number of Elements	100
	Number of DOFs	297

Table 4.3: Geometry, material and FE model properties of the shallow-curved beam model.

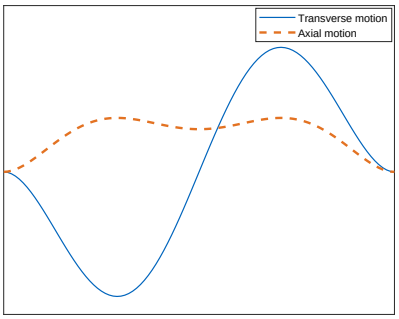

(a) $\varphi_1 : \omega_1 = 179.4$ Hz

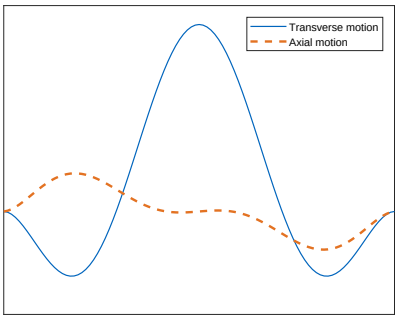

(b) $\varphi_2 : \omega_2 = 298.6$ Hz

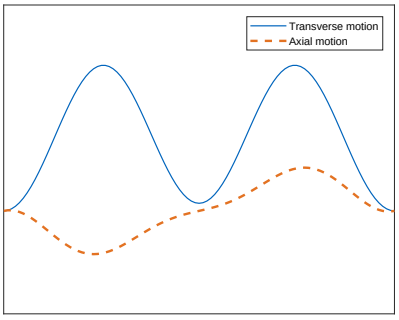

(c) $\varphi_3 : \omega_3 = 477.6$ Hz

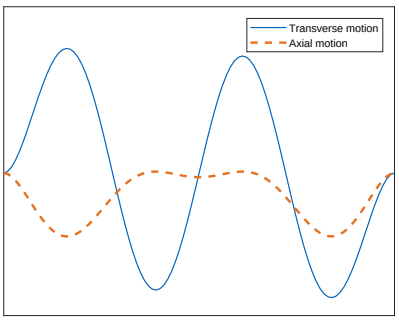

(d) $\varphi_4 : \omega_4 = 582.1$ Hz

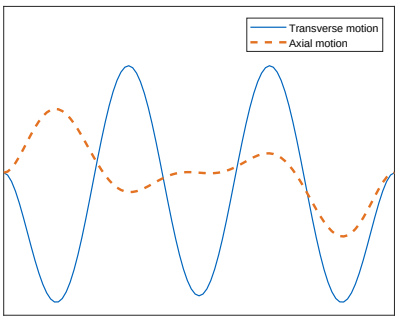

(e) $\varphi_5 : \omega_5 = 879.0$ Hz

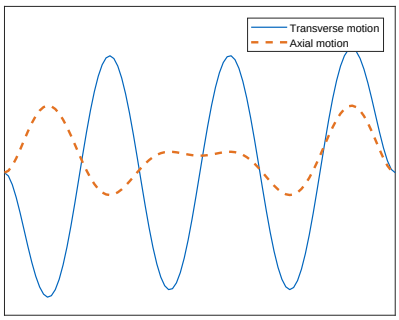

(f) $\varphi_6 : \omega_6 = 1214.0$ Hz

Figure 4.12: The first six vibration modes of the curved beam.

selected and the procedure explained in section 4.3.2 is performed. Fig. 4.15 shows the PSD comparison of these models for the transverse direction of point A and axial direction of point B (see Fig. 4.11) under the two mentioned excitation levels (the maximum transverse and axial motion of the structure occurs near points A and B, respectively). As can be seen, while the performance of NLROMs based on (S)MDs are in the same order as the other ROMs for low level of excitation, for relatively higher excitation level, the NLROM developed by MDs is more accurate than other NLROMs developed by currently available bases for non-intrusive method, especially for the membrane motion (Fig. 4.15d). This improvement can also be seen in Fig.

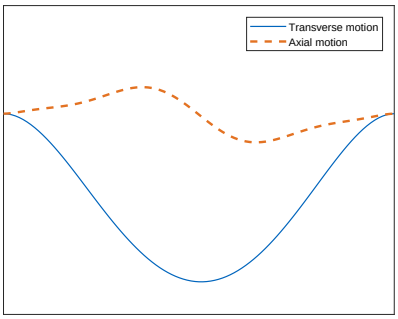

(a) $\theta_{11} = \frac{\partial \phi_1}{\partial q_1}$

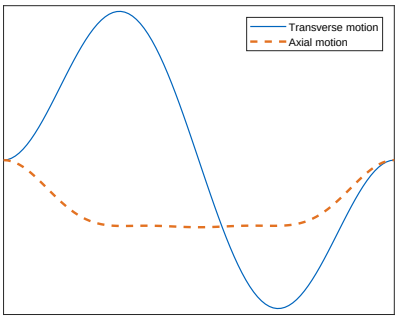

(b) $\theta_{12} = \theta_{21} = \frac{\partial \phi_1}{\partial q_2}$

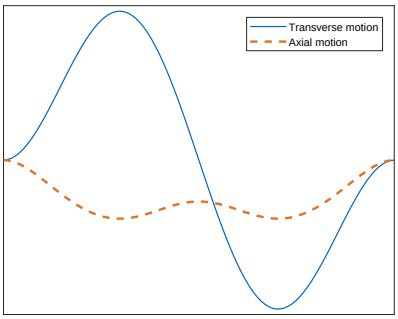

(c) $\theta_{13} = \theta_{31} = \frac{\partial \phi_1}{\partial q_3}$

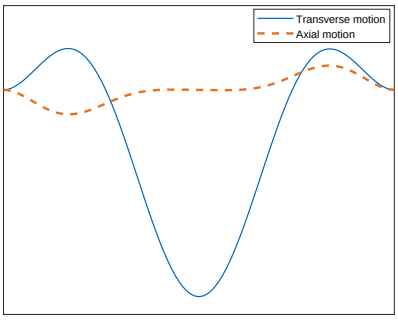

(d) $\theta_{22} = \frac{\partial \phi_2}{\partial q_2}$

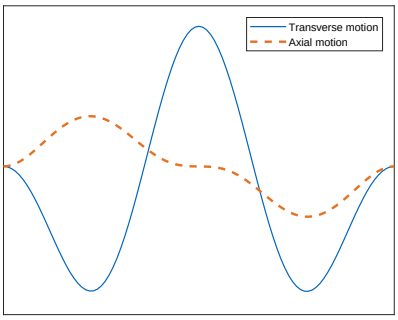

(e) $\theta_{33} = \frac{\partial \phi_3}{\partial q_3}$

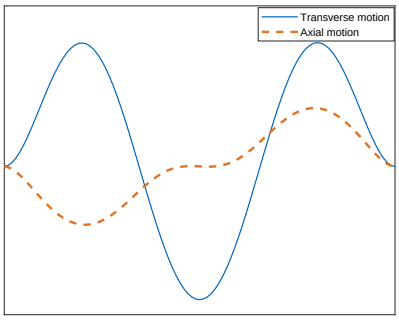

(f) $\theta_{23} = \theta_{32} = \frac{\partial \phi_2}{\partial q_3}$

Figure 4.13: Transverse and in-plane displacements of the curved beam's first six SMDs. The transverse and in-place displacements have different scaling for visual reasons.

4.16, where the relative errors are shown for the first half seconds time responses that are used to compute the PSDs of Fig. 4.15 in both transverse and axial directions of points A and B, respectively. The maximum displacement for this example is 1.1 times the thickness. Finally, one should note that the results obtained by these NLROMs can be improved significantly if the NLROMs are developed in a load-dependent manner, i.e., according to a specific load case, as for instance performed for dual modes in [147], for the case of a curved beam.

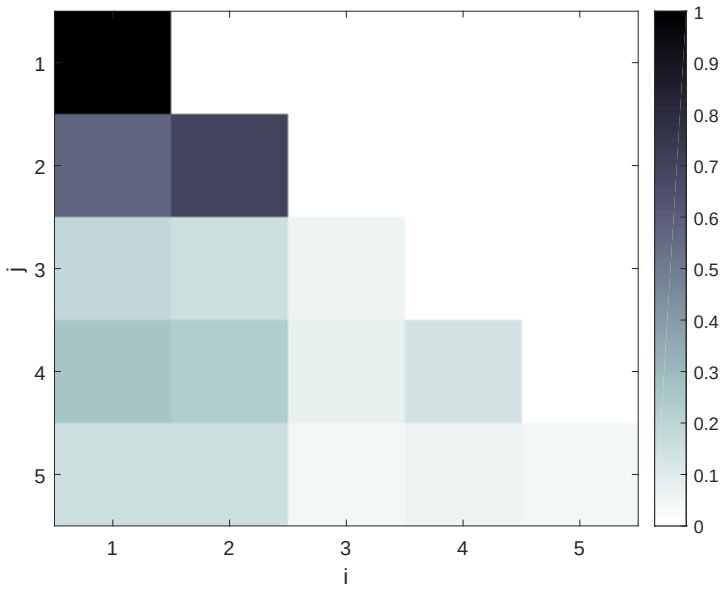

Figure 4.14: Maximum modal interaction matrix values for the curved beam model with five linear modes in the basis. Since this matrix is symmetric, only the lower triangle is shown.

NLROM	ED offline time (sec.)	EED offline time (min.)
NLROM-5VM-10Dual	5	3
NLROM-5VM-10SMD	5	2
NLROM-5VM-10MD	5	2
NLROM-15VM	4	1

Table 4.4: Offline computational time to develop the curved beam's NLROMs, only for NSCs identification part.

Computational costs

The offline computational costs to develop the investigated NLROMs by the proposed bases ((S)MDs), as well as the currently available simulation-free bases (linear and dual modes), are shown in Table 4.4. This table proves that the obtained results of the proposed bases accompany no increase in the offline computational costs compared to the NLROM developed by the dual modes. Furthermore, the online computational costs for 5 seconds time integration of the NLROMs, as well as the full-order model to obtain the results of Figs. 4.15c and 4.15d (under 168 dB SPL) are presented in Table 4.5. The required time to integrate all the NLROMs are in the same order, while they are at least 117 times faster than the full-order model. Furthermore, since the developed NLROMs can be used for different loading conditions, the "one-time" offline computational costs are amortized in case of using them in several loading conditions.

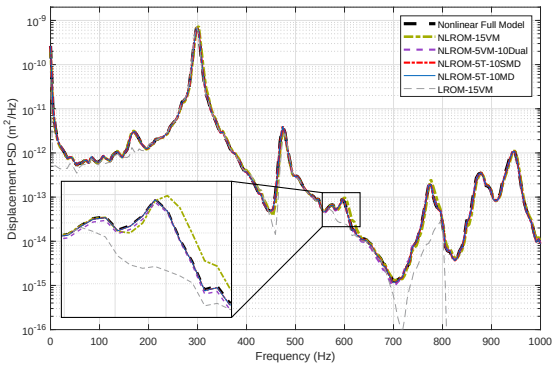

(a) Transverse DOF of point A under 158 dB.

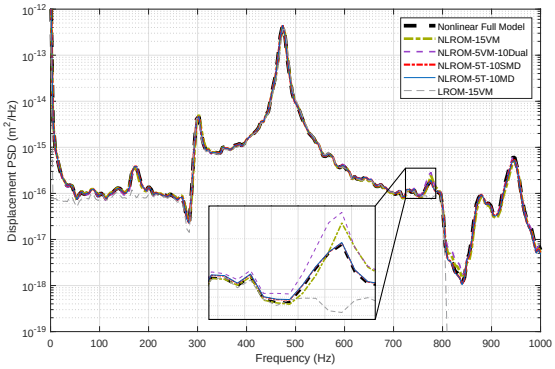

(b) Membrane DOF of point B under 158 dB.

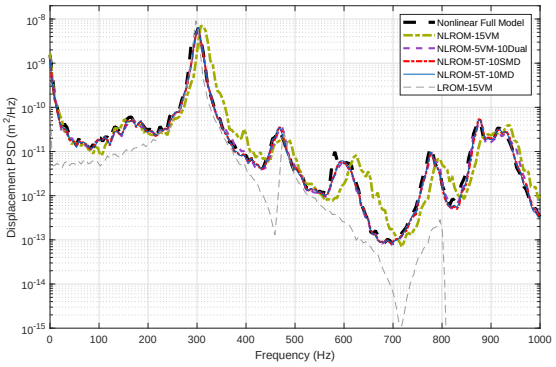

(c) Transverse DOF of point A under 168 dB.

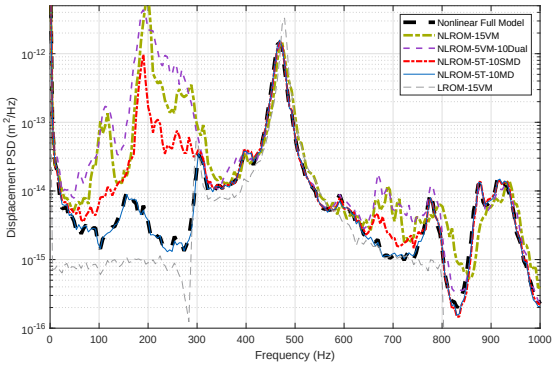

(d) Membrane DOF of point B under 168 dB

Figure 4.15: The curved beam's PSD comparison for the NLROMs based on 5VM-5SMD, 5VM-5MD, 5VM-5Dual and 10VM with the full-order model and the linear reduced model (10VM). The PSDs are obtained under two load cases of 158 dB and 168 dB SPLs.

4.4.2 Panel model

The last example of this chapter examines a panel structure, which is when discretized, of much larger dimensions than the first two beam examples. The model of the plate, shown in Fig. 4.17, is built and analyzed in Abaqus. The structure is simply supported at all edges (as shown by black lines in Fig. 4.17) and is meshed by geometric nonlinear shell elements. The material, geometry and FE properties of this model are outlined in Table 4.6. The Rayleigh damping coefficients for this structure are set to $\alpha = 16.2$ and $\beta = 2.85 \times 10^{-6}$. This choice leads to damping ratios less than 1% for all the modes in the frequency range of excitation. All the time integrations for this example were performed with a constant time increment of 5×10^{-5} s with $100,000$ time steps.

As done for the beam examples, the first six linear modes of the plate are plotted in Fig. 4.18, while the six SMDs relative to the first three VMs are depicted in Fig. 4.19. As can be seen, all of the SMDs shown are membrane-dominated modes. The MDs are not shown, as their shapes are very similar to the SMDs. Furthermore, the MMI of the linear reduced model with 11 linear vibration modes under a random excitation is computed and shown in Fig. 4.20. Those (S)MDs, θ_{ij} (with their counterpart θ_{ji}),

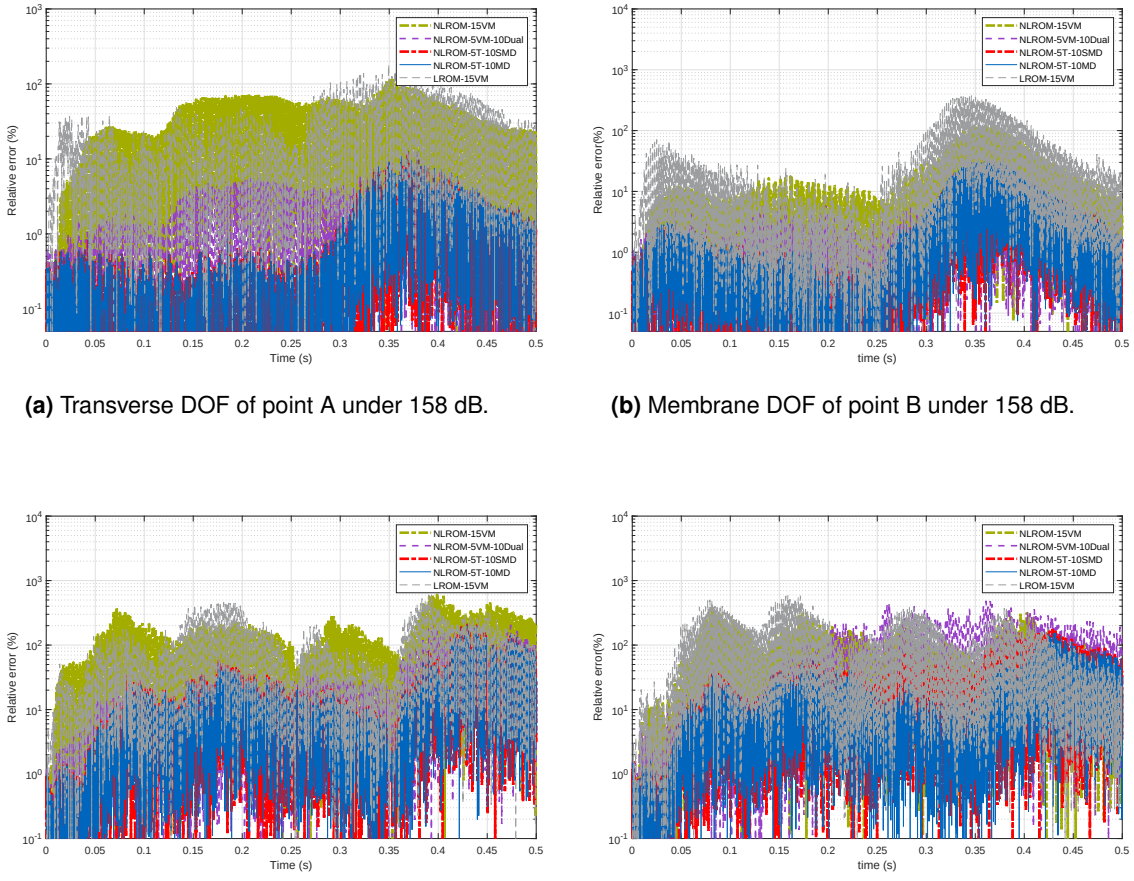

(a) Transverse DOF of point A under 158 dB.

(b) Membrane DOF of point B under 158 dB.

(c) Transverse DOF of point A under 168 dB.

(d) Membrane DOF of point B under 168 dB.

Figure 4.16: Curved beam's relative error comparison for the NLROMs developed by 5VM-10SMD, 5VM-10MD, 5VM-10Dual and 15VM with the full-order model and the linear reduced model (15VM). The relative errors are obtained under two load cases of 158 dB and 168 dB SPLs.

are selected for the development of the NLROMs, based on the corresponding largest components in the MMI matrix, which is obtained under a random excitation.

Convergence check

As done for the flat beam example, a convergence check analysis for the developed NLROMs based on (S)MDs is performed to check the robustness of the proposed approach. In this analysis, the PSDs of the NLROMs under the random loading condition with average SPL level of 155 dB are computed while the number of linear modes as well as (S)MDs are increased for the development of NLROMs. Figs. 4.21a and 4.21c illustrate the PSDs of the NLROMs developed by SMDs for transverse and membrane motions of points A and B, respectively. Likewise, Figs. 4.21b and 4.21d depict the PSDs of the NLROMs based on MDs for the same points and same DOFs. The PSDs of both transverse and membrane DOFs converge to the one of the full-order solution by increasing the number of basis vectors in the NLROMs based on both MD and SMD. These results confirm the convergence as well as robustness of the proposed approach.
The same analysis is performed but this time for the NLROMs, which are developed

Model	online time (min.)
Full model	117
NLROM-5VM-10Dual	1
NLROM-5VM-10SMD	1
NLROM-5VM-10MD	1
NLROM-15VM	1

Table 4.5: Online time for time integration of curved beams's NLROMs and full model for 5 seconds under 168 dB load.

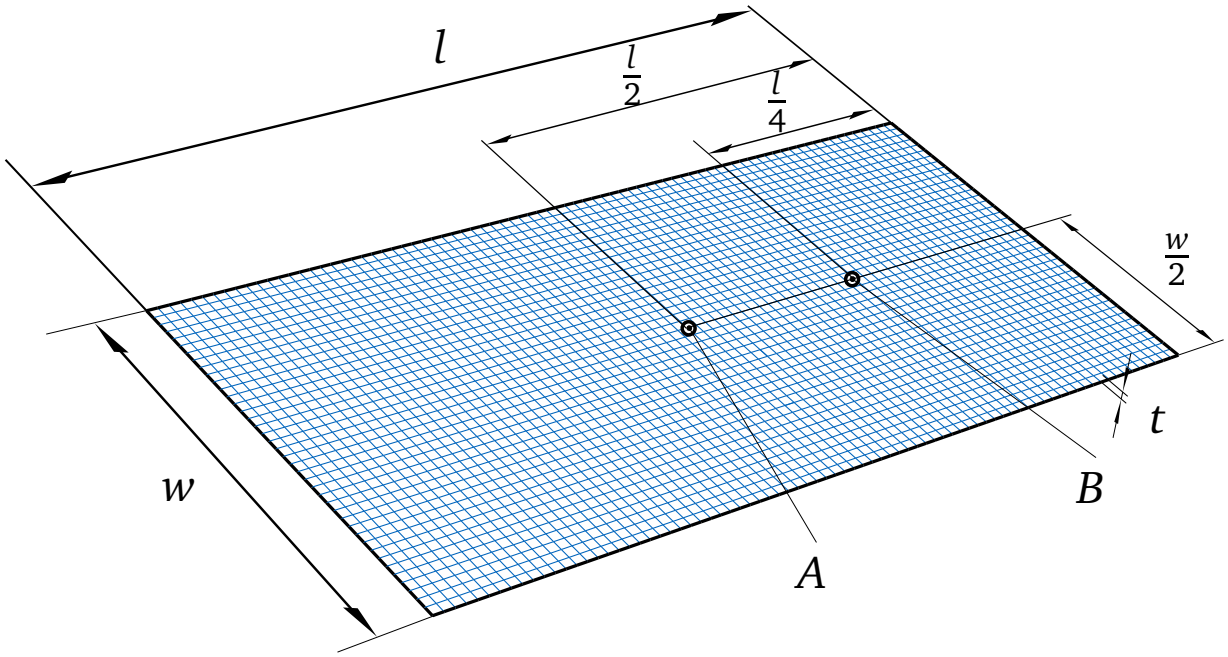

Figure 4.17: The simply-supported panel model made of geometric nonlinear shell elements.

using different numbers of linear modes and dual modes in the basis, and the corresponding PSD results are shown in Fig. 4.22. To develop the dual modes for this example 10 scaling factors α (see. Eqs. (4.22) and (4.23)) ranging from -2.5 to 2.5 are selected and the POD of their corresponding displacements are then analyzed. The NLROMs are improved by increasing the number of VMs as well as dual modes in the basis, which confirms the convergence of the NLROMs developed by this basis. To develop an accurate NLROM with less number of DOFs, one can select only the VMs and duals, which are mostly relevant to a specific load case, as done in [116]. However, the aim of this work is to compare different selection strategies when modes are computed in a load-independent manner.

Comparison of the reduction bases

To further assess the efficiency of the proposed approach, four NLROMs with the same number of basis vectors but built by different ingredients are developed as follows:

- The first 22 linear vibration modes (NLROM-22VM).

- The first 11 linear vibration modes augmented with 11 dual modes (NLROM-11VM-11Dual).
- The first 11 linear vibration modes augmented with 11 static modal derivatives (NLROM-11VM-11SMD).
- The first 11 linear vibration modes augmented with 11 modal derivatives (NLROM-11VM-11MD).

The nonlinear response of these models under two different average SPL excitations of 145 dB and 157 dB are obtained and compared with the ones of the full-order and linear ROM (LROM-22VM) models. The PSD comparison of the transverse DOF of point A for the two loading levels are depicted in Figs. 4.23a and 4.23c and for the membrane DOF of point B are shown in Figs. 4.23b and 4.23d, respectively. The maximum displacement here is 0.8 times the thickness. As can be seen from these figures, for both excitation levels and in both transverse and membrane directions, the proposed NLROMs based on (S)MDs are accurately following the full model's response. Note that all of the bases in this work are selected in a load-independent manner, which means that the developed NLROMs can be used for a variety of load distributions. Furthermore, Fig. 4.24 shows the relative error of the first half second of time responses, which are used to compute the PSDs of Fig. 4.23. In this figure, it is discernible that the relative error of the NLROM developed by MDs is smaller than the NLROMs developed by other bases. The results obtained for this example show that combining non-intrusive nonlinear model reduction methods and modal derivatives allows building accurate NLROMs..

Computational costs

The last study for this example is evaluation of the computational costs for the proposed NLROMs and comparison of it with other bases. Therefore, as a sample, the required offline time to develop the NLROMs used in Fig. 4.23 are computed and listed in Table 4.7. One can note that the offline computational time of the proposed NLROMs with (S)MDs are not more than the previous methods. This result together with the one displayed in Fig. 4.23, implies that while the accuracy of the NLROMs with the proposed bases have been improved, there is no increase in offline computational costs for the development of the NLROMs.

	Property (dimension)	**Value**
Material	Mass density (kg/m^3)	7870
	Young's modulus (GPa)	2.05×10^{11}
	Poisson's ratio	0.28
Geometry	l (mm)	800
	w (mm)	400
	t (mm)	2
FE model	Element-type	Shell 4-node (Abaqus S4R)
	Number of Elements	3200
	Number of DOFs	19202

Table 4.6: Geometry, material and FE model properties of the investigated panel model.

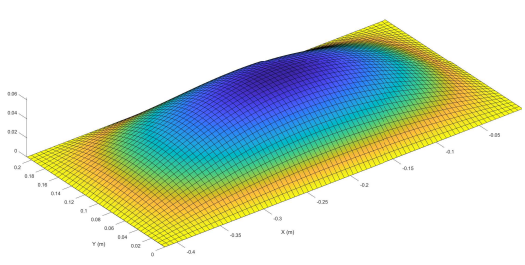

(a) φ_1 : $\omega_1 = 150.5$ Hz

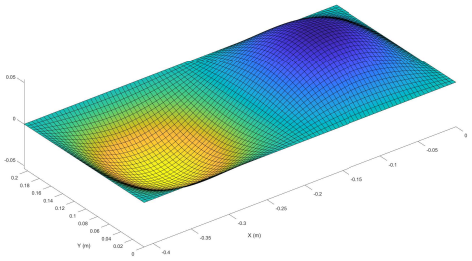

(b) φ_2 : $\omega_2 = 240.6$ Hz

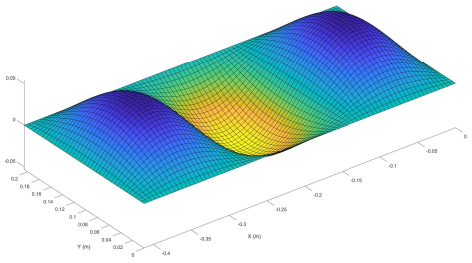

(c) φ_3 : $\omega_3 = 391.2$ Hz

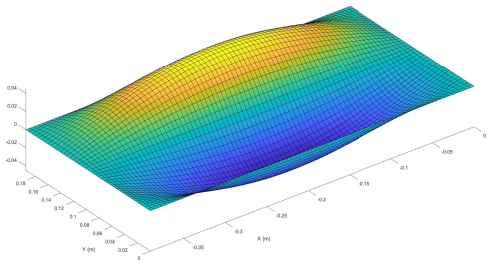

(d) φ_4 : $\omega_4 = 513.1$ Hz

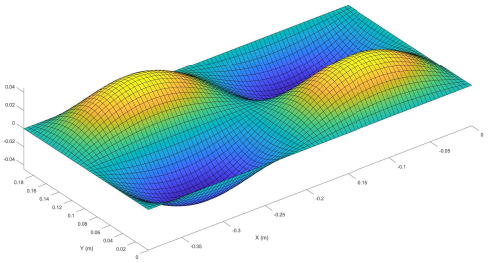

(e) φ_5 : $\omega_5 = 602.6$ Hz

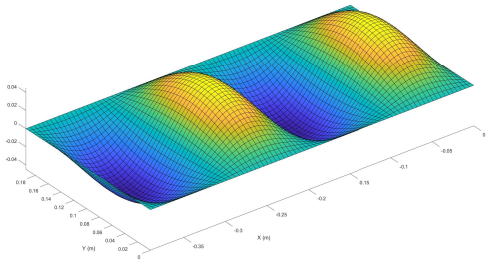

(f) φ_6 : $\omega_6 = 602.6$ Hz

Figure 4.18: The first six vibration modes of the panel structure.

NLROM	ED offline time time (min.)	EED offline time time (min.)
NLROM-11VM-11Dual	193	127
NLROM-11VM-11SMD	78	29
NLROM-11VM-11MD	80	30
NLROM-22VM	91	26

Table 4.7: Offline computational time for development of the panel's NLROMs, only for NSCs identification part.

Furthermore, Table 4.8 reports the required online time for 5 seconds time integration of the NLROMs compared to the full-order model. Although the full model is

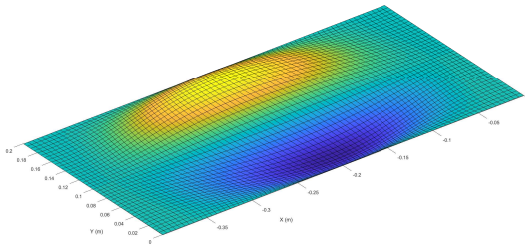

(a) $\theta_{11} = \frac{\partial \phi_1}{\partial q_1}$

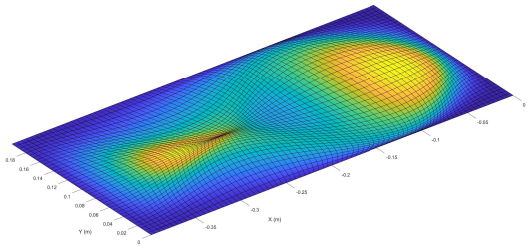

(b) $\theta_{12} = \theta_{21} = \frac{\partial \phi_1}{\partial q_2}$

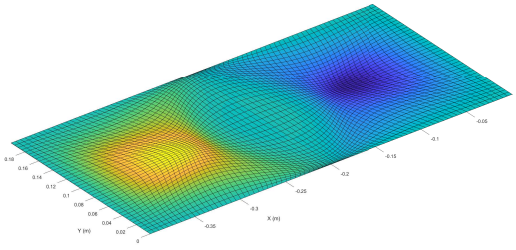

(c) $\theta_{13} = \theta_{31} = \frac{\partial \phi_1}{\partial q_3}$

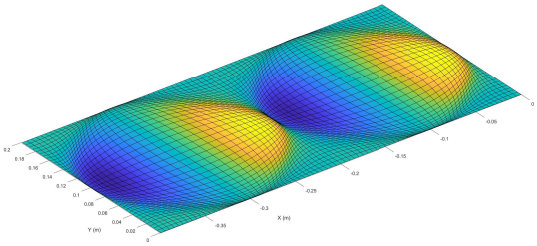

(d) $\theta_{22} = \frac{\partial \phi_2}{\partial q_2}$

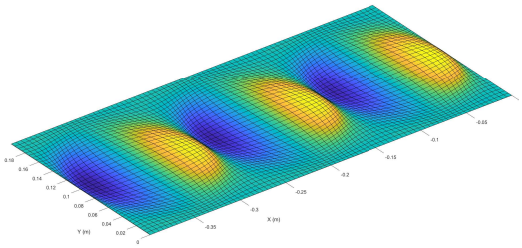

(e) $\theta_{33} = \frac{\partial \phi_3}{\partial q_3}$

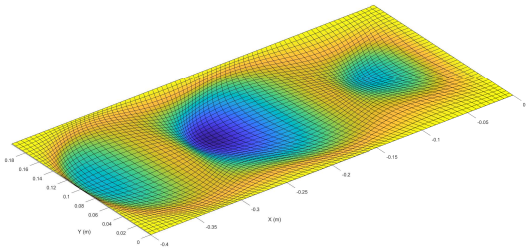

(f) $\theta_{23} = \theta_{32} = \frac{\partial \phi_2}{\partial q_3}$

Figure 4.19: The first six SMDs shown for the panel structure, which are in-plane dominated.

Model	online time (min.)
Full model	971
NLROM-11VM-11Dual	14
NLROM-11VM-11SMD	14
NLROM-11VM-11MD	14
NLROM-22VM	14

Table 4.8: Online time for time integration of the panel's NLROMs and full model for 5 seconds under 157 dB load.

integrated in Abaqus, which usually uses optimized algorithms and NLROMs are integrated in a research code in MATLAB, the online computational cost for NLROMs

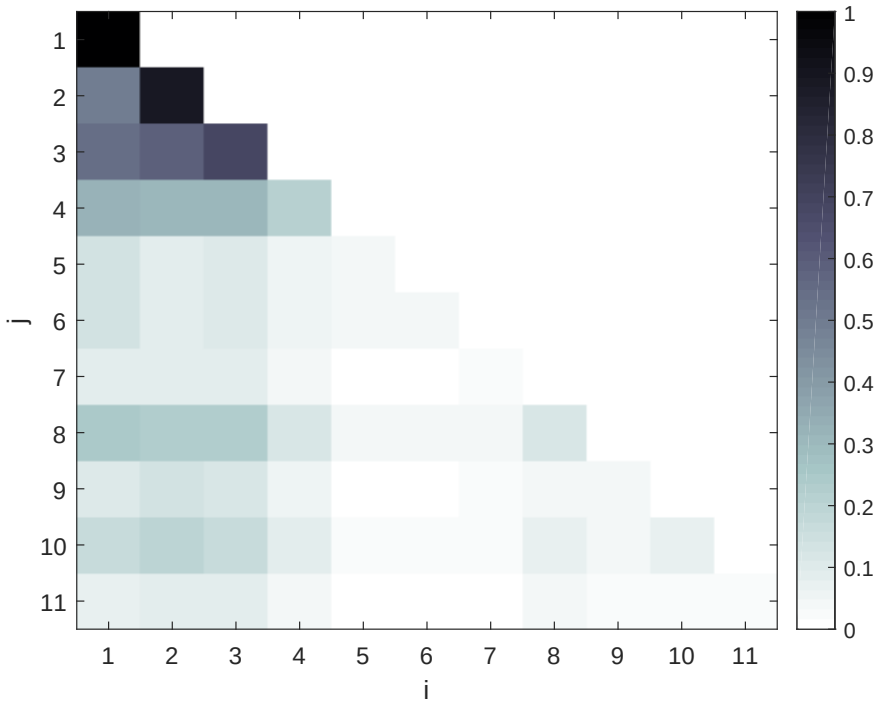

Figure 4.20: Maximum modal interaction matrix values for the panel structure with eleven linear modes in the basis. Since this matrix is symmetric, only the lower triangle is shown.

are at least 69 times faster than the full-model.

4.5 Remarks on displacement-based non-intrusive MOR

As discussed in section 7.4, nonlinear reduced-order models using non-intrusive methods with the proposed basis can improve the accuracy in NLROMs under the defined load-independent conditions. However, there are still some challenges in this context, which can direct future research. Some of these challenges are outlined here:

- While augmentation of the reduction basis with the non-intrusive (S)MDs allows building accurate NLROMs, the resulting size of the generated NLROMs increases significantly. One possibility is to resort on nonlinear projection (e.g. quadratic manifolds, see [63, 64]), which enslave modal derivatives (or the like) to dominant vibration modes, implemented non-intrusively.
- For our investigated examples, it has been observed that the NLROMs developed by the ED method using VMs with either dual modes or (S)MDs, always deliver stable time integration results. However, when the EED method of Perez et al. [116] is used with Abaqus static solutions, sometimes instabilities occur in the time integration of the resulting NLROMs. This can be due to inaccuracies induced by identifying NSCs with the tangent stiffness matrix (instead of reaction forces in ED) exported from Abaqus. This problem might be solved by using a “cleaning” procedure demonstrated in [115].

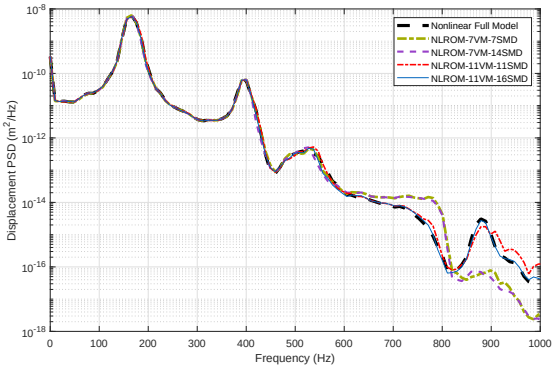

(a) Transverse DOF of A, NLROMs developed by SMDs.

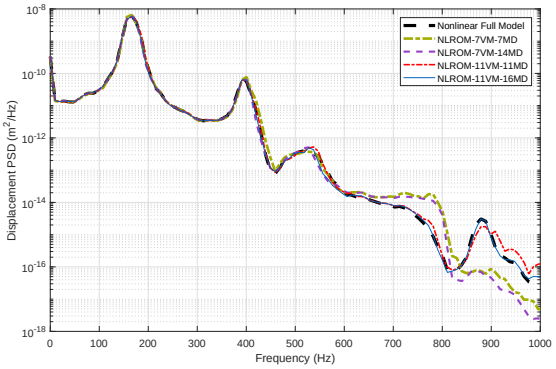

(b) Transverse DOF of A, NLROMs developed by MDs.

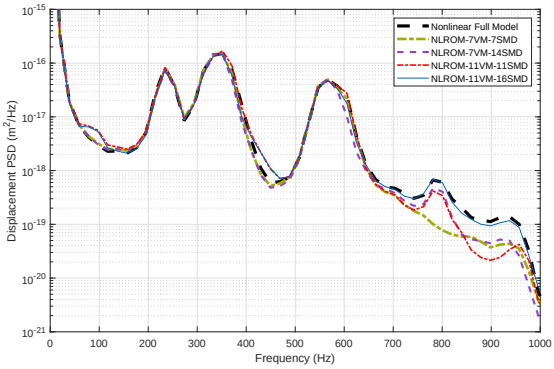

(c) Membrane DOF of B, NLROMs developed by SMDs.

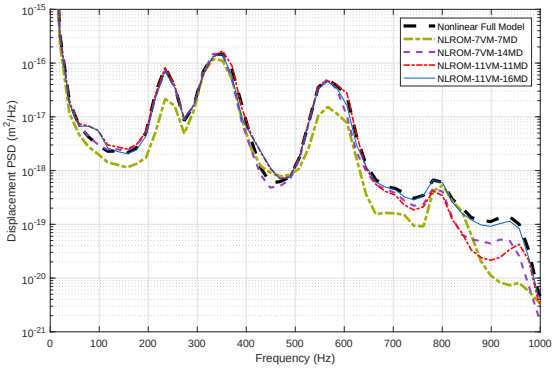

(d) Membrane DOF of B, NLROMs developed by MDs.

Figure 4.21: The panel's PSDs for convergence check of transverse and in-plane directions of the points A and B, respectively, under 155 dB SPL. The panel's NLROMs are developed using linear modes augmented once with SMDs and then with MDs.

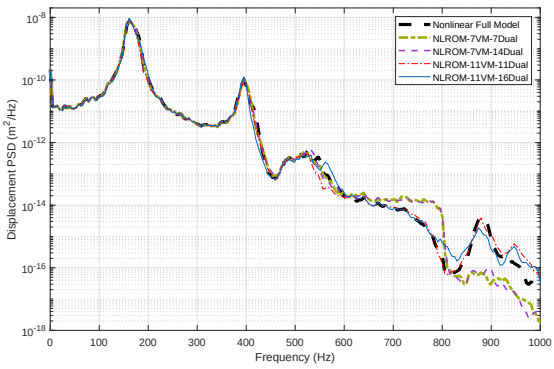

(a) Transverse DOF of A, NLROMs developed by dual modes

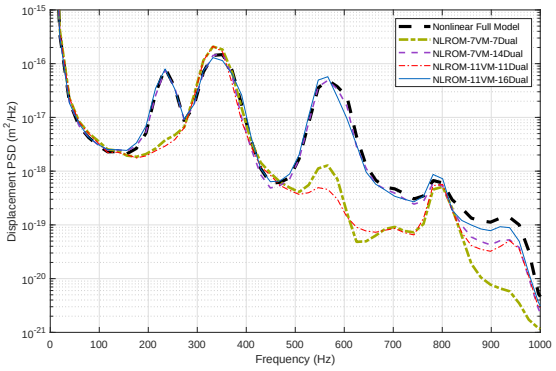

(b) Membrane DOF of B, NLROMs developed by dual modes

Figure 4.22: The panel's PSDs for convergence check of transverse and in-plane directions of points A and B, respectively, under 155 dB SPL. The NLROMs are developed using linear modes augmented with dual modes.

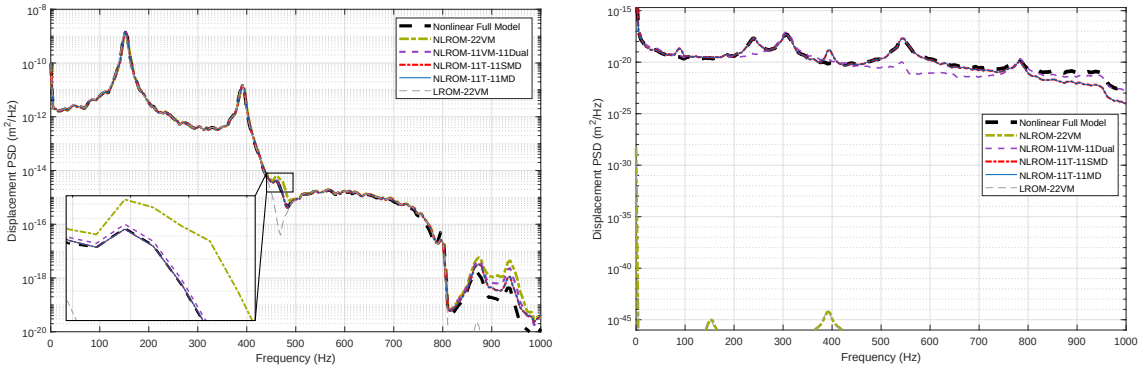

(a) Transverse DOF of point A under 145 dB.

(b) Membrane DOF of point B under 145 dB.

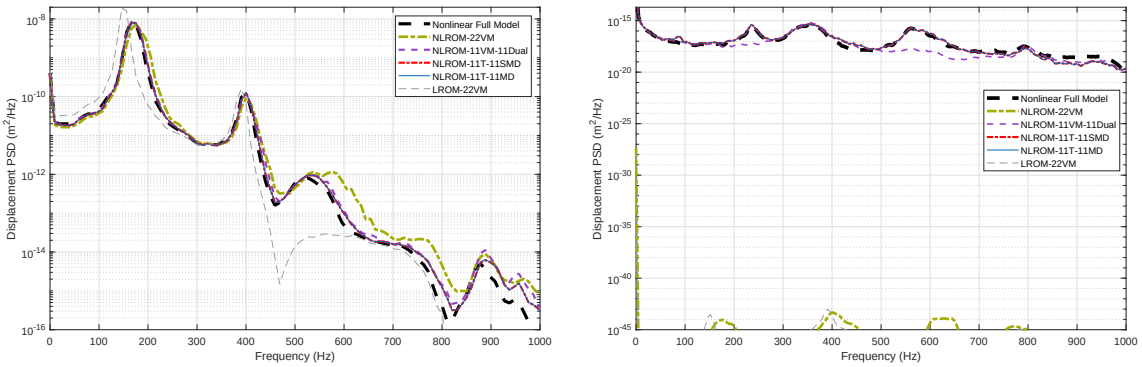

(c) Transverse DOF of point A under 157 dB.

(d) Membrane DOF of point B under 157 dB.

Figure 4.23: The panel's PSDs comparison for the NLROMs developed by 11VM-11SMD, 11VM-11MD, 11VM-11Dual and 22VM with the full-order model and the linear reduced model (22VM). The PSDs are obtained under two load cases of 145 dB 157 dB SPL.

4.6 summary

We propose the use of modal derivatives for the improvement of non-intrusive Model Order Reduction (MOR) of geometrically nonlinear structures. The main advantage of the non-intrusive MOR is that a Nonlinear Reduced Order Model (NLROM) can be developed without having to access nonlinear element formulations of a model. This advantage enables engineers to develop their models in commercial software and simultaneously take the advantage of MOR. However, one of the bottlenecks of the non-intrusive ROM techniques is selection of a proper reduction basis to accurately identify Nonlinear Stiffness Coefficients (NSCs) of the NLROM. This is because the NSCs are identified based on imposition of a series of nonlinear static displacement inputs to the FE package, which are built from the reduction basis. This basis has to capture the most important nonlinear interaction between the modes and also be computed easily. The current available basis vectors in non-intrusive approach include linear vibration modes and dual modes [76, 98, 116]. In this work, we propose augmenting the linear modes with the non-intrusive Modal Derivatives (MDs). We have presented a non-intrusive formulation to compute the MDs for two cases that the underlying FE package releases either tangent stiffness matrix or nonlinear reaction forces due to a nonlinear static displacement. Furthermore, we intro-

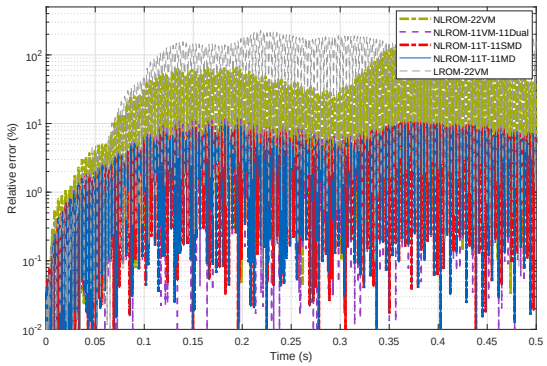

(a) Transverse DOF of point A under 145 dB.

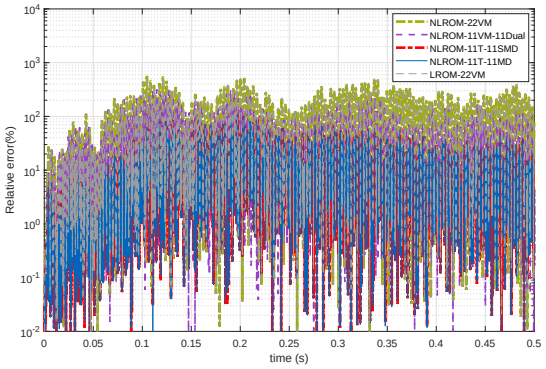

(b) Membrane DOF of point B under 145 dB.

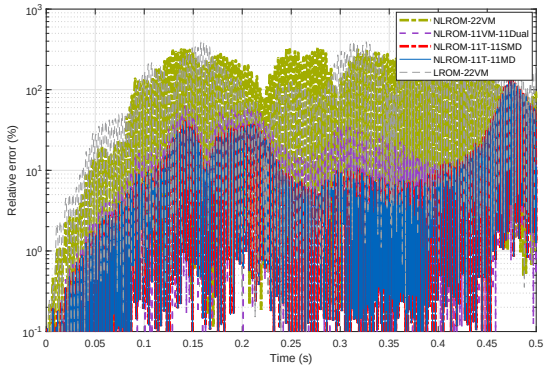

(c) Transverse DOF of point A under 157 dB.

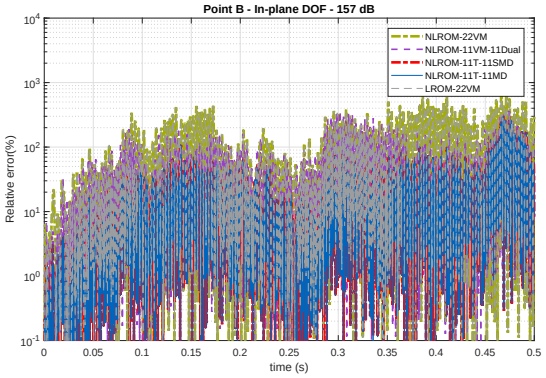

(d) Membrane DOF of point B under 157 dB.

Figure 4.24: The panel's relative error comparison for NLROMs developed by 11VM-11SMD, 11VM-11MD, 11VM-11Dual and 22VM with the full-order model and the linear reduced model (22VM). The relative errors are obtained under two load cases of 145 dB 155 dB SPLs.

duced a systematic way to select the modal derivatives such that they are chosen in a load-independent manner. This is unlike the dual modes, which are usually selected according to the loading conditions of the system. We have applied the proposed method on three geometrically nonlinear structures with beam and shell elements, and compared the nonlinear random responses of the proposed NLROM under different excitations levels with the NLROMs that are developed with available bases and the full-order model. The results show the high accuracy of the proposed basis compared to the other methods. This improvement is achieved without increasing the online and offline computational costs, neither for the computation of the basis nor for identification of NSCs.

Chapter 5

Evaluation and comparison of non-intrusive NLROMs

In this chapter we compare the accuracy as well as computational efficiency of the non-intrusive ROM approaches discussed in Chapters 3 and 4. We then discuss the cases, where each of the methods is more efficient to be employed for NLROM development. To start with the comparison of the methods, let us analyze the number of nonlinear static solutions versus the dimension of the NLROMs, which are required for ICE, ED or EED, regardless of their accuracy. Fig. 5.1 depicts the comparison of these three methods. As can be seen from this figure, for the same number of generalized coordinates in the NLROM, ICE requires the highest number of static solutions, while EED needs much less static solutions. This is due to the fact that EED uses TS matrices instead of displacements to identify nonlinear stiffness coefficients. However, it should be noted that the number of required modes to build an accurate NLROM by ED and EED is more (usually twice) than the number of the modes to build it with ICE. Nevertheless, it can be stated that to generate an NLROM with a large number of modes, EED has the least computational cost.
Furthermore, to assess the accuracy of the discussed MOR methods, they are applied here to two geometric nonlinear FE models, a shallow-curved and a deep-curved beam, and their results are compared. For flat structures it is already shown in Chapters 3 and 4 that both methods can accurately approximate the full-order response. However, ICE only needs linear transverse VMs to deliver an accurate NLROM, in contrast to the (E)ED method that requires also dual modes or (S)MDs. Therefore, for flat structures, ICE has a more compact NLROM compared to (E)ED.

	Property (dimension)	**Value**
Material	Mass density (kg/m^3)	7870
	Young's modulus (GPa)	2.05×10^{11}
	Poisson's ratio	0.28
Geometry	l (mm)	800
	h (mm)	200
	t (mm)	4
FE model	Element-type	Timoshenko (Abaqus B21)
	Number of Elements	80
	Number of DOFs	237

Table 5.1: Geometry, material and FE model properties of the deep-curved beam model

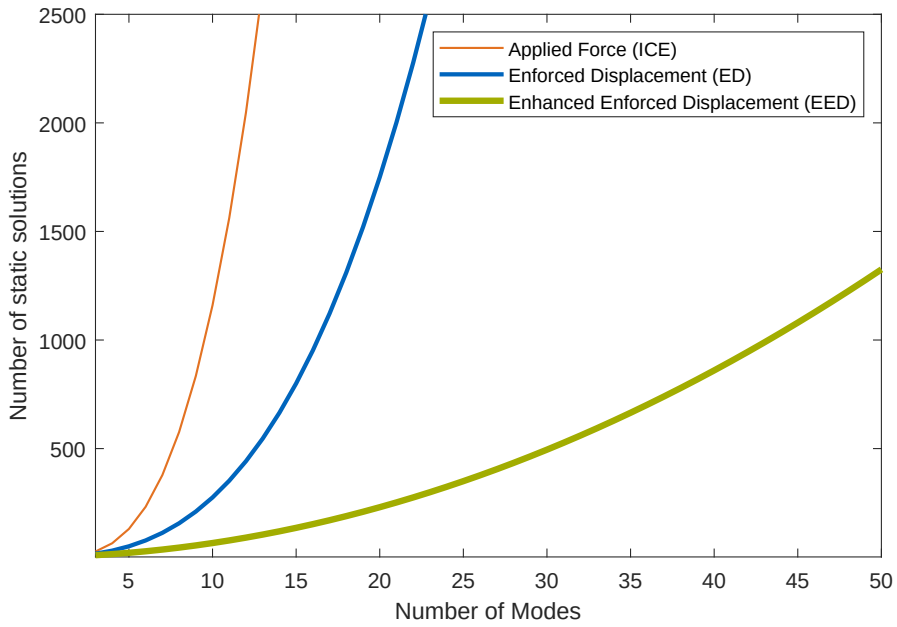

Figure 5.1: Comparison of the required number of nonlinear static solutions versus the number of kept modes for the ICE, ED and EED methods.

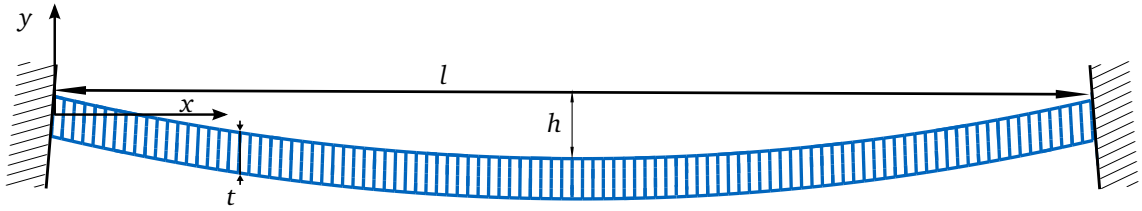

(a) Shallow-curved FE model.

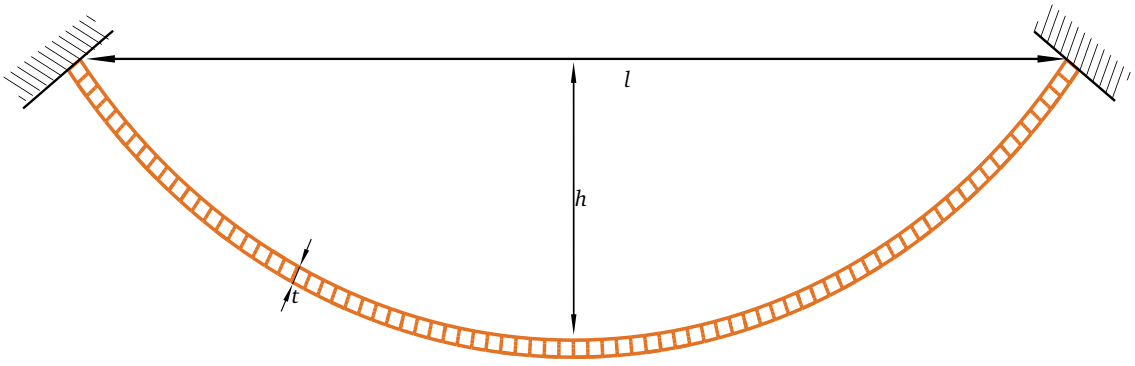

(b) Deep-curved FE model.

Figure 5.2: Schematic of the FE model of the shallow-curved and deep-curved beam structures.

5.1 Examples

In this section we compare the three non-intrusive methods introduced in Chapters 3 and 4 by applying them to a shallow-curved and a deep-curved structure.

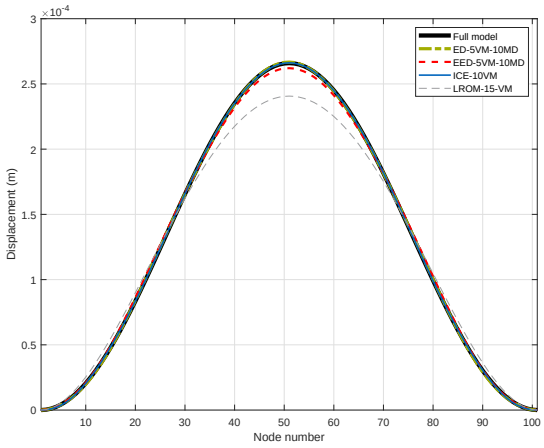

(a) Displacement in y direction under 1 N

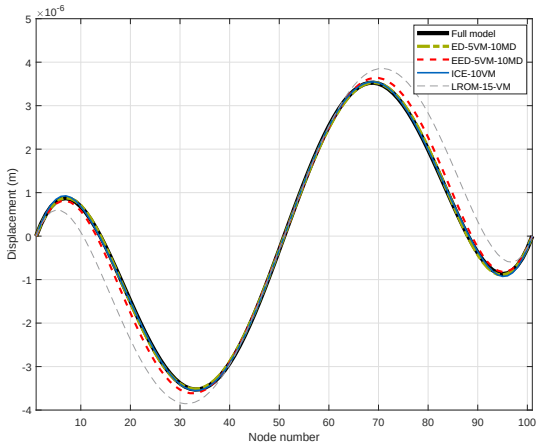

(b) Displacement in x direction under 1 N

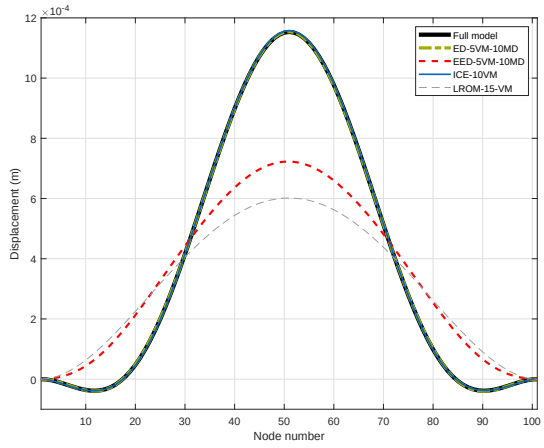

(c) Displacement in y direction under 2.5 N

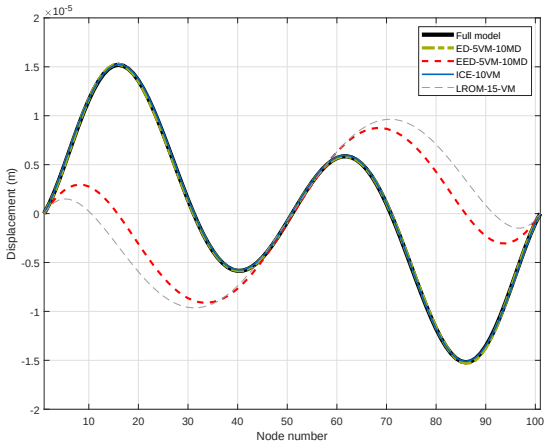

(d) Displacement in x direction under 2.5 N

Figure 5.3: Deformation of the shallow-curved beam in x and y directions under two uniform distributed static loads in y direction, with intensities of 1 N and 2.5 N. The loads are applied to all nodes.

5.1.1 Shallow-curved model

The first example is the shallow-curved beam shown in Fig. 5.2a. The material, geometry and mesh properties of this structure are illustrated in Table 4.3. Three NLROMs with the following reduction bases as well as methods are developed for this model:

- 5 VMs in addition to 10 MDs combined with ED (ED-5VM-10MD).
- 5 VMs in addition to 10 MDs combined with EED (EED-5VM-10MD).
- 10 VMs combined with ICE (ICE-10VM).

Two static uniform distributed loads in y direction with weak and strong intensities (1 N and 2.5 N) are applied to the structure. The responses of the developed NLROMs under both load cases are compared with the full model as well as the linearized model (linear full model), in both x and y directions and shown in Fig. 5.3.

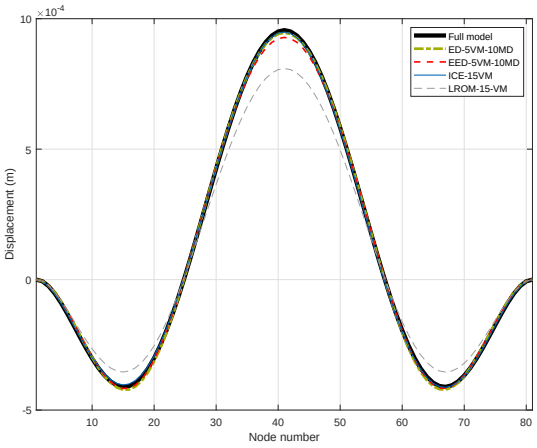

(a) Displacement in y direction under 8 N

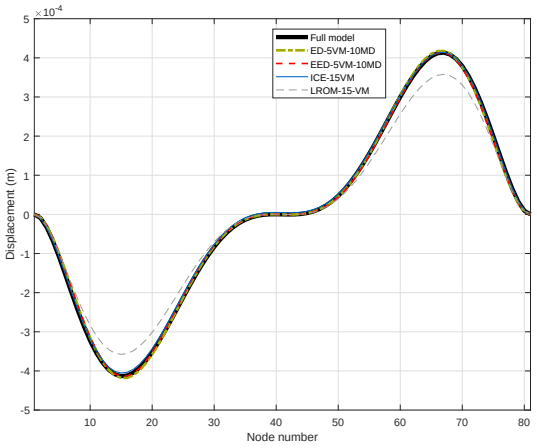

(b) Displacement in x direction under 8 N

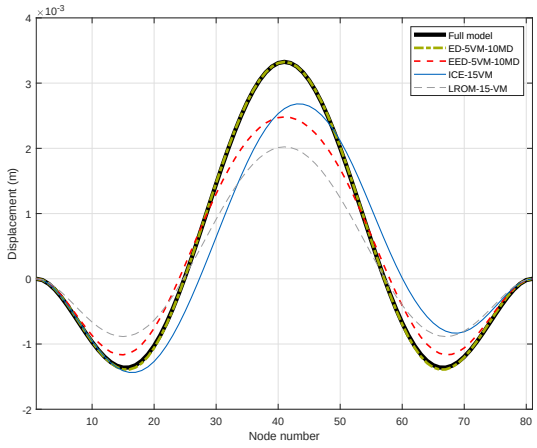

(c) Displacement in y direction under 20 N

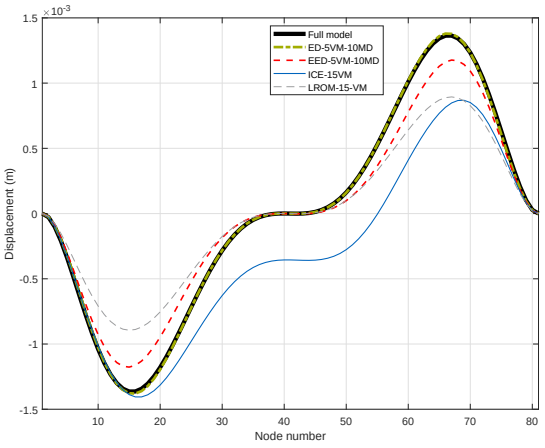

(d) Displacement in x direction under 20 N

Figure 5.4: Deformation of the deep-curved beam in x and y directions under two uniform distributed static loads in y direction, with intensities of 8 N and 20 N. The loads are applied to all nodes.

For the case of weak nonlinearity (Fig. 5.3a and 5.3b), all the developed NLROMs exhibit acceptable results, although the ICE and ED are more accurate than EED in both directions. However, for the strong level of nonlinearity (Fig. 5.3c and 5.3d), EED is totally inaccurate and ED and ICE both represent very accurate deformations compared to the full model response and in both directions. Since, the ED and EED are mathematically equivalent methods, the poor results of the EED for strong nonlinearity can be because of the inaccuracies induced by Abaqus while exporting TS instead of restoring forces and very few utilized static solutions that cannot cancel out some of these inaccuracies.

Furthermore, it should be noted that the NLROM developed by ED contains 15 DOFs, whereas the NLROM developed by ICE comprises 10 DOFs with a similar accuracy as ED, which is the advantage if ICE. However, it is discussed in [150] that when a shallow curved structure is under combined loading conditions (e.g. acoustic and thermal), the expansion part of ICE method does not work accurately anymore. This

is because the assumption of ICE method, which is a quadratic relation between transverse-membrane generalized coordinates is not fulfilled. In these case our proposed methods, namely ED with (S)MDs can be used.

5.1.2 Deep-curved model

The second example of this chapter comprise a deep-curved structure as shown in Fig. 5.2b. The material, geometry and mesh properties of the model are detailed in Table 5.1. The importance of considering such a structure comes from the fact that the assumption of quadratic relation in transverse-membrane generalized coordinate, explained in Nash [104] for flat and shallow-curved structures, does not apply anymore. Therefore, it is interesting to observe the ability of different non-intrusive methods to capture the response of such structures accurately.
To evaluate the performance of different non-intrusive methods on this structure, the following NLROMs with the same number of generalized coordinates are developed for the model as

- 5 VMs in addition to 10 MDs combined with ED (ED-5VM-10MD).
- 5 VMs in addition to 10 MDs combined with EED (EED-5VM-10MD).
- 15 VMs combined with ICE (ICE-15VM).

It should be noted that to develop the NLROM for this example with ICE, the corresponding scaling factors are scaled down such that the nonlinear static solutions for NCSs identification converge to a solution.
Two uniform distributed static loads in y direction with intensity of 8 and 20 N, which activate weak and strong geometric nonlinearity, respectively, are applied to the NLROMs. The response of these NLROMs are compared with the full model and the linearized model in x and y directions and depicted in Fig. 5.4. For the low level of nonlinearity, all the methods can accurately track the full model response, although ICE and ED deliver more accurate results than EED. However, for the strong level of nonlinearity, the only NLROM that can accurately represent the full model response is obtained by ED. This means that the most robust non-intrusive method, which can accurately predict the response of the full model for different structures and under different loading conditions is the ED method combined with modal derivatives.
Moreover, the number of required static solutions to develop each NLROM with different sizes is demonstrated in Table 5.2. As can be seen from this table, although the EED method uses much less static solutions than ICE, the NLROM based on EED represents more accurate results than ICE in x direction. (Fig. 5.4d). This is due to the aforementioned assumption of ICE to approximate the in-plane motion of structures, which does not apply here.

5.2 Concluding remarks on non-intrusive ROM methods

From the results outlined in the Part I of this dissertation, the following remarks can be concluded

NLROM's DOFs	EED	ED	ICE
5	20	50	130
10	65	275	1160
15	135	800	4090

Table 5.2: The number of required nonlinear static solutions for each non-intrusive ROM method to develop NLROMs with different DOFs.

- Non-intrusive model order reduction is a powerful tool to strongly reduce the computational burden of FE models that are developed in commercial FE packages. Besides, an NLROM can be developed by a non-intrusive method such that it is valid for a range of load cases in a broadband frequency, which makes the offline costs reasonable.

- For the case of flat and shallow-curved structures, ICE delivers a more compact model than (E)ED, due to the fact that it can develop an accurate NLROM by only using linear VMs. However, since the number of nonlinear static solutions is a cubic function of the number of the reduced DOFs for ICE (also for ED), its offline computational cost becomes expensive when too many modes must be taken in the reduction basis. In this case, the EED method could be used, at least if the level of nonlinearity is relatively low.

- For MOR of deep-curved structures, the only method that exhibits very accurate results in weak and strong nonlinearity, is the ED method combined with modal derivatives.

- In case of curved-structures under combined loading conditions, the expansion procedure of ICE method does not work as explained in [150], due to its quadratic relation assumption between transverse-membrane coordinates to approximate the in-plane motion. For this case, we propose to employ the ED method combined with non-intrusive modal derivatives, because it is a general method that does not have the restrictive assumption of ICE.

- It is observed during the time integrations with different non-intrusive ROMs that the ED and ICE methods with different reduction bases always result in stable time integrations. However, sometimes instabilities occur while integrating the NLROMs developed by EED. In this cases, either a new NLROM with different number of VMs as well as (S)MDs can be developed and tested or other non-intrusive methods should be used if exactly a certain combination of modes is desired.

- For a large nonlinear structure with several components developed in a commercial software, it is very cumbersome to reduce the FE model monolithically. Instead, non-intrusive MOR methods should be combined with dynamic substructuring approaches (e.g. see [67, 68, 85, 164]) to facilitate model reduction and parallel computation. This will be investigated in Part II if this dissertation.

5.3 Summary

In this Chapter, we compare the available non-intrusive MOR techniques in terms of accuracy and computational efficiency. We first give an insight into the offline computational costs of each method by comparing their required number of nonlinear static solutions. Afterwards, we apply the non-intrusive methods to two geometric nonlinear structures under different loading conditions, which activate weak and strong nonlinearity of the models. We then discuss the advantages and disadvantages of each method when employed for different types of structures. We show that the most robust method to deliver accurate results for different structures under a variety of loading levels is the ED method combined with modal derivatives. Finally, we draw the concluding results for non-intrusive model order reduction of nonlinear structures.

Part II

Nonlinear dynamic substructuring

Chapter 6

Common linear substructuring methods: primal assembly

This chapter is extracted from the author's publication in [65]. In this article, Karamooz had the idea of the work and performed the literature review. Karamooz implemented a considerable part of the work and wrote the manuscript. Xu conducted the primary part of numerical studies and discussed the work. Bartl, Tiso and Rixen gave very useful inputs in the discussions of the work and proof-read the article. Rixen supervised the work.

6.1 Introduction

In this chapter, we study three common CMS methods that will be further extended to nonlinear substructuring. We review one fixed-interface CMS method, known as Hurty/Craig-Bampton (HCB) and two free-interface ones, which we call Goldman-Hou (GH) and MacNeal/Rubin-Martinez (MRM). These methods are widely studied in the literature (e.g. see [27–29]).
The classical CMS methods do not reduced interfaces of substructures while reducing the model of each substructure. However, interface reduction becomes necessary when several DOFs exist at the connecting surfaces of substructures to deliver compact linear and nonlinear ROMs. Therefore, we investigate three Interface Reduction (IR) techniques, which have been mostly used so far for fixed-interface CMS. These IR techniques comprise one system level (after substructures assembly) and two local level (before substructures assembly) methods. We then apply these IR methods to free-interface CMS and show that the accuracy of the free-interface method with IR is better than the accuracy of the fixed-interface method with IR.
Finally, we apply the presented methods in this chapter to two numerical examples and compare the results of free- and fixed- interface methods.

6.2 Fixed-interface method

The first CMS method in the field of finite element analysis is the fixed-interface mode method developed by Hurty [58]. This method, which contains rigid-body modes, constraint modes and fixed interface modes, was modified by Craig and Bampton [26]. They realized that if the constraint modes for all boundary DOFs are calculated

in the reduction basis, rigid-body modes are not required to be inserted in the basis. Before starting with the introduction of the component modes, it is usual to split the substructures' DOFs into a set of master DOFs, $\boldsymbol{u}_b$ (which are the boundary DOFs) and slave DOFs, $\boldsymbol{u}_i$ (which represent the internal DOFs). The set of the system's displacement vector can then be rearranged as

$$\boldsymbol{u} = \begin{bmatrix} \boldsymbol{u}_i \\ \boldsymbol{u}_b \end{bmatrix}. \tag{6.1}$$

Introducing Eq. (6.1) into the governing equation (2.20), the EOM in the rearranged form reads:

$$\begin{bmatrix} \boldsymbol{M}_{ii} & \boldsymbol{M}_{ib} \\ \boldsymbol{M}_{bi} & \boldsymbol{M}_{bb} \end{bmatrix} \begin{bmatrix} \ddot{\boldsymbol{u}}_i \\ \ddot{\boldsymbol{u}}_b \end{bmatrix} + \begin{bmatrix} \boldsymbol{C}_{ii} & \boldsymbol{C}_{ib} \\ \boldsymbol{C}_{bi} & \boldsymbol{C}_{bb} \end{bmatrix} \begin{bmatrix} \dot{\boldsymbol{u}}_i \\ \dot{\boldsymbol{u}}_b \end{bmatrix} + \begin{bmatrix} \boldsymbol{K}_{ii} & \boldsymbol{K}_{ib} \\ \boldsymbol{K}_{bi} & \boldsymbol{K}_{bb} \end{bmatrix} \begin{bmatrix} \boldsymbol{u}_i \\ \boldsymbol{u}_b \end{bmatrix} + \boldsymbol{f}_{nl}\left(\begin{bmatrix} \boldsymbol{u}_i \\ \boldsymbol{u}_b \end{bmatrix} \right) = \begin{bmatrix} \boldsymbol{f}_i \\ \boldsymbol{f}_b \end{bmatrix} + \begin{bmatrix} \boldsymbol{0} \\ \boldsymbol{g} \end{bmatrix}. \tag{6.2}$$

It should be noted that the connecting forces of the substructure, $\boldsymbol{g}$ are added to Eq (2.20), which are non-zero for the interface DOFs only. To present the linear CMS methods, the damping and nonlinear terms in Eq. (6.2) are omitted in this chapter. The modes required in the HCB basis are outlined below.

Fixed interface normal modes

As the name expresses, the fixed interface modes are the vibration modes of a substructure when all boundary DOFs are constrained. The EOM for a constrained linearized problem gives

$$\boldsymbol{M}_{ii}\ddot{\boldsymbol{u}}_i + \boldsymbol{K}_{ii}\boldsymbol{u}_i = \boldsymbol{0}. \tag{6.3}$$

Accordingly, the fixed interface mode matrix $\boldsymbol{\Phi}_{FM}$ is defined as the matrix that contains the eigenvectors of the following eigenvalue problem in its columns

$$(\boldsymbol{K}_{ii} - \omega_{FM,j}^2 \boldsymbol{M}_{ii})\boldsymbol{\varphi}_{FM,j} = \boldsymbol{0}, \tag{6.4}$$

where $\omega_{FM,j}$ and $\boldsymbol{\varphi}_{FM,j}$ are the j^{th} fixed-interface eigenfrequency and VM of the substructure, respectively. The fixed interface mode matrix is then mass-normalized to be used in the HCB transformation matrix.

Constraint Modes

The Constraint Modes are defined as the static deflection of the internal DOFs of a substructure, if a unit displacement is enforced on each of the boundary DOFs while all other boundary DOFs remain fixed. According to this definition, the (linearized)

Eq. (6.2) can be written in the following form to obtain the constraint modes (as they are static modes, the inertia terms are omitted):

$$\begin{bmatrix} \boldsymbol{K}_{ii} & \boldsymbol{K}_{ib} \\ \boldsymbol{K}_{bi} & \boldsymbol{K}_{bb} \end{bmatrix} \begin{bmatrix} \boldsymbol{\Psi}_{ib} \\ \boldsymbol{I}_{bb} \end{bmatrix} = \begin{bmatrix} \boldsymbol{0}_{ib} \\ \boldsymbol{F}_{bb} \end{bmatrix}, \tag{6.5}$$

where, $\boldsymbol{I}_{bb}$ is the identity matrix and $\boldsymbol{F}_{bb}$ is the reaction force matrix corresponding to the fixed interface DOFs. Now, the constraint modes matrix can be given by

$$\boldsymbol{\Psi}_{CM} = \begin{bmatrix} \boldsymbol{\Psi}_{ib} \\ \boldsymbol{I}_{bb} \end{bmatrix}. \tag{6.6}$$

In order to obtain the unknown matrix $\boldsymbol{\Psi}_{ib}$ in Eq. (6.6), the first line of Eq. (6.5) is solved, giving

$$\boldsymbol{\Psi}_{CM} = \begin{bmatrix} \boldsymbol{\Psi}_{ib} \\ \boldsymbol{I}_{bb} \end{bmatrix} = \begin{bmatrix} -\boldsymbol{K}_{ii}^{-1}\boldsymbol{K}_{ib} \\ \boldsymbol{I}_{bb} \end{bmatrix}. \tag{6.7}$$

6.2.1 Hurty/Craig-Bampton basis

Craig and Bampton (CB) [26] described the motion of internal DOFs of a substructure as a superposition of a truncated number of fixed interface normal modes and constraint modes while keeping all the boundary DOFs in the reduction basis, namely

$$\boldsymbol{u}_i \approx \boldsymbol{\Psi}_{CM_i}\boldsymbol{x}_b + \boldsymbol{\Phi}_{FM_i}\boldsymbol{q}_{FM}, \tag{6.8}$$

where the subscript i denotes the components of the matrices corresponding to the internal DOFs and $\boldsymbol{q}_FM$ is the vector of the fixed-interface modes' generalized coordinates. Therefore, the HCB transformation matrix is written as

$$\begin{bmatrix} \boldsymbol{u}_i \\ \boldsymbol{u}_b \end{bmatrix} = \begin{bmatrix} \boldsymbol{\Phi}_{FM} & \boldsymbol{\Psi}_{CM} \\ \boldsymbol{0} & \boldsymbol{I}_{bb} \end{bmatrix} \begin{bmatrix} \boldsymbol{q}_{FM} \\ \boldsymbol{u}_b \end{bmatrix} = \boldsymbol{T}_{CB} \begin{bmatrix} \boldsymbol{q}_{FM} \\ \boldsymbol{u}_b \end{bmatrix}, \tag{6.9}$$

for a linear structure. Keuther et al. [84] used the HCB transformation matrix in the nonlinear substructuring. In fact, they reduced the linear mass and stiffness of substructures using the HCB basis. Afterwards, they used the HCB basis in the ICE method (Chapter 7) to identify the nonlinear stiffness coefficients of each substructure. We propose here a free-interface-based reduction basis with interface reduction for nonlinear substructuring using ICE.

Once the nonlinear substructures are developed, the localization matrix can be formed to couple the substructures, which is the same for linear and nonlinear structuring (see section 6.5). If the system is composed of two substructures, S_1 and S_2 (for instance as shown in Fig. 6.3), the assembly expression is given by

$$\begin{bmatrix} \boldsymbol{q}_i^{(S_1)} \\ \boldsymbol{u}_b^{(S_1)} \\ \boldsymbol{q}_i^{(S_2)} \\ \boldsymbol{u}_b^{(S_2)} \end{bmatrix} = \underbrace{\begin{bmatrix} \boldsymbol{I}_{ii}^{(S_1)} & \boldsymbol{0} & \boldsymbol{0} \\ \boldsymbol{0} & \boldsymbol{0} & \boldsymbol{I}_{bb}^{(S_1)} \\ \boldsymbol{0} & \boldsymbol{I}_{ii}^{(S_2)} & \boldsymbol{0} \\ \boldsymbol{0} & \boldsymbol{0} & \boldsymbol{I}_{bb}^{(S_2)} \end{bmatrix}}_{L_{HCB}} \begin{bmatrix} \boldsymbol{q}_i^{(S_1)} \\ \boldsymbol{q}_i^{(S_2)} \\ \boldsymbol{q}_b^{C} \end{bmatrix}, \tag{6.10}$$

where, $\boldsymbol{L}_{HCB}$ is called the HCB localization matrix.

6.3 Free-interface mode methods

An alternative to build up the reduction basis is the free-interface mode method. The first free-interface methods were proposed by Goldman [45] and Hou [56]. Both methods employ free-interface elastic modes as well as rigid-body modes in the reduction basis for substructures, but the ways they coupled the substructures were different. While the free-interface method of Gordon and Hou (we call it the Gordon-Hou (GH) method here) construct the basis by computing the natural vibration modes of substructures, without imposing additional constraints to them (which is compatible to the experimental test), their accuracy is much lower than the fixed-interface mode methods. Kuether et al. [84] extended this method to nonlinear substructuring and showed that its performance is inferior to their developed nonlinear substructuring based on HCB method.
The free-interface method was augmented with the so-called *attachment modes* by MacNeal [88] and further modified by Rubin [135]. It is shown in many studies (see e.g. [27, 29], also in this chapter) that the augmented free-interface mode method performs remarkably better than the GH method and occasionally superior to the HCB method. In this work, we develop the augmented free-interface method for nonlinear substructuring and compare it to nonlinear GH and HCB substructuring developed in [84]. Next, the original and augmented free-interface mode methods are outlined.
To start with the introduction of free-interface mode methods, it is convenient to split the boundary DOFs, b, of each substructure into the rigid body DOFs set r, and the remaining boundary DOFs sets (or excess DOFs) e, with $b = r + e$. The set r is a chain of DOFs that render the substructure exactly statically determined when they are fixed. Therefore, the Eq. (6.2) can be rewritten as

$$\begin{bmatrix} \boldsymbol{M}_{ii} & \boldsymbol{M}_{ie} & \boldsymbol{M}_{ir} \\ \boldsymbol{M}_{ei} & \boldsymbol{M}_{ee} & \boldsymbol{M}_{er} \\ \boldsymbol{M}_{ri} & \boldsymbol{M}_{re} & \boldsymbol{M}_{rr} \end{bmatrix} \begin{bmatrix} \ddot{\boldsymbol{x}}_i \\ \ddot{\boldsymbol{x}}_e \\ \ddot{\boldsymbol{x}}_r \end{bmatrix} + \begin{bmatrix} \boldsymbol{C}_{ii} & \boldsymbol{C}_{ie} & \boldsymbol{C}_{ir} \\ \boldsymbol{C}_{ei} & \boldsymbol{C}_{ee} & \boldsymbol{C}_{er} \\ \boldsymbol{C}_{ri} & \boldsymbol{C}_{re} & \boldsymbol{C}_{rr} \end{bmatrix} \begin{bmatrix} \dot{\boldsymbol{x}}_i \\ \dot{\boldsymbol{x}}_e \\ \dot{\boldsymbol{x}}_r \end{bmatrix} + \begin{bmatrix} \boldsymbol{K}_{ii} & \boldsymbol{K}_{ie} & \boldsymbol{K}_{ir} \\ \boldsymbol{K}_{ei} & \boldsymbol{K}_{ee} & \boldsymbol{K}_{er} \\ \boldsymbol{K}_{rs} & \boldsymbol{K}_{re} & \boldsymbol{K}_{rr} \end{bmatrix} \begin{bmatrix} \boldsymbol{x}_i \\ \boldsymbol{x}_e \\ \boldsymbol{x}_r \end{bmatrix} + \boldsymbol{f}_{nl}\left(\begin{bmatrix} \boldsymbol{x}_i \\ \boldsymbol{x}_e \\ \boldsymbol{x}_r \end{bmatrix} \right) = \begin{bmatrix} \boldsymbol{f}_i \\ \boldsymbol{f}_e \\ \boldsymbol{f}_r \end{bmatrix} + \begin{bmatrix} \boldsymbol{0}_i \\ \boldsymbol{g}_e \\ \boldsymbol{g}_r \end{bmatrix}. \tag{6.11}$$

The component modes used in free-interface methods are illustrated first.

Free-interface normal modes

The component normal modes of a system are obtained by solving an eigenvalue problem comprising the whole mass and stiffness matrices of the system or just a part of them, depending on the fixing of all, some or none of interface DOFs. The

free-interface normal modes of a system are achieved when all connecting DOFs (not the boundary conditions) in a substructure are let to move freely. Therefore, one can write the eigenvalue problem for the j^{th} free-interface mode as

$$(\boldsymbol{K} - \omega_{free,j}^2 \boldsymbol{M})\boldsymbol{\varphi}_{free,j} = 0 \tag{6.12}$$

where $\omega_{free,j}$ and $\boldsymbol{\varphi}_{free,j}$ are the j^{th} free-interface eigenfrequency and normal mode, respectively. The normal modes are usually normalized with respect to the mass matrix of the system. In other words, the modes are scaled such that

$$\boldsymbol{\Phi}_{free}^T \boldsymbol{M} \boldsymbol{\Phi}_{free} = \boldsymbol{I}, \quad \boldsymbol{\Phi}_{free}^T \boldsymbol{K} \boldsymbol{\Phi}_{free} = \boldsymbol{\Lambda}_{free} = diag(\omega_{free,1}^2, \omega_{free,2}^2, ..., \omega_{free,n-r}^2) \tag{6.13}$$

Here, the matrix of free-interface normal modes is denoted by $\boldsymbol{\Phi}_{free}$, which contains the $n-r$ normal modes of the system in its columns; $\boldsymbol{I}$ is an $(n-r) \times (n-r)$ identity matrix with ones in its diagonal components; and $\boldsymbol{\Lambda}_{free}$ is a diagonal matrix including the square of the eigenfrequencies in its diagonals.

Rigid body modes

Rigid Body Modes (RBMs) are a special type of normal modes that result in rigid displacement of a system while no deformation is induced in the structure. In other words, the system is imposed to a rigid body motion when applying RBMs to the system. Since there is no deformation in the system due to RBMs, the vibration frequencies corresponding to RBMs are zero.
According to the definition of RBMs, they are the normal modes in the system that produce no deformation. Therefore, one may write (for the linearized problem)

$$\boldsymbol{K} \boldsymbol{\Phi}_{RB} = 0, \tag{6.14}$$

where $\boldsymbol{\Phi}_{RB}$ is a matrix whose columns are the RBMs. One can compute the RBMs geometrically or alternatively obtain them as the eigenvectors of the eigenvalue problem of the free-substructures when the eigenfrequencies of the structure are zero. They can also be obtained by computing the null space of the stiffness matrix $\boldsymbol{K}$ in Eq. (6.14), as explained in [25, 44].

Attachment modes and residual flexibility attachment modes

A so-called *attachment mode* is a static deflection of a substructure when a unit force is imposed on one of the m boundary (or master) DOFs while all other boundary DOFs are left force free. If a substructure is constrained such that it has no rigid body modes, the attachment modes are simply the columns of the flexibility matrix (inverse of the stiffness matrix) of the substructure corresponding to the boundary nodes. However, the difficulty in the computation of the attachment modes arises when the substructure is not fully constrained and rigid body modes exist in the

system. In the latter case, the stiffness matrix $\boldsymbol{K}$ is singular and in order to compute the attachment modes, it is usually not possible to apply a unit force to the system because of the rigid motion in the system. One way to compute the attachment modes in the presence of the rigid body modes is to constrain (fix) a set of r DOFs that prevent rigid body motions in the system, and applying a unit force on the remaining master DOFs to compute the cantilever attachment modes as explained in [44, 52].
Alternatively, one can compute the so-called *inertia-relief attachment* modes when a substructure contains rigid body motions, which is first used by MacNeal [88] and Rubin [135]. The inertial relief modes are generated when the original force vector applied to the system is *equilibrated* by the rigid body mode. In other words, the original force vector $\boldsymbol{f}$ is projected out of the space of rigid body modes by subtracting the rigid body d'Alembert force vector from it. The inertial-relief attachment mode (or elastic flexibility) matrix, $\boldsymbol{G}_e$, can then be defined as [27, 28]

$$\boldsymbol{G}_e = \boldsymbol{P}_{IR}{}^T \boldsymbol{G}_c \boldsymbol{P}_{IR}, \tag{6.15}$$

where

$$\boldsymbol{P}_{IR} = \boldsymbol{I} - \boldsymbol{M}\boldsymbol{\Phi}_{RB}(\boldsymbol{\Phi}_{RB}{}^T \boldsymbol{M}\boldsymbol{\Phi}_{RB})^{-1}\boldsymbol{\Phi}_{RB}{}^T, \tag{6.16}$$

is called the inertia-relief projection matrix, and

$$\boldsymbol{G}_{\boldsymbol{c}} = \begin{bmatrix} \boldsymbol{G}_{ii} & \boldsymbol{G}_{ie} & \boldsymbol{0}_{ir} \\ \boldsymbol{G}_{ei} & \boldsymbol{G}_{ee} & \boldsymbol{0}_{er} \\ \boldsymbol{0}_{ri} & \boldsymbol{0}_{re} & \boldsymbol{0}_{rr} \end{bmatrix} = \boldsymbol{K}^+, \tag{6.17}$$

is the cantilever flexibility (or generalized inverse) matrix. Moreover, it can be shown that an alternative form of the elastic flexibility matrix is given by

$$\boldsymbol{G}_e = \boldsymbol{\Phi}_{free}\boldsymbol{\Lambda}_{free}{}^{(-1)}\boldsymbol{\Phi}_{free}{}^T = \sum_{j=1}^{n-r} \frac{\boldsymbol{\phi}^{(s)}_{free,j}(\boldsymbol{\phi}^{(s)}_{free,j})^T}{\omega_j^2}. \tag{6.18}$$

This form of elastic flexibility matrix is useful to compute the residual flexibility matrix.
As mentioned before, one of the aims of CMS methods is the reduction of the model of substructures. Therefore, the whole normal modes of a substructure are truncated to a reduced number of kept modes $\boldsymbol{\Phi}_k$, which depend on the frequency range of interest or cutoff frequency. In this case, to keep at least the static completeness of the reduced model, the contribution of the set of deleted modes of $\boldsymbol{\Phi}_k$ in the flexibility matrix is retained. This contribution is called residual flexibility modes, denoted by $\boldsymbol{G}_{RF}$. Since the deleted modes are usually not desired to be computed, the residual flexibility modes are obtained by subtracting the contribution of the kept modes from the whole elastic flexibility matrix, that is

$$\boldsymbol{G}_{RF} = \boldsymbol{G}_e - \boldsymbol{\Phi}_k\boldsymbol{\Lambda}_k{}^{(-1)}\boldsymbol{\Phi}_k{}^T \tag{6.19}$$

Accordingly, the *Residual Flexibility Attachment* (RFA) modes are achieved when a unit force is applied to each of the master (boundary) DOFs, given by

$$\Psi_{RFA} = G_{RF} f = (G_e - \sum_{j=1}^{n-m} \frac{\phi_{free,j} (\phi_{free,j}^{(s)})^T}{\omega_j^2}) f, \tag{6.20}$$

where, according to the definition of RFA modes, the force vector f is defined as

$$f = \begin{bmatrix} 0_{ie} \\ I_{ee} \\ 0_{re} \end{bmatrix}, \tag{6.21}$$

and Ψ_{RFA} denotes the residual flexibility attachment modes matrix.

6.3.1 Goldman-Hou basis

The displacement of a system by the method of Goldman-Hou (GM) [45, 56] is approximated as a superposition of r rigid body modes and a truncated set of free-interface modes:

$$u \approx \Phi_{RB} q_{RB} + \Phi_{free} q_{free}, \tag{6.22}$$

where, q_{RB} and q_{free} are the vectors of generalized coordinates for rigid body modes and free-interface modes, respectively. It should be noted that unlike the HCB method, the method of Hou reduces both internal and interface DOFs in its definition. Accordingly, the transformation matrix is given by

$$\begin{bmatrix} u_i \\ u_b \end{bmatrix} = \begin{bmatrix} \Phi_{RB} & \Phi_{free} \end{bmatrix} \begin{bmatrix} q_{RB} \\ q_{free} \end{bmatrix} = T_{GH} \begin{bmatrix} q_{RB} \\ q_{free} \end{bmatrix}. \tag{6.23}$$

The advantage of this method is that it does not require any augmented static modes (e.g. the constraint modes). However, it is shown that the accuracy of this method is far less than the methods that use static augmentations. Keuther et al. [84] extended this method for nonlinear substructuring and showed it is inferior compared to the nonlinear HCB method. Since, the boundary DOFs are not conserved in the physical domain as for the HCB method, the localization matrix for the assembly cannot be obtained in the form of Eq. (6.10), which is exact compatibility. Instead, a weak interface compatibility must be satisfied by solving for the null space of the compatibility condition in modal domain,

$$\underbrace{B T_{GH}^U}_{B_m} q^U \approx 0, \tag{6.24}$$

where, B is the signed Boolean matrix, T_{GH}^U contains the GH reduction basis set of all substructures in block diagonal form and B_m is the transformed Boolean matrix in modal domain. The uncoupled set of generalized coordinates are denoted by q^U. The null space of B_m in general does not exist. Therefore the null space of B_m can be approximated by computing its Singular Value Decomposition (SVD) and taking the right singular vectors corresponding to the smallest singular values, in the null space matrix, L_m. This will be explained more in section (6.4.2).

6.3.2 Augmented free-interface: MacNeal/Rubin-Martinez basis

The method of Goldman-Hou failed to approximate the effect of truncated modes in the system due to interface forces. MacNeal [88] developed the Goldman-Hou method by introducing the attachment modes in the reduction, but only for the stiffness matrix of each substructure, which makes his method inconsistent. Rubin [135] defined the residual flexibility modes by modifying the attachment modes. He extended the method of MacNeal by consistently reducing both the mass and stiffness matrices. However, he failed to show that his method is based on the Rayleigh-Ritz procedure. Craig and Chang [27, 30] proved that the augmented free-interface method from MacNeal and Rubin can be derived as a Rayleigh-Ritz approach. They also introduced a generalized procedure for the coupling of the reduced substructures, facilitating the substructuring with augmented free-interface methods. Martinez et al. [91, 92] proposed a transformation matrix for the augmented free-interface mode method in the same format as the HCB transformation matrix. Here, this method is referred to as the *MacNeal/Rubin-Martinez* (MRM) method. Many authors (e.g. see [27, 92]) have shown that the MRM method represents the best accuracy among all free-interface CMS methods. Subsequently, we explain this method and develop it for nonlinear modal substructuring.
To develop a statically complete free-interface method, such as the MRM method, the motion of the system is approximated as a superposition of truncated free-interface normal modes, rigid body modes and residual flexibility attachment modes:

$$\boldsymbol{u} \approx \boldsymbol{\Phi}_{RB}\,\boldsymbol{q}_{RB} + \boldsymbol{\Phi}_{free}\,\boldsymbol{q}_{free} + \boldsymbol{\Psi}_{RFA}\,\boldsymbol{g}. \tag{6.25}$$

The residual flexibility modes are in fact the static deflection of the truncated modes due to interface forces induced by neighboring substructures. In order to provide a transformation matrix in the format of the HCB method, the interface force vector, $\boldsymbol{g}$, has to be computed in terms of the interface displacement vector $\boldsymbol{u}_b$. This can be achieved by introducing a Boolean matrix, $\boldsymbol{A}_1$ for each substructure such that when it premultiplies Eq. (6.25), it gives the components of all matrices corresponding to the boundary DOFs:

$$\boldsymbol{A}_1\boldsymbol{u} = \boldsymbol{u}_b \approx \boldsymbol{\Phi}_{RB,b}\,\boldsymbol{q}_{RB} + \boldsymbol{\Phi}_{free,b}\,\boldsymbol{q}_{free} + \boldsymbol{\Psi}_{RFA,b}\,\boldsymbol{g}. \tag{6.26}$$

The matrix $\boldsymbol{A}_1$ $(b \times n)$ contains zeros in those elements that are multiplied to the components of internal DOFs and ones in the elements that are multiplied to the components of boundary DOFs. The subscript b, denotes the elements of the matrices for the boundary DOFs. Eq. (6.26) is then solved for $\boldsymbol{g}$, giving

$$\boldsymbol{g} \approx \boldsymbol{\Psi}_{RFA,b}^{-1}(\boldsymbol{u}_b - \boldsymbol{\Phi}_{RB,b}\,\boldsymbol{q}_{RB} - \boldsymbol{\Phi}_{free,b}\,\boldsymbol{q}_{free}). \tag{6.27}$$

The Eq. (6.27) is afterwards introduced to Eq. (6.25) to obtain the approximated displacement in terms of physical and modal displacements. However, only the part of the approximated displacement is required that corresponds to the internal DOFs, because the interface DOFs remain unchanged in the physical domain. Therefore, a

Boolean matrix $\boldsymbol{A}_2$ is defined such that it selects all the components of matrices corresponding to the internal DOFs. This matrix is then pre-multiplied by the displacement vector to give the final expression for the approximation of internal DOFs

$$\begin{aligned}\boldsymbol{A}_2\boldsymbol{u} = \boldsymbol{u}_i \approx \boldsymbol{\Psi}_{RFA,i}\boldsymbol{\Psi}_{RFA,b}^{-1}\boldsymbol{u}_b + (\boldsymbol{\Phi}_{RB,i} - \boldsymbol{\Psi}_{RFA,i}\boldsymbol{\Psi}_{RFA,b}^{-1}\boldsymbol{\Phi}_{RB,b})\boldsymbol{q}_{RB} + \\ (\boldsymbol{\Phi}_{free,i} - \boldsymbol{\Psi}_{RFA,i}\boldsymbol{\Psi}_{RFA,b}^{-1}\boldsymbol{\Phi}_{free,b})\boldsymbol{q}_{free},\end{aligned} \tag{6.28}$$

where the subscript i denotes the elements of the matrices with respect to the internal DOFs. Finally, using Eq. (6.28), the transformation matrix for the augmented free-interface mode method is obtained by

$$\boldsymbol{u} = \begin{bmatrix} \boldsymbol{u}_i \\ \boldsymbol{u}_b \end{bmatrix} \approx \boldsymbol{T}_{MRM} \begin{bmatrix} \boldsymbol{q}_{free} \\ \boldsymbol{q}_{RB} \\ \boldsymbol{u}_b \end{bmatrix}, \tag{6.29}$$

where $\boldsymbol{T}_{MRM}$ is called the *MacNeal/Rubin-Martinez* transformation matrix here, and reads

$$\boldsymbol{T}_{MRM} = \begin{bmatrix} \boldsymbol{\Phi}_{free,i} - \boldsymbol{\Psi}_{RFA,i}\boldsymbol{\Psi}_{RFA,b}^{-1}\boldsymbol{\Phi}_{free,b} & \boldsymbol{\Phi}_{RB,i} - \boldsymbol{\Psi}_{RFA,i}\boldsymbol{\Psi}_{RFA,b}^{-1}\boldsymbol{\Phi}_{RB,b} & \boldsymbol{\Psi}_{RFA,i}\boldsymbol{\Psi}_{RFA,b}^{-1} \\ \boldsymbol{0} & \boldsymbol{0} & \boldsymbol{I} \end{bmatrix}. \tag{6.30}$$

This matrix is proposed in the format of the HCB transformation. However, unlike the HCB method it requires no change to the boundary conditions of substructures (i.e. fixing the boundary DOFs) while computing the component modes, which makes it compatible with the experiment (as also discussed by Martinez et al. [91]). Furthermore, the CMS method obtained by the MRM projection basis performs considerably better than the Goldman-Hou method, because it considers the static deflection of the truncated modes due to interface forces. In this work, we propose using the MRM transformation matrix for the NSCs identification of geometric nonlinear FE substructures. Once the substructures are reduced and inserted into block diagonalized matrices, the localization matrix can be obtained like Eq. (6.10) for the assembly of two substructures, for instance.

6.4 Interface Reduction for free- and fixed-interface methods

The classical CMS methods deal with reduction of the internal DOFs of substructures. However, the reduced CMS models can still have large dimensions, because the number of interface DOFs of the substructures after MOR remain the same as the full-order FE model. If a structure contains several substructures with continuous interfaces (i.e. very fine meshes), the computational costs of the reduced order model can become inadmissible. This problem is more crucial when it comes to nonlinear substructuring, due to the extra computational burden of nonlinear terms by adding each single DOF to the reduced model. Therefore, to overcome this problem, interface reduction is developed. A review of these methods applied to the HCB technique is available in [80]. This section reviews the three most efficient interface reduction techniques that have been used in the literature for the HCB method,

namely, *System-Level* (SL-IR), *Local-Level with Exact-Compatibility* (LL-EC), and *Local-Level with Weak-Compatibility* (LL-WC). Moreover, we propose applying these methods to the MRM method as an alternative for the HCB method in linear and nonlinear dynamic substructuring.

6.4.1 System level interface reduction

According to the SL-IR method that was developed by Craig and Chang [31] and further studied by Castanier et al. [18], the substructures are first coupled in the primal assembly without changing the number of boundary DOFs. Afterwards, the interface displacement of the coupled system is approximated by taking a truncated number of modal displacements, namely

$$\boldsymbol{u}_b^C \approx \boldsymbol{\Phi}_{b\theta}^{SL} \boldsymbol{q}_\theta^C, \tag{6.31}$$

where, $\boldsymbol{q}_\theta^C$ (θ being the reduced number of interface modes) is the vector of reduced set of generalized interface coordinates, and $\boldsymbol{\Phi}^{SL}$ is the matrix of interface modes, which are also called *Characteristic Constraint* (CC) modes. The j^{th} CC mode corresponding to the j^{th} column of $\boldsymbol{\Phi}^{SL}$ is obtained from the eigenvalue solution of the global mass and stiffness matrices of the system's interface DOFs, namely

$$(\hat{\boldsymbol{K}}_{bb}^C - \omega_{b,j}^2 \hat{\boldsymbol{M}}_{bb}^C)\boldsymbol{\varphi}_{b,j} = \boldsymbol{0}, \tag{6.32}$$

where, $\hat{\boldsymbol{M}}_{bb}^C$ and $\hat{\boldsymbol{K}}_{bb}^C$ are the interface DOFs' mass and stiffness matrices of the coupled reduced system, respectively. The j^{th} CC eigenfrequency and eigenmode are denoted by $\omega_{b,j}$ and $\boldsymbol{\varphi}_{b,j}$. Furthermore, the transformation matrix to reduce the interface DOFs from b to θ ($\theta << b$) for the s^{th} substructure is given by

$$\boldsymbol{T}_{SL}^{(s)} = \begin{bmatrix} \boldsymbol{I}_{ii}^{(s)} & \boldsymbol{0} \\ \boldsymbol{0} & \boldsymbol{\Phi}_{b\theta}^{SL} \end{bmatrix}, \tag{6.33}$$

where, $\boldsymbol{\Phi}_{b\theta}^{SL}$ contains θ interface modes in its columns. To develop the non-intrusive NLROM of each substructure with SL-IR, the reduction basis to be used for NSCs identification can be obtained as

$$\boldsymbol{T}^{(s)} = \boldsymbol{T}_{CMS}^{(s)} \boldsymbol{T}_{SL}^{(s)}, \tag{6.34}$$

where, the transformation matrix, $\boldsymbol{T}_{CMS}$ can be either free- or fixed-interface transformation matrices without interface reduction (Eqs. (6.9) or (6.30)). After the identification of NSCs with the ICE method, the NLROMs are coupled with an exact interface compatibility. The localization matrix for two substructures are given by

$$\begin{bmatrix} \boldsymbol{q}_i^{(S_1)} \\ \boldsymbol{q}_b^{(S_1)} \\ \boldsymbol{q}_i^{(S_2)} \\ \boldsymbol{q}_b^{(S_2)} \end{bmatrix} = \underbrace{\begin{bmatrix} \boldsymbol{I}_{ii}^{(S_1)} & \boldsymbol{0} & \boldsymbol{0} \\ \boldsymbol{0} & \boldsymbol{0} & \boldsymbol{I}_{\theta\theta}^{(S_1)} \\ \boldsymbol{0} & \boldsymbol{I}_{ii}^{(S_2)} & \boldsymbol{0} \\ \boldsymbol{0} & \boldsymbol{0} & \boldsymbol{I}_{\theta\theta}^{(S_2)} \end{bmatrix}}_{\boldsymbol{L}_{SL}} \begin{bmatrix} \boldsymbol{q}_i^{(S_1)} \\ \boldsymbol{q}_i^{(S_2)} \\ \boldsymbol{q}_\theta^C \end{bmatrix}, \tag{6.35}$$

where, $\boldsymbol{L}_{SL}$ is the localization matrix for SL-IR method.

6.4.2 Local level interface reduction

The idea of local level interface reduction is to reduce the boundary coordinates of each substructure independently before assembly of substructures. In the following, two significant interface reduction techniques are illustrated.

Exact compatibility

The interface reduction developed by Hong et al. [55] proposes performing an eigenvalue analysis on the interface's mass and stiffness matrices of the individual substructures before assembly. They then approximate the interface of each substructure as a superposition of a truncated number of interface modes. For the s^{th} substructure, it reads

$$\boldsymbol{u}_b^{(s)} \approx \boldsymbol{\Phi}_{b\theta_s}^{(s)} \boldsymbol{q}_{\theta_s}^{(s)}, \tag{6.36}$$

where, the j^{th} column of the matrix $\boldsymbol{\Phi}_{b\theta_s}^{(s)}$ is obtained from the following eigenvalue problem

$$(\hat{\boldsymbol{K}}_{bb}^{(s)} - \omega_{b,j}^2 \hat{\boldsymbol{M}}_{bb}^{(s)}) \boldsymbol{\varphi}_{b,j}^{(s)} = \boldsymbol{0}. \tag{6.37}$$

Note that the interface mass and stiffness matrices belong to the reduced substructures. A truncated number of interface modes, θ_s, for each substructure is kept. The IR mode matrices for the corresponding IR DOFs of substructures are cast into an *expanded* matrix of reduced boundary modes. For the two substructures of Fig. 6.3, the expanded matrix is given by

$$\boldsymbol{\Phi}^{exp} = \begin{bmatrix} \boldsymbol{\Phi}_{b\theta_1}^{(S_1)} & \boldsymbol{\Phi}_{b\theta_2}^{(S_2)} \end{bmatrix}, \tag{6.38}$$

where, $\boldsymbol{\Phi}^{exp}$ is the expanded matrix containing the IR modes of both substructures. Since the ingredients of the expanded matrix of reduced boundary nodes do not come from the same eigenvalue analysis, they are not orthogonal to each other, which can lead to ill conditioning in matrix operations. In order to make the columns of the expanded matrices linearly independent from one another, a singular value decomposition is performed on the expanded matrix:

$$\boldsymbol{U}^{exp} \boldsymbol{\Sigma}^{exp} (V^{exp})^T = \boldsymbol{\Phi}^{exp}, \tag{6.39}$$

where, $\boldsymbol{U}^{exp}$ and $\boldsymbol{V}^{exp}$ are the left and right singular vectors, respectively, and $\boldsymbol{\Sigma}^{exp}$ is the diagonal singular value matrix. The ratio of each singular value with respect to the largest one indicates how important the corresponding left singular vectors are. For instance, if the ratio of a singular value with respect to the largest one is very small, it means that the contribution of the corresponding left singular vector in the interface dynamics is tiny and this vector can be removed from the left singular matrix. Vice versa, if this ratio for a singular value is large, this implies that its corresponding singular vector has to be kept in the matrix to maintain good accuracy of the reduced model.

Hong et al. [55] defined a cutoff fraction, σ_{cut}, which is the ratio of the smallest kept singular value to the largest one. In other words, they kept all left singular vectors having a ratio of their corresponding singular values larger than σ_{cut}. They defined this value as $\sigma_{cutoff} = 1 \times 10^{-4}$, and removed the rest of the left singular vectors. However, it is observed that although this criterion preserves very good accuracy for the eigenfrequencies of the reduced model, it is not a fair one to compare it with other IR methods. This is because, with this criterion the number of kept left singular vectors usually significantly exceeds the number of the kept interface modes for each substructure in Eq. (6.36). In other words, for the same number of kept interface modes for different IR methods, the LL-EC can have more interface vectors, increasing the size of the reduced model. Therefore, in this work, another criterion is used, which states a fair condition to compare this method with others. For this method we keep the same number of left singular vectors corresponding to the largest singular values as the primary number of the desired kept interface modes.
In the next step, the matrices of kept left singular vectors from each interface group for individual substructures are collected in a matrix. For the s^{th} substructure, it gives

$$\boldsymbol{U}^{(s)} = BlockDiag(\boldsymbol{U}_1, \boldsymbol{U}_2, ..., \boldsymbol{U}_p), \tag{6.40}$$

where, $\boldsymbol{U}_1$, $\boldsymbol{U}_2$, ..., $\boldsymbol{U}_p$ are the matrices of left singular vectors for the 1^{th}, 2^{th}, ..., p^{th} interface group, respectively. Finally, the LL-EC reduction basis for the s^{th} substructure to be pre- and post-multiplied to its mass and stiffness matrices is given by

$$\boldsymbol{T}^{(s)}_{LL-EC} = \begin{bmatrix} \boldsymbol{I}^{(s)}_{ii} & \boldsymbol{0} \\ \boldsymbol{0} & \boldsymbol{U}^{(s)} \end{bmatrix}. \tag{6.41}$$

To identify the NSCs for a nonlinear structure with the LL-EC interface reduction method, the reduction basis becomes

$$\boldsymbol{T}^{(s)} = \boldsymbol{T}^{(s)}_{CMS}\, \boldsymbol{T}^{(s)}_{LL-EC}. \tag{6.42}$$

To the authors' knowledge, there is no work in the literature investigating nonlinear substructuring with LL-EC interface reduction. In this work, we have developed this method for nonlinear substructuring for both free- and fixed-interface modes.
The last step is the assembly of the substructures, which is performed with the localization matrix $\boldsymbol{L}$. Since, the number of generalized coordinates for common interfaces of substructures are the same, exact compatibility can be applied. For a structure composed of two substructures, this gives

$$\begin{bmatrix} \boldsymbol{q}^{(S_1)}_i \\ \boldsymbol{q}^{(S_1)}_\theta \\ \boldsymbol{q}^{(S_2)}_i \\ \boldsymbol{q}^{(S_2)}_\theta \end{bmatrix} = \underbrace{\begin{bmatrix} \boldsymbol{I}^{(S_1)}_{ii} & \boldsymbol{0} & \boldsymbol{0} \\ \boldsymbol{0} & \boldsymbol{0} & \boldsymbol{I}^{(S_1)}_{\theta\theta} \\ \boldsymbol{0} & \boldsymbol{I}^{(S_2)}_{ii} & \boldsymbol{0} \\ \boldsymbol{0} & \boldsymbol{0} & \boldsymbol{I}^{(S_2)}_{\theta\theta} \end{bmatrix}}_{\boldsymbol{L}_{LL-EC}} \begin{bmatrix} \boldsymbol{q}^{(S_1)}_i \\ \boldsymbol{q}^{(S_2)}_i \\ \boldsymbol{q}^{C}_\theta \end{bmatrix}, \tag{6.43}$$

where, $\boldsymbol{L}_{LL-EC}$ is the global localization matrix for the assembly with LL-EC. Once the global localization matrix is obtained, the assembled system can be achieved by pre- and post-multiplying the block-diagonalized mass and stiffness matrices with the localization matrix.

Weak compatibility

The concept of weak interface compatibility [2, 131] holds for the case where the connecting interface DOFs are allowed to have slight relative movements after assembly, in contrast to the exact compatibility where the matching DOFs are forced to have exactly the same displacements. In other words, the WC allows a small non-matching (or a violation of compatibility) on the interfaces. The WC is beneficial when very few modes for each substructure are kept, leading to a locking problem for interfaces if exact compatibility is enforced. The LL-WC for interface reduction of the HCB method is suggested by Kuether et al. [82] and further developed by Krattiger et al. [80] and is briefly explained next.
Like the LL-EC method, the boundary coordinates of individual DOFs are reduced before coupling, using the MD method (Eq. (6.36)). However, the interface modes are not cast into an expanded matrix to compute the SVD vectors, as done in the LL-EC method; rather, the reduction basis for each substructure is formed using its individual reduced interface modes as

$$\boldsymbol{T}_{SL}^{(s)} = \begin{bmatrix} \boldsymbol{I}_{ii}^{(s)} & \boldsymbol{0} \\ \boldsymbol{0} & \boldsymbol{\Phi}_{b\theta}^{(s)} \end{bmatrix}. \tag{6.44}$$

The mass and stiffness of all substructures are then pre- and post-multiplied with the corresponding interface reduction bases to build up the reduced model of all components before assembly. To develop the NLROM for nonlinear substructures, the transformation matrix is defined as

$$\boldsymbol{T}^{(s)} = \boldsymbol{T}_{CMS}^{(s)}\, \boldsymbol{T}_{LL-WC}^{(s)}. \tag{6.45}$$

Finally, the reduced order substructures have to be coupled. In general, the numbers of kept interface modes of the same interface for different substructures are different. Therefore, traditional localization matrix like Eq. (6.43) by enforcement of an exact compatibility is not possible. As a result, weak interface compatibility is imposed as follows. The compatibility equation for the physical displacement of boundary DOFs is written as

$$\boldsymbol{B}_b \boldsymbol{u}_b^U \approx \boldsymbol{0}, \tag{6.46}$$

where, $\boldsymbol{B}_b$ is the part of global Boolean matrix corresponding to the boundary DOFs and $\boldsymbol{u}_b^U$ is the vector of uncoupled boundary DOFs. The interface displacement of each substructure is substituted by Eq. (6.36), leading to the compatibility condition for the interface DOFs in modal coordinate,

$$\boldsymbol{B}_m \boldsymbol{q}_b \approx \boldsymbol{0}, \tag{6.47}$$

where, the subscript m represents the $\boldsymbol{B}_m$ matrix in modal domain. For a system with two substructures, this gives

$$\begin{bmatrix} \boldsymbol{\Phi}_{b\theta_{S_1}}^{(S_1)} & -\boldsymbol{\Phi}_{b\theta_{S_2}}^{(S_2)} \end{bmatrix} \begin{bmatrix} \boldsymbol{q}_b^{(S_1)} \\ \boldsymbol{q}_b^{(S_2)} \end{bmatrix} \approx \boldsymbol{0}. \tag{6.48}$$

A localization matrix $\boldsymbol{L}_m$ for the interface matrix is required that spans the null space of $\boldsymbol{B}_m$. Since this is not generally achievable in the LL-WC method, the null space is approximated by applying an SVD to $\boldsymbol{B}_m$, namely

$$\boldsymbol{U}^B \boldsymbol{\Sigma}^B (\boldsymbol{V}^B)^T = \boldsymbol{B}_m. \tag{6.49}$$

Krattiger et al. [80] introduced a null space matrix $\boldsymbol{V}$ by collecting those right singular vectors from $\boldsymbol{V}^B$, which correspond to the singular values smaller than a cutoff ratio σ, with respect to the largest singular value. However, in this work, we keep the same number of right singular vectors (corresponding to the smallest singular values) as the number of desired interface modes taken for each substructure. This facilitates a fair comparison of different methods with the same number of kept interface modes. After choosing the null space matrix $\boldsymbol{V}$, it will be positioned in the global localization matrix corresponding to the boundary DOFs of the substructures. For the case of two substructures, the global localization matrix $\boldsymbol{L}_{LL-WC}$ for the LL-WC method is then given by

$$\begin{bmatrix} \boldsymbol{q}_i^{(S_1)} \\ \boldsymbol{q}_b^{(S_1)} \\ \boldsymbol{q}_i^{(S_2)} \\ \boldsymbol{q}_b^{(S_2)} \end{bmatrix} = \underbrace{\begin{bmatrix} \boldsymbol{I}_{ii}^{(S_1)} & \boldsymbol{0} & \boldsymbol{0} \\ \boldsymbol{0} & \boldsymbol{0} & \boldsymbol{V}_1 \\ \boldsymbol{0} & \boldsymbol{I}_{ii}^{(S_2)} & \boldsymbol{0} \\ \boldsymbol{0} & \boldsymbol{0} & \boldsymbol{V}_2 \end{bmatrix}}_{\boldsymbol{L}_{LL-WC}} \begin{bmatrix} \boldsymbol{q}_i^{(S_1)} \\ \boldsymbol{q}_i^{(S_2)} \\ \boldsymbol{q}_b^{C} \end{bmatrix}, \tag{6.50}$$

where, $\boldsymbol{V}_1$ and $\boldsymbol{V}_2$ are the component (lines) of the matrix $\boldsymbol{V}$, corresponding to the interfaces of substructures S_1 and S_2. Krattiger et al. [80] also discussed the *uncoupled weak compatibility* (UWC) method by applying the SVD to each group of interfaces, separately. They showed that the accuracy of LL-UWC is the same as LL-WC. Therefore, this method is not applied here for nonlinear dynamic substructuring.

6.5 Primal assembly of linear substructures

After reducing the matrices of each substructure using its individual reduction basis, all substructures are cast into a block diagonal form as

$$\boldsymbol{M}^U \ddot{\boldsymbol{q}}^U + \boldsymbol{K}^U \boldsymbol{q}^U = \boldsymbol{f}^U + \boldsymbol{g}^U \tag{6.51}$$

where the superscript U denotes the uncoupled matrices and vectors. For instance, the uncoupled mass matrix reads

$$\boldsymbol{M}^U = \begin{bmatrix} \hat{\boldsymbol{M}}^{(S_1)} & \boldsymbol{0} & \cdots & \boldsymbol{0} \\ \boldsymbol{0} & \hat{\boldsymbol{M}}^{(S_2)} & \ddots & \boldsymbol{0} \\ \vdots & \ddots & \ddots & \vdots \\ \boldsymbol{0} & \boldsymbol{0} & \cdots & \hat{\boldsymbol{M}}^{(S_n)} \end{bmatrix} \tag{6.52}$$

where $\hat{\boldsymbol{M}}^{(S_1)}$, $\hat{\boldsymbol{M}}^{(S_2)}$, …, $\hat{\boldsymbol{M}}^{(S_1)}$ are the reduced mass matrices for substructures S_1, S_2, …, S_n, respectively. All other uncoupled matrices and tensors are similarly arranged in their corresponding uncoupled matrices, which are not written here for the sake

of brevity. Furthermore, the vector $\boldsymbol{q}^U$, $\ddot{\boldsymbol{q}}^U$, $\boldsymbol{f}^U$ and $\boldsymbol{g}^U$ are the uncoupled vectors, which are obtained by casting their corresponding vectors of all substructures into a successive form. The uncoupled set of displacements is written below as an example:

$$\boldsymbol{q}^U = \begin{bmatrix} \boldsymbol{q}^{(s_1)} \\ \vdots \\ \boldsymbol{q}^{(s_n)} \end{bmatrix} \tag{6.53}$$

For the coupling of substructures, two conditions have to be satisfied at their interface DOFs: force equilibrium and displacement compatibility. The compatibility condition states that all connection DOFs at the boundary of substructures must be the same. This condition can be written as

$$\boldsymbol{B}\boldsymbol{q}^U = 0 \tag{6.54}$$

where $\boldsymbol{B}$ is a signed Boolean matrix comprising zeros for the internal DOFs of all substructures, and ones (or minus ones) for the boundary DOFs connecting all the DOFs of substructures that have to be joined together. The next boundary condition is the force equilibrium, which means that the reaction forces at the connecting DOFs of substructures must cancel out each other, namely,

$$\boldsymbol{L}^T\boldsymbol{g}^U = \boldsymbol{0} \tag{6.55}$$

Depending on which of the mentioned conditions is enforced a priori, the assembly can be performed in a *Primal* or *Dual* manner. When the compatibility boundary condition is satisfied first to obtain a unique set of interface DOFs, the assembly is called primal, which is also the classical FE assembly method. Conversely, dual assembly denotes the case in which the force equilibrium is enforced a priori, leading to a dual number of all interface DOFs in the global matrices to be solved simultaneously with the compatibility condition. In this work, we have considered primal assembly, because it facilitates the building of individual reduction basis sets per each substructure. Thorough studies of different assemblies are done in [25, 78].
For the primal assembly, the set of coupled DOFs, $\boldsymbol{q}^C$, which comprises a unique set of interface DOFs, is defined such that

$$\boldsymbol{q}^U = \boldsymbol{L}\boldsymbol{q}^C \tag{6.56}$$

Eq. (6.56) is then introduced to the compatibility Eq. (6.54), giving

$$\boldsymbol{B}\boldsymbol{L}\boldsymbol{q}_c = 0 \tag{6.57}$$

This means that in order to satisfy the "exact" compatibility condition, the localization matrix $\boldsymbol{L}$ must span the null space of $\boldsymbol{B}$:

$$\boldsymbol{L} = null(\boldsymbol{B}) \quad and \quad \boldsymbol{B}^T = null(\boldsymbol{L}^T) \tag{6.58}$$

Finally, to assemble all the reduced substructures, the Eq. (6.56) is introduced to (6.51) and is pre-multiplied with $\boldsymbol{L}^T$ to vanish the interface forces. This gives

$$\boldsymbol{L}^T\boldsymbol{M}^U\boldsymbol{L}\ddot{\boldsymbol{q}}^C + \boldsymbol{L}^T\boldsymbol{K}^{(1)^U}\boldsymbol{L}\boldsymbol{q}^C = \boldsymbol{L}^T\boldsymbol{f}^U, \tag{6.59}$$

Which is the EOM for the assembled system. In the next section the accuracy of the mentioned methods are evaluated on two numerical examples.

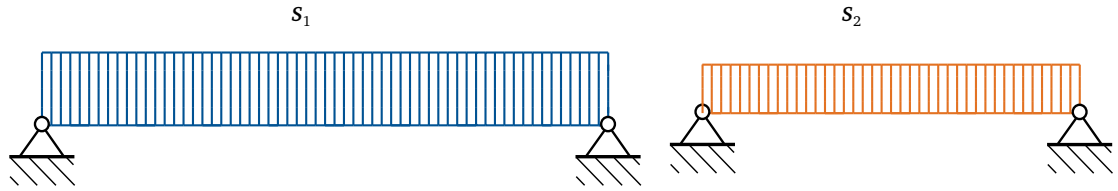

(a) Two substructures, S_1 and S_2 are coupled at their rotational DOFs

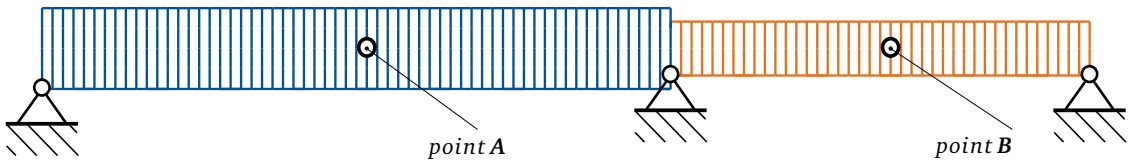

(b) Assembled beam

Figure 6.1: Schematic of the investigated beam FE model and it substructures. Note that the vertical and horizontal scales are not the same. Parameters of the example are given in table 6.1.

6.6 Numerical example

6.6.1 Simply supported beams

In the first example we study the assembly of two simply supported beam models as shown in Fig. 6.1a. The substructures S_1 and S_2 are coupled at their rotational DOF, as depicted in Fig. 6.1a. The material, mesh and size properties of the substructures are illustrated in Table 6.1. To get insight into the utilized linear modes, the first five fixed and free-interface eigenfrequencies of the beam's substructures as well as the eigenfrequencies of the full model are shown in Table 6.2.

	Property(dimension)	**Substructure 1**	**Substructure 2**
Material	Mass density (kg/m^3)	7870	7870
	Young's modulus (GPa)	205	205
	Poisson's ratio	0.28	0.28
Geometry	length (mm)	300	200
	thickness (mm)	1.5	1
FE model	Element-type	Timoshenko Abaqus B21	Timoshenko Abaqus B21
	Number of Elements	60	40
	Number of DOFs	179	119
	Number of interface DOFs	1	1

Table 6.1: Geometry, material and FE model properties of the investigated beam model

	Beam's substructure S_1		Beam's substructure S_2		Coupled beam
Mode number	Free-interface	Fixed-interface	Free-interface	Fixed-interface	
1	38.6 Hz	60.3 Hz	57.9 Hz	90.4 Hz	41.3 Hz
2	154.3 Hz	195.3 Hz	231.5 Hz	293.0 Hz	84.1 Hz
3	347.1 Hz	407.4 Hz	520.8 Hz	611.3 Hz	163.2 Hz
4	617.0 Hz	696.5 Hz	926.0 Hz	1045.6 Hz	275.0 Hz
5	964.0 Hz	1062.7 Hz	1447.2 Hz	1595.9 Hz	365.9 Hz

Table 6.2: Eigenfrequencies of the free- and fixed-interface modes for the beam model.

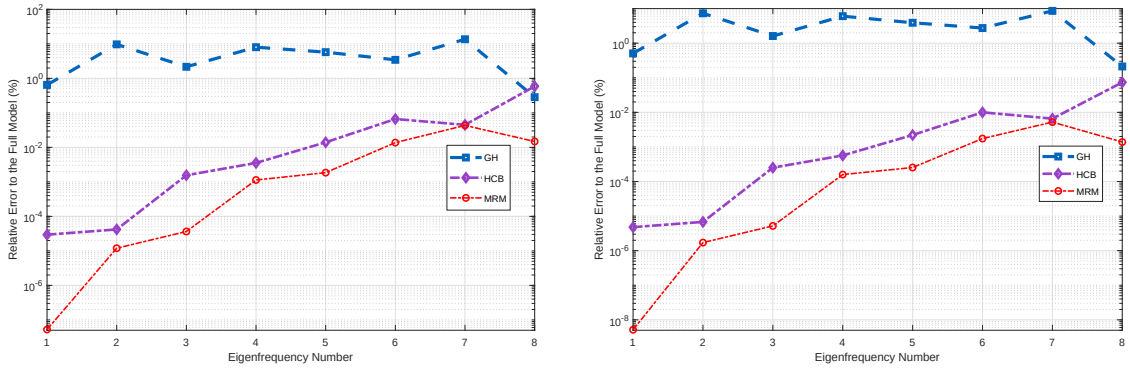

(a) Free-interface modes until 1000 Hz

(b) Free-interface modes until 2000 Hz

Figure 6.2: Beam model's relative error (in percentage) comparison of the eigenfrequencies for the GH, HCB and MRM methods. The same number of modes for free- or fixed-interface modes for each model is used

Linear substructuring results

To develop the NLROM of substructures, first, linear CMS techniques outlined in this chapter are applied to the beam model of Fig. 6.1 to get insight into the development of the NLROMs. Two CMS models are developed for each method with kept free-interface modes of up to 1000 Hz and 2000 Hz, respectively. The same number of modes as free-interface modes are kept for fixed-interface modes in the HCB method. Fig. 6.2 depicts the relative error of eigenfrequencies for three linear CMS methods: GH, MRM, and HCB. The relative error, ε for each eigenfrequency is obtained by

$$\varepsilon_j = \frac{\left|\omega_{full,j} - \omega_{CMS,j}\right|}{\omega_{full,j}} \times 100, \tag{6.60}$$

where, $\omega_{full,j}$ and $\omega_{CMS,j}$ are the j^{th} eigenfrequencies of the full-order and CMS models, respectively. When only the free-interface modes of the system are used in the reduction basis (GH method), the accuracy of the estimated linear frequencies is far inferior to the HCB method. This is due to the fact that the GH method is a statically incomplete method that does not consider the static effect of truncated modes due to the interface forces. However, when the free-interface modes are augmented with the RFA modes (shown as MRM), the eigenfrequency error decreases significantly, such that the overall accuracy of its eigenfrequencies become the same or better than the HCB method. The improved accuracy stays the same when the number of kept modes has been increased to 2000 Hz in Fig 6.2b, confirming the stability of the MRM

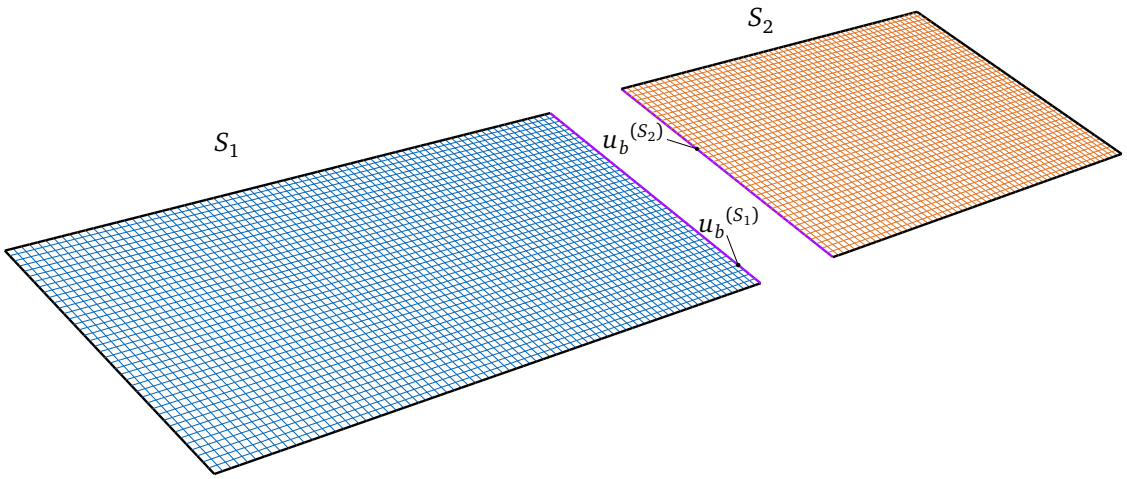

(a) Two substructures S_1 and S_2

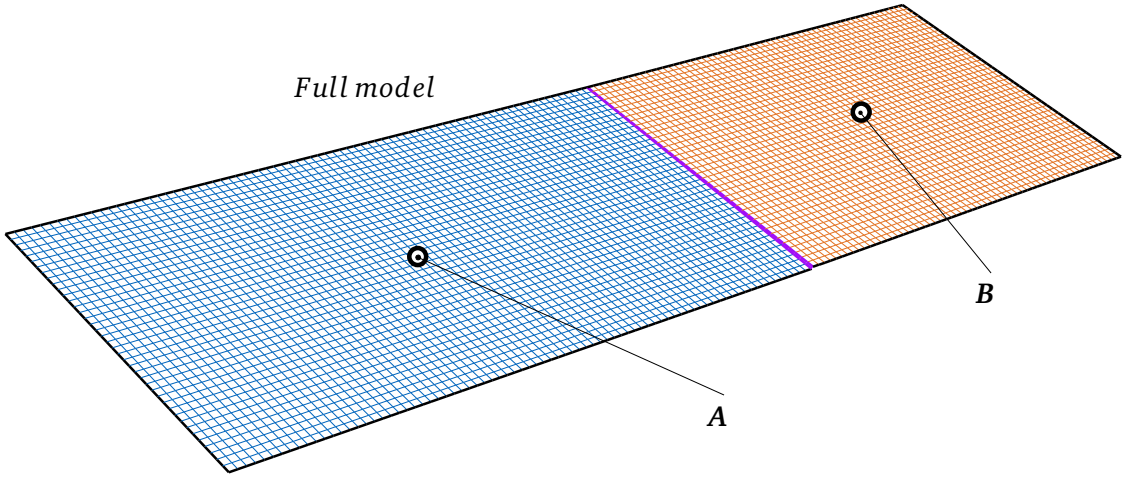

(b) Assembled plate

Figure 6.3: Schematic of the Panel FE model with two substructures and meshed with nonlinear shell element.

method.

6.6.2 Coupling of two panel models

The second example in this work considers a larger FE model with 33485 DOFs in total. The example contains two panels with 3-dimensional shell elements, as shown in Fig. 6.3a, which are assembled in the form depicted in Fig. 6.3b. Both substructures in Fig. 6.3a are simply-supported at all edges (including the interfaces), similar to the example studied in [82]. They are then assembled by all rotational DOFs (three DOFs per node) at the joint nodes, as shown in Fig. 6.3b. The material, geometry and FE properties of the substructures are demonstrated in Table 6.3. The first nine eigenfrequencies corresponding to the fixed- and free-interface modes as well as the eigenfrequencies of the full model are shown in Table 6.4, to have an insight into them.

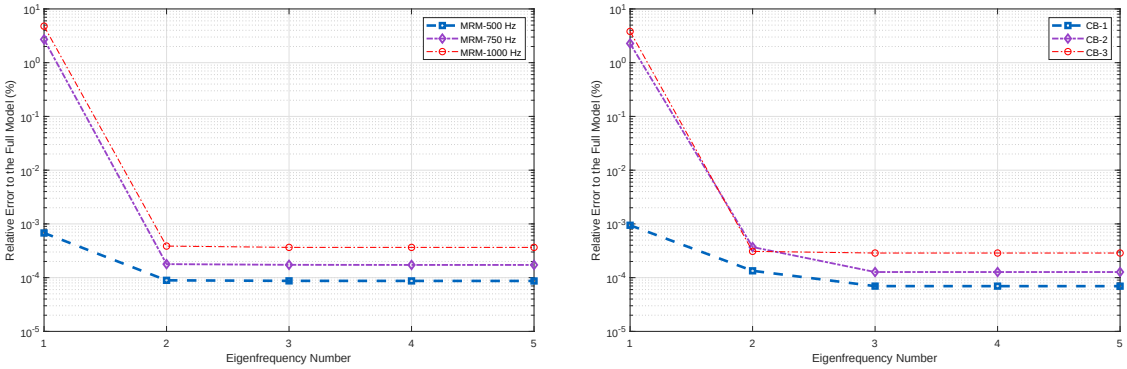

(a) Convergence check analysis for MRM method

(b) Convergence check analysis for HCB method

Figure 6.4: Convergence check analysis for the maximum error induced by IR versus the number of kept SL-IR modes for plate model. For the MRM method, three models are studied: kept free-interface modes of substructures until 500 Hz, 750 Hz and 1000 Hz. The same number of fixed-interface modes is kept for the HCB method.

Linear substructuring results

For this example, the augmented free-interface mode method is combined with three interface reduction techniques explained in section (6.4), namely, SL, LL-EC and LL-WC. The linear eigenfrequency results are compared to the corresponding ones of the HCB method and also the GH method. In order to figure out how many interface DOFs are required to be kept in the SL-IR method, a convergence study is performed for three MRM-reduced systems with kept free-interface modes of the substructures up to 500 Hz (3 for S_1 and 2 for S_2), 750 Hz (7 for S_1 and 5 for S_2) and 1000 Hz (9 for S_1 and 7 for S_2). The same procedure is also performed for the HCB method with SL-IR using the same number of modes as the MRM method. In the linear convergence check study, the maximum relative error of the reduced system with SL-IR to the

	Property(dimension)	S_1	S_2
Material	Mass density (kg/m^3)	7870	7870
	Young's modulus (GPa)	205	205
	Poisson's ratio	0.28	0.28
Geometry	length (mm)	400	300
	width (mm)	200	200
	thickness (mm)	2	2
FE model	Element-type	shell (4-node) Abaqus S4R	shell (4-node) Abaqus S4R
	Number of Elements	3200	2400
	Number of DOFs	19204	14404
	Number of interface DOFs	123	123

Table 6.3: Geometry, material and FE model Properties of the investigated panel model

	Panel's substructure S_1		Panel's substructure S_2		Coupled panel
Mode number	Free-interface	Fixed-interface	Free-interface	Fixed-interface	
1	149.8 Hz	157.0 Hz	173.7 Hz	189.98 Hz	152.7 Hz
2	239.3 Hz	261.1 Hz	333.4 Hz	378.1 Hz	182.0 Hz
3	390.3 Hz	427.8 Hz	535.6 Hz	544.2 Hz	250.0 Hz
4	511.1 Hz	514.6 Hz	601.7 Hz	675.6 Hz	350.6 Hz
5	599.0 Hz	613.3 Hz	694.2 Hz	724.1 Hz	415.1 Hz
6	600.7 Hz	654.9 Hz	961.0 Hz	1018.6 Hz	512.7 Hz
7	749.7 Hz	776.1 Hz	976.7 Hz	1079.6 Hz	540.0 Hz
8	868.8 Hz	941.4 Hz	1137.2 Hz	1143.1 Hz	600.6 Hz
9	957.2 Hz	999.7 Hz	1294.0 Hz	1315.4 Hz	606.7 Hz

Table 6.4: Eigenfrequencies of the free- and fixed-interface modes for the panel model.

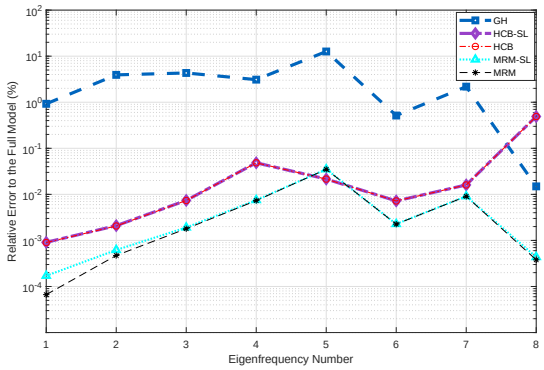

(a) HCB and MRM methods with and without SL-IR compared with GH method.

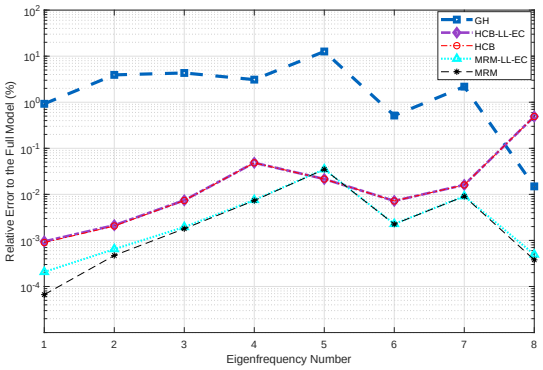

(b) HCB and MRM methods with and without LL-EC IR compared with GH method.

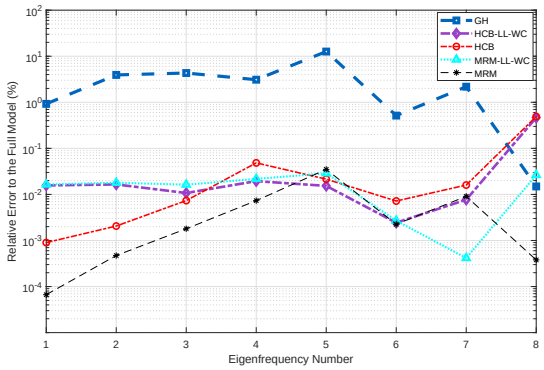

(c) HCB and MRM methods with and without LL-WC IR compared with GH method.

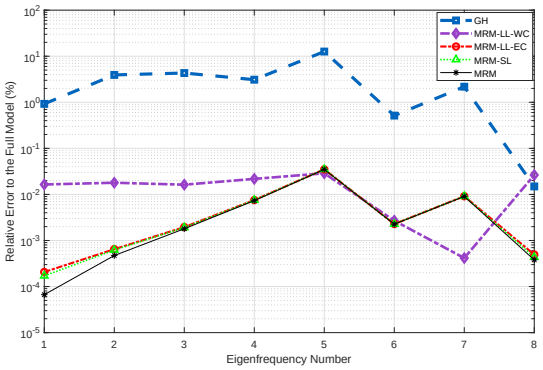

(d) MRM method with and without SL, LL-EC and LL-WC compared with GH method

Figure 6.5: Plate's relative error comparison (in percentage) of the eigenfrequencies for different methods. For each substructure, the free-interface modes up to 750 Hz are kept in the NLROM. The same number of modes for free- and fixed-interface modes as well as the interface modes are used for each method.

original CMS is obtained as

$$\varepsilon = \max\left(\frac{\left|\omega_{CMS,1} - \omega_{CMS-IR,1}\right|}{\omega_{CMS,1}}, \frac{\left|\omega_{CMS,2} - \omega_{CMS-IR,2}\right|}{\omega_{CMS,2}}, \ldots, \frac{\left|\omega_{CMS,m} - \omega_{CMS-IR,m}\right|}{\omega_{CMS,m}}\right) \times 100,$$

(6.61)

where $\omega_{CMS,j}$ is the j^{th} eigenfrequency attained either by the HCB or MRM methods, and $\omega_{CMS-IR,j}$ is its corresponding eigenfrequency with SL-IR. Fig. 6.4a and 6.4b show the maximum relative error for the MRM and HCB methods versus the number of kept interface DOFs. For all three ranges of kept interface modes, after taking only 2 interface modes for the MRM method, the maximum error reaches its plateau and does not decrease anymore. However, the number of IR modes to reach its plateau for the HCB is 3 for all three HCB models.
In the next step, the three IR techniques are applied to HCB and MRM and compared with each other and also with the GH method, which is shown in Fig. 6.5. The kept free-interface modes for substructures are up to 750 Hz with two retained interface modes (according to Fig. 6.4a), and the same number of modes are kept for HCB. Fig. 6.5a illustrates the relative error of linear eigenfrequencies for HCB and MRM, both with and without SL-IR and compared with the GH method. In both HCB and MRM methods, applying SL-IR does not deteriorate their accuracy significantly. While the error of the free-interface method of GH is distinctly inferior to the HCB method, the augmented free-interface method of MRM has overall the same accuracy as HCB or better. Fig. 6.5b exhibits the relative error comparison when the employed IR technique is LL-EC. Likewise, IR does not significantly increase the error of HCB and MRM, but they are both more accurate than GH. Fig. 6.5c demonstrates similar results for the substructuring with the LL-WC interface reduction. This result indicates that applying the LL-WC interface reduction to both methods can noticeably increase the relative error of the CMS methods without IR, for lower frequencies. However, the benefit of the LL-WC is that it can be used for incompatible interfaces between substructures. Nevertheless, the error of high frequencies remains almost in the same order as the original methods. Finally, the comparison of all IR methods applied to MRM with GH is shown in Fig. 6.5d. It can be concluded from this figure that, despite the relatively large error produced by the LL-WC method for lower frequencies, appending only two interface generalized coordinates (regardless of the IR method) to the original GH's DOFs can significantly increase the accuracy of the linear free-interface mode CMS.

6.7 Summary

In this chapter we review the common linear component synthesis methods in primal assembly, namely, fixed-interface mode and free-interface methods. To be able to generate a compact ROM, we furthermore investigate interface reduction techniques, which have have been mostly developed for fixed-interface CMS. Interface reduction is crucial in case of substructures with numerous DOFs at their interfaces to develop a linear and nonlinear compact ROM. We extend the application of local-level interface reduction methods to free-interface CMS. We finally apply the introduced free- and fixed-interface methods to two linear numerical examples with beam and plate elements and compare the results. We show that the augmented free-interface CMS has better accuracy than other methods for the considered examples.

Chapter 7

Non-intrusive nonlinear substructuring based on ICE

This chapter is extracted from the author's publication in [65]. In this article, Karamooz had the idea of the work and performed the literature review. Karamooz implemented a considerable part of the work and wrote the manuscript. Xu conducted the primary part of numerical studies and discussed the work. Bartl, Tiso and Rixen gave very useful inputs in the discussions of the work and proof-read the article. Rixen supervised the work.

7.1 Introduction

This work proposes a free-interface non-intrusive-based dynamic substructuring of geometrically nonlinear FE models using residual flexibilities. As explained before, Keuther et al. developed the first non-intrusive-based nonlinear substructuring method by using ICE for NSCs identification of substructures' NLROMs. As reduction basis to reduce linear matrices as well as identify NSCs of substructures, they proposed using two different bases: free-interface modes (GH basis) and HCB reduction basis. Here, instead of taking only the free-interface modes used in the work of Keuther et al. in [84], we propose the use of the MacNeal/Rubin-Martinez reduction basis to also approximate the effect of the truncated modes for each substructure. This basis is used to reduce the linear mass and stiffness matrices of each substructure. Besides, its columns are taken as the basis to build up the static forces in the nonlinear identification procedure of ICE. As a second novel point, three different interface reduction techniques namely, SL, LL-EC, and LL-WC, are applied to nonlinear substructuring based on residual flexibilities. The proposed methods are applied to two different structures with geometric nonlinear effects. Finally, the results are compared to the nonlinear GH and HCB substructuring methods in [82, 84] with and without interface reduction. We show that the nonlinear dynamic response of the proposed method in this work is improved significantly when compared to the nonlinear GH method, and marginally better than the nonlinear HCB method for relatively high excitation levels.

7.2 Generalized Applied Force for MOR at substructure level

The non-intrusive Applied Force or ICE method [95] proposes the selection of a set of representative static forces to prescribe onto the full-order FE model and solve for

the corresponding displacements. These forces and displacements are then used to identify the NSCs. Consider a substructure with geometrical nonlinear effects that consists of n DOFs.
Let us start with Eq. (2.27) and rewrite the i^{th} Eq. for the NLROM of the substructure (s) in the static form as

$$\hat{K}_{ij}^{(1)^{(s)}} q_j^{(s)} + \hat{K}_{ijl}^{(2)^{(s)}} q_j^{(s)} q_l^{(s)} + \hat{K}_{ijlp}^{(3)^{(s)}} q_j^{(s)} q_l^{(s)} q_p^{(s)} = \hat{f}_i^{(s)} + g_i^{(s)}, \tag{7.1}$$

where, $\boldsymbol{g}^{(s)}$ is the connecting force vector with the neighboring substructures. In the remainder of this chapter, the superscript (s) is omitted for the sake of brevity, unless it is otherwise indicated. The first crucial point in the identification procedure of all nonlinear model reduction techniques is to select a reduction basis that activates and conveys the essential nonlinear effects, e.g. the nonlinear interaction between linear modes and accurately represents the full-model in the desired frequency and intensity range of external loads.
Consider the reduction basis matrix, $\boldsymbol{T}$, possesses the demanded properties for nonlinear MOR problem. Each required static load for the ICE procedure is then constructed as a summation of combinations of the columns of this basis, multiplied by their corresponding weightings (or generalized coordinates)

$$\boldsymbol{f} = \boldsymbol{K}(\boldsymbol{T}_1 q_1 + \boldsymbol{T}_2 q_2 + ... + \boldsymbol{T}_m q_m) = \boldsymbol{K}(\sum_{k=1}^{m} \boldsymbol{T}_k q_k), \tag{7.2}$$

where, q_k is the generalized or modal coordinate corresponding to the k^{th} column of the reduction basis. McEwan et al. [95] proposed using the truncated number of linear VMs as the reduction basis, in case a structure is to be reduced monotonically. However, it is shown by Keuther et al. [84, 85] that in nonlinear substructuring, the linear eigenmodes (free-interface modes) of the substructures do not suffice to develop the NLROM of each substructure accurately. Therefore, in this work, we propose a basis for non-intrusive-based dynamic substructuring that improves the free-interface method. The basis selection methods (as well as the proposed basis) are discussed in Chapter 6.

Once the reduction basis is determined, the magnitude of generalized coordinates must be adapted. These values have to be kept in a certain range where the desired level of nonlinearity in the system response is activated, and the nonlinear static analysis can still converge. Gordon and Hollcamp [46] selected each generalized coordinate for a monolithic ROM as a value that creates the required force to attain a maximum desired linear displacement, which is also physically meaningful. This can be written in a generalized form for substructure-based ROM as

$$q_i = \frac{W_{i,\max}}{T_{q_i,\max}}, \tag{7.3}$$

where, $W_{i,\max}$ is the maximum desired displacement for the i^{th} column of the reduction basis, $\boldsymbol{T}$. The maximum translational component of the i^{th} column of the reduction basis is denoted by $T_{q_i,\max}$. The maximum desired displacement is usually chosen in the order of geometry parameters (e.g. the thickness of the structure). For

a system with only geometric nonlinear effect, a polynomial with maximum cubic terms appears in the EOM, as explained in Chapter 2. Therefore, it is sufficient to generate the static forces as a combination of one, two, or three columns of the reduction basis with both positive and negative signs of the generalized coordinates for a geometric nonlinear structure

$$\boldsymbol{f} = \boldsymbol{K}(\boldsymbol{T}_i q_i + \boldsymbol{T}_j \boldsymbol{q}_j + \boldsymbol{T}_k q_k) \quad i,j,k = 0,1,2,...,m, \tag{7.4}$$

Each static force is imposed on the FE model to solve for the corresponding nonlinear displacement induced by it, and both are transformed to the generalized coordinate. For the r^{th} load case, the transformation is

$$\hat{\boldsymbol{f}}_r = \boldsymbol{T}^T \boldsymbol{f}_r \tag{7.5}$$

and the corresponding displacement transformation reads

$$\boldsymbol{q}_r = \boldsymbol{T}^+ \boldsymbol{u}_r \tag{7.6}$$

Here, the sign (+) expresses the pseudo-inverse of the matrix. By performing this procedure for all p load cases and substituting them in Eq. (7.1), a set of p linear algebraic equations is achieved that exceeds the number of unknown quadratic and cubic stiffness coefficients. The matrix form of these equations writes

$$\boldsymbol{K}_{nl}\boldsymbol{G}_{nl} = \boldsymbol{F}_{nl} \tag{7.7}$$

where $\boldsymbol{K}_{nl}$ is a matrix comprising all unknown coefficients; $\boldsymbol{G}_{nl}$ is the known parameters multiplied by the unknowns; and $\boldsymbol{F}_{nl}$ is the matrix of all known terms, including the linear modal stiffness and modal static loads. The columns of $\boldsymbol{G}_{nl}$ and $\boldsymbol{F}_{nl}$ represent the results of each load case. The contents of the matrices in Eq. (7.7) are presented in Appendix A for an NLROM with two DOFs. Finally, the unknown coefficients in Eq. (7.7) can be determined using a regression analysis (e.g. least squares [95]). As it was mentioned, the main advantage of the ICE method (as well as other non-intrusive nonlinear model reduction methods) is that the NLROM for each substructure is developed without requiring one to treat the full-order FE model in closed form, i.e., it can be combined with commercial FE packages.
The NLROM's EOM for the s^{th} substructure can be written in the matrix form as

$$\hat{\boldsymbol{M}}^{(s)}\ddot{\boldsymbol{q}}^{(s)} + \hat{\boldsymbol{D}}^{(s)}\dot{\boldsymbol{q}}^{(s)} + \hat{\boldsymbol{K}}^{(1)^{(s)}}\boldsymbol{q}^{(s)} + \underbrace{(\hat{\boldsymbol{K}}^{(2)^{(s)}}.\boldsymbol{q}^{(s)})}_{Q_1^{(s)}(q)}\boldsymbol{q}^{(s)} + \underbrace{[(\hat{\boldsymbol{K}}^{(3)^{(s)}}.\boldsymbol{q}^{(s)}).\boldsymbol{q}^{(s)}]}_{Q_2^{(s)}(q)}\boldsymbol{q}^{(s)} = \hat{\boldsymbol{f}}^{(s)} + \hat{\boldsymbol{g}}^{(s)} \tag{7.8}$$

Here the tensors $\boldsymbol{Q}_2^{(s)}$ and $\boldsymbol{Q}_2^{(s)}$ are functions of generalized coordinates and correspond to the quadratic and cubic stiffness tensors, which will be used later for coupling of the substructures.

Expansion for Membrane DOFs

The expansion method for substructures is similar to the monolithic ROM, namely, the membrane motion is defined as a transformation matrix multiplied with the membrane modal coordinates

$$\boldsymbol{u}_m = \boldsymbol{T}_m \boldsymbol{\theta} \tag{7.9}$$

where, $\boldsymbol{T}_m$ is the membrane transformation matrix and $\boldsymbol{\theta}$ denotes the vector of generalized coordinates representing the in-plane motion. The improved displacement of each substructure can be then given by

$$\boldsymbol{u}_{total} = \boldsymbol{T}\boldsymbol{q} + \boldsymbol{T}_m\boldsymbol{\theta} \tag{7.10}$$

After applying p static load cases to the FE package, their corresponding displacements and generalized coordinates are cast into the matrix form as

$$\boldsymbol{U}_{total} = \boldsymbol{T}\boldsymbol{Q} + \boldsymbol{T}_m\boldsymbol{\Theta} \tag{7.11}$$

where $\boldsymbol{U}_{total}$, $\boldsymbol{Q}$ and $\boldsymbol{\Theta}$ denote the matrices of full-static solutions, generalized transverse and generalized membrane coordinates, respectively, and each of their columns serve as the values for individual static load cases. The vector of membrane coordinates is now defined as in [104]:

$$\theta = \begin{bmatrix} q_1^2 & q_1q_2 & q_1q_3 & \cdots & q_1q_n & q_2^2 & q_2q_3 & \cdots & q_{n-1}^2 & q_{n-1}q_n & q_n^2 \end{bmatrix}^T. \tag{7.12}$$

Finally, the only unknown in Eq. (7.11) is the membrane transformation matrix, which can be obtained by

$$\boldsymbol{T}_m \approx (\boldsymbol{U}_{total} - \boldsymbol{T}\boldsymbol{Q})\boldsymbol{\Theta}^{+}. \tag{7.13}$$

The membrane motion for each time step can now be computed from Eq. (7.11). As can be seen from Eq. (7.12), the expansion procedure is valid as long as the relation between the transverse and membrane coordinates in a structure is quadratic (e.g., for flat or shallow curved structures).

7.3 Nonlinear modal substructuring: primal assembly

The final step in the nonlinear substructuring approach is to assemble the reduced order model of substructures. To perform the assembly of components, first, all the matrices and tensors of substructures are written in a block diagonal form,

$$\boldsymbol{M}^U\ddot{\boldsymbol{q}}^U + \boldsymbol{D}^U\dot{\boldsymbol{q}}^U + \boldsymbol{K}^{(1)^U}\boldsymbol{q}^U + \boldsymbol{Q}_1^U(\boldsymbol{q}^U)\boldsymbol{q}^U + \boldsymbol{Q}_2^U(\boldsymbol{q}^U)\boldsymbol{q}^U = \boldsymbol{f}^U + \boldsymbol{g}^U, \tag{7.14}$$

where the superscript U denotes that the matrices and tensors are still uncoupled. The matrices $\boldsymbol{M}^U$, $\boldsymbol{D}^U$ and $\boldsymbol{K}^{(1)^U}$ are the concatenated mass, damping and stiffness matrices of all substructures in a block diagonal form. Likewise, the tensors $\boldsymbol{Q}_1^U(\boldsymbol{q}^U)$ and $\boldsymbol{Q}_2^U(\boldsymbol{q}^U)$ (see definitions in (7.8)) are the block diagonal concatenated form of their corresponding pairs for all substructures . Afterwards, the assembled system is attained by substituting Eq. (6.56) into Eq. (7.14) and pre-multiplying Eq. (7.14) with $\boldsymbol{L}^T$ as

$$\boldsymbol{L}^T\boldsymbol{M}^U\boldsymbol{L}\ddot{\boldsymbol{q}}^C + \boldsymbol{L}^T\boldsymbol{D}^U\boldsymbol{L}\dot{\boldsymbol{q}}^C + \boldsymbol{L}^T\boldsymbol{K}^{(1)^U}\boldsymbol{L}\boldsymbol{q}^C + \boldsymbol{L}^T\boldsymbol{Q}_1^U(\boldsymbol{q})\boldsymbol{L}\boldsymbol{q}^C + \boldsymbol{L}^T\boldsymbol{Q}_2^U(\boldsymbol{q})\boldsymbol{L}\boldsymbol{q}^C = \boldsymbol{L}^T\boldsymbol{f}^U, \tag{7.15}$$

noting that the term $\boldsymbol{L}^T\boldsymbol{g}^U$ vanishes due to Eq. (6.55). Here, $\boldsymbol{L}$ is the standard localization matrix as explained in section 6.5. Moreover, the damping ratio in all parts of this work is assumed in the form of Rayleigh damping. Additionally, the corresponding localization matrix for each method is outlined in Chapter 6, regarding exact or weak compatibility, and interface reduction.

7.4 Numerical examples

This section studies the performance of the proposed methods for the nonlinear substructuring of geometric nonlinear FE models on two examples. In the first example, which is made of beam elements, the nonlinear MRM is assessed and in the second example, which is constructed by shell elements, nonlinear MRM with three interface reduction techniques are evaluated. All of these methods are also compared with the previously developed nonlinear substructuring methods in [82, 84], namely, the nonlinear GH and nonlinear HCB methods with and without IR. For the time integration of all NLROMs with different methods, the implicit Newmark scheme is employed. The time increment of 1×10^{-4} seconds with 4×10^{4} time steps have been taken for both full and reduced models. The full models are constructed and implicitly integrated in Abaqus® and compared with the NLROMs, which are developed and integrated in MATLAB®. During the time integrations, a Rayleigh damping in the form of $\alpha \boldsymbol{M} + \beta \boldsymbol{K}$ is used.
Moreover, all the dynamic loads in this work are sound pressures that are uniformly distributed in space and random in time with the frequency range of excitation between 0−500 Hz. Each example is excited with two different average Sound Pressure Levels (SPLs) to check the accuracy of the developed NLROMs for different excitation levels. Displacement Power Spectral Density (PSD) is utilized as an assessment tool to compare the efficiency of the nonlinear response of NLROMs with the full-order model. The time integrations in this work are performed on a desktop PC with 32 GB RAM and Intel® Xeon® CPU (3.6 GHz).

7.4.1 Simply supported beams

The first example is the assembly of two geometric nonlinear beams as shown in Fig. 6.1. The substructures S_1 and S_2 are simply supported at two ends and coupled at their rotational DOF.

	NLROM-MRM		NLROM-GH		NLROM-CB		Monolithic NLROM
Substructure	S_1	S_2	S_1	S_2	S_1	S_2	
Free/fixed modes	5	4	5	4	5	4	
Interface DOFs	1	1	0	0	1	1	
NLROM DOFs	10		9		10		10
Static solutions	232	130	130	64	232	130	1160

Table 7.1: Number of nonlinear static solutions (offline computational cost) for NLROMs development of the beam model using different methods

NLROM/Full model	NLROM-MRM	NLROM-CB	NLROM-GH	Full Model (145 dB)
Online Cost, IC	38 s	37 s	24 s	1055 s
Online Cost, ICE	38 s	38 s	23 s	

Table 7.2: Online computational time for four seconds time integration of different NLROMs as well as the full-order beam model

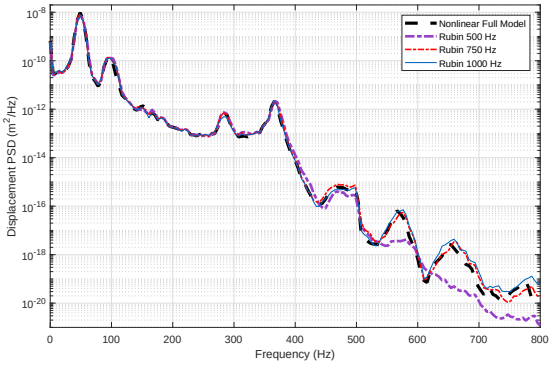

(a) Transverse DOF of point A

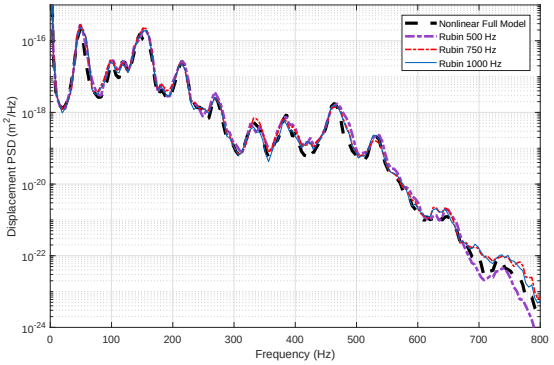

(b) Membrane DOF of point A

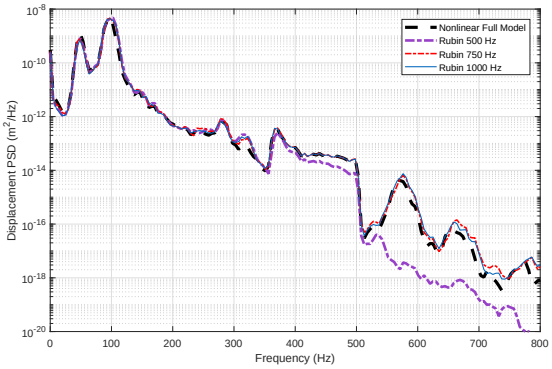

(c) Transverse DOF of point B

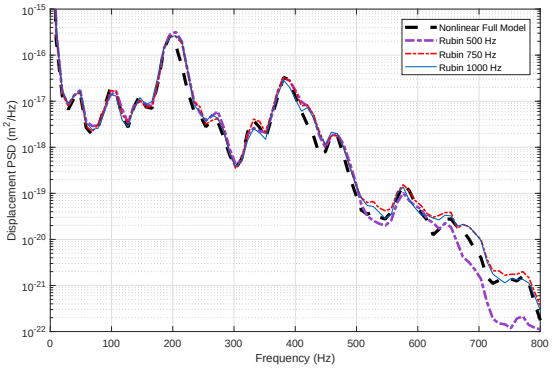

(d) Membrane DOF of point B

Figure 7.1: Displacement power spectral density evaluation for the convergence check of the beam's NLROM developed with the MRM basis. Three NLROMs are developed when the free modes are kept until 500 Hz, 750 Hz and 1000 Hz and integrated under a uniformly distributed random pressure with 135 dB SPL.

The material, geometry and mesh properties of the two substructures are given in Table 6.1. The two substructures as well as the full model are constructed and analyzed in Abaqus®.

Nonlinear substructuring results

The NLROM of each substructure is developed using the non-intrusive method of ICE with three different bases (GH, HCH and MRM). In order to assess the efficiency of the proposed method on the beam example, sound pressures are applied to the assembled structure that are uniform in space and random in time. In this case study, two average SPLs are applied to the system: 135 dB and 145 dB, for both full-order and NLROM models. The coefficients for the Rayleigh damping are chosen ($\alpha = 4.70$ and $\beta = 6.85 \times 10^{-6}$) such that the damping ratio for all the modes in the excitation frequency are less than 1%.
In the first step, the convergence check for the nonlinear MRM substructuring method is performed. The NLROMs are developed with three numbers of kept free-interface modes with eigenfrequencies up to 500 Hz (3 modes S_1 and 2 modes S_2), 750 Hz

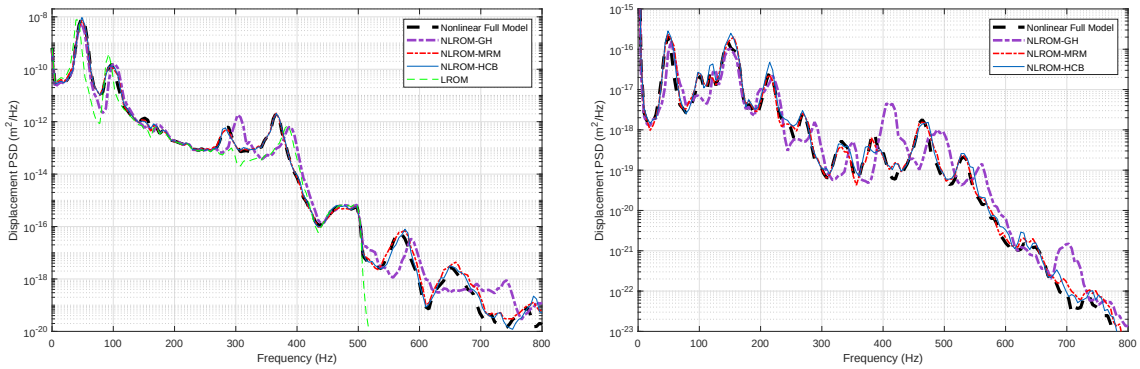

(a) Transverse DOF of point A under 135 dB SPL load. **(b)** Membrane DOF of point A under 135 dB SPL load.

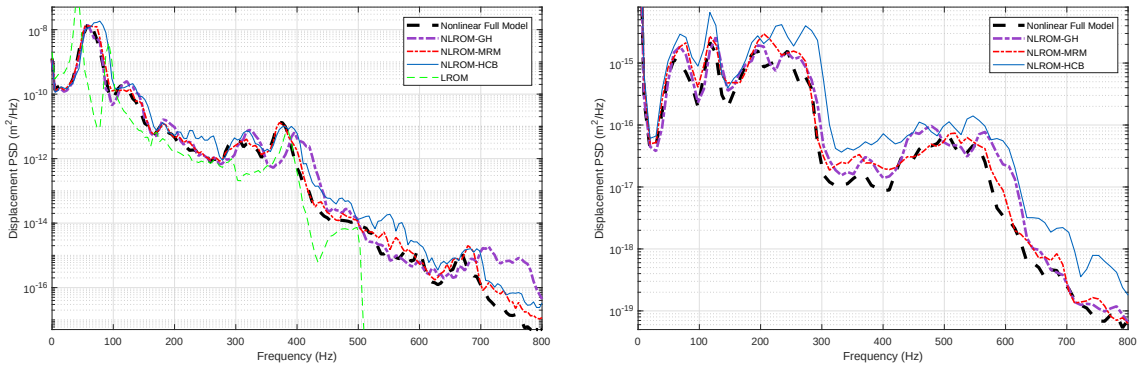

(c) Transverse DOF of point A under 145 dB SPL load. **(d)** Membrane DOF of point A under 145 dB SPL load.

Figure 7.2: Comparison of the beam's full model with the NLROMs using three bases: GH, MRM and HCB, and also the LROM. The displacement power spectral densities for transverse and membrane DOFs of point A are compared. The ingredients of these NLROMs are given in Table 7.1.

(4 modes S_1 and 3 modes S_2), and 1000 Hz (5 modes S_1 and 4 modes S_2). Fig. 7.1 shows the displacement PSD for the three developed NLROMs with nonlinear MRM (NLROM-MRM) using the mentioned number of modes and under the SPL of 135 dB. Transverse as well as membrane motions for the two points A and B (see Fig. 6.1b for the location of the points) are plotted. When the frequency range of the kept free-interface modes is increased from 500 Hz to 1000 Hz, the accuracy of the NLROMs is increased for both transverse (Figs. 7.1a and 7.1c) as well as membrane DOFs (Figs. 7.1b and 7.1d). For the case of kept modes up to 1000 Hz, the NLROM's PSDs match very well the ones of the full model in the whole frequency range of $0-800$ Hz, for both points. This result confirms the convergence as well as the accuracy of the proposed method. According to the results of Fig 7.1, the NLROM based on kept modes up to 1000 Hz is used for the rest of the investigations of this example. It should be noted that the total number of DOFs for the kept modes until 1000 are 10 after assembly, which are much less than the total number of DOFs for the assembled model (297 DOFs), resulting in a very computationally efficient model.
Furthermore, the NLROM-MRM is evaluated under the two mentioned SPL loads and compared with the nonlinear HCB (NLROM-HCB), nonlinear GH (NLROM-GH) substructuring methods, which are proposed by Kuether et al [84], and also linear

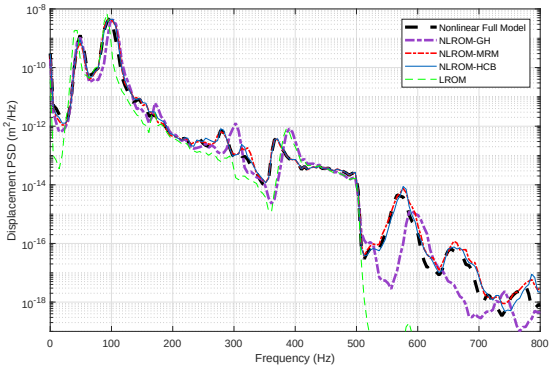

(a) Transverse DOF of point B under 135 dB SPL load.

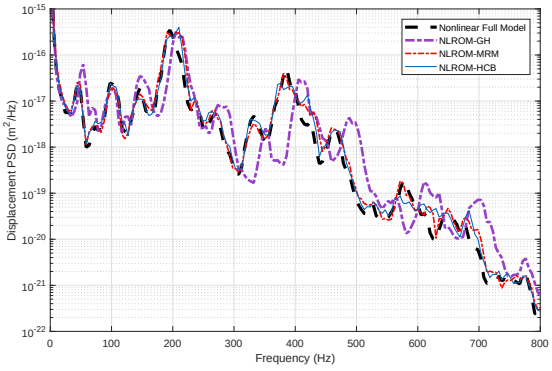

(b) Membrane DOF of point B under 135 dB SPL load.

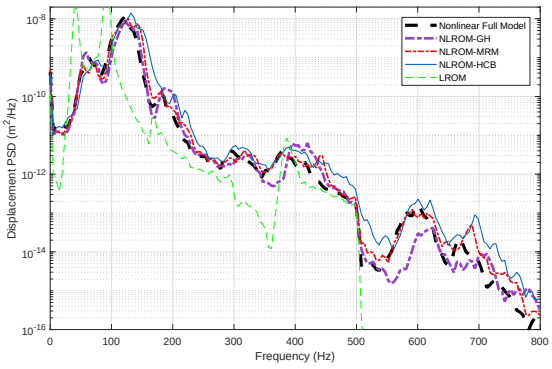

(c) Transverse DOF of point B under 145 dB SPL load.

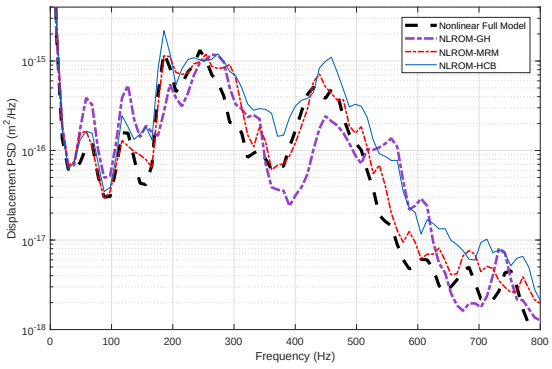

(d) Membrane DOF of point B under 145 dB SPL load.

Figure 7.3: Comparison of the beam's full-order model with the NLROMs using three bases: GH, MRM, HCB, and also the LROM. The displacement power spectral densities for transverse and membrane DOFs of point B are compared.

GH (LROM). The ingredients of these NLROMs are given in Table 7.1. Figs. 7.2a and 7.2b show the PSDs of the developed NLROMs under the low SPL (135 dB) for transverse and membrane DOFs at point A. While the NLROM-GH has a relatively good accuracy in low frequencies up to 250 Hz, it cannot follow the full-order model in higher frequencies, in both transverse and membrane directions. However, the NLROM-MRM, which is based on augmented free-interface modes, has captured the dynamics of the full nonlinear model in the whole investigated frequency range. This is also confirmed by the PSDs shown in Figs. 7.3a and 7.3b for the transverse and membrane motions of point B. The same analysis is performed for a higher SPL (145 dB). The PSD comparison of NLROMs for transverse DOFs of points A and B are presented in Figs. 7.2c and 7.3c, and for their membrane DOFs in Figs. 7.2d and 7.3d. The improved accuracies of NLROM-MRM with respect to NLROM-GH confirms the superiority of the developed NLROM. Moreover, it can be seen from all four figures that the NLROM-HCB is less robust than NLROM-MRM for the high level of external loads, because it exhibits less accurate results than NLROM-MRM.

Computational costs

The number of nonlinear static solutions for the development of each NLROM with different methods is shown in Table 7.1, which indicates the offline computational costs. It can be seen that if the NLROM of two substructures are computed in parallel, it leads to less computational time than the case where the NLROM is developed monolithically without parallel computation, with the same number of reduced DOFs.
Furthermore, the online computational time for the integration of the NLROMs are compared with the cost for the full model in table 7.2. It should be recalled that the integration of the NLROMs is performed in a MATLAB code and compared with the integration of the full model in Abaqus, which usually uses very optimized algorithms for integration. Nevertheless, the computational time for all of the NLROMs are more then 27 times faster than the one of the full model.
Finally, nonlinear model reduction can also be performed using the so-called *Hyper-reduction* methods [20, 39]. These methods are for instance based on the selection of a few elements for the computation of nonlinear internal forces. However, these methods are typically very sensitive to different load cases, which lead to additional offline costs for the computation of the NLROM responses for different load conditions. In contrast, the investigated NLROMs in this work can be valid for several loading conditions up to excitation frequencies of 500 Hz. This means that if the NLROM is used for numerous loading conditions, the “one-time" offline cost for this approach will be amortized.

7.4.2 Simply-supported panels

The second investigated example is the panel model studied in section 6.6.2, which is modeled with geometric nonlinear shell elements. The schematic of the two substructures as well as the assembled model are depicted in Figs. 6.3a and 6.3b, respectively. Moreover, the material, geometry and mesh properties of these models are given in Table 6.3. The Rayleigh damping ratios are chosen ($\alpha = 16.2$ and $\beta = 2.85 \times 10^{-6}$) such that all the damping ratios in the frequency range of interest are less than 1%.

	NLROM-MRM-SL		NLROM-GH		NLROM-HCB-SL		Monolithic NLROM
Substructure	S_1	S_2	S_1	S_2	S_1	S_2	
Free/fixed modes	7	5	7	5	7	5	
Interface DOFs	2	2	0	0	2	2	
NLROM DOFs	14		12		14		14
Static solutions	834	378	378	130	834	378	3304

Table 7.3: Number of nonlinear static solutions (offline computational cost) for NLROMs development of the panel model using different methods.

Nonlinear substructuring

The geometric nonlinear models of the two substructures are reduced using the ICE method. As a reduction basis to generate the nonlinear static forces required in ICE, Kuether et al. used GH and HCB bases in [84]. In a later work in [82], they also combined SL as well as LL-WC interface reduction techniques for nonlinear HCB to

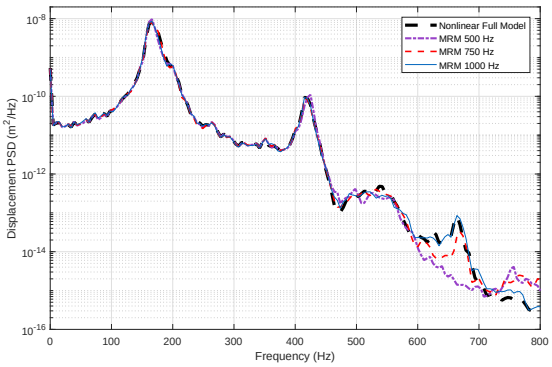

(a) Transverse DOF of point A.

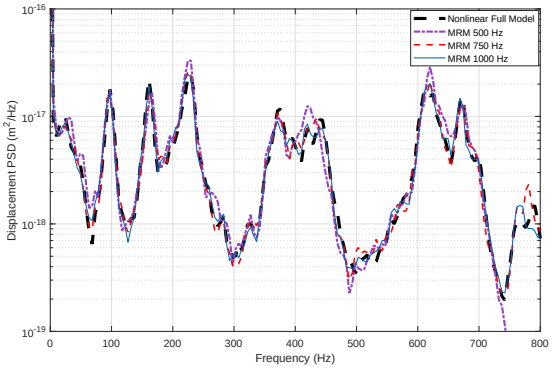

(b) Membrane DOF of point A.

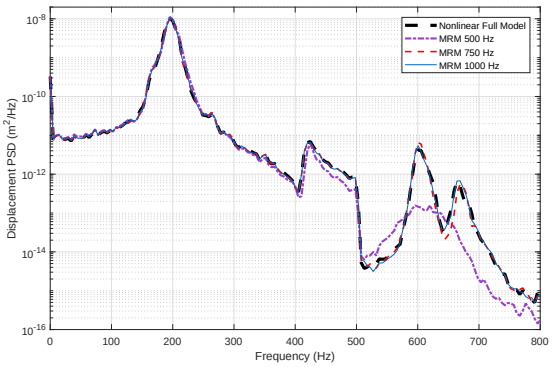

(c) Transverse DOF of point B.

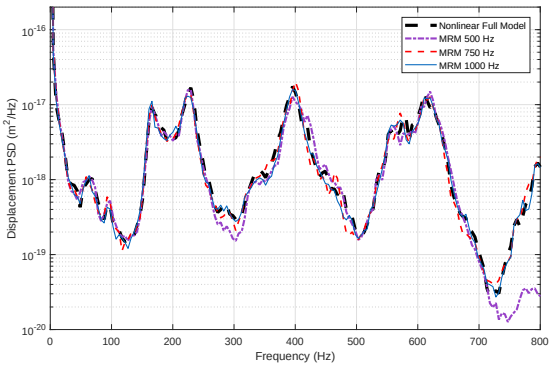

(d) Transverse DOF of point B.

Figure 7.4: Displacement power spectral density evaluation for the convergence check of the plate's NLROM developed with the MRM basis. Three NLROMs are compared when the free modes are kept up to 500 Hz, 750 Hz and 1000 Hz under the loading condition of 155 dB SPL. Two SL interface modes are used for the NLROMs.

NLROM/Full model	NLROM-MRM-SL	NLROM-CB-SL	NLROM-GH	Full Model (155 dB)
Online Cost, IC	4.2 min	4.2 min	3.5 min	597.2 min
Online Cost, ICE	3.5 min	3.4 min	2 min	

Table 7.4: Online computational time for four seconds time integration of the plate FE model with different methods.

reduce the computational costs while developing the NLROMs of substructures. In this work, we develop the augmented free-interface method (MRM) with SL, LL-EC and LL-WC interface reductions for nonlinear substructuring and compare it with corresponding IR methods applied to nonlinear HCB and GH methods. The evaluation and comparison of the results are studied on the points A and B (see Fig. 6.3b).
The nonlinear convergence check study of the proposed method is shown in Fig. 7.4 under 155 dB SPL. This study is performed by retaining the free-interface modes up to 500, 750 Hz and 1000 Hz in the reduction basis. All NLROMs are developed while only two SL-IR modes for each substructure are kept in the reduction bases. The

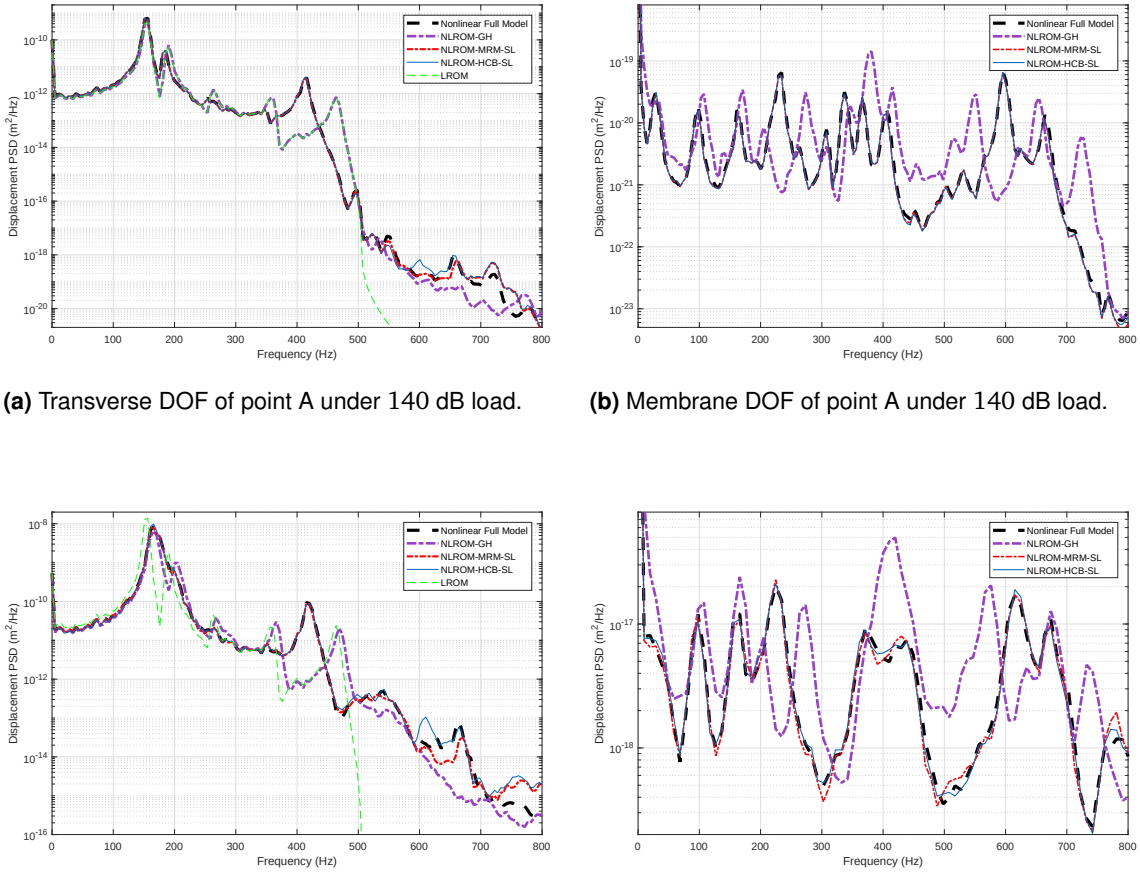

(a) Transverse DOF of point A under 140 dB load.

(b) Membrane DOF of point A under 140 dB load.

(c) Transverse DOF of point A under 155 dB load.

(d) Membrane DOF of point A under 155 dB load.

Figure 7.5: Comparison of the plate's full-order model with the NLROMs using three bases: free-interface, MRM with SL-IR, HCB with SL-IR and also the LROM. The displacement power spectral densities for transverse and membrane DOFs of point A are compared. Two interface modes are used for HCB and MRM.

accuracy of PSDs for transverse as well as membrane motions of both points, A and B, are increased by expanding the number of modes in the basis. This acknowledges the convergence of the proposed method. Considering the accuracy of the NLROM with modes up to 750 Hz, this model is used for further comparisons of this example. Note that the total number of generalized DOFs for NLROM with modes up to 750 Hz is 14, which is only 0.04% of the number of the full-model's DOFs, leading to a very compact nonlinear model.

Furthermore, the NLROM of the nonlinear MRM with SL-IR is evaluated under two uniformly distributed SPLs; 140 dB and 155 dB, with the excitation frequency of $0-500$ Hz. This result (NLROM-MRM-SL) is compared with the nonlinear GH model (NLROM-GH), nonlinear HCB with SL-IR (NLROM-HCB-SL), linear ROM with GH method (LROM) and nonlinear full-order model (time integrated in Abaqus) for the transverse and membrane motion of point A, and presented in Fig. 7.5. Unlike the nonlinear GH method, which fails to capture the dynamics of the full model, the augmented free-interface method of MRM follows very well the PSD of the full-model in the whole investigated frequency range. This result confirms a significant improvement of the free-interface mode method studied in [84], by increasing the DOFs of

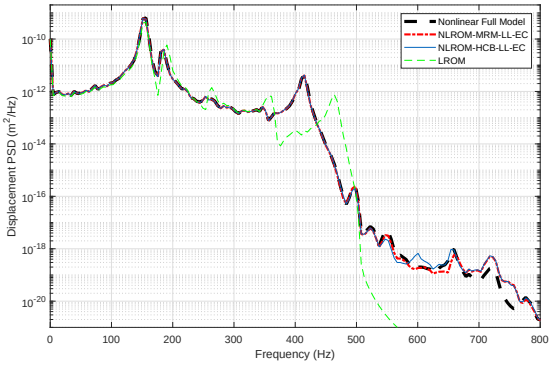

(a) Transverse DOF of point A under 140 dB load.

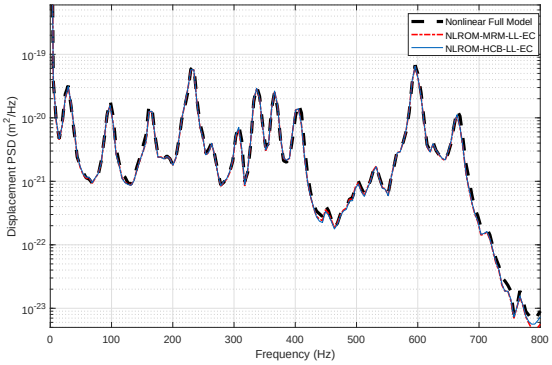

(b) Membrane DOF of point A under 140 dB load.

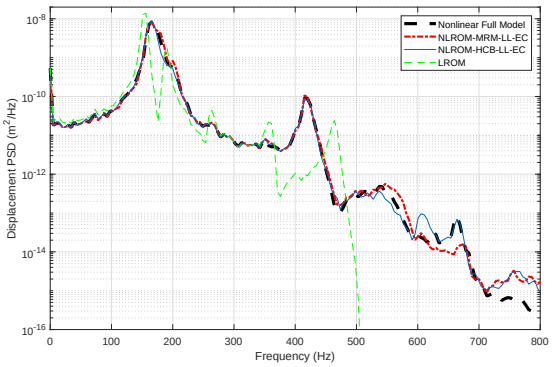

(c) Transverse DOF of point A under 155 dB load.

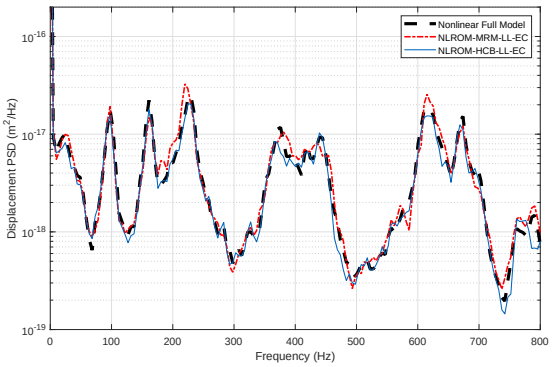

(d) Membrane DOF of point A under 155 dB load.

Figure 7.6: Comparison of the plate's full-order model with the NLROMs using three bases: GH, MRM with LL-EC interface reduction, HCB with LL-EC interface reduction, and also the LROM. The displacement power spectral densities for transverse and membrane DOFs of point A are compared. Two interface modes are used for HCB and MRM.

the GH's NLROM with only two interface generalized coordinates. Since NLROM-GH does not work for this example, it is not considered in further comparisons. Additionally, the accuracy of the NLROM-HCB-SL and NLROM-MRM-SL for frequencies up to 700 Hz are acceptable for both transverse and membrane directions. After about 700 Hz, none of the methods can follow the transverse PSD of the full-model accurately (see Figs. 7.5b and 7.5d), due to the fact that the free-interface modes are kept up to about 750 Hz in the system (and the same number for fixed-interface modes). To get acceptable PSDs for higher frequencies, more modes should be preserved in the reduction basis.

The same analysis for the nonlinear MRM method combined with two interface modes of LL-EC method (NLROM-MRM-LL-EC) under 140 dB and 155 dB SPLs is performed and presented in Fig. 7.6. They are further compared with nonlinear HCB with LL-EC interface reduction (NLROM-HCB-LL-EC), LROM and full-order model. Figs. 7.6a and 7.6c show the PSD comparison for the transverse DOF of point A under two aforementioned SPLs, whereas Figs. 7.6b and 7.6d exhibit the PSD comparison for its membrane DOF. Like the NLROM-MRM-SL, not only does the NLROM-MRM-LL-EC distinctly improve the PSD accuracy of both transverse and membrane motions

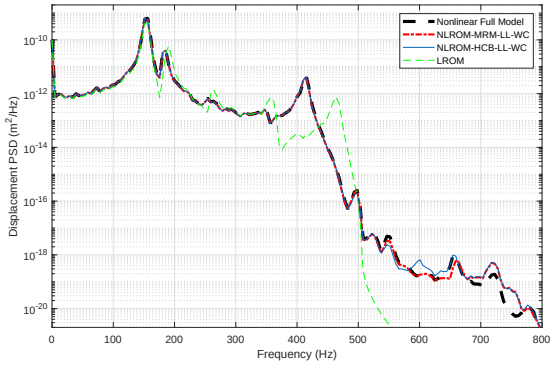

(a) Transverse DOF of point A under 140 dB load.

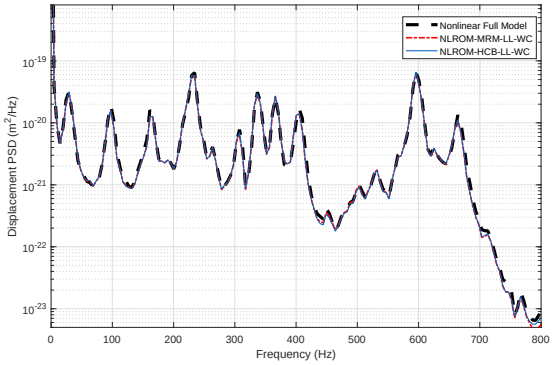

(b) Membrane DOF of point A under 140 dB load.

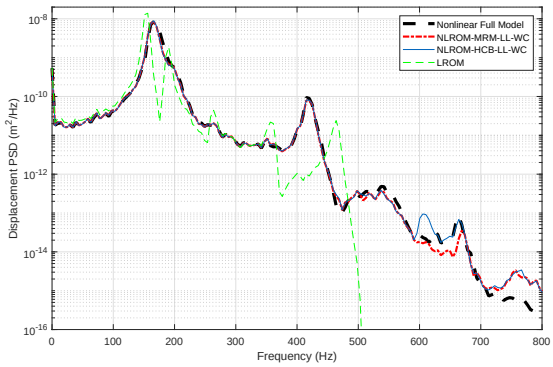

(c) Transverse DOF of point A under 155 dB load.

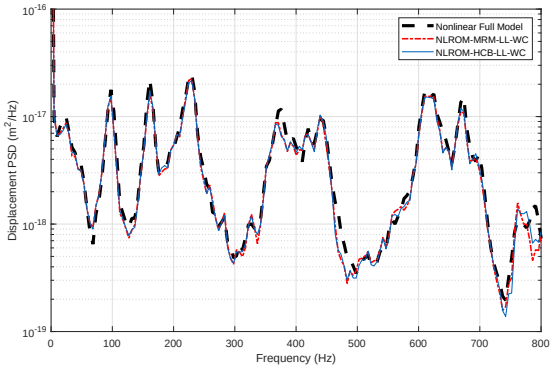

(d) Membrane DOF of point A under 155 dB load.

Figure 7.7: Comparison of the plate's full-order model with the NLROMs using three bases: GH, MRM with LL-WC interface reduction, HCB with LL-WC interface reduction, and also the LROM. The displacement power spectral densities for transverse and membrane DOFs of point A are compared. Two interface modes are used for HCB and MRM.

compared to NLROM-GH, but also it has almost the same accuracy as NLROM-HCB-LL-EC.

Finally, LL-WC interface reduction is combined with MRM for the purpose of nonlinear substructuring (NLROM-MRM-LL-WC) and compared with nonlinear HCB combined with LL-WC (NLROM-HCB-LL-WC), LROM and the nonlinear full-model under the two aforementioned SPLs. Two LL-WC interface mode are used to develop the NLROMs with HCB and MRM. The PSD of these results for the transverse as well as membrane DOFs of point A is depicted in Fig. 7.7. From these results, the same conclusion can be drawn as was made for the other two proposed methods, namely, adding just a few interface DOFs (here two) to the previous nonlinear free-interface substructuring performed in [84] has improved the NLROM in the same order of accuracy as the nonlinear HCB.

Fig. 7.8 compares the accuracy of all three IR techniques applied to the nonlinear MRM method. Although all three NLROMs are superior to the NLROM-GH, there is no notable difference in the accuracy among them in both transverse (Fig. 7.8a) and membrane (Fig. 7.8b) motions. The overall results discussed in this section lead to the conclusion that the NLROM-MRM with all three IR techniques can remarkably

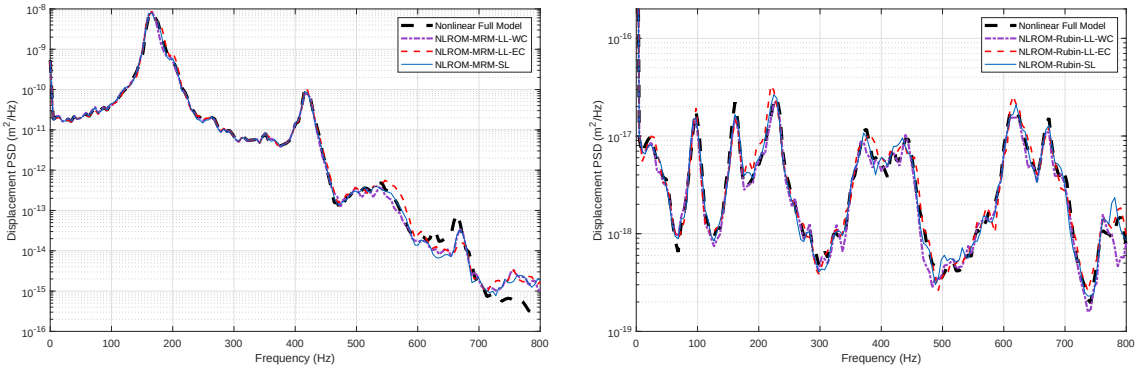

(a) Transverse DOF of point A under 155 dB load.

(b) Membrane DOF of point A under 155 dB load.

Figure 7.8: Comparison of the plate's NLROMs with full-order model based on the MRM method with three interface reductions: SL, LL-EC and LL-WC. The displacement power spectral densities for transverse and membrane DOFs of point A are compared. Two interface modes are used for all NLROMs.

increase the previous nonlinear free-interface (GH) substructuring. The reason why the reduced model is very accurate even with only two interface modes can be explained by the fact that the interface is simply supported. This was done to simulate a similar example as in [82].

Computational costs

The final study for this example investigates the offline as well as online computational costs for the developed NLROMs. Table 7.3 shows the required nonlinear static solutions to generate the NLROM of each substructure using different methods. Like the beam example, it can be seen that if the NLROMs of two substructures are computed in parallel, the maximum number of required static solution to build the NLROM is 836 for the MRM-SL and HCB-SL, and 378 for GH. However, monolithic reduction of the full-model with the same number of reduced DOFs needs 3304 static solutions, which show the advantage of substructuring.
Furthermore, table 7.4 describes the required online time for four seconds time integration of the generated NLROMs described in table 7.3 as well as the full-order model. Although the full-order model is integrated in Abaqus (which has very optimized time integration algorithms) and the NLROMs are integrated in a research MATLAB code, the required online time integration of the NLROM is about 142 times faster than the required time for the integration of the full-order model. Besides, the developed NLROMs can be used for several loading cases with excitation frequencies up to 500 Hz and SPLs up to about 155 dB. This advantage is in contrast to the hyper-reduction methods, which are load dependent and in general, for each loading condition, an additional offline computational cost for snapshot generations will be added.

7.5 summary

We propose an augmented free-interface-based method for modal substructuring of geometrically nonlinear finite element models that can significantly improve the free-interface nonlinear substructuring method. Our novel approach uses the reduction basis of the MacNeal/Rubin-Martinez method on geometrically nonlinear models. This basis comprises free-interface modes, rigid body modes, and residual flexibility attachment modes. Furthermore, we employ three different interface reduction methods to minimized the number of interface modes and further reduce the size of the Reduced Order Model (ROM). The coefficients of the nonlinear terms of the ROM - assumed to be up to cubic order in the modal coordinates - are identified in a non-intrusive manner using the Implicit Condensation and Expansion (ICE) method. This approach has the significant advantage of avoiding the requirement to access finite element formulations for model reduction that are typically not available in commercial finite element programs used for nonlinear structural dynamics. ICE allows to retrieve the membranal behavior accurately, even when the reduction basis only features bending dominated low frequency modes.
The method we propose is then equipped with three interface reduction methods available in literature for the Hurty/Craig-Bampton (HCB) method, namely, system level, local-level with exact compatibility and local-level with weak compatibility. We compare our approach - with and without interface reduction - with the nonlinear HCB and free-interface methods, which were recently presented in [85] and [82] and stand out as reference. The assessment is performed on two numerical examples modeled with beam and shell elements, in Abaqus. The numerical results for both examples show a significant improvement when compared to the free-interface method. This is due to the fact that the residual flexibility attachment modes can properly approximate the effect of truncated modes due to interface forces on the nonlinear response of the system. Furthermore, the nonlinear substructuring developed with the proposed basis performs marginally better than the nonlinear HCB for higher excitation levels. While improving accuracy, this addition does not significantly compromise the online computational costs associated to the method. Finally, the proposed method can facilitate experimental testing of nonlinear substructures, because unlike the HCB method, it does not require to fix the interface DOFs for the measurement of components.

Chapter 8

Improving non-intrusive substructuring with modal derivatives

This chapter is extracted from the author's work in [71], which is in preparation to be submitted for publication. In this article, Karamooz had the idea of the work, derived the numerical results for the shown examples, and wrote the manuscript. Tiso and Rixen give useful inputs in the discussions of the work and proof-read the article. Rixen supervises the work.

8.1 Introduction

In this chapter we introduce a generic nonlinear substructuring approach, which is an extension of our works in Chapters 4 and 7. As discussed before, Kuether et al. [82, 85] developed the first non-intrusive-based substructuring approach for nonlinear FE models, in which the Hurty/Craig-Bampton (HCB) reduction basis is employed to reduce the linear matrices of each substructure. Afterwards, the nonlinear stiffness coefficients of each substructure's NLROM is estimated using ICE. We further extended this method for nonlinear substructuring with free-interface modes in Chapter 7 and discussed the advantages of our approach.
The reduction bases used in Chapter 7 are only based on the classical linear CMS bases. Besides, the ICE method is used in Chapter 7 as well as in [54] to obtain the Nonlinear Stiffness Coefficients (NSCs) of the substructures' NLROMs, which predicts the in-plane motion of the structures only if the relation between the transverse-membrane modes are quadratic (as explained in Chapter 3). This makes the ICE method limited for curved structures, as also discussed in Chapter 5.
Another nonlinear substructuring method developed first by Wenneker and Tiso [157], augments the so called *Modal Derivatives* (MDs) to the linear HCB basis to more accurately predict the nonlinear response of the reduced model from substructuring. Wu later extended this method in [163] for using interface reduction and its corresponding (static) MDs. However, both mentioned augmented nonlinear HCB methods are intrusive methods, which are not applicable when the FE model is developed in a commercial packages.
In this work, we extend the non-intrusive-based nonlinear HCB method proposed by Kuether et al. [82, 85] in two ways. First we enrich the reduction basis by introducing the non-intrusive MDs to the linear HCB basis to increase the accuracy of the NLROMs. Using the proposed basis, the displacement of the membrane-dominated

DOFs are obtained without requiring to employ the expansion process of the ICE method, meaning that our method is more general. As the second novelty of this work, we propose the use of displacement-based non-intrusive ROM methods, introduced in [103, 116], instead of the forced-based ones (like IC and ICE) to develop the substructures' NLROMs. The advantage of the displacement-based methods are that they usually require less number of nonlinear static solutions (If tangent stiffness methodology is used) to obtain the NSCs of each substructure, leading to less *offline* computational costs. We apply the proposed method to the FE models of two numerical examples with geometric nonlinear effect and show the accuracy of the results obtained from this method.

8.2 Governing equations for substructures' ROMs

Let us revisit the governing equations for a geometric nonlinear substructure (s) as

$$\boldsymbol{M}^{(s)}\ddot{\boldsymbol{u}}^{(s)} + \boldsymbol{D}^{(s)}\dot{\boldsymbol{u}}^{(s)} + \boldsymbol{K}^{(s)}\boldsymbol{u}^{(s)} + \boldsymbol{f}_{nl}^{(s)}(\boldsymbol{u}) = \boldsymbol{f}^{(s)} + \boldsymbol{g}^{(s)}, \tag{8.1}$$

where $\boldsymbol{M} \in \mathbb{R}^{n^{(s)}\times n^{(s)}}$, $\boldsymbol{D} \in \mathbb{R}^{n^{(s)}\times n^{(s)}}$ and $\boldsymbol{K} \in \mathbb{R}^{n^{(s)}\times n^{(s)}}$ are the mass, damping and stiffness matrices, respectively, and the superscript (s) denote the entities corresponding to the s^{th} substructure. The displacement vector is denoted by $\boldsymbol{u} \in \mathbb{R}^{n^{(s)}\times 1}$ and each overdot represents one time derivative of this vector. Moreover, the vectors $\boldsymbol{f}_{nl} \in \mathbb{R}^{n^{(s)}\times 1}$, $\boldsymbol{f} \in \mathbb{R}^{n^{(s)}\times 1}$ and $\boldsymbol{g} \in \mathbb{R}^{n^{(s)}\times 1}$ are the nonlinear internal forces, applied external loads and the connecting forces at the interface, respectively. The superscript (s) is omitted in the remainder of this chapter for the sake of simplicity, unless otherwise stated. The matrices as well as the vectors in Eq. (8.1) are then split into their internal and boundary DOFs as

$$\begin{aligned}&\begin{bmatrix} \boldsymbol{M}_{ii} & \boldsymbol{M}_{ib} \\ \boldsymbol{M}_{bi} & \boldsymbol{M}_{bb} \end{bmatrix}\begin{bmatrix} \ddot{\boldsymbol{u}}_i \\ \ddot{\boldsymbol{u}}_b \end{bmatrix} + \begin{bmatrix} \boldsymbol{C}_{ii} & \boldsymbol{C}_{ib} \\ \boldsymbol{C}_{bi} & \boldsymbol{C}_{bb} \end{bmatrix}\begin{bmatrix} \dot{\boldsymbol{u}}_i \\ \dot{\boldsymbol{u}}_b \end{bmatrix} + \begin{bmatrix} \boldsymbol{K}_{ii} & \boldsymbol{K}_{ib} \\ \boldsymbol{K}_{bi} & \boldsymbol{K}_{bb} \end{bmatrix}\begin{bmatrix} \boldsymbol{u}_i \\ \boldsymbol{u}_b \end{bmatrix} \\ &+\boldsymbol{f}_{nl}\left(\begin{bmatrix} \boldsymbol{u}_i \\ \boldsymbol{u}_b \end{bmatrix}\right) = \begin{bmatrix} \boldsymbol{f}_i \\ \boldsymbol{f}_b \end{bmatrix} + \begin{bmatrix} \boldsymbol{0} \\ \boldsymbol{g}_b \end{bmatrix},\end{aligned} \tag{8.2}$$

where the subscripts i and b denote the DOFs corresponding to internal and boundary DOFs, respectively. To reduce the dimension of the substructures' governing equations, a reduction basis $\boldsymbol{T} \in \mathbb{R}^{n\times m}$ is defined as

$$\begin{bmatrix} \boldsymbol{u}_i \\ \boldsymbol{u}_b \end{bmatrix} \approx \boldsymbol{T}\begin{bmatrix} \boldsymbol{q}_i \\ \boldsymbol{q}_b \end{bmatrix}, \tag{8.3}$$

where $\boldsymbol{q} \in \mathbb{R}^{m\times 1}$ is the vector of generalized (modal) DOFs and $m << n$. Substituting Eq. (8.3) into Eq. (8.1) and pre-multiplying it with $\boldsymbol{T}^T$ results in the reduced set of governing equations for the substructure:

$$\hat{\boldsymbol{M}}\ddot{\boldsymbol{q}} + \hat{\boldsymbol{D}}\dot{\boldsymbol{q}} + \hat{\boldsymbol{K}}\boldsymbol{q} + \hat{\boldsymbol{f}}_{nl}(\boldsymbol{q}) = \hat{\boldsymbol{f}} + \hat{\boldsymbol{g}}, \tag{8.4}$$

where the sign '$\hat{}$' denotes the reduced matrices and vectors of the corresponding ones in Eq. 8.1. Furthermore, using the Taylor expansion, the i^{th} component of the

reduced nonlinear internal force vector is approximated as[1]

$$\hat{f}_{nl_i} = \hat{K}^{(2)}_{ijl} q_j q_l + \hat{K}^{(3)}_{ijlp} q_j q_l q_p, \tag{8.5}$$

where $\hat{K}^{(2)}$ and $\hat{K}^{(3)}$ are the quadratic and cubic NSCs, respectively. The aim of this work is to obtain the NSCs in a non-intrusive manner which has the advantages explained in Chapter 1. We introduce first a new reduction basis for non-intrusive substructuring using the HCB basis, which is augmented with non-intrusive MDs. Afterwards, we identify the NSCs of each substructure using the Enforced Displacement method.

8.3 Enhanced Craig-Bampton reduction basis: non-intrusive approach

When no interface reduction is intended for a substructure, the motion of its internal DOFs can be approximated as

$$\boldsymbol{u}_i \approx \boldsymbol{\Phi}_{FM} \boldsymbol{q}_{FM} + \boldsymbol{\Theta}_{FM} \boldsymbol{\xi}_{FM} + \boldsymbol{\Psi}_{CM} \boldsymbol{u}_b, \tag{8.6}$$

where $\boldsymbol{\Phi}_{FM} \in \mathbb{R}^{i \times m_1}$ contains the truncated number of fixed-interface modes and its j^{th} column, $\boldsymbol{\varphi}_{FM,j}$ is obtained as

$$(\boldsymbol{K}_{ii} - \omega^2_{FM,j} \boldsymbol{M}_{ii}) \boldsymbol{\varphi}_{FM,j} = 0. \tag{8.7}$$

Moreover, the Constraint Modes (CMs) matrix $\boldsymbol{\Psi}_{CM} \in \mathbb{R}^{i \times b}$ is given by

$$\boldsymbol{\Psi}_{CM} = -\boldsymbol{K}_{ii}^{-1} \boldsymbol{K}_{ib} \tag{8.8}$$

The matrix $\boldsymbol{\Theta}_{FM} \in \mathbb{R}^{i \times m_2}$ contains the Modal Derivatives (MDs) of the fixed-interface modes. The concept of MDs and their non-intrusive computation was already discussed in section 4.3.3 for monolithic reduction. Here, we summarize them for the context of substructuring. The jk^{th} MD in Eq. (8.6) can be obtained by differentiating the eigenvalue problem of the fixed-interface modes (Eq. (8.7)) [105, 157]:

$$\left(\boldsymbol{K}^{(1)}_{ii} - \omega^2_{FM,j} \boldsymbol{M}_{ii}\right) \frac{\partial \boldsymbol{\varphi}_{FM,j}}{\partial q_k} = \left(\frac{\partial \omega^2_{FM,j}}{\partial q_j} \boldsymbol{M}_{ii} - \frac{\partial \boldsymbol{K}_{ii}}{\partial q_k} \right) \boldsymbol{\varphi}_{FM,j}, \tag{8.9}$$

where

$$\boldsymbol{\theta}_{jk} = \frac{\partial \boldsymbol{\varphi}_{FM,j}}{\partial q_k}, \tag{8.10}$$

is the jk^{th} fixed-interface MD. The matrix of fixed-interface MDs, $\boldsymbol{\Theta}_{FM}$ is then obtained by symmetrizing all the MDs and concatenating them in a matrix as

$$\boldsymbol{\Theta}_{FM} = \left[\boldsymbol{\theta}_{11}, \frac{1}{2}(\boldsymbol{\theta}_{12} + \boldsymbol{\theta}_{21}), \cdots, \boldsymbol{\theta}_{kk}, \boldsymbol{\theta}_{jj}, \frac{1}{2}(\boldsymbol{\theta}_{kj} + \boldsymbol{\theta}_{jk}), \cdots, \boldsymbol{\theta}_{mm} \right], \tag{8.11}$$

[1] For solid elements and plates with von Kármán assumption, this expression is exact

The derivative of the eigenfrequency, $\frac{\partial \omega_{FM,j}^2}{\partial q_j}$ in Eq. (8.9) is attained by pre-multiplying this equation with $\boldsymbol{\varphi}_{FM,j}^T$ and the only left unknown is then the MD. Since the l.h.s of the Eq. (8.9) is singular, the MDs can be either computed by Nelson's method [105] or using the generalized inverse methodology as explained in [44] (also see section 4.3.3 for more details).
The computation of MDs can be simplified by neglecting the inertia term, which is first proposed by Idelsohn and Cardona [61]. Accordingly, the Eq. (8.9) reduces to

$$\boldsymbol{K}_{ii} \frac{\partial \boldsymbol{\varphi}_{FM,j}}{\partial q_k} = \frac{\partial \boldsymbol{K}_{ii}}{\partial q_k} \boldsymbol{\varphi}_{FM,j}. \tag{8.12}$$

To obtain the MDs by the simplified Eq. (8.12), which are called *Static Modal Derivatives* (SMDs), one does not need to factorize the mass matrix for each mode. The *Enahnced Hurty/Craig-Bampton* (EHCB) reduction basis for the s^{th} substructure is finally defined as

$$\boldsymbol{T}_{EHCB}^{(s)} = \begin{bmatrix} \boldsymbol{\Phi}_{FM}^{(s)} & \boldsymbol{\Theta}_{FM}^{(s)} & \boldsymbol{\Psi}_{CM}^{(s)} \\ \boldsymbol{0} & \boldsymbol{0} & \boldsymbol{I} \end{bmatrix}, \tag{8.13}$$

This basis is employed to reduce the linear mass and stiffness matrices as well as identify the NSCs for each substructure.

Interface reduction

In case several DOFs exist at the interface of substructures, reduction of internal DOFs does not suffice to build a compact NLROM with substructuring. Therefore, several Interface Reduction (IR) techniques for linear CMS methods have been investigated in recent years, a review of which can be found in [80]. The main idea of IR is to approximate the full-order interface DOFs with a reduced set of interface modal coordinates using a modal reduction of interface's mass and stiffness matrices, either from coupled system (System-Level (SL)) or individual substructures (local level (LL)). For a nonlinear structure, the interface modes can be augmented with their corresponding modal derivative [163], namely,

$$\boldsymbol{u}_b \approx \boldsymbol{\Phi}_{IR} \boldsymbol{q}_{IR} + \boldsymbol{\Theta}_{IR} \boldsymbol{\xi}_{IR}, \tag{8.14}$$

where $\boldsymbol{\Phi}_{IR} \in \mathbb{R}^{b \times m_3}$ and $\boldsymbol{q}_{IR} \in \mathbb{R}^{m_3 \times 1}$ contain a reduced set of interface modes and model coordinates, respectively. The (S)MDs of the interface as well as its modal coordinate are denoted by $\boldsymbol{\Theta}_{IR} \in \mathbb{R}^{b \times m_4}$ and $\boldsymbol{\xi}_{IR} \in \mathbb{R}^{m_4 \times 1}$, respectively. When an SL-IR is desired, the j^{th} column (mode) of the matrix $\boldsymbol{\Phi}_{IR}$ for SL-IR is obtained from an eigenvalue problem of the interface mass and stiffness matrices of the coupled structure:

$$(\boldsymbol{K}_{bb}^C - \omega_{b,j}^2 \boldsymbol{M}_{bb}^C) \boldsymbol{\varphi}_{b,j} = \boldsymbol{0}, \tag{8.15}$$

where the superscript C denotes the matrices of the coupled system. Furthermore, to calculate the columns of $\boldsymbol{\Theta}_{IR}$, the boundary mass and stiffness of the coupled system must be differentiated similar to the (S)MDs of the fixed-interface modes (Eqs (8.9) and (8.12), which require dealing with full-order nonlinear coupled reduced system.

Since in substructuring we avoid working with the full nonlinear system, the (S)MDs of the SL-IR are neglected. However, the (S)MDs of the interface can computed while LL-IR is desired.
Once the interface modes as well as (S)MDs (only for LL-IR) are computed, the projection matrix for IR of the s^{th} substructure yields

$$\boldsymbol{T}_{IR}^{(s)} = \begin{bmatrix} \boldsymbol{I}_{m_1 m_1}^{(s)} & \boldsymbol{0} & \boldsymbol{0} & \boldsymbol{0} \\ \boldsymbol{0} & \boldsymbol{I}_{m_2 m_2}^{(s)} & \boldsymbol{0} & \boldsymbol{0} \\ \boldsymbol{0} & \boldsymbol{0} & (\boldsymbol{\Phi}_{IR}^{(s)})_{bm_3} & (\boldsymbol{\Theta}_{IR}^{(s)})_{bm_4} \end{bmatrix} \tag{8.16}$$

where $\boldsymbol{T}_{IR}^{(s)}$ is the IR projection matrix. Finally, the total reduction basis with IR for the substructure s is given by

$$\boldsymbol{T}_{EHCB,IR}^{(s)} = \boldsymbol{T}_{EHCB}^{(s)} \boldsymbol{T}_{IR}^{(s)}, \tag{8.17}$$

where $\boldsymbol{T}_{EHCB,IR}^{(s)}$ is total reduction basis for the substructure with interface reduction. All of the ingredients in the EHCB reduction basis, except the (S)MD, can be computed from linear mass and stiffness of matrices of each substructure, which are available. In the following, we discuss how to compute (S)MDs non-intrusively, namely, without having to access the closed form governing equations.

Non-intrusive computation of modal derivatives

Since the aim of this work is to develop the NLROM of each substructure non-intrusively, we introduce two ways for non-intrusive computation of the fixed-interface (or boundary modes) (S)MD using central finite difference. In case the FE code releases the TS matrix after solving a nonlinear static solution, the derivative of the TS matrix is given by

$$\left.\frac{\partial \boldsymbol{K}_{ii}^{t}(\boldsymbol{\varphi}_{FM,j} q_j)}{\partial q_j}\right|_{q_j=0} = \frac{\boldsymbol{K}_{ii}^{t}(\boldsymbol{u}_i = \boldsymbol{\varphi}_{FM,j} h) - \boldsymbol{K}_{ii}^{t}(\boldsymbol{u}_i = -\boldsymbol{\varphi}_{FM,j} h)}{2h}, \tag{8.18}$$

where K_{ii}^{t} denotes the TS matrix corresponding to the internal DOFs and h is a small increment for finite difference perturbation. It should be noted that the nonlinear static solution for each increment is computed while the interface DOFs are made fixed in the FE code. The second case is when only the reaction forces due to a prescribed displacement is released by the FE code. In this case the derivative of the TS, multiplied with each fixed-interface mode is written as

$$\frac{\partial \boldsymbol{K}_{ii}^{t}}{\partial q_j} \boldsymbol{\varphi}_{FM,k} = \left.\frac{\partial^2 \boldsymbol{f}_{\mathrm{int}_i}}{\partial q_k \partial q_j}\right|_{\substack{q_k=0 \\ q_j=0}} =$$

$$\frac{\boldsymbol{f}_{\mathrm{int}_i}(\boldsymbol{u}=\boldsymbol{\varphi}_{FM,k}h_i+\boldsymbol{\varphi}_{FM,j}h_j) - \boldsymbol{f}_{\mathrm{int}_i}(\boldsymbol{u}=\boldsymbol{\varphi}_{FM,k}h_i-\boldsymbol{\varphi}_{FM,j}h_j) - \boldsymbol{f}_{\mathrm{int}_i}(\boldsymbol{u}=-\boldsymbol{\varphi}_{FM,k}h_i+\boldsymbol{\varphi}_{FM,j}h_j) + \boldsymbol{f}_{\mathrm{int}_i}(\boldsymbol{u}=-\boldsymbol{\varphi}_{FM,k}h_i-\boldsymbol{\varphi}_{FM,j}h_j)}{4h_i h_j}. \tag{8.19}$$

Once the l.h.s of the Eqs. (8.18) and (8.19) are calculated, they can be introduced to either Eqs. (8.9) or (8.12) to gain the (S)MDs.

Load-independent selection of modal derivatives

Since the number of (S)MDs increase quadratically ($O(m^2)$) when increasing the number of fixed interface as well as boundary modes, only the most important ones are selected in the reduction basis. Here, we use the Maximum Modal Interaction (MMI) method [64, 154] with a small modification. We use a random signal for excitation of the system as the modification of this method. We reduce the linear mass and stiffness matrices, which correspond to the internal DOFs using only the fixed-interface modes in the basis. Then a linear time integration for the reduced set of fixed-interface coordinates is performed. The load excitation in this case is random in time with a desired frequency band, and an arbitrary load distribution. In this work, we choose the load distribution as a unit load applied to all DOFs (transverse/membrane/rotation). Each component of the MMI matrix is finally computed as

$$W_{FM_{ij}} = \int_0^T \left| q_i(t)\, q_j(t) \right| dt, \tag{8.20}$$

where $W_{FM_{ij}}$ is the ij^{th} component of the MMI matrix. Then those (S)MDs are selected that their corresponding MMI have the maximum values. The same procedure can be applied to the linear mass and stiffness matrices of the boundary DOFs and select the (S)MDs of the interface modes. In other words, this time the mass and stiffness of the boundary DOFs reduced with IR can be integrated and the generalized coordinates, $\boldsymbol{q}_{IR}$, corresponding to the reduced boundary DOF can be used in Eq. (8.20) for the selection of interface (S)MDs.
The MMI criterion is a heuristic method, which works for (S)MDs selection in some structures. However, it is more efficient for some examples to simply select those (S)MDs with lowest indices number (e.g., 11, 12, 22, ...), which is used for the second example of this work.

8.4 Non-intrusive development of substructures' NLROMs

To obtain the NSCs of each substructure non-intrusively, a set of nonlinear static solutions must be performed. Therefore, the i^{th} line of Eq. (8.4) for a substructure reduces to

$$\hat{K}^{(1)}_{ij} q_j + \hat{K}^{(2)}_{ijl} q_j q_l + \hat{K}^{(3)}_{ijlp} q_j q_l q_p = \hat{f}_i + g_i. \tag{8.21}$$

The first step of non-intrusive identification of NSCs is selection of a reduction basis, which can accurately convey linear as well as nonlinear properties of the full-order model. Here, we introduced the EHCB as a novel basis for non-intrusive modal substructuring that enriches the reduction basis with modal derivatives. In this section, we briefly present three approaches to identify the NSCs of each substructure

8.4.1 Enhanced Applied Force for substructuring

The applied force method (also known as Implicit Condensation (IC)) [95] was already explained in section 7.2; however, we briefly review it here, and explain its

extension. This method was first developed for monolithic ROM and prescribes a set of nonlinear static forces to the FE code to solve for the corresponding induced displacements. These forces are built from a truncated number of linear Vibration Modes (VMs) of the system that are usually transverse-dominated forces. Therefore, the membrane-dominated DOFs are not accurately retrieved while using this method. To also accurately obtain the dynamic response of membrane DOF, the method of Implicit Condensation and Expansion (ICE) was introduced in [54]. Later, Kuether et al. [84] extended this method for nonlinear substructuring by using only the HCB modes as the reduction basis. Here, we extend this method by computing the MDs of the HCB modes in a non-intrusive approach and augmenting it to the reduction basis to identify the substructures' NSCs with IC. In this way, we show that no expansion as in [54, 84] is required to obtain the motion of the membrane DOFs at the cost of adding extra generalized coordinates to the reduction basis.
To compute the NCSs with the EHCB reduction basis, first a set of static forces are built from a combination of one, two or three columns of the basis as

$$\boldsymbol{f} = \begin{bmatrix} \boldsymbol{K}_{ii} & \boldsymbol{K}_{ib} \\ \boldsymbol{K}_{bi} & \boldsymbol{K}_{bb} \end{bmatrix} (\boldsymbol{T}_i q_i + \boldsymbol{T}_j \boldsymbol{q}_j + \boldsymbol{T}_k q_k), \quad i, j, k = 0, 1, 2, ..., m, \tag{8.22}$$

where $\boldsymbol{T}_i$ is the i^{th} column of the reduction basis $\boldsymbol{T}_{EHCB}$. These static forces are then prescribed to the FE code, where the substructure's FE model is developed to solve for the resulting displacement fields. The applied forces and obtained displacements are then projected into the modal domain. For the r^{th} load case, this reads,

$$\begin{aligned} \hat{\boldsymbol{f}}_r &= \boldsymbol{T}_{EHCB}^T \boldsymbol{f}_r \\ \boldsymbol{q}_r &= \boldsymbol{T}_{EHCB}^+ \boldsymbol{u}_r, \end{aligned} \tag{8.23}$$

where $\boldsymbol{u}_r$ and $\boldsymbol{q}_r$ are physical and modal displacements, respectively, and $\boldsymbol{f}_r$ and $\hat{\boldsymbol{f}}_r$ denote the physical and modal force vectors. After applying all the forces from the mentioned combination of the columns of the reduction basis, the resulting modal forces as well as displacements are introduced into the Eq. (8.4), where we are left with a set of over-determined linear equations and the NSCs are the only unknowns. The unknown NSCs are finally calculated using a regression method (e.g. least squares). We call our method for combining the IC method with the EHCB, the *IC-MD* or *IC-SMD* depending on the type of the modal derivatives that is used in the basis.

8.4.2 Enforced Displacement for substructuring

An alternative to the IC method is the Enforced Displacement (ED) method to identify the NSCs of a substructure, which is already described in Chapter 4 for monolithic ROM and we briefly review it here in substructuring framework. The original ED method [103] prescribes a set of nonlinear static displacement vectors to the FE code to solve for the corresponding reaction forces. As a novel approach, we extend the ED method for nonlinear substructuring and compare it with the IC-based approach. Here, the procedure of NSCs identification is the same as the work of Muravyov et al. [103], except that instead of the linear VMs, we use the EHCB reduction basis (Eqs. (8.13 or 8.17)) in the ED approach. In case the reduced linear stiffness matrix of

the substructure is obtained by direct projection of its full one, the first step is to set up two displacements from each column of the reduction basis with different signs, namely,

$$\boldsymbol{u}_r^{(a)} = q_r^{(a)} \boldsymbol{T}_r, \quad a = 1, 2, \tag{8.24}$$

The resulting reaction forces from these displacement are then projected into modal domain and substituted in Eq. (8.21) along with the modal coordinates to solve for $K_{irr}^{(2)}$ and $K_{irrr}^{(3)}$, which are the coefficients multiplied with the modal coordinates q_r^2 and q_r^3, respectively. The second step is to prescribe the displacements obtained from a combination of two columns of the EHCB reduction basis, namely,

$$\boldsymbol{u} = \begin{bmatrix} \boldsymbol{T_r} & \boldsymbol{T_s} \end{bmatrix} \begin{bmatrix} q_r & -q_r & q_r \\ q_s & -q_s & -q_s \end{bmatrix}, \; s \geq r. \tag{8.25}$$

To identify the coefficients $K_{isr}^{(2)}$ and $K_{issr}^{(3)}$, which are multiplied with the terms containing multiplication of two different modal coordinates (e.g., $q_s q_r$ and $q_s^2 q_r$). Finally, the last set of displacements are prescribed using combinations of three columns of the EHCB basis as

$$\boldsymbol{u} = \begin{bmatrix} \boldsymbol{T_r} & \boldsymbol{T_s} & \boldsymbol{T_t} \end{bmatrix} \begin{Bmatrix} q_r & q_s & q_t \end{Bmatrix}^T, \; t \geq s \geq r, \tag{8.26}$$

which result in identification of the coefficients $K_{itsr}^{(3)}$ that are multiplied with three different modal coordinates ($q_s q_r q_t$). When the ED method is combined with the EHCB basis, we call it *ED-MD* or *ED-SMD* depending on the type of the employed modal derivatives.

Enhanced Enforced Displacement

To speed up the identification process of ED in monolithic MOR, Perez et al. [116] introduced an approach of NSCs calculation from tangent stiffnesses, as output of the FE package, instead of reaction forces. We call this method as *Enhanced Enforced Displacement* (EED) and further use it for modal substructuring by employing the EHCB as the reduction basis to identify the NSCs of each substructure. The procedure of EED starts similar to the ED by applying two static displacements per columns of the EHCB basis. However, this time the nonlinear static analysis is sought for the TS instead of reaction forces as output. Each TS is then projected to the modal domain as

$$\hat{\boldsymbol{K}}^t(\boldsymbol{q}) = \boldsymbol{T}_{EHCB}^T \boldsymbol{K}^t(\boldsymbol{u}) \boldsymbol{T}_{EHCB}, \tag{8.27}$$

where $\boldsymbol{K}^t$ and $\hat{\boldsymbol{K}}^t$ are the full and reduced TS matrices, respectively. The relation between the NCSs and ir^{th} component of the reduced TS matrix reads

$$\begin{aligned} \hat{K}_{ir}^t &= \tfrac{\partial}{\partial q_r}[K_{ij}^{(1)} q_j + K_{ijl}^{(2)} q_j q_l + K_{ijlp}^{(3)} q_j q_l q_p] \\ &= K_{ir}^{(1)} + [K_{ijr}^{(2)} + K_{irj}^{(2)}] q_j + [K_{ijlr}^{(3)} + K_{ijrl}^{(3)} + K_{irjl}^{(3)}] q_j q_l. \end{aligned} \tag{8.28}$$

This implies that prescribing all displacements of the first step yields the coefficients $\hat{K}_{irj}^{(2)}$, $\hat{K}_{irjj}^{(3)}$, $\hat{K}_{ijjr}^{(3)}$, and $\hat{K}_{irrr}^{(3)}$ of the NSCs ($j > r$), as explained in Chapter 4. In the

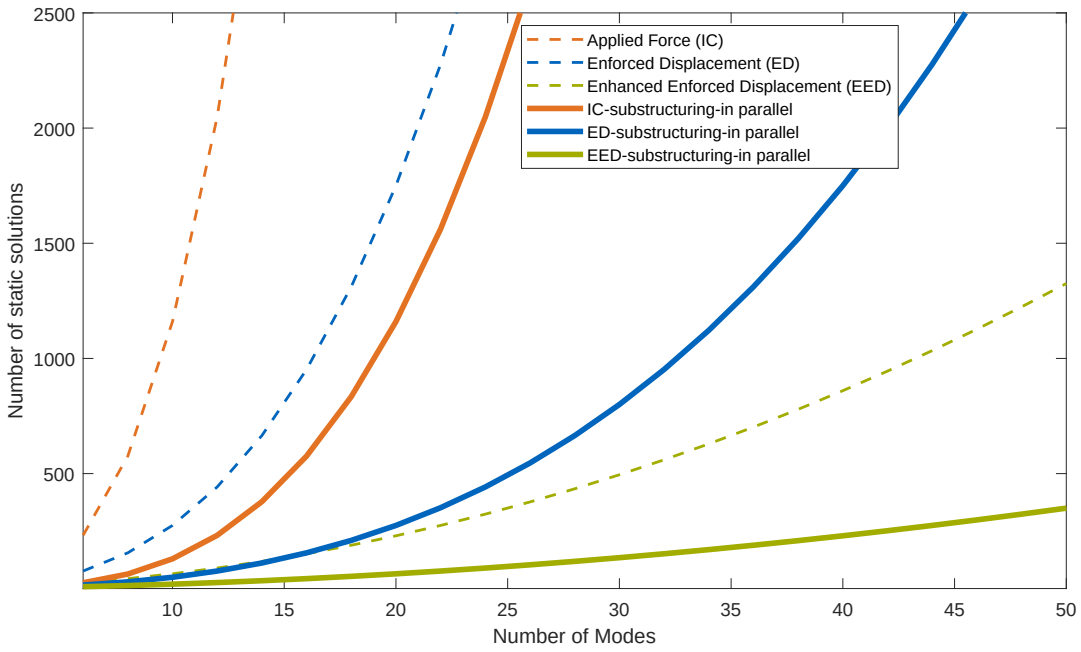

Figure 8.1: The number of required nonlinear static solutions versus the number of kept modes for different non-intrusive methods. For substructuring, the number of DOFs for the coupled system is divided into two equal substructures (as an example), and the curves are obtained for one substructure, assuming the identification procedure of substructures is performed in parallel.

second and last step, one displacement per combination of two columns of the the EHCB basis is generated and prescribed to the FE code:

$$\boldsymbol{u} = \boldsymbol{T}_j q_j + \boldsymbol{T}_l q_l. \tag{8.29}$$

This leads to obtaining the rest of the coefficients, namely $K^{(3)}_{iljr}$ $(l > j > r >)$. As can be observed in this method, the last step of the ED method is omitted for NSC's identification, which reduces the number of required nonlinear static solutions from $O(m^3)$ to $O(m^2)$.

Fig. 8.1 compares the number of static solutions versus the number of the kept modes in the reduction basis of each substructure's NLROM, when a structure is divided into two substructures, compared to the ones of monolithic NLROM. By dividing the structure into substructures, the NSCs identification procedure can be parallelized, leading to less offline computational costs. Even if the NSCs identification of substructures are not parallelized, the sum of the total static solutions for the NLROMs of two substructures are less than the number of static solutions required for developing a monolithic NLROM with the same number of the DOFs as the coupled system. This will be shown for the examined examples of this chapter. This figure also confirms the significant reduction in nonlinear solution while using EED. However, since we show in Chapters 9 and 5 that the accuracy of EED is less than ED when Abaqus is used, we only use ED for the displacement-based substructuring in this chapter.

8.5 Coupling of substructures' NLROM

After the NSCs of all substructures are computed, the NLROM for each substructure can be written as

$$\hat{\boldsymbol{M}}^{(s)}\ddot{\boldsymbol{q}}^{(s)}+\hat{\boldsymbol{D}}^{(s)}\dot{\boldsymbol{q}}^{(s)}+\hat{\boldsymbol{K}}^{(1)^{(s)}}\boldsymbol{q}^{(s)}+\underbrace{(\hat{\boldsymbol{K}}^{(2)^{(s)}}.\boldsymbol{q}^{(s)})}_{\boldsymbol{Q}_1^{(s)}(\boldsymbol{q})}\boldsymbol{q}^{(s)}+\underbrace{[(\hat{\boldsymbol{K}}^{(3)^{(s)}}.\boldsymbol{q}^{(s)}).\boldsymbol{q}^{(s)}]}_{\boldsymbol{Q}_2^{(s)}(\boldsymbol{q})}\boldsymbol{q}^{(s)}=\hat{\boldsymbol{f}}^{(s)}+\hat{\boldsymbol{g}}^{(s)} \tag{8.30}$$

where $\boldsymbol{Q}_1^{(s)}$ and $\boldsymbol{Q}_2^{(s)}$ are the displacement-dependent stiffness coefficients. To perform the coupling of substructures, the matrices as well as the tensors of the substructures' NLROM are cast into a block diagonal matrix form. Without loss of generality, for two substructures s_1 and s_2, this reads

$$\begin{aligned}
&\begin{bmatrix} \hat{\boldsymbol{M}}^{(s_1)} & \boldsymbol{0} \\ \boldsymbol{0} & \hat{\boldsymbol{M}}^{(s_2)} \end{bmatrix}\begin{Bmatrix} \ddot{\boldsymbol{q}}^{(s_1)} \\ \ddot{\boldsymbol{q}}^{(s_2)} \end{Bmatrix}+\begin{bmatrix} \hat{\boldsymbol{D}}^{(s_1)} & \boldsymbol{0} \\ \boldsymbol{0} & \hat{\boldsymbol{D}}^{(s_2)} \end{bmatrix}\begin{Bmatrix} \dot{\boldsymbol{q}}^{(s_1)} \\ \dot{\boldsymbol{q}}^{(s_2)} \end{Bmatrix}+\\
&\begin{bmatrix} \hat{\boldsymbol{K}}^{(s_1)} & \boldsymbol{0} \\ \boldsymbol{0} & \hat{\boldsymbol{K}}^{(s_2)} \end{bmatrix}\begin{Bmatrix} \boldsymbol{q}^{(s_1)} \\ \boldsymbol{q}^{(s_2)} \end{Bmatrix}+\begin{bmatrix} \boldsymbol{Q}_1^{(s_1)}(q^{(s_1)}) & \boldsymbol{0} \\ \boldsymbol{0} & \boldsymbol{Q}_1^{(s_2)}(\boldsymbol{q}^{(s_2)}) \end{bmatrix}\begin{Bmatrix} \boldsymbol{q}^{(s_1)} \\ \boldsymbol{q}^{(s_2)} \end{Bmatrix}+\\
&\begin{bmatrix} \boldsymbol{Q}_2^{(s_1)}(\boldsymbol{q}^{(s_1)}) & \boldsymbol{0} \\ \boldsymbol{0} & \boldsymbol{Q}_2^{(s_2)}(\boldsymbol{q}^{(s_2)}) \end{bmatrix}\begin{Bmatrix} \boldsymbol{q}^{(s_1)} \\ \boldsymbol{q}^{(s_2)} \end{Bmatrix}=\begin{Bmatrix} \hat{\boldsymbol{f}}^{(s_1)}+\hat{\boldsymbol{g}}^{(s_1)} \\ \hat{\boldsymbol{f}}^{(s_2)}+\hat{\boldsymbol{g}}^{(s_2)} \end{Bmatrix}
\end{aligned} \tag{8.31}$$

Then, a localization matrix $\boldsymbol{L}$ as in the classical FE method is defined that fulfills

$$\begin{Bmatrix} \boldsymbol{q}^{(s_1)} \\ \boldsymbol{q}^{(s_2)} \end{Bmatrix}=\boldsymbol{L}\,\boldsymbol{q}^{C} \tag{8.32}$$

where $\boldsymbol{q}^{C}$ is the unique set of coupled generalized coordinates [78]. Eq. (8.32) is finally introduced to Eq. (8.31) and the whole expression is pre-multiplied with $\boldsymbol{L}^T$ to nullify the interface forces. The coupled reduced system is then given by

$$\begin{aligned}
&\boldsymbol{L}^T\begin{bmatrix} \hat{\boldsymbol{M}}^{(s_1)} & \boldsymbol{0} \\ \boldsymbol{0} & \hat{\boldsymbol{M}}^{(s_2)} \end{bmatrix}\boldsymbol{L}\ddot{\boldsymbol{q}}^{C}+\boldsymbol{L}^T\begin{bmatrix} \hat{\boldsymbol{D}}^{(s_1)} & \boldsymbol{0} \\ \boldsymbol{0} & \hat{\boldsymbol{D}}^{(s_2)} \end{bmatrix}\boldsymbol{L}\dot{\boldsymbol{q}}^{C}+\\
&\boldsymbol{L}^T\begin{bmatrix} \hat{\boldsymbol{K}}^{(s_1)} & \boldsymbol{0} \\ \boldsymbol{0} & \hat{\boldsymbol{K}}^{(s_2)} \end{bmatrix}\boldsymbol{L}\boldsymbol{q}^{C}+\boldsymbol{L}^T\begin{bmatrix} \boldsymbol{Q}_1^{(s_1)}(\boldsymbol{q}^{(s_1)}) & \boldsymbol{0} \\ \boldsymbol{0} & \boldsymbol{Q}_1^{(s_2)}(\boldsymbol{q}^{(s_2)}) \end{bmatrix}\boldsymbol{L}\boldsymbol{q}^{C}+\\
&\boldsymbol{L}^T\begin{bmatrix} \boldsymbol{Q}_2^{(s_1)}(\boldsymbol{q}^{(s_1)}) & \boldsymbol{0} \\ \boldsymbol{0} & \boldsymbol{Q}_2^{(s_2)}(\boldsymbol{q}^{(s_2)}) \end{bmatrix}\boldsymbol{L}\boldsymbol{q}^{C}=\boldsymbol{L}^T\begin{Bmatrix} \hat{\boldsymbol{f}}^{(s_1)} \\ \hat{\boldsymbol{f}}^{(s_2)} \end{Bmatrix}
\end{aligned} \tag{8.33}$$

The localization matrix for the nonlinear EHCB without interface reduction can be written as

$$\begin{bmatrix} \boldsymbol{q}_{FM}^{(s_1)} \\ \boldsymbol{\xi}_{FM}^{(s_1)} \\ \boldsymbol{u}_b^{(s_1)} \\ \boldsymbol{q}_{FM}^{(s_2)} \\ \boldsymbol{\xi}_{FM}^{(s_2)} \\ \boldsymbol{u}_b^{(s_2)} \end{bmatrix}=\underbrace{\begin{bmatrix} \boldsymbol{I}_{m_1m_1}^{(s_1)} & \boldsymbol{0} & \boldsymbol{0} & \boldsymbol{0} & \boldsymbol{0} \\ \boldsymbol{0} & \boldsymbol{I}_{m_2m_2}^{(s_1)} & \boldsymbol{0} & \boldsymbol{0} & \boldsymbol{0} \\ \boldsymbol{0} & \boldsymbol{0} & \boldsymbol{0} & \boldsymbol{0} & \boldsymbol{I}_{bb}^{(s_1)} \\ \boldsymbol{0} & \boldsymbol{0} & \boldsymbol{I}_{m_1m_1}^{(s_2)} & \boldsymbol{0} & \boldsymbol{0} \\ \boldsymbol{0} & \boldsymbol{0} & \boldsymbol{0} & \boldsymbol{I}_{m_2m_2}^{(s_2)} & \boldsymbol{0} \\ \boldsymbol{0} & \boldsymbol{0} & \boldsymbol{0} & \boldsymbol{0} & \boldsymbol{I}_{bb}^{(s_2)} \end{bmatrix}}_{L_{EHCB}}\begin{bmatrix} \boldsymbol{q}_{FM}^{(s_1)} \\ \boldsymbol{\xi}_{FM}^{(s_1)} \\ \boldsymbol{q}_{FM}^{(s_2)} \\ \boldsymbol{\xi}_{FM}^{(s_2)} \\ \boldsymbol{u}_b^{C} \end{bmatrix} \tag{8.34}$$

where $\boldsymbol{L}_{EHCB}$ is the localization matrix for the EHCB reduced system. Furthermore, the localization matrix for system and local level IR methods with exact compatibility [80], when the (S)MDs of the interface modes are neglected, is given by

$$\begin{bmatrix} \boldsymbol{q}_{FM}^{(s_1)} \\ \boldsymbol{\xi}_{FM}^{(s_1)} \\ \boldsymbol{q}_{IR}^{(s_1)} \\ \boldsymbol{q}_{FM}^{(s_2)} \\ \boldsymbol{\xi}_{FM}^{(s_2)} \\ \boldsymbol{q}_{IR}^{(s_2)} \end{bmatrix} = \underbrace{\begin{bmatrix} \boldsymbol{I}_{m_1m_1}^{(s_1)} & \boldsymbol{0} & \boldsymbol{0} & \boldsymbol{0} & \boldsymbol{0} \\ \boldsymbol{0} & \boldsymbol{I}_{m_2m_2}^{(s_1)} & \boldsymbol{0} & \boldsymbol{0} & \boldsymbol{0} \\ \boldsymbol{0} & \boldsymbol{0} & \boldsymbol{0} & \boldsymbol{0} & \boldsymbol{I}_{m_3m_3}^{(s_1)} \\ \boldsymbol{0} & \boldsymbol{0} & \boldsymbol{I}_{m_1m_1}^{(s_2)} & \boldsymbol{0} & \boldsymbol{0} \\ \boldsymbol{0} & \boldsymbol{0} & \boldsymbol{0} & \boldsymbol{I}_{m_2m_2}^{(s_2)} & \boldsymbol{0} \\ \boldsymbol{0} & \boldsymbol{0} & \boldsymbol{0} & \boldsymbol{0} & \boldsymbol{I}_{m_3m_3}^{(s_2)} \end{bmatrix}}_{\boldsymbol{L}_{EHCB,IR}} \begin{bmatrix} \boldsymbol{q}_{FM}^{(s_1)} \\ \boldsymbol{\xi}_{FM}^{(s_1)} \\ \boldsymbol{q}_{FM}^{(s_2)} \\ \boldsymbol{\xi}_{FM}^{(s_2)} \\ \boldsymbol{q}_{b}^{C} \end{bmatrix} \tag{8.35}$$

and in case the (S)MDs for the LL-IR is included (for the SL-IR we cannot compute the (S)MDs, because the coupled full-order model is not accessible), it reads

$$\begin{bmatrix} \boldsymbol{q}_{FM}^{(s_1)} \\ \boldsymbol{\xi}_{FM}^{(s_1)} \\ \boldsymbol{q}_{IR}^{(s_1)} \\ \boldsymbol{\xi}_{IR}^{(s_1)} \\ \boldsymbol{q}_{FM}^{(s_2)} \\ \boldsymbol{\xi}_{FM}^{(s_2)} \\ \boldsymbol{q}_{IR}^{(s_2)} \\ \boldsymbol{\xi}_{IR}^{(s_2)} \end{bmatrix} = \underbrace{\begin{bmatrix} \boldsymbol{I}_{m_1m_1}^{(s_1)} & \boldsymbol{0} & \boldsymbol{0} & \boldsymbol{0} & \boldsymbol{0} & \boldsymbol{0} \\ \boldsymbol{0} & \boldsymbol{I}_{m_2m_2}^{(s_1)} & \boldsymbol{0} & \boldsymbol{0} & \boldsymbol{0} & \boldsymbol{0} \\ \boldsymbol{0} & \boldsymbol{0} & \boldsymbol{0} & \boldsymbol{0} & \boldsymbol{I}_{m_3m_3}^{(s_1)} & \boldsymbol{0} \\ \boldsymbol{0} & \boldsymbol{0} & \boldsymbol{0} & \boldsymbol{0} & \boldsymbol{0} & \boldsymbol{I}_{m_4m_4}^{(s_1)} \\ \boldsymbol{0} & \boldsymbol{0} & \boldsymbol{I}_{m_1m_1}^{(s_2)} & \boldsymbol{0} & \boldsymbol{0} & \boldsymbol{0} \\ \boldsymbol{0} & \boldsymbol{0} & \boldsymbol{0} & \boldsymbol{I}_{m_2m_2}^{(s_2)} & \boldsymbol{0} & \boldsymbol{0} \\ \boldsymbol{0} & \boldsymbol{0} & \boldsymbol{0} & \boldsymbol{0} & \boldsymbol{I}_{m_3m_3}^{(s_2)} & \boldsymbol{0} \\ \boldsymbol{0} & \boldsymbol{0} & \boldsymbol{0} & \boldsymbol{0} & \boldsymbol{0} & \boldsymbol{I}_{m_4m_4}^{(s_2)} \end{bmatrix}}_{\boldsymbol{L}_{EHCB,IR}} \begin{bmatrix} \boldsymbol{q}_{FM}^{(s_1)} \\ \boldsymbol{\xi}_{FM}^{(s_1)} \\ \boldsymbol{q}_{FM}^{(s_2)} \\ \boldsymbol{\xi}_{FM}^{(s_2)} \\ \boldsymbol{q}_{IR}^{C} \\ \boldsymbol{\xi}_{IR}^{C} \end{bmatrix} \tag{8.36}$$

where $\boldsymbol{L}_{EHCB,IR}$ is the localization matrix with IR.

8.6 Application to beam models

To evaluate the performance of the proposed approach, we first investigate modal substructuring of two simply-supported beam models with geometric nonlinear effect, as shown in Fig. 6.1. The material, geometry and mesh properties of the beams are given in Table 6.1. Moreover, the first six fixed-interface modes of the two substructures are shown in Figs. 8.2 and 8.3. The first six SMDs of the substructures are also depicted in Figs. 8.4 and 8.5. Since the shape of the SMDs and MDs are very similar to each other, the MDs are not plotted here. As can be seen from Figs 8.2 and 8.3, the fixed-interface modes are transverse dominated modes, while their corresponding SMDs represent the membrane motion of the beams. Therefore, the (S)MDs can take into account the transverse-membrane stretching effect and approximate in-plane motion while identifying NSCs.

NLROM	S_1	S_2	interface modes	total DOFs
	number of FIM		1	
NLHCB-ED-SMD-11	3	2		
or	number of (S)MDs			
NLHCB-IC-SMD-11	3 SMDs	2 SMDs		11
	number of FIM		1	
NLHCB-ED-SMD-22	4	3		
or	number of (S)MDs			
NLHCB-IC-SMD-22	8 SMDs	6 SMDs		22
	number of FIM		1	
NLHCB-ED-MD-11	3	2		
or	number of (S)MDs			
NLHCB-IC-MD-11	3 MDs	2 MDs		11
	number of FIM		1	
NLHCB-ED-MD-22	4	3		
or	number of (S)MDs			
NLHCB-IC-MD-22	8 MDs	6 MDs		22
	number of FIM		1	
NLHCB-ED-22	12	9		
or	number of (S)MDs			
NLHCB-IC-22	0	0		22

Table 8.1: The number of modes included in different developed NLROMs of the beam model by ED-(S)MD or IC-(S)MD.

Since the number of (S)MDs increase quadratically with respect to the number of modes, the MMI heuristic criterion is used for this example to select a few (S)MDs from a linear time integration of the reduced model (see section 8.3). Figs. 8.6a and 8.6b show the MMI of substructures S_1 and S_2 when 4 and 3 fixed-interface modes are used in the substructures' reduction basis, respectively. The (S)MDs are then selected according to the components of the MMI matrices with maximum components.
We developed NLROMs of this work in MATLAB and integrated them using the implicit Newmark time integration scheme, while the full-model is implicitly integrated in Abaqus, both with a time increment of 1×10^{-4} seconds and 4×10^4 time steps. All the NLROMs as well as the full-model are evaluated under different SPLs with the excitation frequency of $0-500$ Hz, which are uniformly distributed in space and random in time.
To compare different developed NLROMs with the full model, their PSDs are computed from their corresponding time integrated displacements. The Rayleigh damping of the form $\alpha\boldsymbol{M} + \beta\boldsymbol{K}$ with the parameters $\alpha = 4.70$ and $\beta = 6.85 \times 10^{-6}$ is used throughout all the time integrations, which keeps the damping ratios for all the modes in the excitation frequency less than 1%. Finally all the simulations throughout this work is performed on a desktop PC with 32 GB RAM and Intel® Xeon® CPU (3.6 GHz).

Convergence check

First a convergence check study is performed to investigate the robustness of the proposed methods. Table 8.1 demonstrates the different developed NLROMs with the ED-(S)MD method. The PSD of these NLROMs for the transverse as well as membrane directions of the points A and B are computed under 145dB SPL and shown in Fig. 8.7. It can be seen from this figure that as the number of fixed-interface modes as well as (S)MDs increases in the reduction basis of the NLROMs, the accuracy of their corresponding PSDs for both transverse and membrane directions improves significantly.
Furthermore, we performed the same analysis for the convergence check of the NLROMs developed by IC-(S)MD. Table 8.1 illustrates the ingredients of the reduction bases that are used to develop the NLROMs. Figs. 8.8a and 8.8c depict the PSDs of the NLROMs as well as the full-model for the transverse direction of points A and B, respectively. Figs. 8.8b and 8.8d show the PSDs of the membrane direction of A and B. As can be seen from these figures, increasing the number linear modes as well as the (S)MDs results in more accuracy of the obtained PSDs from the NLROMs.
The presented results of this section confirms the convergence of the proposed methods and also shows the number of fixed-interface modes and (S)MDs that are required to obtain accurate NLROMs.

Comparison of accuracy

Now we compare the accuracy of the NLROMs developed with different reduction bases and methods but with the same number of generalized coordinate. Four different NLROMs are evaluated under two SPLs of 135dB and 145dB, all with 22 DOFs and compared with the linear ROM with the same DOFs (LHCB-22) as well as the nonlinear full-order model.
Fig. 8.9 shows this comparison under the two mentioned excitation levels for the transverse as well as in-plane directions of point A (on substructure (S_1)). Fig. 8.11 shows the same analysis on the point B (on substructure (S_2)). As can be seen from these figures, nonlinear substructuring by the ED method and only with the linear HCB basis does not deliver accurate results for both transverse and in-plane directions, whereas the substructuring method based on IC with HCB delivers very accurate results only for the transverse direction. To obtain the accurate results also for membrane motion, the expansion procedure in [54] must be further performed, which is widely discussed in Chapter 7. However, the expansion procedure is avoided in this chapter, because it limits the relation between the transverse and membrane coordinates to be quadratic (which is valid for flat and shallow curved structures, but for some other structures it may be invalid).

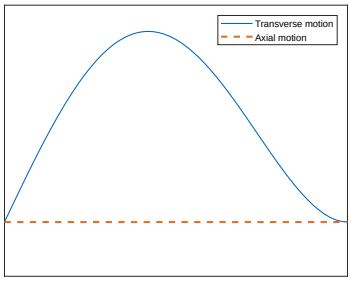

(a) $\varphi_1 : \omega_1 = 60.3$ Hz

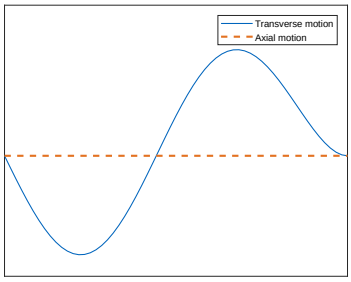

(b) $\varphi_2 : \omega_2 = 195.3$ Hz

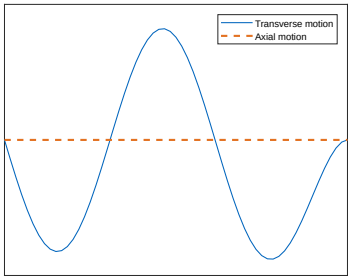

(c) $\varphi_3 : \omega_3 = 407.4$ Hz

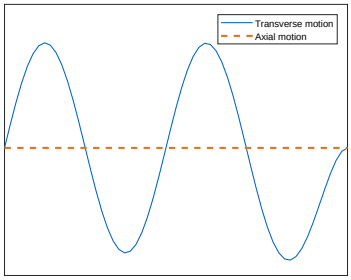

(d) $\varphi_4 : \omega_4 = 696.5$ Hz

Figure 8.2: The first four fixed-interface modes for the substructure S_1 of the flat beam model.

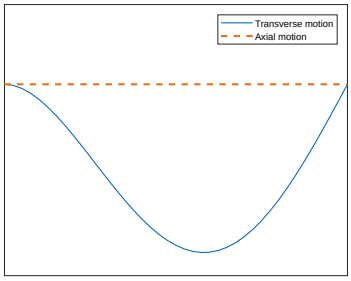

(a) $\varphi_1 : \omega_1 = 90.4$ Hz

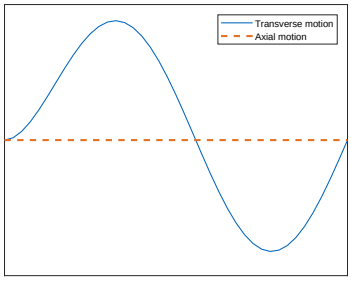

(b) $\varphi_2 : \omega_2 = 293.0$ Hz

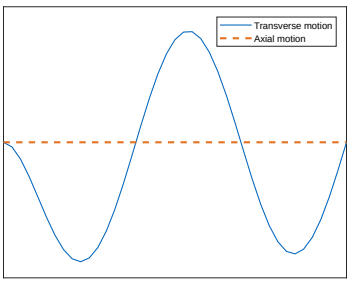

(c) $\varphi_3 : \omega_3 = 611.3$ Hz

Figure 8.3: The first three fixed-interface modes for the substructure S_2 of the flat beam model.

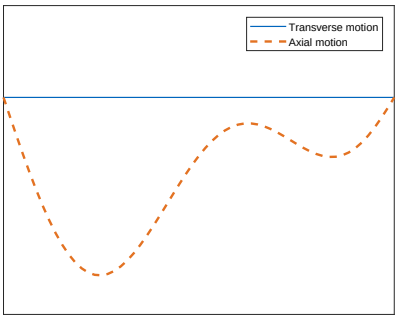

(a) $\theta_{11} = \frac{\partial \phi_1}{\partial q_1}$

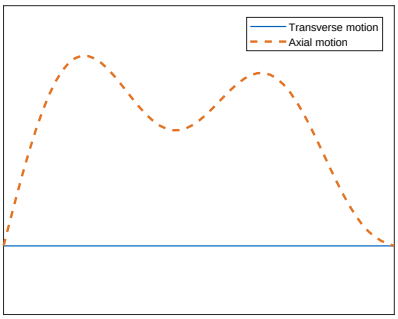

(b) $\theta_{12} = \theta_{21} = \frac{\partial \phi_1}{\partial q_2}$

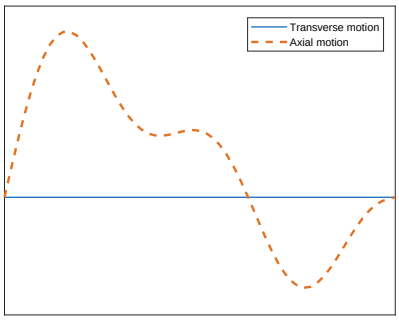

(c) $\theta_{13} = \theta_{31} = \frac{\partial \phi_1}{\partial q_3}$

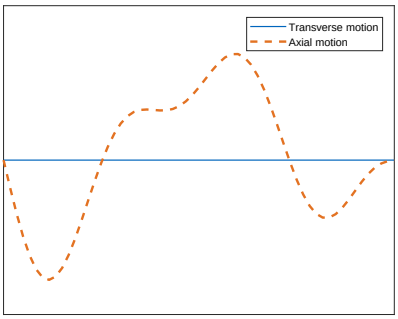

(d) $\theta_{14} = \theta_{41} = \frac{\partial \phi_1}{\partial q_4}$

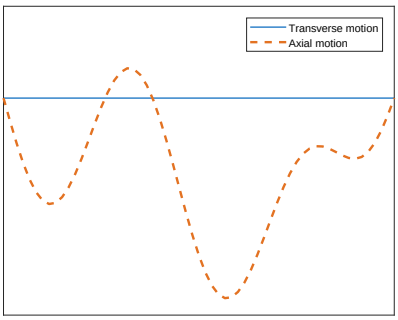

(e) $\theta_{22} = \frac{\partial \phi_2}{\partial q_2}$

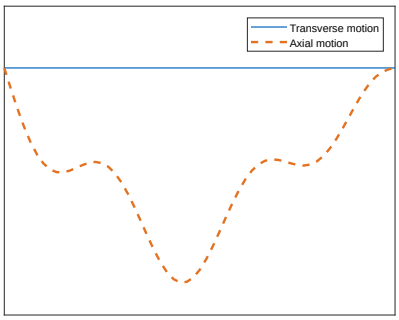

(f) $\theta_{23} = \theta_{32} = \frac{\partial \phi_2}{\partial q_3}$

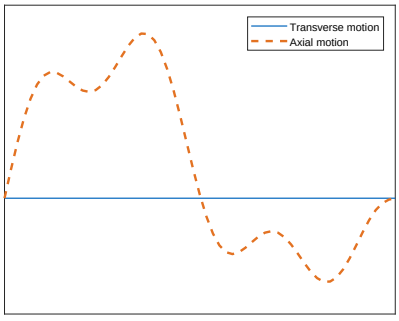

(g) $\theta_{24} = \theta_{42} = \frac{\partial \phi_2}{\partial q_4}$

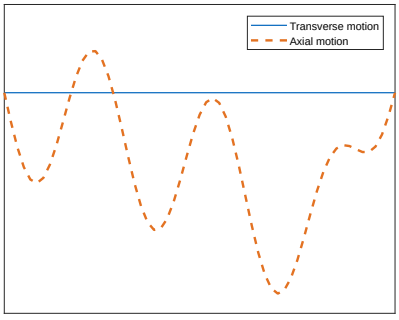

(h) $\theta_{33} = \frac{\partial \phi_3}{\partial q_3}$

Figure 8.4: The first eight static modal derivatives for the substructure S_1 of the flat beam model.

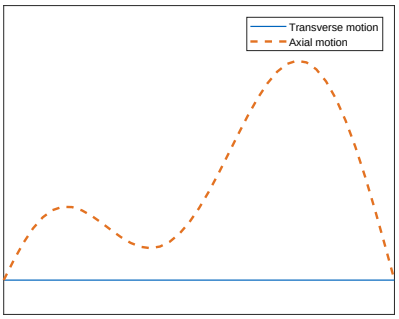

(a) $\theta_{11} = \frac{\partial \phi_1}{\partial q_1}$

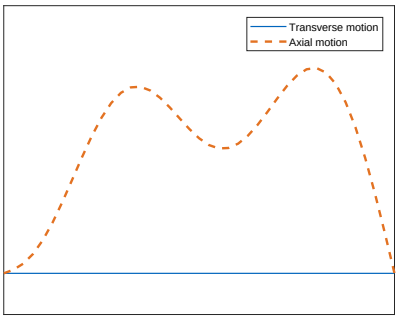

(b) $\theta_{12} = \theta_{21} = \frac{\partial \phi_1}{\partial q_2}$

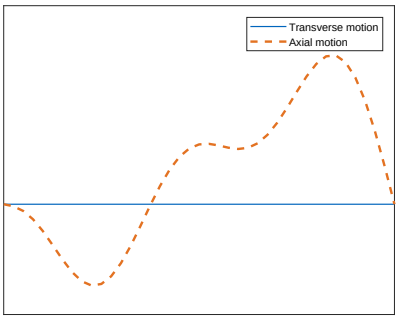

(c) $\theta_{13} = \theta_{31} = \frac{\partial \phi_1}{\partial q_3}$

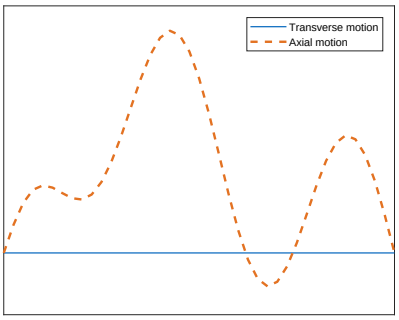

(d) $\theta_{22} = \frac{\partial \phi_2}{\partial q_2}$

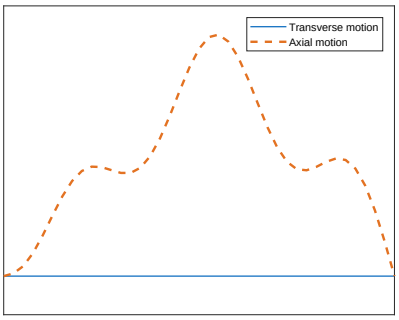

(e) $\theta_{23} = \theta_{32} = \frac{\partial \phi_2}{\partial q_3}$

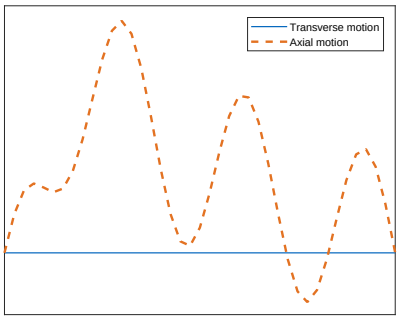

(f) $\theta_{33} = \frac{\partial \phi_3}{\partial q_3}$

Figure 8.5: The first six static modal derivatives for the substructure S_2 of the flat beam model.

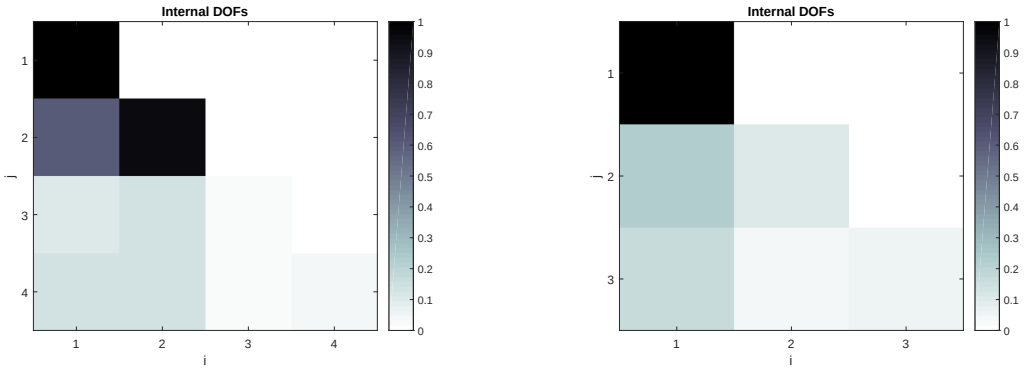

(a) MMI for substructure S_1

(b) MMI for substructure S_2

Figure 8.6: The maximum modal interaction criterion for the first four fixed-interface modes of substructure S_1 and the first three fixed-interface modes of substructure S_2 to select (S)MDs.

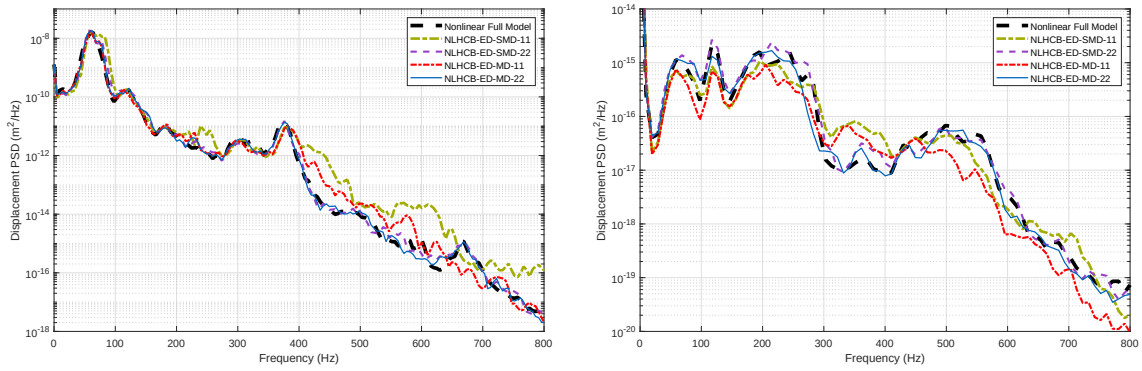

(a) Transverse DOF of point A.

(b) Membrane DOF of point A.

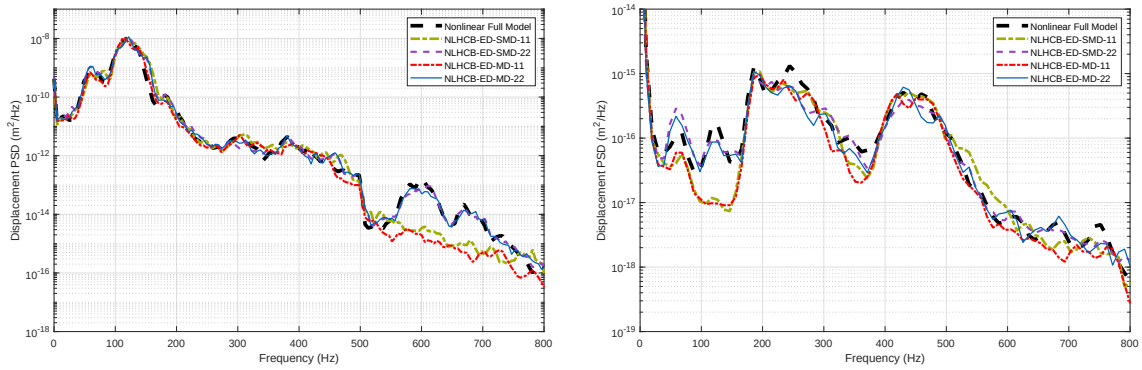

(c) Transverse DOF of point B.

(d) Membrane DOF of point B.

Figure 8.7: Flat beam model's displacement PSDs for convergence check analysis of the NLROMs developed by ED-(S)MD under 145 dB. The ingredients of the NLROM are demonstrated in Table 8.1.

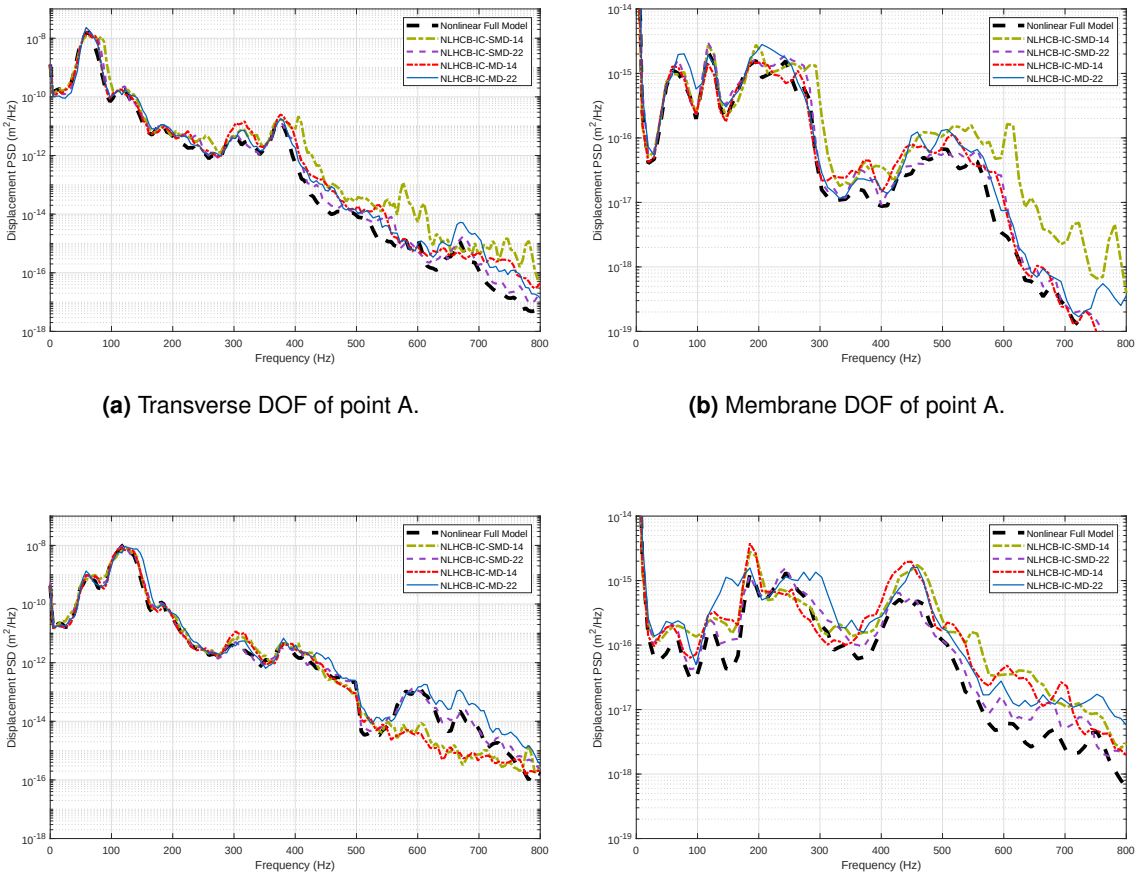

(a) Transverse DOF of point A.

(b) Membrane DOF of point A.

(c) Transverse DOF of point B.

(d) Membrane DOF of point B.

Figure 8.8: Flat beam model's displacement PSDs for convergence check analysis of the NLROMs developed by IC-(S)MD under 145 dB. The ingredients of the NLROMs are outlined in Table 8.1.

Furthermore, we observe from Figs. 8.9 and 8.11 that both proposed methods, namely, ED-(S)MD and IC-(S)MD exhibit accurate PSDs for both directions and in both shown points, compared to the reference results. Furthermore, the relative error of the investigated methods are compared for the first half seconds (out of four seconds) of the time signals that are used to compute the PSDs of Figs. 8.9 and 8.11 and depicted in Figs. 8.10 and 8.12. These figures confirm that the relative error of the NLROMs from the proposed substructuring methods are less than the other investigated methods and the least relative error belongs to the nonlinear substructuring approach with ED-(S)MD.

Finally, we compare the number of nonlinear static solutions that are required to identify the NSCs of each substructure to obtain the assembled NLROMs used in Figs. 8.9 and 8.11. Table 8.2 shows the number of these static solution for the substructures as well as the whole assembly. As can be seen from this table, if the same number of generalized coordinates are used in the NLROMs, the number of required static solutions by the displacement-based method is less than the force-based method. This was also visualized in Fig. 8.1. However, the number of required DOFs to develop a proper NLROM with ICE is usually half of those required by (E)ED, at least for flat structures.

This result together with the accuracy comparison that is performed in Figs. 8.9 and

8.11 draw the conclusion that our developed modal substructuring based on ED-(S)MD is performing well, because it presents accurate dynamic results in transverse and membrane directions, compared to the full-order model. It can also have moderate offline computational costs to develop an NLROM, if the tangent stiffness procedure can be employed to identify its NSCs. Moreover, it does not have the expansion limitation of ICE, which requires a quadratic relation between transverse-membrane DOFs to obtain the displacements of in-plane DOFs.

Model	S_1	S_2	Total substructuring	Monolithic ROM
NLHCB-IC-22	2626	1160	3786	13288
NLHCB-IC-SMD-22	2626	1160	3786	13288
NLHCB-ED-22	546	275	821	2277
NLHCB-ED-SMD-22	546	275	821	2277

Table 8.2: Number of nonlinear static solutions for NSCs identification of the beam's NLROMs with substructuring and monolithic.

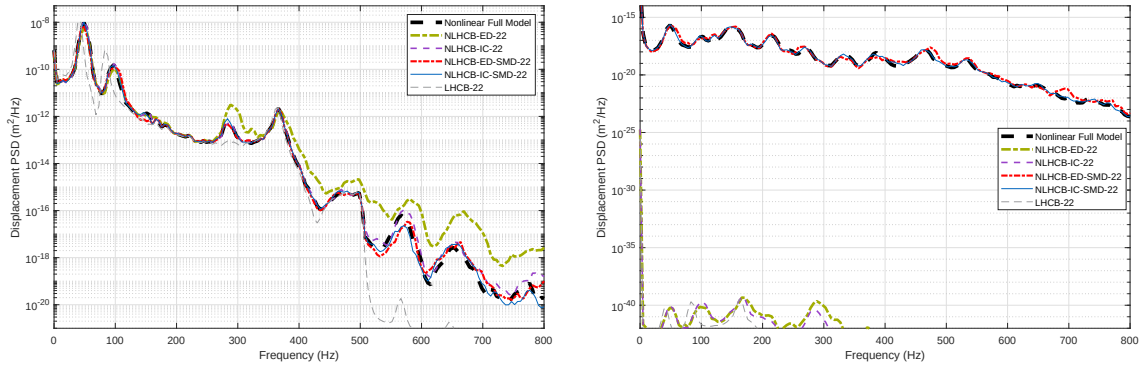

(a) Transverse DOF of point A under 135 dB SPL load. **(b)** Membrane DOF of point A under 135 dB SPL load.

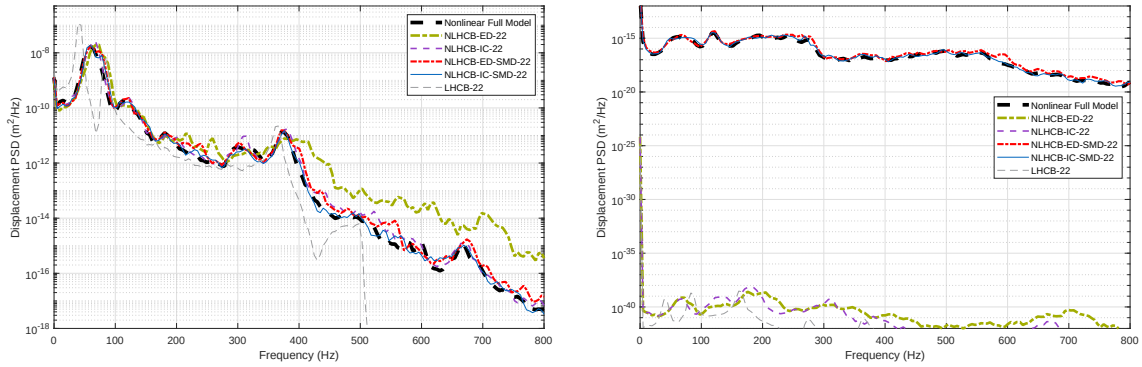

(c) Transverse DOF of point A under 145 dB SPL load. **(d)** Membrane DOF of point A under 145 dB SPL load.

Figure 8.9: Displacement PSD comparison of the beam's full model with the NLROMs developed by different methods and bases, all with 22 DOFs. The comparison is performed under 135 and 145 dB SPL for transverse and membrane directions. The ingredients of the NLROMs are outlined in Table 8.1.

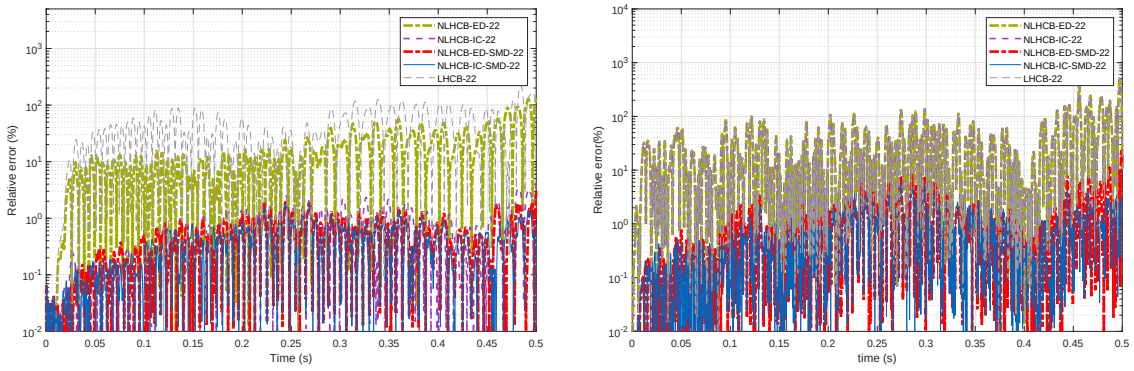

(a) Transverse DOF of point A under 135 dB SPL load. **(b)** Membrane DOF of point A under 135 dB SPL load.

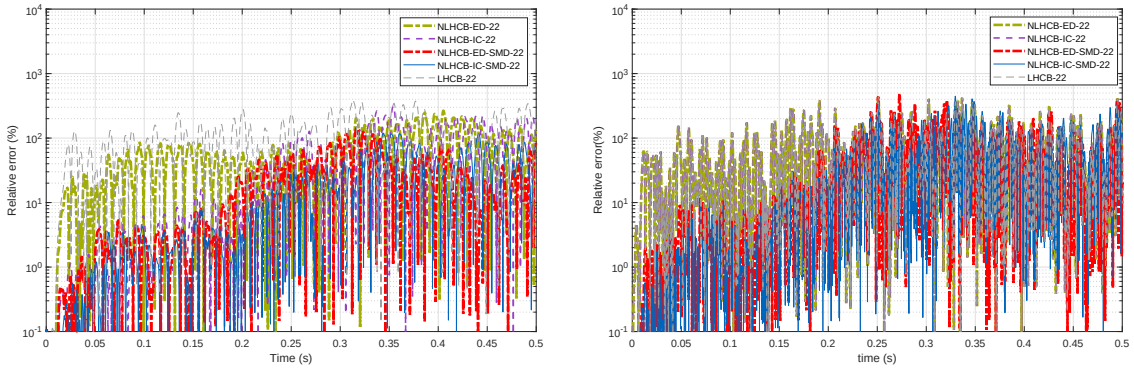

(c) Transverse DOF of point A under 145 dB SPL load. **(d)** Membrane DOF of point A under 145 dB SPL load.

Figure 8.10: Flat beam's relative error comparison for the first half seconds (out of four seconds) of the time signals that are used to compute the PSDs of Fig. 8.9.

8.7 Application on nonlinear panels

The second case study to assess the performance of the proposed method is the panel structure composed of two substructures, as shown in Fig. 6.3. Both substructure are simply supported at all edges and coupled through three rotational DOFs per node. The material, geometry and mesh properties of the substructures are given in Table 6.3. The time integration conditions for developed NLROMs as well as the full model for this example are chosen the same as the beam model. like the previous example, we impose SPL excitations, which are random in time and uniform in space and all have the excitation frequency range of $0-500$ Hz. The Rayleigh damping coefficients are chosen as $\alpha = 16.2$ and $\beta = 2.85 \times 10^{-6}$, which lead to damping ratios less than 1% for all the modes within the frequency range of excitation.
To have an insight into the fixed-interface mode shapes of the substructures, the first seven and five of them for the substructures S_1 and S_2 are plotted in Figs. 8.13 and 8.14, respectively. As can be seen from these figures, the first kept fixed-interface modes for both substructures are transverse modes and cannot represent the membrane motion in the presence of nonlinearity. To obtain the membrane motion of the nonlinear substructures, we compute the (S)MDs of the fixed-interface modes and

append them to the basis. Figs. 8.15 and 8.16 depict the first eight and six SMDs of the substructures S_1 and S_2, respectively, which are used in the reduction basis of the substructures. Since the shape of MDs are very similar to the SMDs, they are not depicted here. These figures display that all the used (S)MDs are membrane-dominated vectors, which can approximate the membrane-stretching effects for nonlinear deformations.
Furthermore, to select the kept (S)MDs in the reduction basis, the ones with lowest indices are chosen in this example instead of using the MMI heuristic criterion, because it is found that choosing the (S)MDs with lowest indices delivers better results.

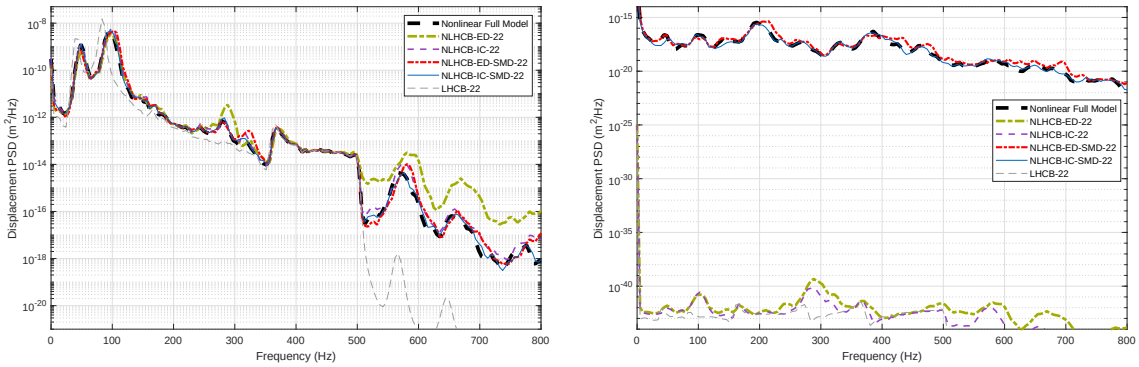

(a) Transverse DOF of point B under 135 dB SPL load. **(b)** Membrane DOF of point B under 135 dB SPL load.

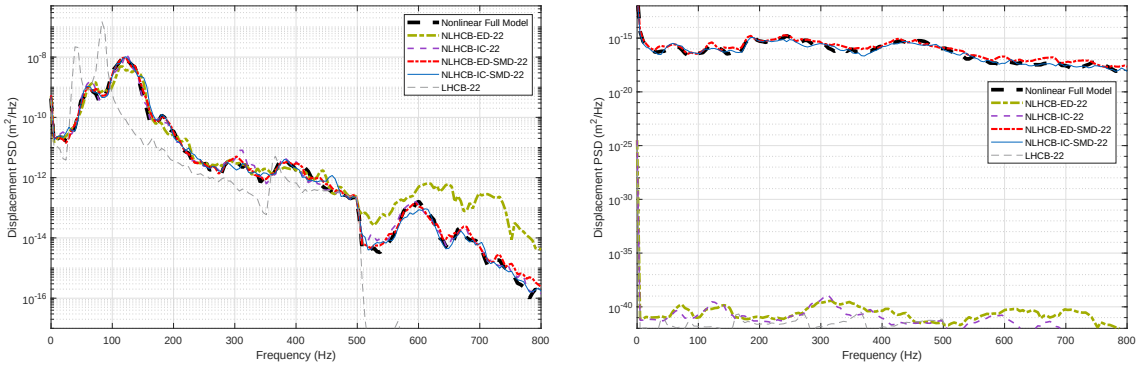

(c) Transverse DOF of point B under 145 dB SPL load. **(d)** Membrane DOF of point B under 145 dB SPL load.

Figure 8.11: Displacement PSD comparison of the beam's full model with the NLROMs developed by different methods and bases, all with 22 DOFs. The comparison is performed under 135 and 145 dB SPL for transverse and membrane directions. The ingredients of the NLROMs are outlined in Table 8.1.

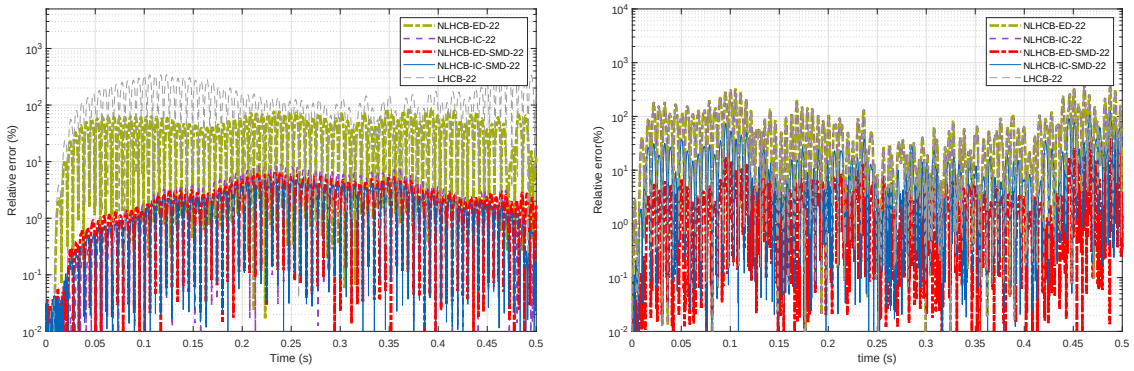

(a) Transverse DOF of point A under 135 dB SPL load. **(b)** Membrane DOF of point A under 135 dB SPL load.

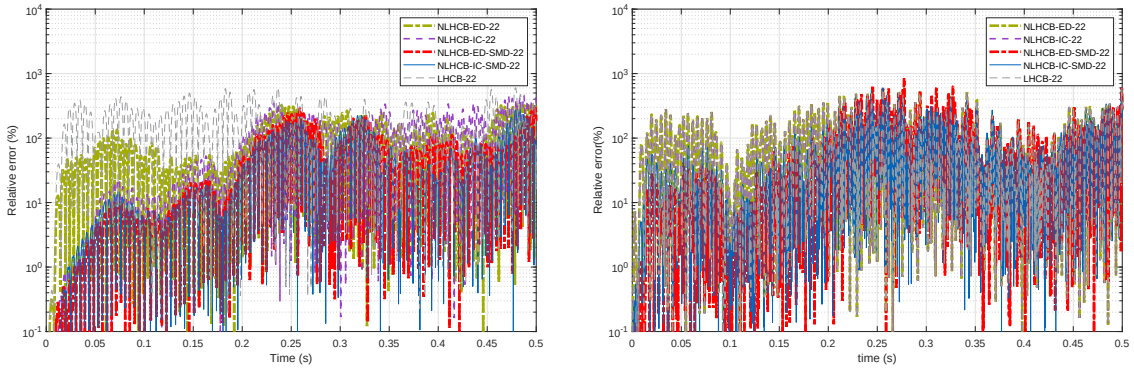

(c) Transverse DOF of point A under 145 dB SPL load. **(d)** Membrane DOF of point A under 145 dB SPL load.

Figure 8.12: Flat beam's relative error comparison for the first half seconds of the time signal that is used to compute the PSDs of Fig. 8.11.

Convergence check

The convergence check analysis of nonlinear substructuring with both ED-(S)MD and IC-(S)MD is performed for this example. For each method four different reduction bases are selected and their corresponding NLROMs are developed. The ingredients of the two substructures' reduction bases for the developed NLROMs by ED-(S)MD and IC-(S)MDs are illustrated in Table 8.3. The number of SL interface modes are selected as three modes, according to the convergence study performed in section 6.6.2.

Figs. 8.17a and 8.17b display the PSDs of the transverse and membrane directions of point A (on substructure S_1), respectively, for the defined NLROMs in Table 8.3 and developed by ED-(S)MD, under an SPL of 155 dB. The same results for the point B on substructure S_2 are depicted in Appendix B. These figures show that increasing the number of fixed interface modes as well as (S)MDs in the reduction basis of the substructuring by ED-(S)MD result in improvement of the PSDs accuracy for both directions. Besides, it can be seen from these figures that using SMDs instead of MDs does not induce any significant difference in the accuracy of the PSDs in both directions.

Moreover, Figs. 8.17c and 8.17d depict the PSDs of the defined NLROMs in Table 8.3 and developed by IC-(S)MD, for the transverse and membrane directions of point *A*, and the same PSDs for point *B* are shown in Appendix B. These figures acknowledge the convergence of the developed NLROMs using IC-(S)MD method to the full model response by increasing the number of fixed-interface modes and (S)MDs.

NLROM	S_1	S_2	interface modes	total DOFs
	number of FIM		3	
NLHCB-ED-SMD-13	3	2		
or	number of (S)MDs			
NLHCB-IC-SMD-13	3 SMDs	2 SMDs		13
	number of FIM		3	
NLHCB-ED-SMD-32	7	5		
or	number of (S)MDs			
NLHCB-IC-SMD-32	12 SMDs	5 SMDs		32
	number of FIM		3	
NLHCB-ED-MD-13	3	2		
or	number of (S)MDs			
NLHCB-IC-MD-13	3 MDs	2 MDs		13
	number of FIM		3	
NLHCB-ED-MD-32	7	5		
or	number of (S)MDs			
NLHCB-IC-MD-32	12 MDs	5 MDs		32
	number of FIM		3	
NLHCB-ED-32	19	10		
or	number of (S)MDs			
NLHCB-IC-32	0	0		32

Table 8.3: The number of modes included in different developed NLROMs of the panel model by ED-(S)MD or IC-(S)MD.

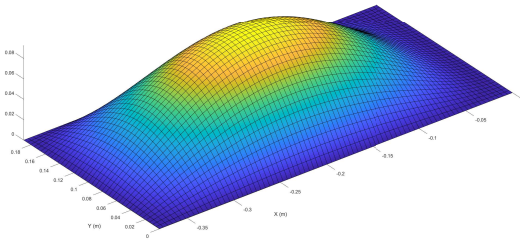

(a) φ_1 : $\omega_1 = 157.0$ Hz

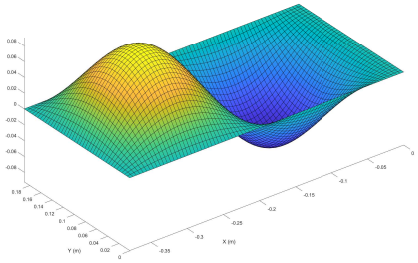

(b) φ_2 : $\omega_2 = 261.1$ Hz

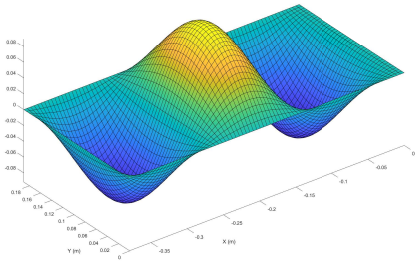

(c) φ_3 : $\omega_3 = 427.8$ Hz

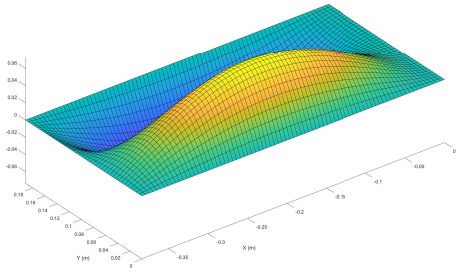

(d) φ_4 : $\omega_4 = 514.6$ Hz

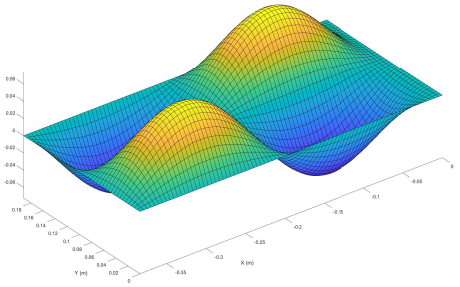

(e) φ_5 : $\omega_5 = 613.3$ Hz

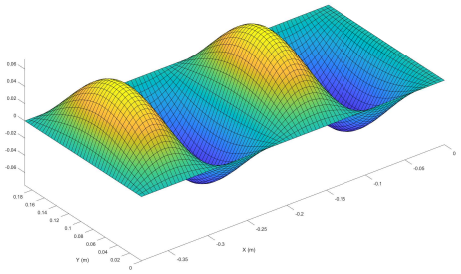

(f) φ_6 : $\omega_6 = 654.9$ Hz

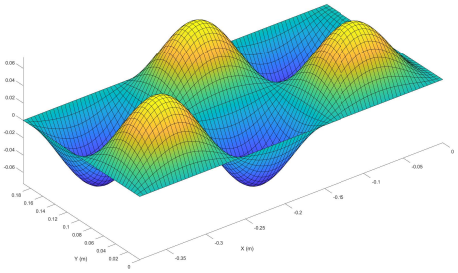

(g) φ_7 : $\omega_7 = 776.1$ Hz

Figure 8.13: The first seven vibration modes for the substructure S_1 of the flat beam model.

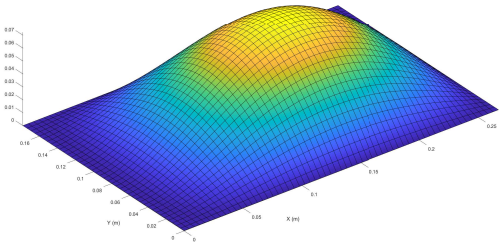

(a) $\varphi_1 : \omega_1 = 190.0$ Hz

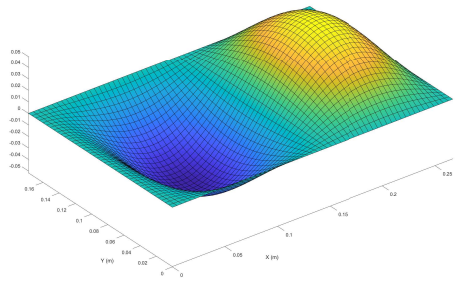

(b) $\varphi_2 : \omega_2 = 378.1$ Hz

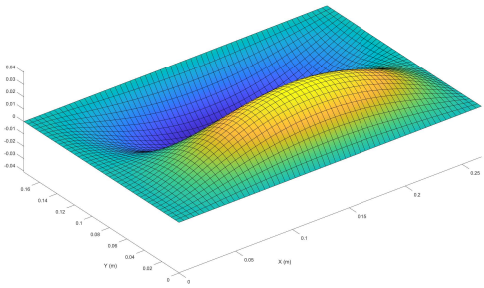

(c) $\varphi_3 : \omega_3 = 544.2$ Hz

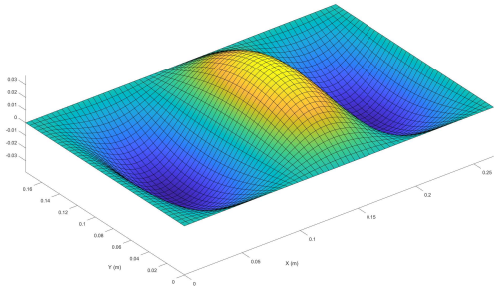

(d) $\varphi_4 : \omega_4 = 675.6$ Hz

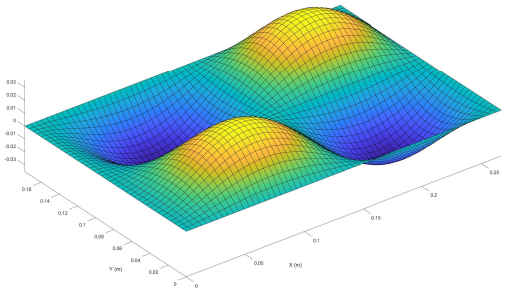

(e) $\varphi_5 : \omega_5 = 724.1$ Hz

Figure 8.14: The first five vibration modes for the substructure S_2 of the flat beam model.

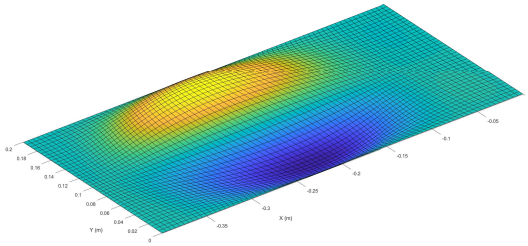

(a) $\theta_{11} = \frac{\partial \phi_1}{\partial q_1}$

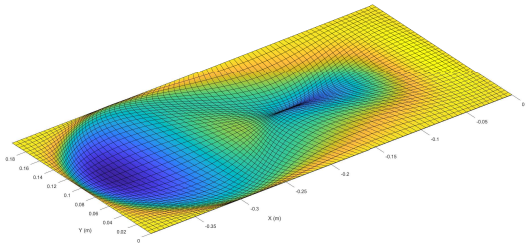

(b) $\theta_{12} = \theta_{21} = \frac{\partial \phi_1}{\partial q_2}$

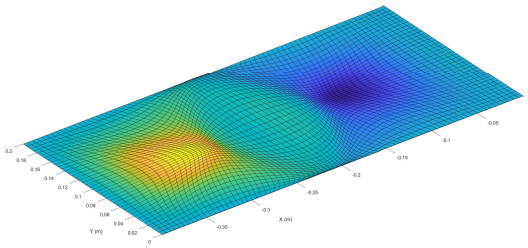

(c) $\theta_{13} = \theta_{31} = \frac{\partial \phi_1}{\partial q_3}$

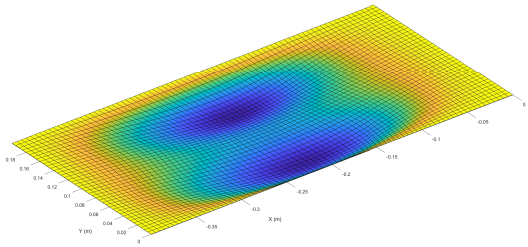

(d) $\theta_{14} = \theta_{41} = \frac{\partial \phi_1}{\partial q_4}$

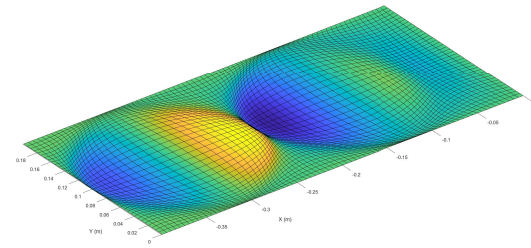

(e) $\theta_{22} = \frac{\partial \phi_2}{\partial q_2}$

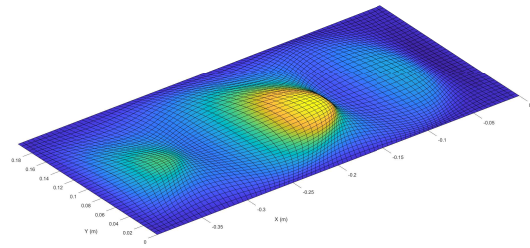

(f) $\theta_{23} = \theta_{32} = \frac{\partial \phi_2}{\partial q_3}$

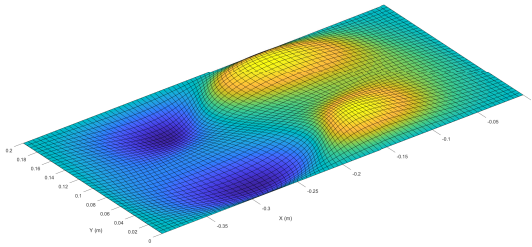

(g) $\theta_{24} = \theta_{42} = \frac{\partial \phi_2}{\partial q_4}$

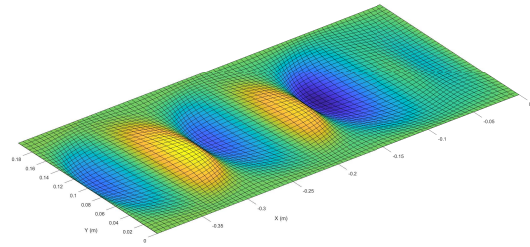

(h) $\theta_{33} = \frac{\partial \phi_3}{\partial q_3}$

Figure 8.15: The first eight static modal derivatives for the substructure S_1 of the panel model.

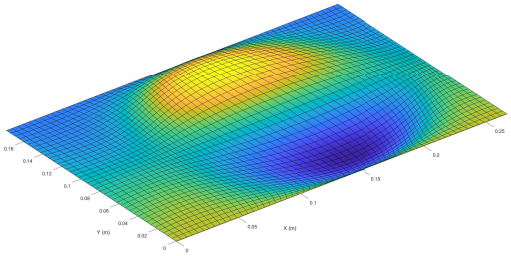

(a) $\theta_{11} = \frac{\partial \phi_1}{\partial q_1}$

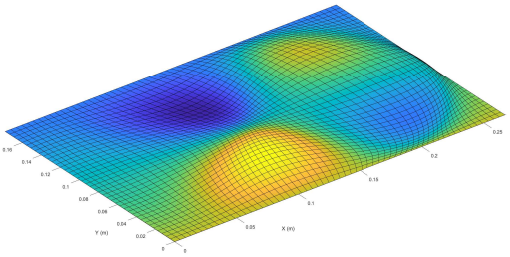

(b) $\theta_{12} = \theta_{21} = \frac{\partial \phi_1}{\partial q_2}$

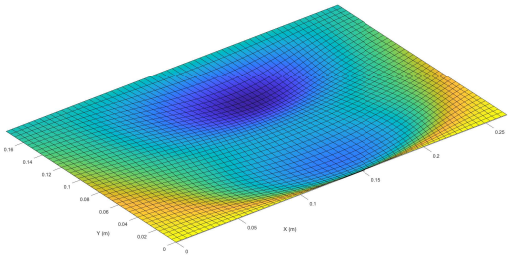

(c) $\theta_{13} = \theta_{31} = \frac{\partial \phi_1}{\partial q_3}$

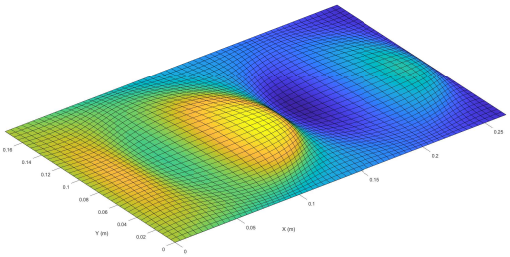

(d) $\theta_{22} = \frac{\partial \phi_2}{\partial q_2}$

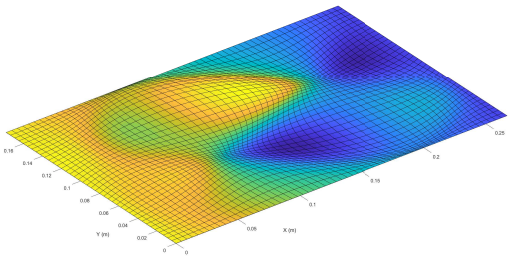

(e) $\theta_{23} = \theta_{32} = \frac{\partial \phi_2}{\partial q_3}$

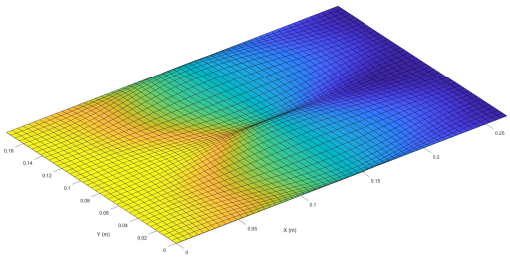

(f) $\theta_{33} = \frac{\partial \phi_3}{\partial q_3}$

Figure 8.16: The first six static modal derivatives for the substructure S_2 of the flat panel model.

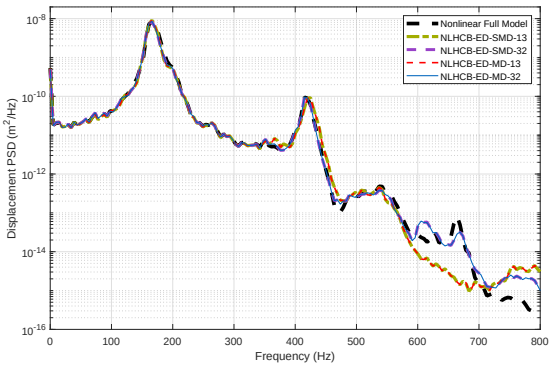

(a) Transverse DOF of point A.

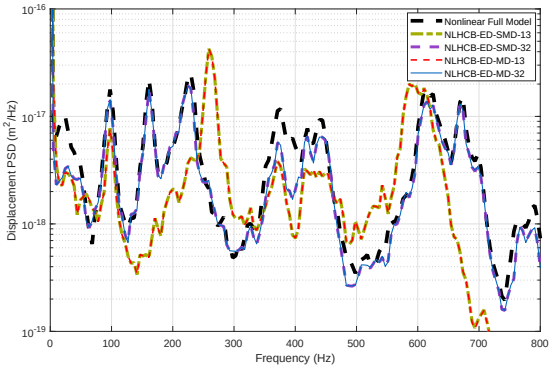

(b) Membrane DOF of point A.

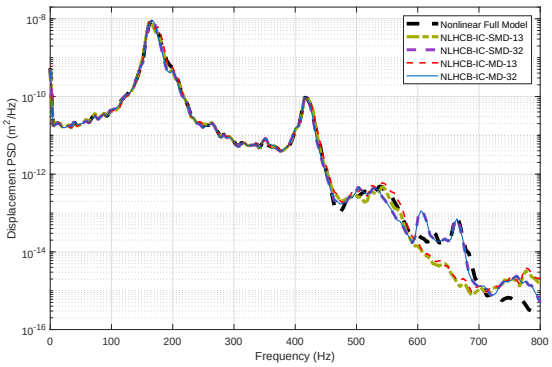

(c) Transverse DOF of point A.

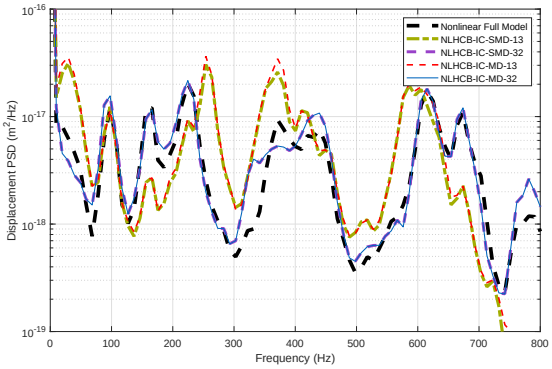

(d) Membrane DOF of point A.

Figure 8.17: Panel model's displacement PSDs for convergence check analysis of the NLROMs developed by ED-(S)MD and IC-(S)MD under 155 dB. The ingredients of the NLROM are outlined in Table 8.3.

Comparison of accuracy

The NLROMs of the panel assembly are developed by four different methods, namely, ED, IC, ED-SMD and IC-SMD, and compared under two SPLs of 140 dB and 155 dB. All the NLROMs have the same dimension (32 DOFs) and are compared with the nonlinear full model as well as the linear reduced model with 32 DOFs (LHCB-32). This comparison is shown in Figs. 8.18a and 8.18c for the transverse direction and in Figs. 8.18b and 8.18d for the in-plane direction of point *A*. The ingredients of the developed NLROMs (their names are in the legend of the figures) are shown in Table 8.3. For the transverse direction of point *A*, the PSD of three methods, namely, NLHCB-IC, NLHCB-ED-SMD and NLHCB-IC-SMD are accurately representing the full model for both low and high excitation levels. However, the PSD of NLHCB-ED is not as accurate as the other methods for both excitation levels. This is due to the fact that in this method only linear transverse-dominated HCB displacements are used to identify the NSCs of each substructures, which does not serve appropriately when the transverse-membrane coupling of the modes are activated.
Furthermore, for the membrane direction of point A, our proposed methods, NLHCB-

ED-SMD and NLHCB-IC-SMD, represent accurate PSDs for both excitation levels. Among these NLROMs, NLHCB-ED-SMD represents the best approximation of the full model's PSD. This is because the utilized modal derivatives instead of linear HCB modes in the reduction basis of the substructures are in-plane dominated modes, as shown in Figs. 8.15 and 8.16. Therefore, the modal coordinates and their corresponding identified NSCs for each substructure contain their representative in-plane displacements when they are transformed back to to the physical domain.

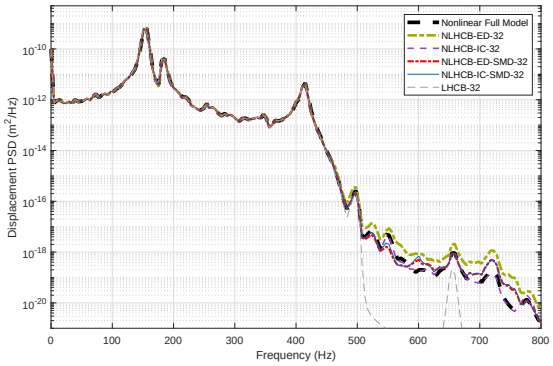

(a) Transverse DOF of point A under 140 dB SPL load.

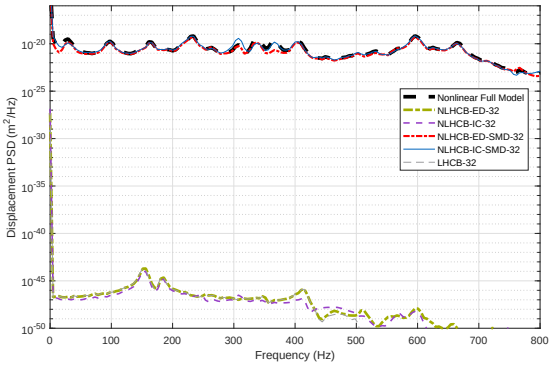

(b) Membrane DOF of point A under 140 dB SPL load.

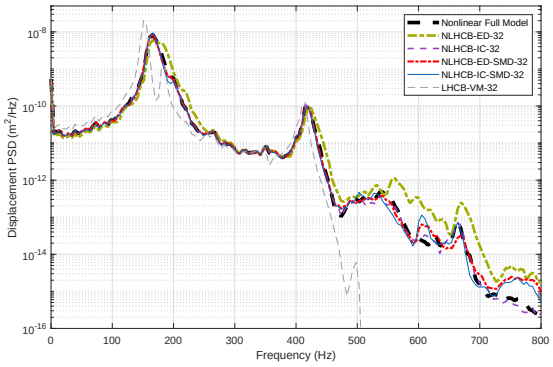

(c) Transverse DOF of point A under 155 dB SPL load.

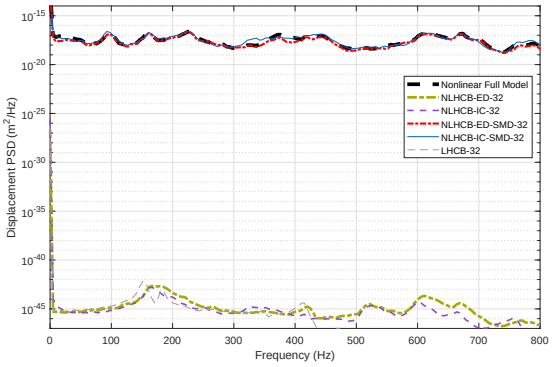

(d) Membrane DOF of point A under 155 dB SPL load.

Figure 8.18: Displacement PSD comparison of the panel's full model with the NLROMs developed by different methods and bases, all with 32 DOFs. The comparison is performed under 140 dB and 155 dB SPL for transverse and membrane directions. The ingredients of the NLROM are outlined in Table 8.3.

Model	S_1	S_2	Total substructuring	Monolithic ROM
NLHCB-IC-32	13288	2626	15914	41728
NLHCB-IC-SMD-32	13288	2626	15914	41728
NLHCB-ED-32	2277	546	2823	6512
NLHCB-ED-SMD-32	2277	546	2823	6512

Table 8.4: Number of nonlinear static solutions for NSCs identification of the panel's NLROMs with substructuring and monolithic.

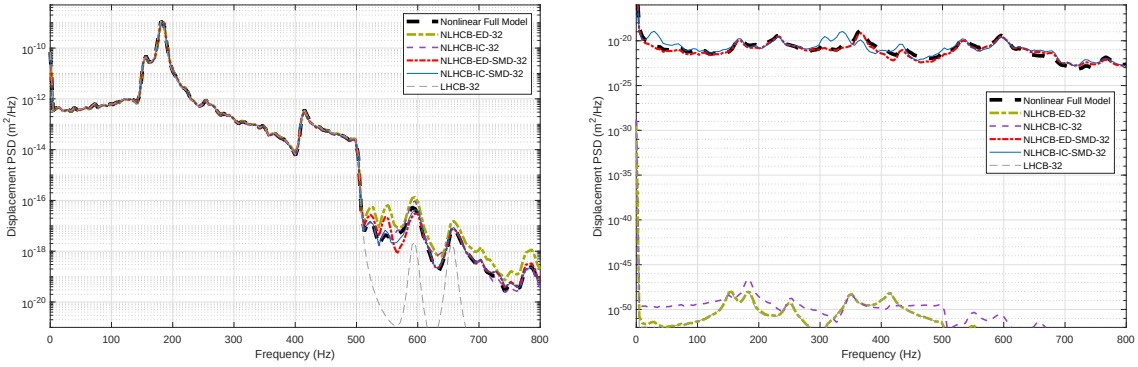

(a) Transverse DOF of point B under 140 dB SPL load. **(b)** Membrane DOF of point B under 140 dB SPL load.

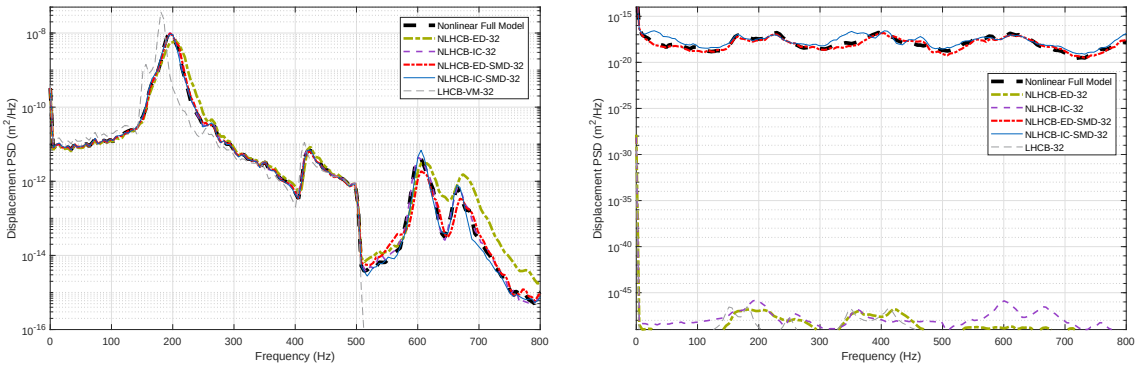

(c) Transverse DOF of point B under 155 dB SPL load. **(d)** Membrane DOF of point B under 155 dB SPL load.

Figure 8.19: Displacement PSD comparison of the panel's full model with the NLROMs developed by different methods and bases, all with 32 DOFs. The comparison is performed under 140 dB and 155 dB SPLs for transverse and membrane directions. The ingredients of the NLROM are outlined in Table 8.3.

To show the same accuracy on substructure S_2, the developed NLROMs are compared for the transverse and in-plane DOFs of point B. Fig. 8.19 shows this comparison for both directions and under the two mentioned SPLs. This figure shows that all the NLROMs except the NLHCB-ED have acceptable PSDs in transverse direction compared to the reference one, although the NLHCB-IC has the highest accuracy for high frequency levels ($500-800$ Hz). The reason for this is that all the used modes in the reduction basis of NLHCB-IC contain transverse dominated HCB modes, which can capture all the internal resonances with high frequency transverse modes. However, for the in-plane motion of point B, those NLROMs have acceptable results whose reduction basis comprise non-intrusive modal derivatives, namely, NLHCB-ED-SMD and NLHCB-IC-SMD. As can be seen from Figs. 8.19b and 8.19d, the nonlinear substructuring based on ED-SMD (NLHCB-ED-SMD) has the most accurate PSD result in membrane direction for both excitation levels.
Finally, the number of required nonlinear static solutions to develop the NLROMs, which are used in Figs. 8.18 and 8.19 for both substructures are shown in Table 8.4. This table compares these numbers when the same number of DOFs is used in the NLROMs developed by different methods. However, to develop proper NLROMs

with different methods, the numbers of required DOFs can be different, which is not considered in this table.

8.8 Summary

This chapter proposes a generic form of modal substructuring of geometrically nonlinear FE models, which can be used in efficient dynamic analysis of structures. This method is based on non-intrusive model order reduction approach, which has the advantage of being useful in case an FE model is developed in a commercial software.
In this method, we present a non-intrusive Enhanced Hurty/Craig-Bampton (EHCB) reduction basis to reduce the linear matrices of substructures as well as identify their nonlinear stiffness coefficients. The EHCB basis contains the classical HCB modes augmented with the non-intrusive modal derivatives of them to account the nonlinear interaction between the modes.
The procedure of identification of nonlinear stiffness coefficients for each substructure can be performed either by force-based or displacement-based non-intrusive methods. However, we demonstrate in this work that using the displacement-based method results in less offline computational costs while more accuracy of the nonlinear reduced order models is achieved.
One reason that nonlinear modal substructuring with displacement-based substructuring approach was not possible before, is that it was not possible to obtain accurate result using only the HCB modes as for substructuring with ICE. However, we solve this problem with our presented basis and show that it delivers accurate results. To assess the performance of the proposed method, we apply it to two finite element examples containing geometric nonlinear beam and shell elements. We develop the nonlinear reduced order models with the presented procedure as well as the classical methods. We impose random sound pressure levels on the reduced models as well as the full one and compare the accuracy of our reduced models with respect to the full one. Finally, we show that our presented results can accurately represent the nonlinear full-order models.

Chapter 9

Evaluation of the nonlinear substructuring methods to arch models

In this chapter, we compare our developed enhanced HCB nonlinear substructuring approaches presented in Chapter 8 with the HCB nonlinear substructuring developed by Keuther et al. [84]. It is already shown in Chapters 7 and 8 that both the nonlinear HCB and EHCB methods work accurately for flat structures. Furthermore, when the dimension of the required substructures' reduction bases to obtain accurate NLROMs increases, the number of needed static solutions to build the NLROMs increases in the order $O(m^3)$ for ED and ICE and $O(m^2)$ for EED, regardless of their accuracies. Here we apply these methods to an arch structure and compare the accuracy of different NLROMs.

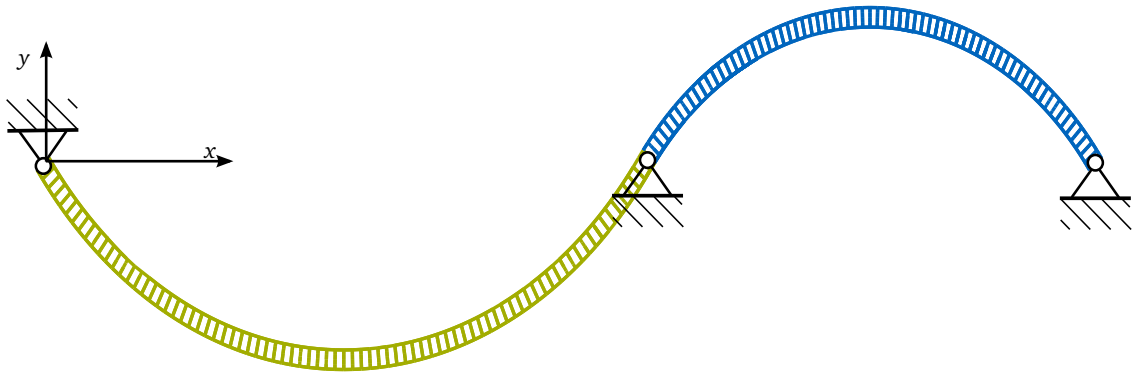

(a) Assembled arches

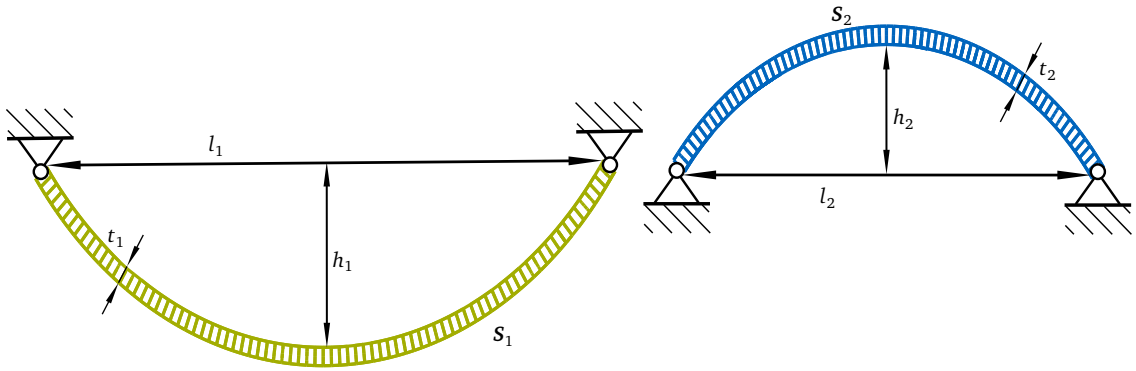

(b) Two substructures S_1 and S_2

Figure 9.1: Schematic of the Deep-curved arch FE model with two substructures and meshed with geometric nonlinear beam elements.

9.1 Deep-curved arch

To compare the performance of the presented substructuring methods, a deep-curved arch structure is investigated, as depicted in Fig. 9.1a. The arch model is made of two simply-supported substructures as shown in Fig. 9.1b, which are coupled at their rotational DOF. The material, geometry and mesh properties of the model are illustrated in Table 9.1.
To compare the accuracy of the nonlinear substructuring methods, NLROMs are developed using four different methods and bases, but all with the same dimension of 24 DOFs. The ingredients of these NLROMs as well as the methods that are used to generate them are given in Table 9.2. To develop the NLROM of each substructure for this example with ICE, the corresponding scaling factors should be scaled down to avoid convergence problems in the nonlinear static solutions required for NSCs identification.
Four static uniform distributed loads in y direction with negative and positive signs are imposed to the NLROMs that induce displacements from weak to strong nonlinearities and their deformation are compared with the nonlinear full-order and the linearized models.
Fig. 9.2 shows this static comparison under different load levels and the responses are plotted for both x and y directions. As can be seen from this figure, both force-based nonlinear substructuring methods, namely NLHCB-ICE of Kuether et al. [84] and NLHCB-IC-MD do not work accurately for both weak and strong level of nonlinearity, although NLHCB-ICE performs significantly better than NLHCB-IC-MD. For the displacement-based methods, NLHCB-EED-MD, which is based on NSCs identification from tangent stiffness, cannot present acceptable results for different levels of nonlinearity. For strong level of nonlinearity, this method becomes even unstable, as for instance is depicted in Figs. 9.2c and 9.2d. However, NLHCB-ED-MD performs accurately for negative and positive load cases, weak and strong level of nonlinearity and in both x and y directions.
Moreover, it is studied by Spottswood et al. [150] that the expansion procedure of ICE does not work for curved structures under combined loading conditions. Therefore, we propose to use NLHCB-ED-MD for the substructuring of FE models that are

	Property(dimension)	S_1	S_2
Material	Mass density (kg/m^3)	7870	7870
	Young's modulus (GPa)	205	205
	Poisson's ratio	0.28	0.28
Geometry	l (mm)	800	600
	h (mm)	20	15
	thickness (mm)	4	4
FE model	Element-type	beam (2-node) Abaqus B21	beam (2-node) Abaqus B21
	Number of Elements	80	70
	Number of DOFs	239	209
	Number of interface DOFs	81	71

Table 9.1: Geometry, material and FE model Properties of the investigated arch model

subject to these loading conditions, which needs to be verified in future research.
Finally, we assess the number of required static solutions for the development of the NLROMs that are used in Fig. 9.2. These numbers are presented in Table 9.3 for the considered four substructuring methods. As can be seen from this table, the displacement-based substructuring methods require less number of nonlinear static solutions, although NLHCB-EED-MD was not working for this case.
From the results presented in this Chapter as well as in Chapter 7, we conclude that the most robust nonlinear substructuring method that performs accurately for flat and curved structures, and under weak and strong level of nonlinearity, is our proposed NLHCB-ED-MD method. This method is a load-independent method that can be extended for free-interface mode substructuring in future works.

NLROM	method	S_1	S_2	Total DOFs
NLHCB-ICE	1	number of FIM		
		15	9	
		number of (S)MDs		
		0 SMDs	0 SMDs	24
NLHCB-IC-MD	1	number of FIM		
		5	3	
		number of (S)MDs		
		10 MDs	6 MDs	24
NLHCB-ED-MD	1	number of FIM		
		5	3	
		number of (S)MDs		
		10 MDs	6 MDs	24
NLHCB-EED-MD	1	number of FIM		
		5	3	
		number of (S)MDs		
		10 MDs	6 MDs	24

Table 9.2: The utilized modes in different developed NLROMs of the arch model.

Substructure	NLHCB-IC	NLHCB-IC-MD	NLHCB-ED-MD	NLHCB-EED-MD
S_1 (15 DOFs)	4090	4090	800	135
S_2 (9 DOFs)	834	834	210	54

Table 9.3: The number of required nonlinear static solutions to develop different NLROMs of each substructure.

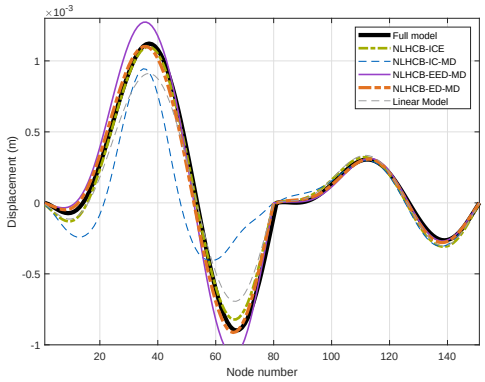

(a) Displacement in y direction under 5 N

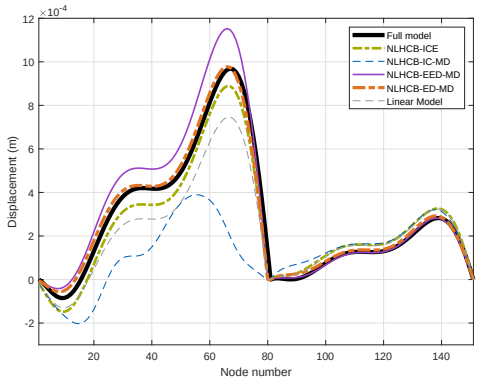

(b) Displacement in x direction under 5 N

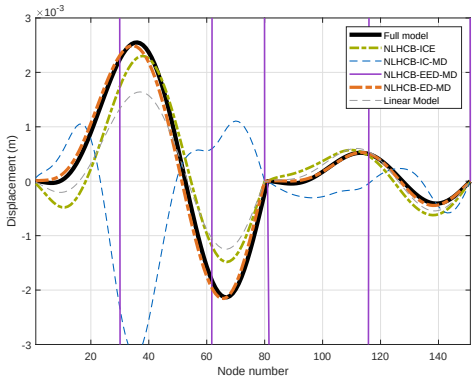

(c) Displacement in y direction under 9 N

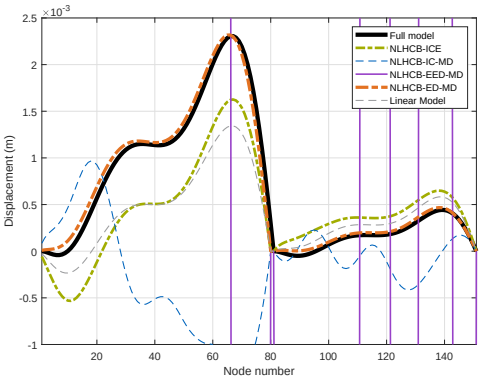

(d) Displacement in x direction under 9 N

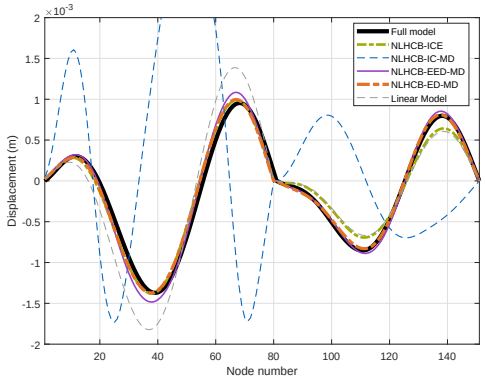

(e) Displacement in y direction under -10 N

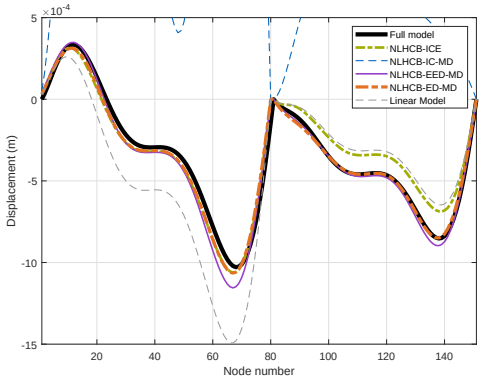

(f) Displacement in x direction under -10 N

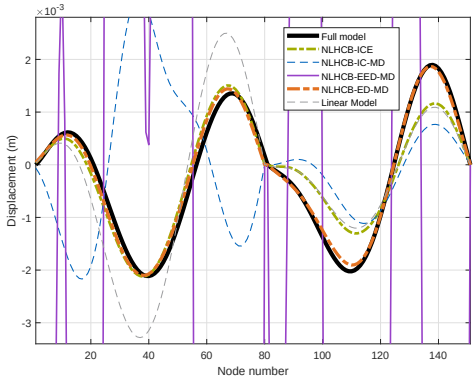

(g) Displacement in y direction under -18 N

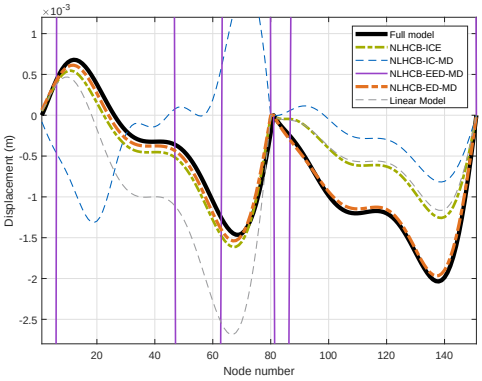

(h) Displacement in x direction under -18 N

Figure 9.2: Deformation in x and y directions of the deep-curved arch model under four uniform distributed static loads of 5 N, 9 N, -10 N and -18 N, applied in y direction. The loads are applied to all nodes.

Part III

Closure

Chapter 10

Conclusion and future work

10.1 Summary and conclusion of part I

Model order reduction (MOR) has become an important topic in many industrial applications, which deal with nonlinear finite element (FE) models. This is due to the fact that prediction of the structural response of large nonlinear FE models to static and dynamic loads is extremely time consuming. Therefore, the full order FE model is mapped to a reduced number of generalized coordinates, to increase the computational efficiency. The number of reduced coordinates is generally much smaller than the number of the full-order FE model. Accordingly, the structural response to different load cases (acoustic, thermal, etc.) can be computed much faster using the reduced order model (ROM). One general way to reduce the model of a nonlinear structure is indirect or non-intrusive approach, which does not require to access the internals of an FE code while building the NLROM. This dissertation focuses on expanding non-intrusive ROM methods to increase their accuracy as well as decreasing their computational burden.
One of the bottlenecks for developing a non-intrusive reduced order model comes from performing a "correct" basis selection, which is compact enough, easy to compute, and possibly load-independent. It should also convey the most essential nonlinear properties of the full-order model. In Chapter 3, we investigate accuracy improvement of the ICE method, which is a force-based non-intrusive ROM approach. The main advantage of ICE is that to develop an NLROM, a truncated number of linear vibration modes as the reduction basis suffices to accurately predict the most important nonlinear properties of the full model, e.g. the transverse-membrane stretching effect for shell-like structures. However, in case the model is always operating under a specific load distribution condition, the effect of truncated modes of the system on spatial distribution of external loads is not considered in ICE.
We propose two reduction bases to improve the accuracy of ICE . In the first method, which is called Mode Acceleration Correction, the quasi-static contribution of the truncated modes due to forced excitation is added to the NLROM response. In the second method, known as Modal Truncation Augmentation, Ritz vectors, which compensate the mode truncation inaccuracies on the spatial distribution of the applied loads, are used to determine modal truncation (MT) vectors. The MT vectors are then appended to the linear basis for nonlinear stiffness coefficient identification procedure of the NLROM. The proposed approaches are examined using a numerical example under a distributed load as well as a point load with random time signals and the results are compared with the classically developed NLROM. We show in

Chapter 3 that the MT vectors has slightly improved the accuracy of NLROM responses, while the effect of MA correction is almost negligible for nonlinear MOR. However, it should be noted that in this way the developed NLROMs are not load-independent anymore.
Furthermore, due to the high number of required nonlinear static solutions in ICE, which is a cubic function of generalized coordinates of the NLROM, it can only be used when the dimension of the NLROM remains small (say less than thirty DOFs). The expansion part of ICE also does not work for curved structures under combined loading conditions, see [150].
To develop a generalized non-intrusive MOR, we investigate the displacement-based non-intrusive methods in Chapter 4. One of the challenges of this method is to develop a desired reduction basis that considers the nonlinear coupling between the modes. The novelty of this chapter consists in combining the so-called modal derivatives with non-intrusive methods. We demonstrate in this work that if the reduction basis is selected in a systematic manner, then using modal derivatives can increase the accuracy of nonlinear reduced order models when compared to previously proposed methods. Moreover, modal derivatives are relatively straightforward to be obtained and selected, as explained in Chapter 4.
We compute the modal derivatives in a non-intrusive manner using finite deference and append them to the basis of truncated linear VMs. Then, we employ such basis to identify nonlinear stiffness coefficients of the reduced model. Another advantage of the proposed approach is that it is a simulation-free method, namely, it requires no dynamic simulation of the full-order model to be obtained. Also, the reduced model developed by non-intrusive modal derivatives can be used for a variety of load cases in a frequency and amplitude range in which it is designed. We use two alternatives to compute the modal derivatives non-intrusively and compare them to each other. The first method comprises differentiation of the whole eigenvalue problem and the second one is obtained by neglecting the inertia terms when differentiating the eigenvalue problem.
The proposed approach is applied to three finite element examples. The dynamic responses from random excitation at different levels obtained with the reduced order model we propose are compared to those computed with other available techniques. Our numerical tests confirm the accuracy of the proposed approach.
We finally compare the non-intrusive MOR methods in Chapter 5 in terms of accuracy and computational efficiency. We apply them to two numerical FE examples with geometric nonlinear effect and under weak and strong nonlinear deformations. From the result of Chapters 3, 4 and 5 we conclude that

- Non-intrusive model order reduction can be used as an efficient tool in a variety of applications in industries, which deal with large and complex structures. This is because non-intrusive MOR can reduce the model of nonlinear structures even when they are developed in commercial FE packages (e.g. Abaqus, Nastran, etc.), in contrast to the direct (intrusive) methods. The second advantage of non-intrusive method relies on the fact that the nonlinear reduced order models in this way can be developed such that they are valid for a variety of load cases in a broadband frequency.

- All the non-intrusive methods can develop accurate NLROMs for flat and shallow-

curved structures under weak nonlinear excitations. However, for strong level of nonlinearity only ICE and ED perform accurately. In these cases, ICE usually delivers more compact NLROMs than ED.

- For MOR of deep-curved structures, the only method that performs accurately in both weak and strong nonlinear response is the ED method. Furthermore, we discuss in Chapter 4 that our proposed basis for ED, namely the non-intrusive modal derivatives, can improve the performance of this method.

- It is discussed in [150] that the expansion procedure of ICE does not work for curved structures under combined loads, which could be due to the quadratic assumption for approximation of in-plane motion. In this cases we recommend to use the ED method with our proposed reduction basis, because it does not have the constraining assumption of ICE for in-plane dominated DOFs. This should be verified in future research.

- For large multi-component structures writing the input files for the FE package as well as reading the output vectors and matrices from it becomes a time consuming process. This can be alleviated by combining substructuring with non-intrusive MOR to divide large files to smaller ones and facilitate parallel computing, as we investigated in the Part II of this dissertation.

10.2 Summary and conclusion of part II

The second part of this dissertation expands on nonlinear modal substructuring for geometric nonlinear multi-component FE models, based on non-intrusive MOR. It is usually very cumbersome to reduce or analyze an FE model, which comprises multi-components with numerous number of DOFs in a monolithic way. Therefore, nonlinear substructuring methods are developed in recent years to speed up the design procedure of large FE models by dividing a structure into smaller components (called substructures) and then analyzing (reducing) each substructure to take advantage of previously analyzed components and parallel computation. The analyzed substructures are afterwards assembled to construct the dynamic properties of the whole structure. Since many industries use commercial FE packages to developed their models therein, it is important to develop the nonlinear substructuring methods based on non-intrusive approaches.
To start with the development of nonlinear substructuring methods, we review some common linear component mode synthesis methods with free- and fixed-interface DOFs in Chapter 6. Generally, the interface of substructures can contain many DOFs leading to reduced order models, which are still computationally expensive. Therefore, we discuss afterwards three interface reduction techniques developed so far for the Hurty/Craig-Bampton (HCB) method, namely, system level, local level with weak compatibility and local level with exact compatibility interface reduction methods. As the novelty of this chapter, we apply these interface reduction methods to the MacNeal/Rubin-Martinez (MRM), which is an augmented free-interface CMS approach (To the author's knowledge, the system level interface reduction was already applied to the free-interface mode methods in [155]). We then apply all the reviewed

methods of this chapter to two multi-component FE models. We show that the MRM method with and without interface reduction has accurate eigenfrequencies compared to other investigated CMS methods, for the investigated examples.
Afterwards, in Chapter 7, we propose a nonlinear dynamic substructuring of geometrical nonlinear FE models, based on MRM reduction basis and interface reduction. This work conveys two main novel aspects. Firstly, the NLROM of an individual substructure is developed by an augmented free-interface method with Residual Flexibility Attachment (RFA) modes, as a reduction basis. The RFA modes are adapted such that they approximate the contribution of deleted modes to the nonlinear response of the system. Secondly, the NLROMs of substructures are developed when the augmented free-interface-based method is combined with three interface reduction techniques (one system-level and two local-level), which so far have only been used with the fixed-interface method of nonlinear HCB. Finally, the proposed methods are compared with two previously developed non-intrusive-based modal substructuring methods: nonlinear free-interface and nonlinear HCB methods.
The performance of the improved free-interface method is examined on two geometrically nonlinear structures. The dynamic results show a remarkable improvement of accuracy compared to the nonlinear free-interface method and the same order or slightly better accuracy compared to the nonlinear HCB method. The performance of the reduced order models are assessed by imposing random pressures on the structures and comparing the power spectral densities of the responses obtained from the reduced order models and the full-order one.
In Chapter 8, we propose a generic non-intrusive-based nonlinear substructuring method. First we present an Enhance Hurty/Craig-Bampton (EHCB) reduction basis, which contains fixed-interface modes, (characteristic) constraint modes and their corresponding non-intrusive modal derivatives. By augmenting the reduction basis with the modal derivatives, we can accurately estimate the most important nonlinear properties of the full model and approximate the in-plane motion of the structure. Therefore, this method can be used for flat, shallow-curved and deep-curved structures.
Furthermore, we combine the EHCB reduction basis with both IC (EHCB-IC) and ED (EHCB-ED) and apply them to two numerical examples with geometric nonlinear beam and plate elements. We compare the power spectral density of the proposed NLROMs under random sound pressures with different levels of intensities. Based on the obtained results, we conclude that our developed EHCB substructuring using non-intrusive approach is an accurate method to be applied to different structures.
Finally, we compare the investigated nonlinear substructuring methods based on HCB in Chapter 9 by applying them to a deep-curved FE model with two substructures. We evaluate the accuracy of these methods under weak and strong nonlinear response. From the results obtained in Chapters 7, 8 and 9 we conclude that the most accurate method for MOR of different structures is our developed EHCB-ED.

10.3 Future work

The possible future works in the field of non-intrusive ROM and substructuring can be investigated at least in the following directions:

10.3.1 Non-intrusive MOR and substructuring with nonlinear manifold

Although we show in Chapters 4 and 8 that the developed non-intrusive MOR and substructuring methods by ED and linear manifold basis (linear mode and (S)MDs) perform accurately, the challenge is the increased number of NLROM's DOFs due to appended (S)MDs in the reduction basis. Therefore, it is sometimes desired to use nonlinear projectors that have configuration dependent vectors and contain the nonlinear properties of the model without increasing the size of the reduction basis. For instance, Jain et al. [64] developed the quadratic manifold method, which consider the effect of modal derivative as a quadratic enslavement of the linear generalized coordinates without adding additional coordinates. However, their method is a direct method, which can not be used in commercial FE packages. We recommend to extend the quadratic manifold for non-intrusive ROM approaches.
Furthermore, quadratic manifold can be extended for nonlinear substructuring to reduced the model of multi-component systems and facilitate parallel computation. In this case, instead of linear vibration modes and their corresponding modal derivatives, component modes and the modal derivatives of them should be used to build the nonlinear projectors.

10.3.2 Non-intrusive MOR for flexible multi-body systems

To the author's knowledge, the non-intrusive MOR techniques in the literature usually have been investigated for the structures, which have no rigid body motion. However, in many applications, like wind turbine blades, nonlinear structures endure rigid body motions in operating conditions. A few works exist in the literature, which investigated nonlinear model reduction in multi body systems using for instance the floating frame of reference, see [162, 165]. To further facilitate MOR of multi-body structures that are developed in commercial FE packages, we recommend to extend the non-intrusive MOR approach for the structures, which are moving in a floating frame.

10.3.3 Modal derivative-based non-intrusive ROM and substructuring under thermal field

In some applications like hypersonic air vehicles [93, 94], the structures are subjected to combined acoustic and thermal loads. In this case the coupled thermoelastic governing equations have to be investigated, which require model-reduction due to extreme computational burden of their full models. While nonlinear ROM for such cases have been developed in the recent years (e.g. in [94, 114]), we propose to extend the modal derivative-based non-intrusive MOR for them as we showed that it is the most accurate and robust non-intrusive ROM for elastodynamic problems.
Moreover, the structures under thermal loading condition can contain multi-component structures that cannot be reduced monolithically, because of their large dimension of matrices to be imported in-or exported from-the FE package. To facilitate MOR of such structures, the nonlinear substructuring approaches that developed in Chapters 7 and 8 can be expanded for the thermoelastodynamic multi-component structure.

10.3.4 Modal derivative-based nonlinear substructuring with free-interface modes

In Chapter 7 of this dissertation, we extended the work of Keuther et al. [84] using the augmented free-interface mode method instead of GH and HCB bases and discussed its advantages. However, the work of Chapter 7 is based on ICE, which sometimes has the studied limitation for curved structure. Therefore, the augmented free-interface mode substructuring can be combined with nonlinear substructuring approach based on ED and modal derivatives to take the advantage of free-interface mode method and modal derivatives.

List of Figures

1.1 Schematic of the Helios prototype in idle (down configuration) and operating (above configuration) conditions [110, 156] 2
1.2 Schematic of deformation of wind turbine blades under wind flow. . . 2
1.3 Schematic of the rotor assembly of the Ampair 600 wind turbine [37]. 4
1.4 Schematic of the matrix operation for the full model and the NLROM. 5
1.5 Work flow of non-intrusive model order reduction. 7
1.6 Flowchart for the scope of the main chapters of this dissertation. 14

2.1 Flowchart of the nonlinear static solution using Newton-Raphson [33]. 24
2.2 Flowchart of the implicit Newmark method [44]. 27

3.1 Schematic of the two side clamped beam model. 41
3.2 PSDs Comparison of three NLROMs: NLROM-6VM, NLROMMA-6VM, NLROM-5VM-1MTA with the full-order model and linear reduced model (LROM-6VM) under two excitation levels of 135dB and 150dB. 42
3.3 Relative error comparison for the first half seconds (out of five seconds) of the time signals that are used to compute the PSDs of Fig. 3.2. 43
3.4 PSDs Comparison of three NLROMs: NLROM-6VM, NLROMMA-6VM, NLROM-5VM-1MTA with the full-order model and linear reduced model (LROM-6VM) under two point loads of 0.5 and 2 N. 44
3.5 Relative error comparison for the first half seconds (out of five seconds) of the time signals that are used to compute the PSDs of Fig. 3.4. 45

4.1 Flowchart of the steps to identify nonlinear stiffness coefficients of an NLROM using ED and EED. 53
4.2 The number of required nonlinear static solutions versus the number of kept modes in the reduction basis for the ED and EED methods. . . 54
4.3 Schematic of the clamped-clamped flat beam model. 61
4.4 The first six vibration modes of the flat beam model. 62
4.5 Displacement of the first six SMDs of the flat beam model in axial and transverse directions. 63
4.6 Maximum modal interaction matrix values for the flat beam model with seven linear modes in the basis. Since this matrix is symmetric, only the lower triangle is shown. 64

4.7 The flat beam's displacement power spectral densities for convergence check of transverse and in-plane DOFs of the points A and B, respectively, under 150 dB SPL. The NLROM are developed using VMs augmented once with SMDs and another time with MDs. 65
4.8 Flat beam's PSDs for convergence check of transverse and in-plane DOFs of the points A and B, respectively, under 150 dB SPL. The NLROM are developed using VMs augmented with dual modes. 65
4.9 The flat beam's PSD comparison for the NLROMs developed by 5VM-5SMD, 5VM-5MD, 5VM-5Dual and 10VM with the full-order model and the linear reduced model (10VM). The PSDs are obtained under two load cases of 135 dB and 150 dB SPLs. 66
4.10 Relative error comparison for the flat beam's NLROMs developed by 5VM-5SMD, 5VM-5MD, 5VM-5Dual and 10VM with the full-order model and the linear reduced model (10VM). The relative errors are obtained under two load cases of 135 dB and 150 dB SPLs. 67
4.11 Schematic of the curved beam model. 68
4.12 The first six vibration modes of the curved beam. 70
4.13 Transverse and in-plane displacements of the curved beam's first six SMDs. The transverse and in-place displacements have different scaling for visual reasons. 71
4.14 Maximum modal interaction matrix values for the curved beam model with five linear modes in the basis. Since this matrix is symmetric, only the lower triangle is shown. 72
4.15 The curved beam's PSD comparison for the NLROMs based on 5VM-5SMD, 5VM-5MD, 5VM-5Dual and 10VM with the full-order model and the linear reduced model (10VM). The PSDs are obtained under two load cases of 158 dB and 168 dB SPLs. 73
4.16 Curved beam's relative error comparison for the NLROMs developed by 5VM-10SMD, 5VM-10MD, 5VM-10Dual and 15VM with the full-order model and the linear reduced model (15VM). The relative errors are obtained under two load cases of 158 dB and 168 dB SPLs. 74
4.17 The simply-supported panel model made of geometric nonlinear shell elements. 75
4.18 The first six vibration modes of the panel structure. 77
4.19 The first six SMDs shown for the panel structure, which are in-plane dominated. 78
4.20 Maximum modal interaction matrix values for the panel structure with eleven linear modes in the basis. Since this matrix is symmetric, only the lower triangle is shown. 79
4.21 The panel's PSDs for convergence check of transverse and in-plane directions of the points A and B, respectively, under 155 dB SPL. The panel's NLROMs are developed using linear modes augmented once with SMDs and then with MDs. 80
4.22 The panel's PSDs for convergence check of transverse and in-plane directions of points A and B, respectively, under 155 dB SPL. The NLROMs are developed using linear modes augmented with dual modes. 80

4.23 The panel's PSDs comparison for the NLROMs developed by 11VM-11SMD, 11VM-11MD, 11VM-11Dual and 22VM with the full-order model and the linear reduced model (22VM). The PSDs are obtained under two load cases of 145 dB 157 dB SPL. 81

4.24 The panel's relative error comparison for NLROMs developed by 11VM-11SMD, 11VM-11MD, 11VM-11Dual and 22VM with the full-order model and the linear reduced model (22VM). The relative errors are obtained under two load cases of 145 dB 155 dB SPLs. 82

5.1 Comparison of the required number of nonlinear static solutions versus the number of kept modes for the ICE, ED and EED methods. . . . 84

5.2 Schematic of the FE model of the shallow-curved and deep-curved beam structures. 84

5.3 Deformation of the shallow-curved beam in x and y directions under two uniform distributed static loads in y direction, with intensities of 1 N and 2.5 N. The loads are applied to all nodes. 85

5.4 Deformation of the deep-curved beam in x and y directions under two uniform distributed static loads in y direction, with intensities of 8 N and 20 N. The loads are applied to all nodes. 86

6.1 Schematic of the investigated beam FE model and it substructures. Note that the vertical and horizontal scales are not the same. Parameters of the example are given in table 6.1. 108

6.2 Beam model's relative error (in percentage) comparison of the eigenfrequencies for the GH, HCB and MRM methods. The same number of modes for free- or fixed-interface modes for each model is used 109

6.3 Schematic of the Panel FE model with two substructures and meshed with nonlinear shell element. 110

6.4 Convergence check analysis for the maximum error induced by IR versus the number of kept SL-IR modes for plate model. For the MRM method, three models are studied: kept free-interface modes of substructures until 500 Hz, 750 Hz and 1000 Hz. The same number of fixed-interface modes is kept for the HCB method. 111

6.5 Plate's relative error comparison (in percentage) of the eigenfrequencies for different methods. For each substructure, the free-interface modes up to 750 Hz are kept in the NLROM. The same number of modes for free- and fixed-interface modes as well as the interface modes are used for each method. 112

7.1 Displacement power spectral density evaluation for the convergence check of the beam's NLROM developed with the MRM basis. Three NLROMs are developed when the free modes are kept until 500 Hz, 750 Hz and 1000 Hz and integrated under a uniformly distributed random pressure with 135 dB SPL. 120

7.2 Comparison of the beam's full model with the NLROMs using three bases: GH, MRM and HCB, and also the LROM. The displacement power spectral densities for transverse and membrane DOFs of point *A* are compared. The ingredients of these NLROMs are given in Table 7.1. 121
7.3 Comparison of the beam's full-order model with the NLROMs using three bases: GH, MRM, HCB, and also the LROM. The displacement power spectral densities for transverse and membrane DOFs of point *B* are compared. 122
7.4 Displacement power spectral density evaluation for the convergence check of the plate's NLROM developed with the MRM basis. Three NLROMs are compared when the free modes are kept up to 500 Hz, 750 Hz and 1000 Hz under the loading condition of 155 dB SPL. Two SL interface modes are used for the NLROMs. 124
7.5 Comparison of the plate's full-order model with the NLROMs using three bases: free-interface, MRM with SL-IR, HCB with SL-IR and also the LROM. The displacement power spectral densities for transverse and membrane DOFs of point *A* are compared. Two interface modes are used for HCB and MRM. 125
7.6 Comparison of the plate's full-order model with the NLROMs using three bases: GH, MRM with LL-EC interface reduction, HCB with LL-EC interface reduction, and also the LROM. The displacement power spectral densities for transverse and membrane DOFs of point *A* are compared. Two interface modes are used for HCB and MRM. 126
7.7 Comparison of the plate's full-order model with the NLROMs using three bases: GH, MRM with LL-WC interface reduction, HCB with LL-WC interface reduction, and also the LROM. The displacement power spectral densities for transverse and membrane DOFs of point *A* are compared. Two interface modes are used for HCB and MRM. 127
7.8 Comparison of the plate's NLROMs with full-order model based on the MRM method with three interface reductions: SL, LL-EC and LL-WC. The displacement power spectral densities for transverse and membrane DOFs of point *A* are compared. Two interface modes are used for all NLROMs. 128

8.1 The number of required nonlinear static solutions versus the number of kept modes for different non-intrusive methods. For substructuring, the number of DOFs for the coupled system is divided into two equal substructures (as an example), and the curves are obtained for one substructure, assuming the identification procedure of substructures is performed in parallel. 139
8.2 The first four fixed-interface modes for the substructure S_1 of the flat beam model. 144
8.3 The first three fixed-interface modes for the substructure S_2 of the flat beam model. 144
8.4 The first eight static modal derivatives for the substructure S_1 of the flat beam model. 145

8.5 The first six static modal derivatives for the substructure S_2 of the flat beam model. 146
8.6 The maximum modal interaction criterion for the first four fixed-interface modes of substructure S_1 and the first three fixed-interface modes of substructure S_2 to select (S)MDs. 147
8.7 Flat beam model's displacement PSDs for convergence check analysis of the NLROMs developed by ED-(S)MD under 145 dB. The ingredients of the NLROM are demonstrated in Table 8.1. 147
8.8 Flat beam model's displacement PSDs for convergence check analysis of the NLROMs developed by IC-(S)MD under 145 dB. The ingredients of the NLROMs are outlined in Table 8.1. 148
8.9 Displacement PSD comparison of the beam's full model with the NLROMs developed by different methods and bases, all with 22 DOFs. The comparison is performed under 135 and 145 dB SPL for transverse and membrane directions. The ingredients of the NLROMs are outlined in Table 8.1. 149
8.10 Flat beam's relative error comparison for the first half seconds (out of four seconds) of the time signals that are used to compute the PSDs of Fig. 8.9. 150
8.11 Displacement PSD comparison of the beam's full model with the NLROMs developed by different methods and bases, all with 22 DOFs. The comparison is performed under 135 and 145 dB SPL for transverse and membrane directions. The ingredients of the NLROMs are outlined in Table 8.1. 151
8.12 Flat beam's relative error comparison for the first half seconds of the time signal that is used to compute the PSDs of Fig. 8.11. 152
8.13 The first seven vibration modes for the substructure S_1 of the flat beam model. 154
8.14 The first five vibration modes for the substructure S_2 of the flat beam model. 155
8.15 The first eight static modal derivatives for the substructure S_1 of the panel model. 156
8.16 The first six static modal derivatives for the substructure S_2 of the flat panel model. 157
8.17 Panel model's displacement PSDs for convergence check analysis of the NLROMs developed by ED-(S)MD and IC-(S)MD under 155 dB. The ingredients of the NLROM are outlined in Table 8.3. 158
8.18 Displacement PSD comparison of the panel's full model with the NLROMs developed by different methods and bases, all with 32 DOFs. The comparison is performed under 140 dB and 155 dB SPL for transverse and membrane directions. The ingredients of the NLROM are outlined in Table 8.3. 159
8.19 Displacement PSD comparison of the panel's full model with the NLROMs developed by different methods and bases, all with 32 DOFs. The comparison is performed under 140 dB and 155 dB SPLs for transverse and membrane directions. The ingredients of the NLROM are outlined in Table 8.3. 160

9.1 Schematic of the Deep-curved arch FE model with two substructures and meshed with geometric nonlinear beam elements. 163
9.2 Deformation in x and y directions of the deep-curved arch model under four uniform distributed static loads of 5 N, 9 N, −10 N and −18 N, applied in y direction. The loads are applied to all nodes. 166

B.1 Panel model's displacement PSDs for convergence check analysis of the NLROMs developed by ED-(S)MD and IC-(S)MD under 155 dB. The ingredients of the NLROM are demonstrated in Table 8.3. 185

List of Tables

3.1 Geometry, material and FE model properties of the investigated flat beam model. 41

4.1 Number of nonlinear static solutions (offline computational cost), only for NSCs identification part of the flat beam's NLROMs. 64
4.2 Online time for integration of flat beams's NLROMs and full model for 5 seconds under 150 dB load. 64
4.3 Material, geometry and FE model properties of the clamped-clamped beam model of Fig. 4.3 69
4.4 Offline computational time to develop the curved beam's NLROMs, only for NSCs identification part. 72
4.5 Online time for time integration of curved beams's NLROMs and full model for 5 seconds under 168 dB load. 75
4.6 Material, geometry and FE model properties of the clamped-clamped beam model of Fig. 4.17 76
4.7 Offline computational time for development of the panel's NLROMs, only for NSCs identification part. 77
4.8 Online time for time integration of the panel's NLROMs and full model for 5 seconds under 157 dB load. 78

5.2 The number of required nonlinear static solutions for each non-intrusive ROM method to develop NLROMs with different DOFs. 88

6.1 Geometry, material and FE model properties of the investigated beam model 108
6.2 Eigenfrequencies of the free- and fixed-interface modes for the beam model. 109
6.3 Geometry, material and FE model properties of the investigated plate model 111
6.4 Eigenfrequencies of the free- and fixed-interface modes for the panel model. 112

7.1 Number of nonlinear static solutions (offline computational cost) for NLROMs development of the beam model using different methods . . 119
7.2 Online computational time for four seconds time integration of different NLROMs as well as the full-order beam model 119
7.3 Number of nonlinear static solutions (offline computational cost) for NLROMs development of the panel model using different methods. . . 123

7.4 Online computational time for four seconds time integration of the plate FE model with different methods. 124

8.1 The number of modes included in different developed NLROMs of the beam model by ED-(S)MD or IC-(S)MD. 142
8.2 Number of nonlinear static solutions for NSCs identification of the beam's NLROMs with substructuring and monolithic. 149
8.3 The number of modes included in different developed NLROMs of the panel model by ED-(S)MD or IC-(S)MD. 153
8.4 Number of nonlinear static solutions for NSCs identification of the panel's NLROMs with substructuring and monolithic. 159

9.1 Geometry, material and FE model properties of the investigated plate model 164
9.2 The utilized modes in different developed NLROMs of the arch model. 165
9.3 The number of required nonlinear static solutions to develop different NLROMs of each substructure. 165

Appendix A

Construction of static equations for ICE method

Consider a nonlinear reduced order model in the form of Eq. (3.1) with two DOFs. The static equilibrium equations corresponding to the r^{th} static load case for this NLROM writes

$$\begin{bmatrix} \hat{K}_{11}^{(1)} & \hat{K}_{12}^{(1)} \\ \hat{K}_{21}^{(1)} & \hat{K}_{22}^{(1)} \end{bmatrix} \begin{Bmatrix} q_1^{(r)} \\ q_2^{(r)} \end{Bmatrix} + \begin{Bmatrix} \hat{K}_{111}^{(2)} q_1^{2^{(r)}} + \hat{K}_{112}^{(2)} q_1^{(r)} q_2^{(r)} + \hat{K}_{122}^{(2)} q_2^{2^{(r)}} \\ \hat{K}_{211}^{(2)} q_1^{2^{(r)}} + \hat{K}_{212}^{(2)} q_1^{(r)} q_2^{(r)} + \hat{K}_{222}^{(2)} q_2^{2^{(r)}} \end{Bmatrix} + \begin{Bmatrix} \hat{K}_{1111}^{(3)} q_1^{3^{(r)}} + \hat{K}_{1112}^{(3)} q_1^{2^{(r)}} q_2^{(r)} + \hat{K}_{1122}^{(3)} q_1^{(r)} q_2^{2^{(r)}} + \hat{K}_{1222}^{(3)} q_2^{3^{(r)}} \\ \hat{K}_{2111}^{(3)} q_1^{3^{(r)}} + \hat{K}_{2112}^{(3)} q_1^{2^{(r)}} q_2^{(r)} + \hat{K}_{2122}^{(3)} q_1^{(r)} q_2^{2^{(r)}} + \hat{K}_{2222}^{(3)} q_2^{3^{(r)}} \end{Bmatrix} = \begin{Bmatrix} \hat{f}_1^{(r)} \\ \hat{f}_2^{(r)} \end{Bmatrix} \tag{A.1}$$

Note in this equation that the linear and nonlinear stiffness tensors are considered symmetric, namely

$$\begin{aligned} \hat{K}_{iij}^{(2)} &= \hat{K}_{iji}^{(2)} \\ \hat{K}_{iiij}^{(3)} &= \hat{K}_{iiji}^{(3)} = \hat{K}_{ijii}^{(3)} \end{aligned} \tag{A.2}$$

In order to obtain the unknown coefficients corresponding to the quadratic and cubic terms in Eq. (A.1), p static load cases are applied to the full-order model (see Section 7.2) leading to the following over-determined equation:

$$\boldsymbol{K}_{nl} \boldsymbol{G}_{nl} = \boldsymbol{F}_{nl} \tag{A.3}$$

where

$$\boldsymbol{K}_{nl} = \begin{bmatrix} \hat{K}_{111}^{(2)} & \hat{K}_{112}^{(2)} & \hat{K}_{122}^{(2)} & \hat{K}_{1111}^{(3)} & \hat{K}_{1112}^{(3)} & \hat{K}_{1122}^{(3)} & \hat{K}_{1222}^{(3)} \\ \hat{K}_{211}^{(2)} & \hat{K}_{212}^{(2)} & \hat{K}_{222}^{(2)} & \hat{K}_{2111}^{(3)} & \hat{K}_{2112}^{(3)} & \hat{K}_{2122}^{(3)} & \hat{K}_{2222}^{(3)} \end{bmatrix} \tag{A.4}$$

contains the unknown nonlinear stiffness coefficients,

$$\boldsymbol{G}_{nl} = \begin{bmatrix} q_1^{2^{(1)}} & q_1^{2^{(2)}} & \cdots & q_1^{2^{(p)}} \\ q_1^{(r)} q_2^{(1)} & q_1^{(2)} q_2^{(2)} & \cdots & q_1^{(p)} q_2^{(p)} \\ q_2^{2^{(1)}} & q_2^{2^{(2)}} & \cdots & q_2^{2^{(p)}} \\ q_1^{3^{(1)}} & q_1^{3^{(2)}} & \cdots & q_1^{3^{(p)}} \\ q_1^{2^{(1)}} q_2^{(1)} & q_1^{2^{(2)}} q_2^{(2)} & \cdots & q_1^{2^{(p)}} q_2^{(p)} \\ q_1^{(1)} q_2^{2^{(1)}} & q_1^{(2)} q_2^{2^{(2)}} & \cdots & q_1^{(p)} q_2^{2^{(p)}} \\ q_2^{3^{(1)}} & q_2^{3^{(2)}} & \cdots & q_2^{3^{(p)}} \end{bmatrix} \tag{A.5}$$

comprise the known quadratic (and cubic when more than two modes exist in ROM) combination of generalized coordinates. The matrix $\boldsymbol{F}_{nl}$ is given by

$$\boldsymbol{F}_{nl} = \begin{Bmatrix} \hat{f}_1^{(1)} - \hat{K}_{11}^{(1)} q_1^{(1)} - \hat{K}_{12}^{(1)} q_2^{(1)} & \hat{f}_1^{(2)} - \hat{K}_{11}^{(1)} q_1^{(2)} - \hat{K}_{12}^{(1)} q_2^{(2)} & \cdots & \hat{f}_1^{(p)} - \hat{K}_{11}^{(1)} q_1^{(p)} - \hat{K}_{12}^{(1)} q_2^{(p)} \\ \hat{f}_2^{(1)} - \hat{K}_{21}^{(1)} q_1^{(1)} - \hat{K}_{22}^{(1)} q_2^{(1)} & \hat{f}_2^{(2)} - \hat{K}_{21}^{(1)} q_1^{(2)} - \hat{K}_{22}^{(1)} q_2^{(2)} & \cdots & \hat{f}_2^{(p)} - \hat{K}_{21}^{(1)} q_1^{(p)} - \hat{K}_{22}^{(1)} q_2^{(p)} \end{Bmatrix}. \tag{A.6}$$

The Eq. A.3 can be solved by using a regression approach (e.g. least squares, see [95]).

Appendix B

Supplementary plot of Chapter 8

Figs. B.1 depicts the PSDs of the defined NLROMs in Table 8.3 for the transverse and membrane directions of point B (on the panel model) to check the convergence of of the investigated methods. This figure acknowledges the convergence of the developed NLROMs using ED-(S)MD and IC-(S)MD methods to the full model response by increasing the number of fixed-interface modes and (S)MDs.

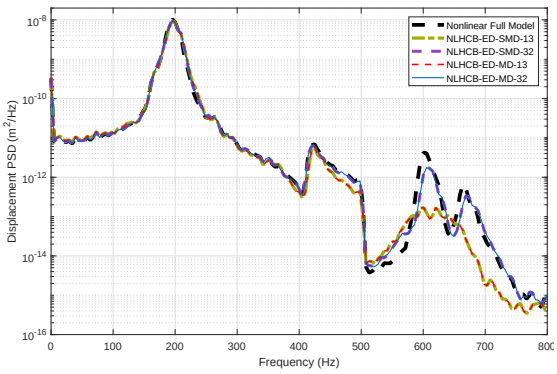

(a) Transverse PSD of point B.

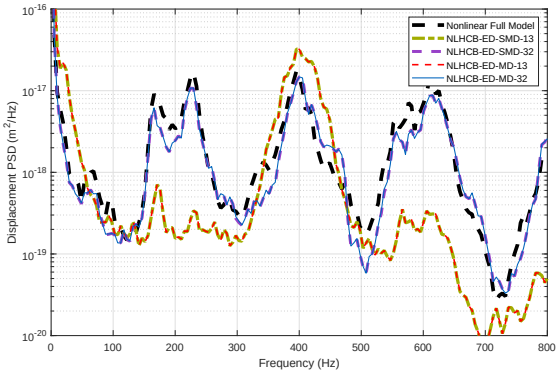

(b) Membrane PSD of point B.

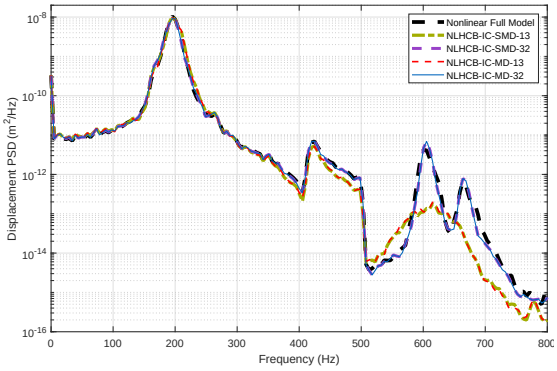

(c) Transverse PSD of point B.

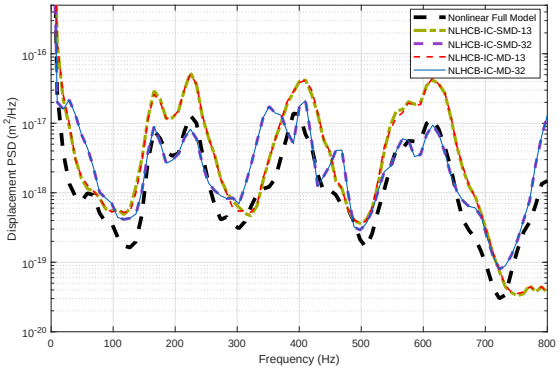

(d) Membrane PSD of point B.

Figure B.1: Panel model's displacement PSDs for convergence check analysis of the NLROMs developed by ED-(S)MD and IC-(S)MD under 155 dB. The ingredients of the NLROM are demonstrated in Table 8.3.

Bibliography

[1] Akguen, M. “A New Family Of Mode-Superposition Methods For Response Calculations”. In: *Journal of Sound and Vibration* 167.2 (1993), pp. 289–302. ISSN: 0022-460X. DOI: https://doi.org/10.1006/jsvi.1993.1336.

[2] Allen, M. S., Mayes, R. L., and Bergman, E. J. “Experimental modal substructuring to couple and uncouple substructures with flexible fixtures and multi-point connections”. In: *Journal of Sound and Vibration* 329.23 (2010), pp. 4891–4906. ISSN: 0022460X. DOI: 10.1016/j.jsv.2010.06.007.

[3] Amsallem, D., Cortial, J., and Farhat, C. “Towards Real-Time Computational-Fluid-Dynamics-Based Aeroelastic Computations Using a Database of Reduced-Order Information”. In: *AIAA Journal* 48.9 (2010), pp. 2029–2037. DOI: 10.2514/1.J050233.

[4] Bai, Z. “Krylov subspace techniques for reduced-order modeling of large-scale dynamical systems”. In: *Applied Numerical Mathematics* 43.1-2 (2002), pp. 9–44. ISSN: 01689274. DOI: 10.1016/S0168-9274(02)00116-2.

[5] Bathe, K.-J. and Bolourchi, S. “A geometric and material nonlinear plate and shell element”. In: *Computers & Structures* 11.1 (1980), pp. 23–48. DOI: 10.1016/0045-7949(80)90144-3.

[6] Belytschko, T., Liu, W., and Moran, B. *Nonlinear finite elements for continua and structures*. Wiley, 2000. ISBN: 9780471987734. URL: https://books.google.de/books?id=C6goAQAAMAAJ.

[7] Ben-Israel, A. and Greville, T. N. *Generalized Inverses: Theory and Applications*. 2nd ed. New York: Springer-Verlag, 2003, p. 420. ISBN: 978-0-387-21634-8. DOI: 10.1007/b97366.

[8] Benner, P., Hinze, M., and Maten, E. J. W. ter. *Model Reduction for Circuit Simulation*. 1st ed. Springer Netherlands, 2011, p. 315. ISBN: 978-94-007-3283-4. DOI: 10.1007/978-94-007-0089-5.

[9] Besselink, B., Tabak, U., Lutowska, A., Wouw, N. van de, Nijmeijer, H., Rixen, D., Hochstenbach, M., and Schilders, W. “A comparison of model reduction techniques from structural dynamics, numerical mathematics and systems and control”. In: *Journal of Sound and Vibration* 332.19 (2013), pp. 4403–4422. ISSN: 0022-460X. DOI: 10.1016/j.jsv.2013.03.025.

[10] Bischoff, J. E., Arruda, E. M., and Grosh, K. “Finite element modeling of human skin using an isotropic, nonlinear elastic constitutive model”. In: *Journal of Biomechanics* 33.6 (2000), pp. 645–652. ISSN: 0021-9290. DOI: https://doi.org/10.1016/S0021-9290(00)00018-X.

[11] Blair, M., Canfield, R. A., and Roberts, R. W. “Joined-wing aeroelastic design with geometric nonlinearity”. In: *Journal of Aircraft* 42.4 (2005), pp. 832–848. ISSN: 0021-8669. DOI: 10.2514/1.2199.

[12] Bonet, J. and Wood, R. D. *Nonlinear Continuum Mechanics for Finite Element Analysis*. Vol. 24. 11. Cambrige: Cambrige University Press, 2008, pp. 1567–1568. ISBN: 052157272X. DOI: 10.1017/CBO9780511755446. arXiv: arXiv:1011.1669v3.

[13] Borst, R. de, Crisfield, M., Remmers, J., and Verhoosel, C. *Non-Linear Finite Element Analysis of Solids and Structures: Second Edition*. 2012. DOI: 10.1002/9781118375938.

[14] Brandt, A. “Non-intrusive model order reduction of geometrically nonlinear FEMs using linear manifold”. Master Thesis. Technical University of Munich, 2018.

[15] Buchmann, E. “Dynamic substructuring and interface reduction in geometric nonlinear finite element models”. Master Thesis. Technical University of Munich, 2016.

[16] Carlberg, K., Farhat, C., Cortial, J., and Amsallem, D. “The GNAT method for nonlinear model reduction: Effective implementation and application to computational fluid dynamics and turbulent flows”. In: *Journal of Computational Physics* 242 (2013), pp. 623–647. DOI: 10.1016/j.jcp.2013.02.028.

[17] Carter, B. and Mancini, R. *Op Amps for Everyone*. Ed. by Elsevier. 3rd ed. Oxford, 2009. ISBN: 978-0080949482.

[18] Castanier, M. P., Tan, Y. C., and Pierre, C. “Characteristic constraint modes for component mode synthesis”. In: *AIAA Journal* 39.6 (2001), pp. 1182–1187. ISSN: 00011452. DOI: 10.2514/3.14854.

[19] Chang, Y., Wang, X. Q., and Mignolet, M. P. “Reduced order modelling for the nonlinear geometric response of some curved structures”. In: (2012).

[20] Chaturantabut, S. and Sorensen, D. C. “Nonlinear Model Reduction via Discrete Empirical Interpolation”. In: *SIAM Journal on Scientific Computing* 32.5 (2010), pp. 2737–2764. ISSN: 1064-8275. DOI: 10.1137/090766498.

[21] Chelidze, D. and Zhou, W. “Smooth orthogonal decomposition-based vibration mode identification”. In: *Journal of Sound and Vibration* 292.3 (2006), pp. 461–473. ISSN: 0022-460X. DOI: https://doi.org/10.1016/j.jsv.2005.08.006.

[22] Chinesta, F., Ladeveze, P., and Cueto, E. “A Short Review on Model Order Reduction Based on Proper Generalized Decomposition”. In: *Archives of Computational Methods in Engineering* 18.4 (2011), pp. 395–404. ISSN: 11343060. DOI: 10.1007/s11831-011-9064-7.

[23] Chung, J. and Hulbert, G. “A Time Integration Algorithm for Structural Dynamics With Improved Numerical Dissipation: The Generalized-α Method”. In: *ASME. J. Appl. Mech* 60.2 (1993), pp. 371–375. DOI: 10.1115/1.2900803.

[24] Correa, J. M., Farret, F. A., Canha, L. N., and Simoes, M. G. "An electrochemical-based fuel-cell model suitable for electrical engineering automation approach". In: *IEEE Transactions on Industrial Electronics* 51.5 (Oct. 2004), pp. 1103–1112. ISSN: 0278-0046. DOI: 10.1109/TIE.2004.834972.

[25] Craig, R. R. and Kurdila, A. J. *Fundamentals of Structural Dynamics*. New Jersey: Wiley, 2006, p. 744. ISBN: 978-0-471-43044-5.

[26] Craig, R.-R. and Bampton, M. C. C. "Coupling of Substructures for Dynamics Analyses". In: *AIAA Journal* 6.7 (1968), p. 1313. ISSN: 0001-1452. DOI: 10.2514/3.4741.

[27] Craig, R. R. and Chang, C.-J. "On the use of attachment modes in substructure coupling for dynamic analysis". In: *18th AIAA Structures, Structural Dynamics and Materials Conference* (1977), pp. 89–99. ISSN: 0146-3705. DOI: 10.2514/6.1977-405.

[28] Craig, R. R. "Coupling of Substructures for Dynamic Analyses: an Overview". In: *Structures, Structural Dynamics and Material Conference*. 41st AIAA/ASME/ASCE/AHS/ASC. Atlanta, Apr. 2000.

[29] Craig, R. R. and Chang, C.-J. "A review of substructure coupling methods for dynamic analysis". In: *Advances in Engineering Science NASA* 2 (1976), pp. 393–408. ISSN: 0001-1452. DOI: 10.2514/3.7264.

[30] Craig, R. R. and Chang, C.-J. "Free-interface methods of substructure coupling for dynamic analysis". In: *AIAA Journal* 14.11 (1976), pp. 1633–1635. ISSN: 0001-1452. DOI: 10.2514/3.7264.

[31] Craig, R. R. and Chang, C.-J. *Substructure coupling for dynamic analysis and testing*. Tech. rep. National Aeronautics and Space Administration, 1977. URL: http://ntrs.nasa.gov/search.jsp?R=19770010568.

[32] Dahl, P. R. "Solid Friction Damping of Mechanical Vibrations". In: *AIAA Journal* 14.12 (1976), pp. 1675–1682. DOI: 10.2514/3.61511.

[33] De Crescenzo, F. "Reduced order modeling of geometrically nonlinear structures under thermal loads". Master Thesis. Technical University of Munich, 2017.

[34] Dickens, J., Nakagawa, J., and Wittbrodt, M. "A critique of mode acceleration and modal truncation augmentation methods for modal response analysis". In: *Computers and Structures* 62.6 (1997), pp. 985–998. ISSN: 0045-7949. DOI: https://doi.org/10.1016/S0045-7949(96)00315-X.

[35] Dickens, J. and Pool, K. "Modal truncation vectors and periodic time domain analysis applied to a cyclic symmetry structure". In: *Computers & Structures* 45.4 (Nov. 1992), pp. 685–696. ISSN: 0045-7949. DOI: 10.1016/0045-7949(92)90487-K.

[36] Eliasdottir, B. "Experimental-Analytical Coupling in Dynamic Subtructuring: Application to Wind Turbines". Master Thesis. Technical University of Munich, 2016.

[37] Eliasdottir, B. B., Karamooz Mahdiabadi, M., Bartl, A., and Rixen, D. J. "An Experimental-Numerical Substructuring Approach in Dual Form". In: *Proceedings of the 27th ISMA, A Conference on Noise and Vibration Engineering*. KU Leuven, 2016.

[38] *European Commission webpage*. URL: https://ec.europa.eu/energy/en/topics/renewable-energy.

[39] Farhat, C., Avery, P., Chapman, T., and Cortial, J. "Dimensional reduction of nonlinear finite element dynamic models with finite rotations and energy-based mesh sampling and weighting for computational efficiency". In: *International Journal for Numerical Methods in Engineering* 98.9 (2014), pp. 625–662.

[40] Farhat, C. and Geradin, M. "On the general solution by a direct method of a large-scale singular system of linear equations: application to the analysis of floating structures". In: *International Journal for Numerical Methods in Engineering* 41.4 (1998), pp. 675–696. DOI: 10.1002/(SICI)1097-0207(19980228)41:4<675::AID-NME305>3.0.CO;2-8.

[41] Fortuna, L., Nunnari, G., and Gallo, A. *Model Order Reduction Techniques with Applications in Electrical Engineering*. 1st ed. London: Springer-Verlag, 1992, p. 232. ISBN: 978-1-4471-3198-4. DOI: 10.1007/978-1-4471-3198-4.

[42] Fung, Y., Tong, P., and Chen, X. *Classical and Computational Solid Mechanics*. Advanced series in engineering science. World Scientific Publishing Company Pte Limited, 2017. ISBN: 9789814713658. URL: https://books.google.de/books?id=lRxtjgEACAAJ.

[43] Gellmann, R. and Ricoeur, A. "Nonlinear Constitutive Model and Finite Element Analysis of Damage Processes in Ferroelectrics". In: *Procedia Materials Science* 3 (2014). 20th European Conference on Fracture, pp. 2117–2121. ISSN: 2211-8128. DOI: 10.1016/j.mspro.2014.06.342.

[44] Geradin, M. and Rixen, D. *Mechanical Vibrations: Theory and Application to Structural Dynamics*. en. Wiley, 2015. ISBN: 978-1-118-90020-8.

[45] Goldman, R. L. "Vibration analysis by dynamic partitioning". In: *AIAA Journal* 7.6 (1969), pp. 1152–1154.

[46] Gordon, R. W. and Hollkamp, J. J. *Reduced-Order Models for Acoustic Response Prediction*. Tech. rep. July. AFRL-RB-WP-TR-2011-3040, 2011.

[47] Gordon, R. W. and Hollkamp, J. J. "Reduced-Order Models for Acoustic Response Prediction of a Curved Panel". In: *52nd AIAA/ASME/ASCE/AHS/ASC Structures, Structural Dynamics and Materials Conference*. Ed. by AIAA. AIAA 2011-2081. AIAA. Apr. 2011.

[48] Guerin, L. C. M., Kuether, R. J., and Allen, M. S. "Considerations for Indirect Parameter Estimation in Nonlinear Reduced Order Models". In: *Nonlinear Dynamics, Volume 1*. Ed. by Kerschen, G. Cham: Springer International Publishing, 2016, pp. 327–342. ISBN: 978-3-319-15221-9.

[49] Gugercin, S. and Antoulas, A. C. "A Survey of Model Reduction by Balanced Truncation and Some New Results". In: *International Journal of Control* 77.8 (2004), pp. 748–766. DOI: 10.1080/00207170410001713448.

[50] Guo, X., College, D. W., Przekop, A., and Services, A. “Energy-Based Modal Basis Selection Procedure for Reduced-Order Nonlinear Simulation”. In: *51st AIAA/ASME/ASCE/AHS/ASC Structures, Structural Dynamics, and Materials Conference*. April. 2010.

[51] Hilber, H. M., Hughes, T. J. R., and Taylor, R. L. “Improved numerical dissipation for time integration algorithms in structural dynamics”. In: *Earthquake Engineering & Structural Dynamics* 5.3 (1977), pp. 283–292. DOI: 10.1002/eqe.4290050306.

[52] Hintz, R. M. “Analytical Methods in Component Modal Synthesis”. In: *AIAA Journal* 13.8 (1975), pp. 1007–1016. ISSN: 0001-1452. DOI: 10.2514/3.60498.

[53] Hinze, M. and Kunkel, M. “Discrete Empirical Interpolation in POD Model Order Reduction of Drift-Diffusion Equations in Electrical Networks”. In: *Scientific Computing in Electrical Engineering SCEE 2010*. Ed. by Michielsen, B. and Poirier, J.-R. Berlin, Heidelberg: Springer Berlin Heidelberg, 2012, pp. 423–431. ISBN: 978-3-642-22453-9. DOI: 10.1007/978-3-642-22453-9_45.

[54] Hollkamp, J. J. and Gordon, R. W. “Reduced-order models for nonlinear response prediction: Implicit condensation and expansion”. In: *Journal of Sound and Vibration* 318.4-5 (2008), pp. 1139–1153. DOI: 10.1016/j.jsv.2008.04.035.

[55] Hong, S.-k., Epureanu, B. I., and Castanier, M. P. “Next-generation parametric reduced-order models”. In: *Mechanical Systems and Signal Processing* 37.1-2 (2013), pp. 403–421. ISSN: 0888-3270. DOI: 10.1016/j.ymssp.2012.12.012.

[56] Hou, S. *Review of Modal Synthesis Techniques a New Approach*. Tech. rep. Washington, D.C., Naval Research Laboratory, 1969, pp. 25–39.

[57] Hurty, W. “Vibrations of Structural Systems by Component Mode Synthesis”. In: *Journal of the Engineering Mechanics Division* 86.4 (1960), pp. 51–70. ISSN: 0044-7951.

[58] Hurty, W. C. “Dynamic analysis of structural systems using component modes”. In: *AIAA journal* 3.4 (1965), pp. 678–685. ISSN: 0001-1452. DOI: 10.2514/3.2947.

[59] Ibrahimbegovic, A. “On finite element implementation of geometrically nonlinear Reissner’s beam theory: three-dimensional curved beam elements”. In: *Computer Methods in Applied Mechanics and Engineering* 122.1 (1995), pp. 11–26. ISSN: 0045-7825. DOI: https://doi.org/10.1016/0045-7825(95)00724-F.

[60] Idelsohn, S. R. and Cardona, A. “A load-dependent basis for reduced nonlinear structural dynamics”. In: *Computers & Structures* 20.1-3 (Jan. 1985), pp. 203–210. ISSN: 0045-7949. DOI: 10.1016/0045-7949(85)90069-0.

[61] Idelsohn, S. R. and Cardona, A. “A reduction method for nonlinear structural dynamic analysis”. In: *Computer Methods in Applied Mechanics and Engineering* 49.3 (June 1985), pp. 253–279. ISSN: 0045-7825. DOI: 10.1016/0045-7825(85)90125-2.

[62] Jain, S. and Tiso, P. “Simulation-Free Hyper-Reduction for Geometrically Nonlinear Structural Dynamics A Quadratic Manifold Lifting Approach”. In: *ASME. J. Comput. Nonlinear Dynam* 13.7 (2018), pp. 071003–071003–12. DOI: 10.1115/1.4040021.

[63] Jain, S., Tiso, P., and Haller, G. “Exact nonlinear model reduction for a von Kármán beam: Slow-fast decomposition and spectral submanifolds”. In: *Journal of Sound and Vibration* 423 (2018), pp. 195–211. ISSN: 0022-460X. DOI: 10.1016/j.jsv.2018.01.049.

[64] Jain, S., Tiso, P., Rutzmoser, J. B., and Rixen, D. J. “A quadratic manifold for model order reduction of nonlinear structural dynamics”. In: *Computers and Structures* 188 (2017), pp. 80–94. ISSN: 00457949. DOI: 10.1016/j.compstruc.2017.04.005.

[65] Karamooz Mahdiabadi, M., Bartl, A., Xu, D., Tiso, P., and Rixen, D. J. “An augmented free-interface-based modal substructuring for nonlinear structural dynamics including interface reduction”. In: *Journal of Sound and Vibration* 462 (2019), p. 114915. ISSN: 0022-460X. DOI: https://doi.org/10.1016/j.jsv.2019.114915.

[66] Karamooz Mahdiabadi, M., Brandt, A., Tiso, P., and Rixen, D. J. “A non-intrusive model-order reduction of geometric nonlinear structural dynamics using modal derivatives”. In: *International Journal of Nonlinear Mechanics* (Submitted and under review).

[67] Karamooz Mahdiabadi, M., Buchmann, E., and Rixen, D. J. “Modal Substructuring of Geometrically Nonlinear Plates”. In: *PAMM* 17.1 (2017), pp. 515–516. ISSN: 1617-7061. DOI: 10.1002/pamm.201710227.

[68] Karamooz Mahdiabadi, M., Buchmann, E., Xu, D., Bartl, A., and Rixen, D. J. “Dynamic Substructuring of Geometrically Nonlinear Finite Element Models Using Residual Flexibility Modes”. In: *Dynamics of Coupled Structures, Volume 4, Springer International Publishing, 215-223*. Springer. 2017. DOI: 10.1007/978-3-319-54930-9_19.

[69] Karamooz Mahdiabadi, M., Qi, Y., and Rixen, D. J. “Experimental-Numerical Substructuring: a Comparison of Assemblies in Primal and Dual Forms”. In: *PAMM* 17.1 (2017), pp. 3–6. ISSN: 1617-7061. DOI: 10.1002/pamm.201710002.

[70] Karamooz Mahdiabadi, M. and Rixen, D. J. “Non-intrusive model-order reduction of geometrically nonlinear finite elements: enhancement with static augmentation”. In: *Proceedings of ISMA2018 including USD2018*. KU Leuven, 2018.

[71] Karamooz Mahdiabadi, M., Tiso, P., and Rixen, D. J. “An Enhanced modal substructuring of geometric nonlinear structure based on non-intrusive method”. In: *AIAA Journal* (In prepration).

[72] Kerfriden, P., Gosselet, P., Adhikari, S., and Bordas, S. “Bridging proper orthogonal decomposition methods and augmented Newton–Krylov algorithms: An adaptive model order reduction for highly nonlinear mechanical problems”. In: *Computer Methods in Applied Mechanics and Engineering* 200.5 (2011), pp. 850–866. ISSN: 0045-7825. DOI: https://doi.org/10.1016/j.cma.2010.10.009.

[73] Kerschen, G., Peeters, M., Golinval, J.-C., and Vakakis, A. F. "Nonlinear normal modes, Part I: A useful framework for the structural dynamicist". In: *Mechanical Systems and Signal Processing* 23.1 (2009), pp. 170–194.

[74] Kienholz, C. D. J. and A., D. "Finite Element Prediction of Damping in Structures with Constrained Viscoelastic Layers". In: *AIAA Journal* 20.9 (1982), pp. 1284–1290.

[75] Kim, K., Khanna, V., Wang, X. Q., and Mignolet, M. P. "Nonlinear Reduced Order Modeling of Flat Cantilevered Structures". In: *Proceedings of the 50th Structures, Structural Dynamics, and Materials Conference, Palm Springs, California, May*. May. 2009, pp. 4–7. ISBN: 9781563479731.

[76] Kim, K., Radu, A. G., Wang, X. Q., and Mignolet, M. P. "Nonlinear reduced order modeling of isotropic and functionally graded plates". In: *International Journal of Non-Linear Mechanics* 49.March 2013 (2013), pp. 100–110. ISSN: 00207462. DOI: 10.1016/j.ijnonlinmec.2012.07.008.

[77] Kim, S., Moon, W., and Yoo, Y. "An efficient method for calculating the nonlinear stiffness of progressive multi-leaf springs". In: *International Journal of Vehicle Design* 29.4 (2002), pp. 403–422. DOI: 10.1504/IJVD.2002.002021.

[78] Klerk, D. D., Rixen, D. J., and Voormeeren, S. N. "General Framework for Dynamic Substructuring: History, Review and Classification of Techniques". In: *AIAA Journal* 46.5 (2008), pp. 1169–1181. ISSN: 0001-1452. DOI: 10.2514/1.33274.

[79] Kokotovic, P., O'Malley, R., and Sannuti, P. "Singular perturbations and order reduction in control theory — An overview". In: *Automatica* 12.2 (1976), pp. 123–132. ISSN: 0005-1098. DOI: https://doi.org/10.1016/0005-1098(76)90076-5.

[80] Krattiger, D., Wu, L., Zacharczuk, M., Buck, M., Kuether, R. J., Allen, M. S., Tiso, P., and Brake, M. R. "Interface reduction for Hurty/Craig-Bampton substructured models: Review and improvements". In: *Mechanical Systems and Signal Processing* 114 (2019), pp. 579–603. ISSN: 08883270. DOI: 10.1016/j.ymssp.2018.05.031.

[81] Krishnan, V. *PROBABILITY AND RANDOM PROCESSES*. John Wiley & Sons, 2006. ISBN: 9780471998303. DOI: 10.1002/0471998303.

[82] Kuether, R. J., Allen, M. S., and Hollkamp, J. J. "Modal Substructuring of Geometrically Nonlinear Finite Element Models with Interface Reduction". In: *AIAA Journal* 55.5 (2017), pp. 1695–1706. ISSN: 0001-1452. DOI: 10.2514/1.J055215.

[83] Kuether, R. J., Deaner, B. J., Hollkamp, J. J., and Allen, M. S. "Evaluation of Geometrically Nonlinear Reduced-Order Models with Nonlinear Normal Modes". In: *AIAA Journal* 53.11 (2015), pp. 3273–3285. ISSN: 0001-1452. DOI: 10.2514/1.J053838.

[84] Kuether, R. J., Allen, M. S., and Hollkamp, J. J. "Modal Substructuring of Geometrically Nonlinear Finite-Element Models". In: *AIAA Journal* 54.2 (2015), pp. 1–12. ISSN: 0001-1452. DOI: 10.2514/1.J054036.

[85] Kuether, R. J. “Nonlinear Modal Substructuring of Geometrically Nonlinear Finite Element Models”. PhD thesis. Wisconsin-Madison, 2014, p. 181.

[86] Lassila, T., Manzoni, A., Quarteroni, A., and Rozza, G. “Model Order Reduction in Fluid Dynamics: Challenges and Perspectives”. In: *Reduced Order Methods for Modeling and Computational Reduction*. Ed. by Quarteroni, A. and Rozza, G. Cham: Springer International Publishing, 2014, pp. 235–273. ISBN: 978-3-319-02090-7. DOI: 10.1007/978-3-319-02090-7_9.

[87] Laursen, T. A. *Computational Contact and Impact Mechanics*. 1st ed. Springer-Verlag Berlin Heidelberg, 2003, p. 454. ISBN: 978-3-642-07685-5. DOI: 10.1007/978-3-662-04864-1.

[88] MacNeal, R. H. “A hybrid method of component mode synthesis”. In: *Computers and Structures* 1.4 (1971), pp. 581–601. DOI: 10.1016/0045-7949(71)90031-9.

[89] Mahmoud, M. S. “Order reduction and control of discrete systems”. In: *IEE Proceedings D - Control Theory and Applications* 129.4 (July 1982), pp. 129–135. ISSN: 0143-7054. DOI: 10.1049/ip-d:19820026.

[90] Manolas, D., Riziotis, V., and Voutsinas, S. “Assessing the Importance of Geometric Nonlinear Effects in the Prediction of Wind Turbine Blade Loads”. In: *ASME. J. Comput. Nonlinear Dynam* 10.4 (2015), pp. 041008–041008–15. DOI: 10.1115/1.4027684.

[91] Martinez, D. R., Carne, T. G., Gregory, D., and Miller, A. K. “Combined experimental / analytical modeling using component mode synthesis”. In: *25th Structures, Structural Dynamics and Materials Conference. Palm Springs, CA, U.S.A.*. 1984. DOI: 10.2514/6.1984-941.

[92] Martinez, D. R. and Gregory, D. L. *Comparison of free component mode synthesis techniques using MSC/NASTRAN*. Tech. rep. Albuquerque, NM: SAND83-0025, Sandia National Laboratories, 1984.

[93] Matney, A. “Reduced Order Model-Based Prediction of the Nonlinear Geometric Response of a Panel Under Thermal, Aerodynamic and Acoustic Loads”. PhD thesis. Arizona State University, 2014, p. 126.

[94] Matney, A., Perez, R., Spottswood, S., Wang, X., and Mignolet, M. “Nonlinear structural reduced order modeling methods for hypersonic structures”. In: *53rd AIAA/ASME/ASCE/AHS/ASC Structures, Structural Dynamics and Materials Conference*. April. AIAA, 2012. ISBN: 9781600869372 (ISBN). DOI: https://doi.org/10.2514/6.2012-1972.

[95] McEwan, M. I., Wright, J. R., Cooper, J. E., and Leung, A. Y. “A combined modal/finite element analysis technique for the dynamic response of a nonlinear beam to harmonic excitation”. In: *Journal of Sound and Vibration* 243.4 (2001), pp. 601–624. ISSN: 0022460X. DOI: 10.1006/jsvi.2000.3434.

[96] McEwan, M., Wright, J., Cooper, J., and Leung, A. “A finite element/modal technique for nonlinear plate and stiffened panel response prediction”. In: vol. 5. cited By 20. 2001, pp. 3061–3070.

[97] Mei, C. “A Finite-Element Approach for Nonlinear Panel Flutter”. In: *AIAA Journal* 15.8 (1977), pp. 1107–1110. DOI: 10.2514/3.60760.

[98] Mignolet, M. P., Przekop, A., Rizzi, S. A., and Spottswood, S. M. "A review of indirect/non-intrusive reduced order modeling of nonlinear geometric structures". In: *Journal of Sound and Vibration* 332.10 (2013), pp. 2437–2460. ISSN: 0022-460X. DOI: 10.1016/j.jsv.2012.10.017.

[99] Mignolet, M. P. and Radu, A. G. "Validation of Reduced Order Modeling for the Prediction of the Response and Fatigue Life of Panels Subjected To Thermo-Acoustic Effects". In: 55 (2003), pp. 14–16.

[100] Moore, B. "Principal component analysis in linear systems: Controllability, observability, and model reduction". In: *IEEE Transactions on Automatic Control* 26.1 (Feb. 1981), pp. 17–32. ISSN: 0018-9286. DOI: 10.1109/TAC.1981.1102568.

[101] Moore, G. E. "Cramming more components onto integrated circuits". In: *Electronics* 38 (1965), pp. 114–117.

[102] Mottershead, J. E., Link, M., and Friswell, M. I. "The sensitivity method in finite element model updating: A tutorial". In: *Mechanical Systems and Signal Processing* 25.7 (2011), pp. 2275–2296. ISSN: 0888-3270. DOI: 10.1016/j.ymssp.2010.10.012.

[103] Muravyov, A. A. and Rizzi, S. A. "Determination of nonlinear stiffness with application to random vibration of geometrically nonlinear structures". In: *Computers and Structures* 81.15 (2003), pp. 1513–1523. ISSN: 00457949. DOI: 10.1016/S0045-7949(03)00145-7.

[104] Nash, M. "Nonlinear Structure Dynamics by Finite Element Modal Synthesis". PhD thesis. Imperial College London, 1977.

[105] Nelson, R. B. "Simplified calculation of eigenvector derivatives". In: *AIAA Journal* 14.9 (1976), pp. 1201–1205. ISSN: 0001-1452. DOI: 10.2514/3.7211.

[106] Neuenhofer, A. and Filippou, F. C. "Geometrically Nonlinear Flexibility-Based Frame Finite Element". In: *Journal of Structural Engineering* 124.6 (1998), pp. 704–711. DOI: 10.1061/(ASCE)0733-9445(1998)124:6(704).

[107] Newmark, N. M. "A Method of Computation for Structural Dynamics". In: *Journal of the Engineering Mechanics Division* 85.3 (1959), pp. 67–94.

[108] Nilson, H. "Nonlinear Analysis of Reinforced Concrete by the Finite Element Method". In: *Journal Proceedings* 65.9 (1968), pp. 757–766. DOI: 10.14359/7510.

[109] Nilsson, O. "On Modeling and Nonlinear Model Reduction in Automotive Systems". PhD thesis. Department of Automatic Control, Lund Institute of Technology, Lund University, 2009.

[110] Noll, T. E., Brown, J. M., Perez-Davis, M. E., Ishmael, S. D., Tiffany, G. C., and Gaier, M. *Investigation of the Helios Prototype Aircraft Mishap*. Tech. rep. Hampton, VA: NASA, 2004, p. 100.

[111] Orfanidis, S. J. *Introduction to signal processing*. Prentice Hall, 1996. ISBN: 0-13-209172-0.

[112] Peeters, M., Viguié, R., Sérandour, G., Kerschen, G., and Golinval, J.-C. "Nonlinear normal modes, Part II: Toward a practical computation using numerical continuation techniques". In: *Mechanical systems and signal processing* 23.1 (2009), pp. 195–216.

[113] Perez, R., Bartram, G., Beberniss, T., Wiebe, R., and Spottswood, S. "Calibration of aero-structural reduced order models using full-field experimental measurements". In: *Mechanical Systems and Signal Processing* 86 (2017). Full-field, non-contact vibration measurement methods: comparisons and applications, pp. 49–65. ISSN: 0888-3270. DOI: 10.1016/j.ymssp.2016.04.013.

[114] Perez, R., Wang, X. Q., and Mignolet, M. P. "Nonlinear reduced order models for thermo-elastodynamic response of isotropic and FGM panels". In: *AIAA Journal* 49 (2011), pp. 630–641.

[115] Perez, R. A. "Multiscale Reduced Order Models for the Geometrically Nonlinear Response of Complex Structures". PhD Thesis. Arizona State University, 2012, p. 153.

[116] Perez, R., Wang, X. Q., and Mignolet, M. P. "Nonintrusive Structural Dynamic Reduced Order Modeling for Large Deformations: Enhancements for Complex Structures". In: *Journal of Computational and Nonlinear Dynamics* 9 (2014), pp. 031008–12. ISSN: 1555-1415. DOI: 10.1115/1.4026155.

[117] Praveen, G. and Reddy, J. "Nonlinear transient thermoelastic analysis of functionally graded ceramic-metal plates". In: *International Journal of Solids and Structures* 35.33 (1998), pp. 4457–4476. ISSN: 0020-7683. DOI: 10.1016/S0020-7683(97)00253-9.

[118] Przekop, A. and Rizzi, S. "Efficient modal basis selection criteria for reduced-order nonlinear simulation". In: *7th European Conference on Structural Dynamics, EURODYN 2008*. Southampton, 2008.

[119] Przekop, A. "Dynamic Snap-Through of Thin-Walled Structures". In: *AIAA Journal* 45.Ottober (2007), pp. 2510–2519. DOI: 10.2514/1.26351.

[120] Przekop, A. and Rizzi, S. A. "Nonlinear Reduced-Order Analysis with Time-Varying Spatial Loading Distributions". In: *Journal of Aircraft* 46.4 (2009), pp. 1395–1402. ISSN: 0021-8669. DOI: 10.2514/1.39790.

[121] Przekop, A. and Rizzi, S. a. "Nonlinear Reduced Order Random Response Analysis of Structures with Shallow Curvature". In: *AIAA Journal* 44.8 (2006), pp. 1767–1778. ISSN: 0001-1452. DOI: 10.2514/1.18868.

[122] Qi, Y. "Experimental-Analytical Substructuring in Dual Form Using the Transmission Simulator Method". Master Thesis. Technical University of Munich, 2017.

[123] Ravindran, S. S. "A reduced-order approach for optimal control of fluids using proper orthogonal decomposition". In: *International Journal for Numerical Methods in Fluids* 34.5 (2000), pp. 425–448. DOI: 10.1002/1097-0363(20001115)34:5<425::AID-FLD67>3.0.CO;2-W.

[124] Rayleigh, J. W. S. *The Theory of Sound*. London: University of Cambridge Press, 1877.

[125] Rewienski, M. and White, J. “A trajectory piecewise-linear approach to model order reduction and fast simulation of nonlinear circuits and micromachined devices”. In: *IEEE Transactions on Computer-Aided Design of Integrated Circuits and Systems* 22.2 (Feb. 2003), pp. 155–170. ISSN: 0278-0070. DOI: 10.1109/TCAD.2002.806601.

[126] Rewienski, M. and White, J. “Improving Tra jectory Piecewise-Linear Approach to Nonlinear Model Order Reduction for Micromachined Devices Using an Aggregated Pro jection Basis”. In: *TechConnect Briefs* (2002), pp. 128–131.

[127] Rezaei, M. M., Behzad, M., Haddadpour, H., and Moradi, H. “Development of a reduced order model for nonlinear analysis of the wind turbine blade dynamics”. In: *Renewable Energy* 76 (2015), pp. 264–282. ISSN: 0960-1481. DOI: 10.1016/j.renene.2014.11.021.

[128] Rienstra, S. and Hirschberg, A. *An Introduction to Acoustics*. Eindhoven: Eindhoven University of Technology, 2004.

[129] Riks, E. “An incremental approach to the solution of snapping and buckling problems”. In: *International Journal of Solids and Structures* 15.7 (1979), pp. 529–551. ISSN: 0020-7683. DOI: https://doi.org/10.1016/0020-7683(79)90081-7.

[130] Rixen, D. “Generalized Mode Acceleration methods and Modal Truncation Augmentation”. In: *Structures, Structural Dynamics and Material Conference and Exhibit*. 42st AIAA/ASME/ASCE/AHS/ASC. Seattle, WA, USA, Apr. 2001.

[131] Rixen, D. J. “A dual Craig-Bampton method for dynamic substructuring”. In: *Journal of Computational and Applied Mathematics* 168.1-2 (2004), pp. 383–391. DOI: 10.1016/j.cam.2003.12.014.

[132] Rizzi, S. A. and Przekop, A. “System identification-guided basis selection for reduced-order nonlinear response analysis”. In: *Journal of Sound and Vibration* 315.3 (2008), pp. 467–485. ISSN: 0022460X. DOI: 10.1016/j.jsv.2007.12.031.

[133] Rizzi, S. A. and Przekop, A. *The Effect of Basis Selection on Static and Random Acoustic Response Prediction Using a Nonlinear Modal Simulation*. Tech. rep. December. NASA/TP-2005-213943, 2005.

[134] Rosenberg, R. M. “Normal modes of nonlinear dual-mode systems”. In: *Journal of Applied Mechanics* 27.2 (1960), pp. 263–268.

[135] Rubin, S. “Improved Component-Mode Representation for Structural Dynamic Analysis”. In: *AIAA Journal* 13.8 (1975), pp. 995–1006. ISSN: 0001-1452. DOI: 10.2514/3.60497.

[136] Rutzmoser, J. B., Rixen, D. J., Tiso, P., and Jain, S. “Generalization of Quadratic Manifolds for Reduced Order Modeling of Nonlinear Structural Dynamics”. In: *Computers & Structures* 192 (2017), pp. 196–209. DOI: 10.1016/j.compstruc.2017.06.003. eprint: 1610.09906.

[137] Rutzmoser, J. and Rixen, D. “A lean and efficient snapshot generation technique for the Hyper-Reduction of nonlinear structural dynamics”. In: *Computer Methods in Applied Mechanics and Engineering* 325 (2017), pp. 330–349. ISSN: 0045-7825. DOI: 10.1016/j.cma.2017.06.009.

[138] Rutzmoser, J. “Model Order Reduction for Nonlinear Structural Dynamics”. Dissertation. München: Technische Universität München, 2018.

[139] Saied, S. A., Abbaszadeh, K., and Fadaie, M. “Reduced Order Model of Developed Magnetic Equivalent Circuit in Electrical Machine Modeling”. In: *IEEE Transactions on Magnetics* 46.7 (July 2010), pp. 2649–2655. ISSN: 0018-9464. DOI: 10.1109/TMAG.2010.2044511.

[140] Saxena, S. and Hote, Y. V. “Load Frequency Control in Power Systems via Internal Model Control Scheme and Model-Order Reduction”. In: *IEEE Transactions on Power Systems* 28.3 (2013), pp. 2749–2757. ISSN: 0885-8950. DOI: 10.1109/TPWRS.2013.2245349.

[141] Schaefer, P. “Efficient Hyper-Reduction in Geometrical Nonlinear Finite Element Analysis”. Semester Thesis. Technical University of Munich, 2018.

[142] SHARIFI, P. and YATES, D. “Nonlinear Thermo-Elastic-Plastic and Creep Analysis by the Finite-Element Method”. In: *AIAA Journal* 12.9 (1974), pp. 1210–1215. DOI: 10.2514/3.49455.

[143] Siewert, C., Panning, L., Wallaschek, J., and Richter, C. “Multiharmonic Forced Response Analysis of a Turbine Blading Coupled by Nonlinear Contact Forces”. In: *ASME. J. Eng. Gas Turbines Power* 132.8 (2010). DOI: 10.1115/1.4000266.

[144] Slaats, P. M. A., Jongh, J. de, and Sauren, A. “Model Reduction Tools for Nonlinear Structural Dynamics”. In: *Computers & Structures* 54.6 (1995), pp. 1155–1171.

[145] Sofyan, S. “Evaluation of Component Mode Synthesis Methods based on Higher Order Static Correction Modes with Interface Reduction”. Semester Thesis. Technical University of Munich, 2018.

[146] Sombroek, C., Tiso, P., Renson, L., and Kerschen, G. “Numerical computation of nonlinear normal modes in a modal derivative subspace”. In: *Computers and Structures* 195 (2018), pp. 34–46. ISSN: 0045-7949. DOI: 10.1016/j.compstruc.2017.08.016.

[147] Spottswood, S. M., Eason, T. G., Wang, X. Q., and Mignolet, M. P. “Nonlinear Reduced Order Modeling of Curved Beams : a Comparison of Methods”. In: *Proceedings of the 50th Structures, Structural Dynamics, and Materials Conference* May (2009), pp. 1–14. ISSN: 02734508. DOI: 10.2514/6.2009-2433.

[148] Spottswood, S. M. and Allemang, R. J. “Identification of nonlinear parameters for reduced order models”. In: *Journal of Sound and Vibration* 295.1-2 (2006), pp. 226–245. ISSN: 10958568. DOI: 10.1016/j.jsv.2006.01.009.

[149] Spottswood, S. and Allemang, R. “Identifying nonlinear parameters for reduced order models. Part II, validation using experimental data”. In: 2006.

[150] Spottswood, S. M., Hollkamp, J. J., and Eason, T. G. “Reduced-Order Models for a Shallow Curved Beam Under Combined Loading”. In: *AIAA Journal* 48.1 (2010), pp. 47–55. ISSN: 0001-1452. DOI: 10.2514/1.38707.

[151] Stein, M. *Interpolation of Spatial Data: Some Theory for Kriging*. New York: Springer, 1999. ISBN: 978-1-4612-7166-6. DOI: 10.1007/978-1-4612-1494-6.

[152] Stoica, P. and Moses, R. *SPECTRAL ANALYSIS OF SIGNALS*. New Jersey: Prentice Hall, 2005. ISBN: 0-13-113956-8.

[153] Tabod, G. "Non-intrusive dynamic substructuring of geometric nonlinear finite element models: a comparison of methods". Semester Thesis. Technical University of Munich, 2019.

[154] Tiso, P. "Reduction Method for Finite Element Nonlinear Dynamic Analysis of Shells". In: 49.10 (2011). DOI: 10.2514/1.J051003.

[155] Tran, D. M. "Component mode synthesis methods using interface modes. Application to structures with cyclic symmetry". In: *Computers and Structures* 79.2 (2001), pp. 209–222. ISSN: 00457949. DOI: 10.1016/S0045-7949(00)00121-8.

[156] Tschida, T. *Dryden Flight Research Center*. 1999. URL: https://www.dfrc.nasa.gov/Gallery/Photo/Helios/Large/EC99-45210-1.jpg.

[157] Wenneker, F. and Tiso, P. "A Substructuring Method for Geometrically Nonlinear Structures". In: *Dynamics of Coupled Structures, Volume 1: Proceedings of the 32nd IMAC, A Conference and Exposition on Structural Dynamics, 2014*. Ed. by Allen, M., Mayes, R., and Rixen, D. Cham: Springer International Publishing, 2014, pp. 157–165. DOI: 10.1007/978-3-319-04501-6_14.

[158] Willcox, K. and Peraire, J. "Balanced Model Reduction via the Proper Orthogonal Decomposition". In: *AIAA Journal* 40.11 (2002), pp. 2323–2330. ISSN: 0001-1452. DOI: 10.2514/2.1570.

[159] Wilson, E. L. "Dynamic Analysis By Direct Superposition of Ritz Vectors". In: *Earthquake Engineering and Structural Dynamics* 10.October 1981 (1982), pp. 813–821. DOI: 10.1002/eqe.4290100606.

[160] Wood, R. and Zienkiewicz, O. "Geometrically nonlinear finite element analysis of beams, frames, arches and axisymmetric shells". In: *Computers & Structures* 7.6 (1977), pp. 725–735. DOI: 10.1016/0045-7949(77)90027-X.

[161] Wriggers, P. *Nonlinear Finite Element Methods*. Springer Berlin Heidelberg, 2010. ISBN: 9783642090028.

[162] Wu, L., Tiso, P., and Keulen, F. V. "A modal derivatives enhanced Craig-Bampton method for geometrically nonlinear structural dynamics". In: Proceedings of ISMA 2016 - International Conference on Noise and Vibration Engineering, 2016, pp. 3615–3524.

[163] Wu, L. "Model order reduction and substructuring methods for nonlinear structural dynamics". PhD thesis. Delft University of Technology, 2018. DOI: 10.4233/uuid:f9736e8b-d00f-4e25-b456-48bd65b43788.

[164] Wu, L. and Tiso, P. "Nonlinear model order reduction for flexible multibody dynamics: a modal derivatives approach". In: *Multibody System Dynamics* 36.4 (2016), pp. 405–425. DOI: 10.1007/s11044-015-9476-5.

[165] Wu, L., Tiso, P., Tatsis, K., Chatzi, E., and Keulen, F. van. “A modal derivatives enhanced Rubin substructuring method for geometrically nonlinear multibody systems”. In: *Multibody System Dynamics* 45.1 (Jan. 2019), pp. 57–85. ISSN: 1573-272X. DOI: 10.1007/s11044-018-09644-2.

[166] Xu, D. “Dynamic Substructuring of Geometrically Nonlinear FEMs Using Craig-Bampton Method as a Linear Basis”. Semester Thesis. Technical University of Munich, 2016.

[167] Xu, D. “Hyper reduction of geometric nonlinear finite element models using quadratic manifold method”. Master Thesis. Technical University of Munich, 2018.

[168] Zhang, J., Guo, L., Wu, H., Zhou, A., Hu, D., and Ren, J. “The influence of wind shear on vibration of geometrically nonlinear wind turbine blade under fluid–structure interaction”. In: *Ocean Engineering* 84 (2014), pp. 14–19. ISSN: 0029-8018. DOI: 10.1016/j.oceaneng.2014.03.017.

[169] Zhu, Y. “Non-intrusive reduced order modeling of geometric nonlinear finite element models with tangent stiffness”. Master Thesis. Technical University of Munich, 2017.